DISSERTATION

GLOBAL MAPPING OF ATTENUATION AT KU- AND KA- BANDS: STATISTICAL AND MICROPHYSICAL STUDIES

Submitted by

Khalid Mubarak

Department of Electrical and Computer Engineering

In partial fulfillment of the requirements

for the Degree of Doctor of Philosophy

Colorado State University

Fort Collins, Colorado

Fall, 2003

COLORADO STATE UNIVERSITY

August 26th, 2003

WE HEREBY RECOMMEND THAT THE DISSERTATION PREPARED UNDER OUR SUPERVISION BY KHALID MUBARAK ENTITLED GLOBAL MAPPING OF ATTENUATION AT KU- AND KA- BANDS: STATISTICAL AND MICROPHYSICAL STUDIES BE ACCEPTED AS FULFILLING IN PART REQUIREMENTS FOR THE DEGREE OF DOCTOR OF PHILOSOPHY.

Committee on Graduate Work

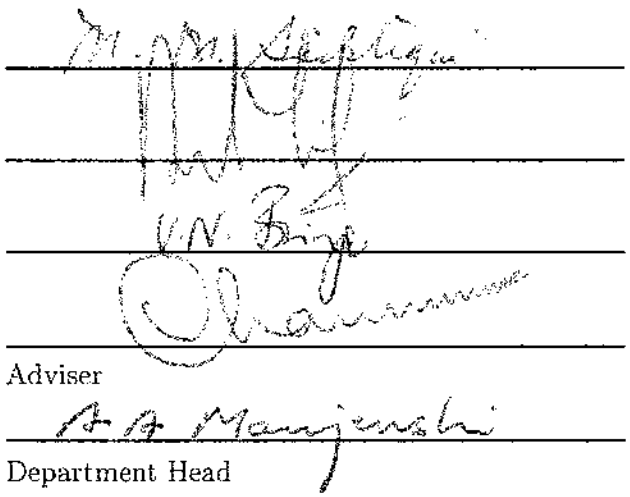

Adviser

Department Head

ABSTRACT OF DISSERTATION

GLOBAL MAPPING OF ATTENUATION AT KU- AND KA- BANDS: STATISTICAL AND MICROPHYSICAL STUDIES

The propagation of radio waves for earth-space slant path at C-band and higher frequencies are dominated by precipitation in the atmosphere. At a given frequency, attenuation depends on the length of the radio path, the size distribution and the phase state of the hydrometeor profile. Using the observations from the Tropical Rainfall Measurements Mission (TRMM) spaceborne Ku-band (13.8GHz) radar at Low Earth Orbit of 350km above earth, global attenuation maps are produced at the Ku-band frequency. A simple precipitation microphysical model developed using hydrometeor size distributions and thermodynamic phase state is used to estimate attenuation and reflectivity observations at Ka-band (35GHz) where numerous high bandwidth satellite applications are being planned including the next generation space-based radar for the Global Precipitation Mission (GPM). Differences in the microphysical structure in convective and stratiform precipitation are also incorporated in the model. The results show substantial attenuation variation in a 12-month period at both Ku- and Ka-bands over the various regions of the globe. Including the contrast between land and ocean, the estimates made at Ku- and Ka-band will be useful in the design and development of space systems.

The precipitation radar uses surface reference method to estimate the attenuation encountered in the observation of radar reflectivity. The cumulative attenuation (A) estimated from the surface reference method can be distributed along the

radar range using a power law relation between the specific attenuation (k) and reflectivity factor (Z) written as, $k = \alpha Z^{\beta}$. A commonly used approximation is that β is constant and α changes according to the precipitation microphysics. More recently physical interpretation of α has been provided with the normalized drop size distributions. This research describes a procedure to estimate the raindrop size distribution (RSD) parameters from the measured attenuation and reflectivity values obtained from TRMM precipitation radar observations at a global scale. Coincident data collected with ground radar during the TRMM field campaigns have been used to cross-validate the estimates of RSD parameters obtained from TRMM precipitation radar measurements with those obtained from ground polarimetric radar observations. The results of cross-validation show fairly good agreement with the RSD parameters retrieved from TRMM precipitation radar and the ground radar based estimates. The algorithm is also used to generate monthly global maps of RSD parameters.

Finally, data from TRMM are used to examine the surface cross section as well as the height of bright band (HBB) over the ocean and land in rain and rain-free regions.

Khalid Mubarak
Department of Electrical and Computer Engineering
Colorado State University
Fort Collins, Colorado 80523
Fall, 2003

ACKNOWLEDGEMENTS

First of all, I would like to thank God for everything. I also would like to thank everyone who helped me during this project. I am especially thankful to my advisor Dr. V. Chandrasekar for his kindness, support, guidance, and encouragement during my graduate study. Also, I would like to express my gratitude to Dr. Derek Lile, Dr. V. N. Bringi and Dr. Paul Mielke for serving as my committee members.

During all my research effort, I received much help from the crew at the Radar and Communication Group. Here, I would like to express my sincere thanks to Dr. Wanyu Li, Dr. Gwo Huang, Dr. Awad Al-Zaben, Basim Zafar, Sang Lim and Konrad Gojara for their friendship and for their help during this project. This research is supported by the NASA-TRMM program.

I would also like to thank Emirates Telecommunication Corporation Company, and the especially to Etisalat College of Engineering for their financial support and for being my sponsor during my study abroad.

Also, I would like to thank my parents, brothers and sisters for their love and support while I was far away from home.

Finally, I would like to thank my wife (Badria) and my sons (Fahad, Hamad and Suood) for their love and support and engorgement and being there when I needed them.

TABLE OF CONTENTS

LIST OF FIGURES

LIST OF TABLES

Chapter 1

INTRODUCTION

1.1 General Description of the Problem

The potential use of space-based radar for meteorological interests was first explored as early as the mid 1950s (Wexler, 1954, 1957; and, Widger and Touart, 1957). But, due to the technical limitations of space craft components to meet the required science objectives (Dennis, 1963a and 1963b), it remained largely neglected in the United States until the mid 1970s when meteorological applications were reevaluated as technology advanced. During this time, one of the catalysts for the renewed interest stemmed from the science planning for the space shuttle orbiter program (Eckerman, 1975). Over the next 2 decades following this period, various systems were studied and proposed. During the last decade, an increasing number of studies investigated the use of radar in addition to passive techniques (visible, infrared, and microwave radiometry) for future space-based rainfall measurements. Several profiling methods were also proposed during this time, such as dual beam systems (Testude, et al., 1992) and dual frequency systems (Goldhirsh, 1988; Im and Li, 1989; and, Im and Kellog, 1990).

While the use of space-based platforms for making meteorological observations on a global, synoptic and climatological scale is of scientific value, the cost of these systems, however, can be substantial. Short wavelength radars can be used to reduce costs by deploying smaller antennas while maintaining the required

resolution necessary for adequate meteorological sampling (Meneghini and Kuzo, 1990).

With an increased demand in satellite communications, the current spectrum allocations at C- and Ku-bands are quickly becoming over crowded. This has led to an increased interest from industry to utilize the Ku- and Ka- bands frequency spectrum. Currently, several industry leaders are in the process of developing satellite communications systems that operate at the Ka-band frequencies or already have systems in place (Beaver and Bringi, 1997). Benefits of operating at the Ka-band frequencies include increase in data transmission rates and the amount of data transmitted, smaller earth receiving stations, which leads to greater mobility. Along, with the benefits of operating at these frequencies, however, there are some disadvantages, such as increased attenuation effects due to atmospheric conditions (Beaver and Bringi, 1997). One of the attractive features that led to the use of the lower frequency for satellite communications was the low susceptibility to attenuation effects caused by rain or clouds. The larger wavelengths are minimally affected by atmospheric conditions. The Ka-band frequencies, however, are very susceptible to weather-related events. Rain, clouds, and even gaseous absorption by oxygen and water vapor can adversely affect the signal and must be considered. Rain can easily produce 20-30 dB of attenuation at the Ka-band frequencies (Beaver and Bringi, 1997). Thus, estimation of attenuation and intrinsic reflectivity are some of the most important issues for space borne radar operations.

For systems operating with a single attenuation frequency, Hitschfeld and Bordan (1954) were among the first to propose a method of attenuation estimation by forward integration of the backscattered radar signal by using a power-law relation ($k = \alpha Z^{\beta}$). This method gives a reasonable estimate if the attenuation effect is small. However, when the attenuation is large, the Hitschfeld-Bordan solution can become unstable unless the raindrop size distribution (RSD) along the

path and radar constant are known to a high degree, which is seldom the case. To solve this instability problem, the surface reference technique (SRT) has been proposed (Iguchi and Meneghini, 1994; Marzoug and Amayence, 1994; Marzoug and Amayence, 1991; Kozu and Nakamura, 1991a and 1991b; Meneghini, 1978; Meneghini et al., 1983; and Menghini and Nakamura 1990). SRT estimates the path integration attenuation (PIA) through rain from the decrease in the surface return. In particular, an estimate of the attenuation factor at the surface is obtained from the ratio of the surface return power measured in rain to that measured in adjacent rain-free areas.

Data collected from airborne experiments was used in several studies such as: Meneghini et al. (1989), Meneghini and Nakamura (1990), Fujita et al. (1985), Marzoug and Amayenc (1991, 1992, and 1993), and Amayence and Marzoug (1992) to evaluate various attenuation estimation and rain rate retrieval schemes. Beaver and Bringi (1997) used becan data from the advanced Communication Technology Satellite (ACTS) and radar data from the Colorado State University (CSU) CHILL radar facility to characterize the relationship between Ka-band attenuation and the ground radar observations.

In November 1997, the Tropical Rainfall Measuring Mission (TRMM) observatory was launched as a joint project between the United States National Aeronautics and Space Administration (NASA) and the Japanese National Space Agency (NASDA). TRMM is the first mission dedicated to measuring the vertical distribution of tropical and subtropical rainfall through microwave and visible infrared sensors, and includes the first spaceborne radar to observe precipitation. TRMM was developed by the collaboration of two nations. The National Space Development Agency of Japan (NASDA) provided the Precipitation Radar (PR) and an H-II rocket that launched the TRMM observatory and NASA's Goddard Space Flight Center (GSFC) in Greenbelt, Md., provided the observatory, four

instruments, integration and test of the observatory.

1.2 Objectives of the Research

The following are the main objectives of this research:

- To obtain a global map of attenuation and reflectivity over various frequency bands. First, precipitation-induced attenuation at 13.8 GHz is calculated from TRMM data to map global attenuation and then this data was used to estimate attenuation at another frequency such as 35 GHZ. Data from TRMM are used to develop monthly maps of attenuation, in the earth-space propagation paths, over the tropical regions of the globe at Ku-band. A simple precipitation model is developed that consists of layers of hydrometeors as a function of altitude such as ice crystals, aggregates, graupel and rain. Using the hydrometeor size distribution as well as the thermodynamic phase states as the descriptors, estimates of specific attenuation and reflectivity at Ka-band are obtained from Ku-band observations.

- To develop an estimate the raindrop size distribution (RSD) parameters from TRMM precipitation radar observations. Cross validate the TRMM RSD retrievals with coincident data collected with ground radar.

- To develop and obtain monthly maps of RSD parameters over the tropical region of the globe at Ku-band.

- Study of surface cross section (σ^0) as a function of rain/rain-free for the same region. Estimates of rain rate from the PR aboard the TRMM satellite requires a means by which the radar signal attenuation can be corrected. One of the methods available is the surface reference technique in which the

radar surface return in rain-free areas is used as a reference against which the path-integrated attenuation is obtained. Despite the simplicity of the basic concept, an assessment of the reliability of the technique is difficult because the statistical properties of the surface return depend not only on surface type (land/ocean) and incident angle, but also on the detailed nature of the surface scattering.

- Study in detail the global statistics of the melting layer using TRMM data.

1.3 Overview of the Dissertation

The dissertation is organized as follows:

Chapter 2 - TRMM system and Data Characteristics

This chapter provides the overview of the TRMM spacecraft systems, the TRMM Precipitation Radar (PR) parameters and the scan geometry and finally the TRMM data characteristics for PR that used in this research.

Chapter 3 - Attenuation Correction Background and theoretical models

This chapter describes the background of attenuation correction used in TRMM (Ku-band) algorithm such as surface reference technique (SRT) and Hitschfeld-Bordan method. Also this chapter provides the theoretical computation results of attenuation and reflectivity through various hydrometeors such as rain, graupel, aggregates of ice crystal and snow at Ku- and Ka- bands.

Chapter 4 - Global Map of Attenuation and Reflectivity

This chapter describes the microphysical model, which was developed in order to estimate the attenuation as well as the observed reflectivity pattern at Ka-band. Global maps of attenuation, reflectivities, and reflectivity ratio are presented in this chapter. The results of the measured attenuation are presented as monthly maps over the globe for a 12-month period, for the year 2000. Estimated attenuation maps for a 12-month period useful for both radar and communication applications are presented for Ka-band (35 GHz).

Chapter 5 - Estimation of Raindrop Size Distribution

This chapter describes a procedure to estimate the raindrop size distribution (RSD) parameters from the measured attenuation and reflectivity values obtained from TRMM PR observations. Coincident data collected with ground radar during the TRMM field campaigns have been used to cross-validate the estimates of RSD parameters obtained from TRMM PR measurements with those obtained from ground polarimetric radar observations. Finally, the algorithm is also used to generate monthly global maps of RSD parameters.

Chapter 6 - Examination of the Surface Cross Section Statistics over Ocean and Land

This chapter provides a brief description of the surface reference technique (SRT) algorithm for the TRMM PR, the basic equations of the SRT, the behavior of the surface cross sections and their statistics, examples of sample results of

the SRT as a function of rain/rain-free regions and finally a global map of σ^0 for no-rain as a function of incident angle. These maps are represented as a monthly average of normalized radar surface cross section for the year of 2000.

Chapter 7 - Melting Layer

This chapter presents a statistical study of the melting layer. Statistics of the height and thickness of the bright band (BB) over the land and ocean and as well in tropical systems are presented.

Chapter 8 - Summary and Suggestion for Future Work

The results of the research are summarized and the major contributions of the dissertation are reviewed. Suggestions for future work are proposed.

Chapter 2

TRMM SYSTEM AND DATA CHARACTERISTICS

2.1 Introduction

In November 1997 a successful mission called the Tropical Rain Measuring Mission (TRMM), which includes the first spaceborne radar for observing precipitation, was launched. This project was a joint project between the United States National Aeronautics and Space Administration (NASA) and the Japanese National Space Development Agency (NASDA). The Precipitation Radar (PR), on board the satellite, is the first weather radar to be deployed in space and is one of several instruments being used to provide a three-dimensional structure of rainfall by measuring the radar reflectivity of the cloud system and the attenuation of a signal as it passes through the precipitation. The major advantage of such a system is its global coverage. These measurements include large ocean areas where our knowledge of precipitation is poor. Important applications of this project are immediate practical benefits to agricultural, water resources management, and flood warnings (TRMM, 2000). This chapter provides the overview of the TRMM spacecraft systems, PR parameters, the scan geometry, and finally its data characteristics.

2.2 Spacecraft

The TRMM Observatory is comprised of a main body structure, eight housekeeping subsystems, and five science instruments. Table 2.1 adapted from the TRMM handbook (2001) shows the main characteristics of the TRMM satellite.

Parameter	Value
Launch weight	Approx. 3.62 ton
Launcher	H-II Rocket
Launch date (JST)	November 28, 1997
Altitude	Approx. 350 km, boosted to 402 km by August 2001
Inclination	Approx. 35 degrees
Weight	Total: 3620 kg [3524 kg] Fuel: 890 kg Dry weight: 2730 kg [2634 kg]
Power	Approx. 1100 W [Ave. 850 W]
Attitude control	Zero momentum three-axis stabilized
Data transmission	via TDRS 32Kbps (Real Time), 2Mbps (Play Back)
Design life	3 years and 2 months
Mission instrument	Precipitation Radar (PR) TRMM Microwave Imager (TMI) Visible and Infrared Scanner (VIRS) Clouds and the Earths Radiant Energy System (CERES) Lightning Imaging Sensor (LIS)

[ ] means the measured value.

Table 2.1: Main Characteristics of the TRMM Satellite (Ref:TRMM handbook, 2001).

2.3 PR Radar and the Scan Geometry

The TRMM Precipitation Radar (PR) is one of the five instruments on the TRMM satellite. PR records power reflected from precipitation and surface targets. The principle objectives of this radar are:

1. Provide a three-dimensional description of the rain profile.
2. Obtain a quantitative estimation of rainfall over land and ocean.
3. Improve the overall accuracy of precipitation retrieval algorithms by combining the active and passive systems on the TRMM satellite.

The TRMM PR, built by the National Space and Development Agency of Japan, operates at a frequency of 13.8 GHz (Ku-band) and uses a 2m x 2m phased-array antenna consisting of 128 slotted waveguides. A peak power greater than 500 W is achieved using 128 solid-state power amplifiers. The PR electronically scans from right to left, looking in the flight direction across the ground track of the satellite every 0.6 seconds, with a horizontal resolution at the ground of 4.3 km and a swath width of 215 km. Figure 2.1 shows the concept of the TRMM PR while the complex scan geometry is represented in Figure 2.2.

The starting distance and the number of samples are different for each ray. Rays other than nadir also sample below the surface. The purpose of this extension below the surface is to clearly detect the location of the surface. One of the PR's most important features is the ability to provide vertical profiles of rain and snow from the surface up to a height of about 20 km.

One orbit of the satellite from its southernmost latitude to the next southernmost latitude is called a granule. One granule takes 5490 seconds (9150 scans on average) and the satellite orbits the earth about 16 times a day (Figure 2.3).

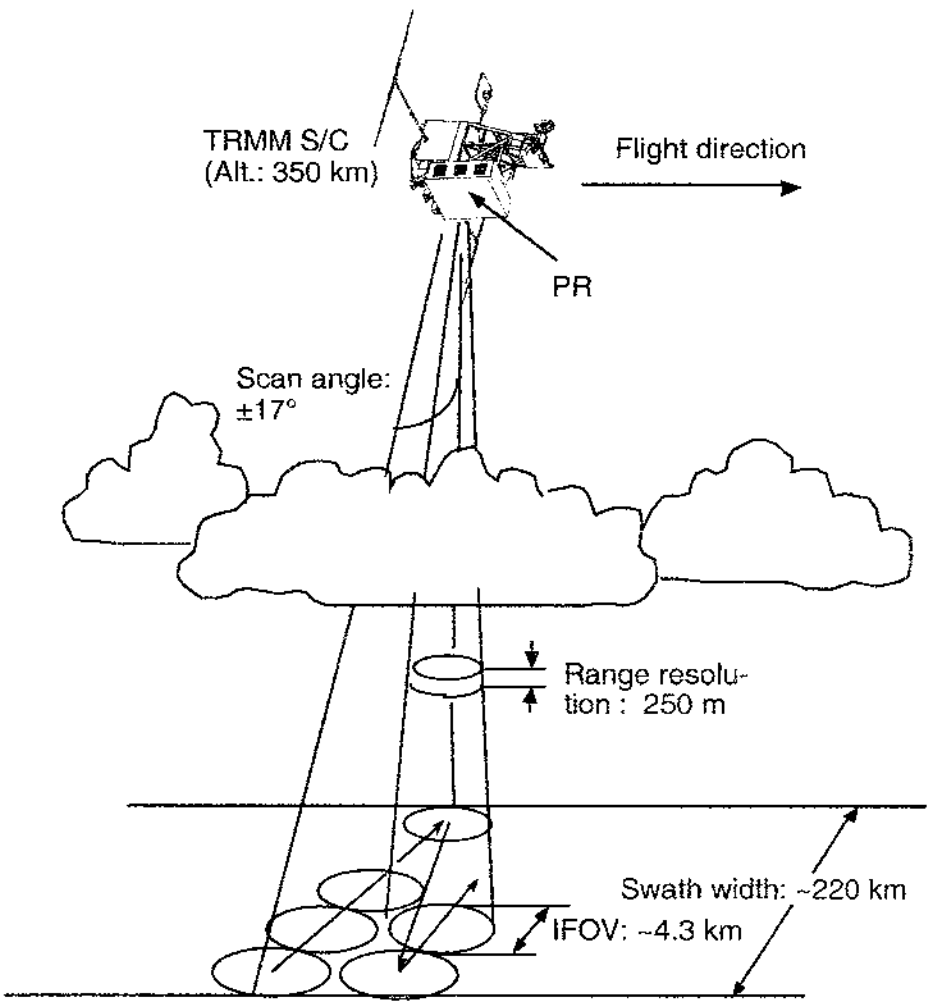

Figure 2.1: Observation concept of the PR (adapted from TRMM handbook, 2001).

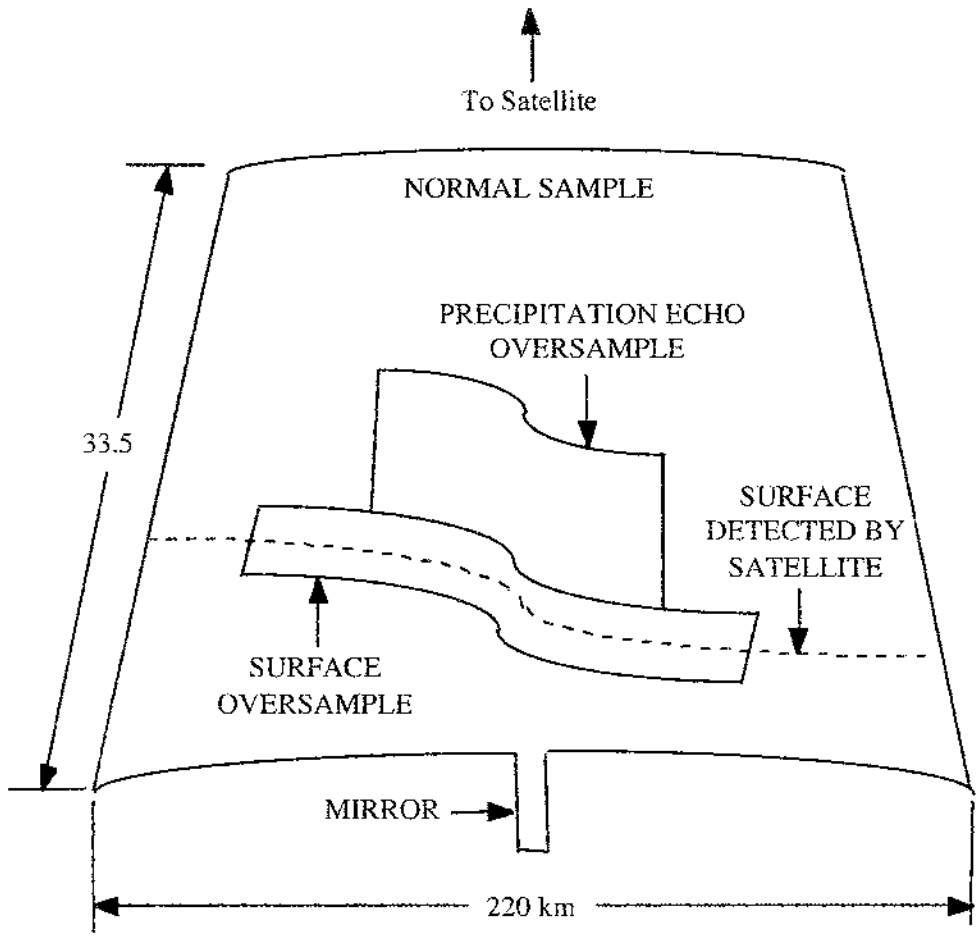

The outer outline encloses the normal sample. The rain echo oversample and the surface oversample occupy subsets of the normal sample region. Both oversamples are vertically located with respect to the surface level detected by the satellite.

Figure 2.2: PR scan geometry (adapted from TRMM handbook, 2001).

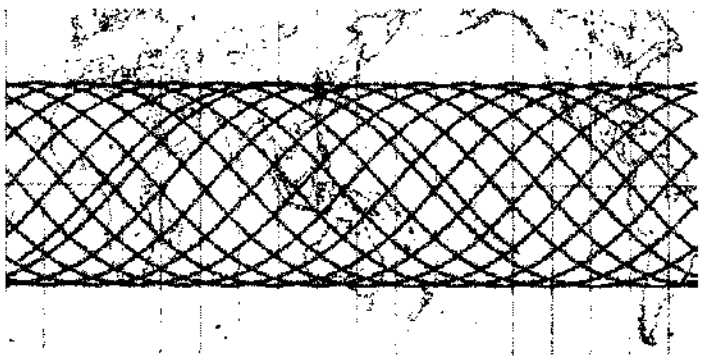

Figure 2.3: Satellite orbit for a day (adapted from TRMM handbook, 2001).

Each PR scan contains 49 rays over an angular sector of 34 degrees. For any given ray, the satellite begins recording samples at a fixed distance from the satellite and records a certain number of samples along the ray. The PR is able to detect fairly light rain rates down to 0.7 mm/h. At intense rain rates, where the attenuation effects can be strong, new methods of processing have been developed that help correct for this effect. The PR is able to separate out rain echoes for vertical sample size of about 250 m when looking straight down. Assuming the satellite altitude is 350 km, the sampling begins about 23 km above mean sea level and extends for a certain distance along the ray. This distance along the ray is 33.5 km at the two rays farthest from nadir, monotonously declining to 30.25 km at the two rays adjacent to nadir, and jumping to 34.75 km at the single nadir ray. The extra data in the nadir ray is known as the mirror, because it records energy reflected not once from a target, but three times (ground to target to ground). Rays other than the nadir ray also sample below the surface.

The satellite saves data in three samples. Every other data point in the vertical is saved in the normal sample as shown in Figure 2.4. Thus, the normal sample has spacing of 250 m along the ray. The mirror image is contained in the normal sample. A subset of the remaining data points is saved in two oversamples: the surface oversample and the rain echo oversample. Both oversamples have a spacing of 250

m along a ray, but a region with both normal sample and oversample has a spacing of 125 m. The PR determines which levels to save in the oversamples based on its on board determination of the surface bin. No data are saved as oversamples in rays 1-10 and 40-49. Five levels are saved from rays 11-39 in the surface oversample. If the PR detects the surface in an oversample bin, the surface oversample is centered on the detected surface. If, on the other hand, the PR detects the surface in a normal sample bin, 3 oversample bins are above and 2 oversample bins are below the detected surface. In addition, 28 levels (immediately above the surface oversample) are saved from rays 20-30 in the rain echo oversample. NASDA defines a range bin number, which is related to the distance from the satellite along the ray. It starts at roughly 327 km from the satellite, increments by 1 roughly every 125 m, and increases to a maximum of 400 at roughly 377 km from the satellite. The exact value for the starting distance of the nadir ray is written in Starting Bin Distance of the 1B21 and 1C21 files. Twice the exact value of the increment for any ray is written in Range Bin Size of the 1B21 and 1C21 files, TRMM Science Data and Information System Vol.3 (2000). A summary of the main characteristics of the TRMM PR is given in Table 2.2.

2.4 PR Data Product Category

The TRMM Science Data and Information System (TSDIS) processes TRMM data from the Precipitation Radar (PR), the TRMM Microwave Imager (TMI), and the Visible and Infrared Scanner (VIRS) into data products oriented toward measuring rainfall in the tropics. Most TRMM data products are written using Hierarchical Data Format (HDF). This section summarize these data products only for the PR used in this research. More details on these data products are found in the six volumes of the Interface Control specification (ICS). The following data were used in this research:

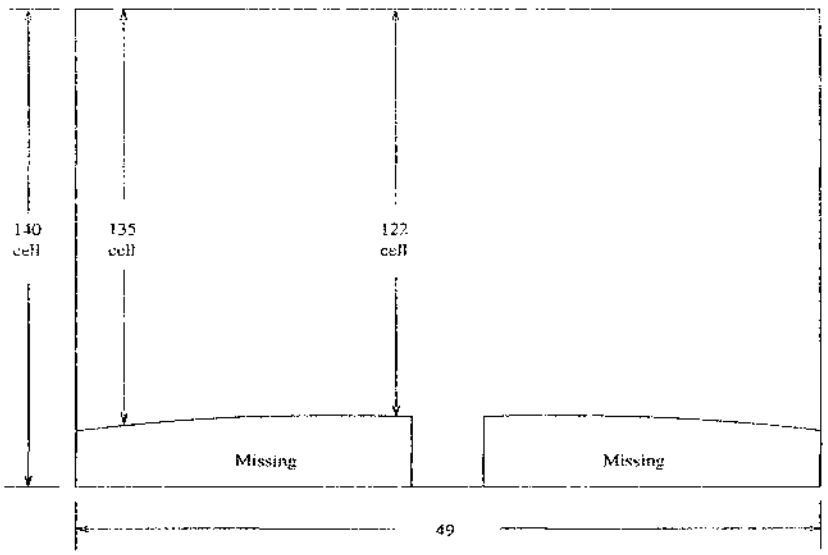

Figure 2.4: Normal sample data array (adapted from TRMM handbook, 2001).

Radar Type	Active phased-array radar
Frequency	13.796 GHz and 13.802 GHz (two-channel frequency agility)
Swath Width	About 215 km
Observable Range	over 20 km
Range Resolution	250 km
Horizontal Resolution	4.3 km (nadir)
Sensitivity	S/N per pulse $\geq$0 dB for 0.5 mm/h rain at rain top
Independent Samples	64
Data Rate	93.5 kbps
Weight	465 kg
Power	213 watts
Antenna Type	128-element slotted wave guide array antenna
Beam Width	0.71^{o} x 0.71^{o}
Aperture	2.1m x 2.1m
Scan Angle	$\pm 17^{o}$
Gain	About 47.4 dB
Transmitter Type	SSPA and LNA (128 channels)
Peak Power	over 700 W
Pulse Width	1.6 μs x 2ch.
Pulse Repetition Frequency	2776 Hz
Dynamic Range	About 81.5 dB

Table 2.2: TRMM PR Parameters (adopted from http://hdsn.eoc.nasda.go.jp).

1. The PR level-1B product (1B21).
2. The PR level-1C product (1C21).
3. The PR level-2A product (2A21).
4. The PR level-2A product (2A23).
5. The PR level-2A product (2A25).

2.4.1 Level-1B Product (1B21)

The PR Level-1B product, 1B21, calculates the received power and contains calibrated powers in three-dimensional arrays whose dimensions are scan, ray, and range bin. Power is written in three arrays: normal sample, surface oversample, and rain oversample. The vertical spacing is 250 m for the normal sample. If the surface oversample and rain oversample are combined with the normal sample, the result is 125 m vertical spacing in limited regions.

2.4.2 Level-1C Product (1C21)

The PR Level-1C product, 1C21, calculates the effective radar reflectivity factor (dBZ, mm^6/m^3), which is converted from the PR received powers in the corresponding places in 1B21 output, at 13.8 GHz without any propagation loss (due to rain or any other atmospheric gas) correction (Z_m). The 1C21 product has the same format as 1B21 except that radar quantity is Z_m (dBZ) in the 1C21 product instead of received power (dBm) in the 1B21 product. Therefore, the Z_m value can be calculated just by applying a radar equation for volume scatter with PR system parameters. The following radar equation is used:

$$dBZm = 10log(10^{Ps/10} - 10^{Pn/10}) - C + 20log(r) \tag{2.1}$$

$$C = P_t + G_t + G_r + 10log\,(a \times cr) + 10log(c \times T) - 20log(\lambda) + C_o \tag{2.2}$$

where,

- P_s : 1B21 received power
- P_n : 1B21 noise level
- r : Distance
- P_t : transmitted power
- G_t : transmit antenna gain
- G_r : receive antenna gain
- a :along-track beam width
- cr :cross-track beam width
- c :speed of light
- λ :wavelength
- C_o :Radar constant defined as follows:

$$C_o = 10log\left[p^3\frac{|K|^2}{2}2^{10}ln210^{-18}\right] \tag{2.3}$$

where $|K|^2$ is the dielectric factor and taken to be equal to 0.93. Figure 2.5 shows the structure of the 1C21 product. The following data are used from 1C21 PR reflectivity in this research:

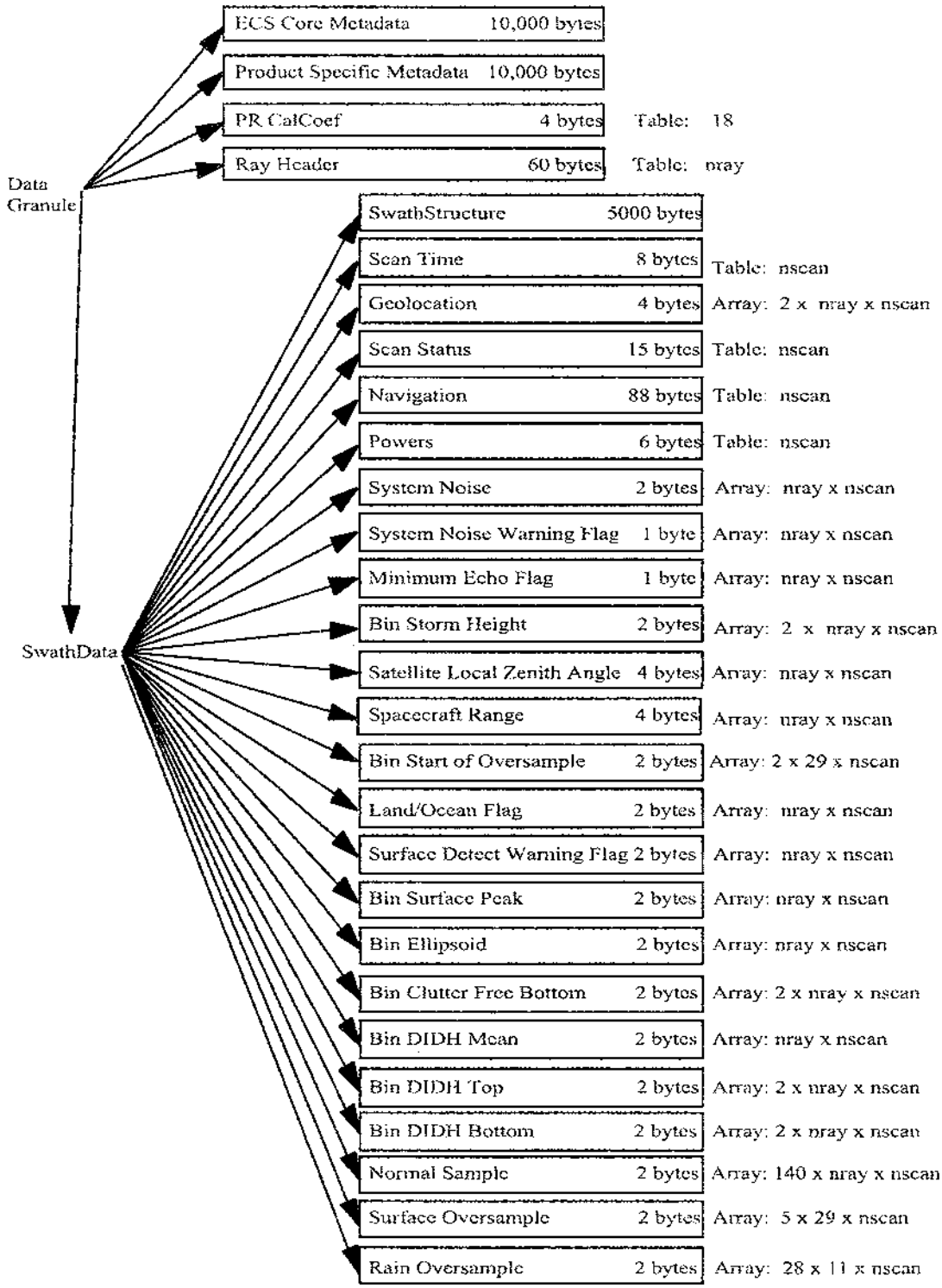

Figure 2.5: 1C21 data structure (Ref:TRMM handbook, 2001).

2.4.2.1 Ray Header

The ray header contains information that is constant in the granule, such as the parameters used in the radar equation, the parameters in the minimum echo test, and the sample start bin number. These parameters are provided for each angle bin. The starting bin distance is determined by the sampling timing of the PR. The distance between the satellite and the center of the Nth normal sample bin is calculated as follows:

$$Distance = startingbindistance + Rangebinsize \times (N - 1) \tag{2.4}$$

This distance is defined as the center of a radar resolution volume. Range bin size is the PR range resolution and is the width at which pulse electric power decreases 6 dB.

2.4.2.2 Normal Sample

The reflectivity [dBZ](Z = mm^6mm^{-3}) of the normal sample is multiplied by 100 and stored as a 2-byte integer. The data ranges from -20 dBZ to 120 dBZ with an accuracy of 0.9 dBZ. If a cell (range bin) is determined to have no echo, the reflectivity is set to -32700.

2.4.2.3 Bin Clutter Free Bottom

The bin clutter free bottom is the range bin number of the lowest clutter free bin. Clutter free bin numbers are given for clutter free certain and possible. For this research the certain clutter free bottom is applied.

2.4.2.4 Bin Ellipsoid

Bin ellipsoid is the range bin number of the earth ellipsoid.

2.4.2.5 Geolocation

Geolocation is the earth location of the beam center per angle bins at the altitude of the earth ellipsoid. This is recorded as latitude and longitude. If the earth location cannot be calculated, the geolocation output becomes -9999. Latitude is positive north and negative south while longitude is positive east and negative west.

2.4.2.6 Data Quality

Data quality is a summary of data quality in the scan. This data consists of 8 bits. Unless all bits are 0 (normal), the scan data is meaningless to higher processing.

Bit	Meaning
0	missing
5	Geolocation Quality is not normal
6	Validity is not normal

Table 2.3: 1C21 Minimum Echo Flag.

2.4.2.7 Missing

Missing indicates whether information is contained in the scan data. The values are:

Value	Meaning
0	Normal
1	Missing (missing packet and calibration mode)
2	No-rain

Table 2.4: 1C21 Missing.

2.4.3 Level-2A Product (2A21)

The primary objective is to compute the path-integrated attenuation (PIA) using the surface reference technique (SRT). The surface reference technique rests on the assumption that the difference between the measurements of the normalized surface cross section within and outside the rain provides a measure of PIA.

Two types of non-rain normalized radar surface cross section (σ^0) estimates are used: spatial and temporal. In the spatial surface reference data set, the mean and standard deviation of the surface cross sections are calculated over a running window of Ns fields of view before rain is encountered. These operations are performed separately for each of the 49+2 incidence angles of TRMM, corresponding to the cross-track scan from -17 to +17 degrees with respect to nadir. The two additional angle bins are used to take care of non-zero pitch/roll angles that can shift the incidence angle outside the normal range.

For the temporal surface reference data set, the running mean and standard deviation are computed over a 1 x 1 degree (latitude, longitude) grid. Within each 1 x 1 degree cell, the data are further categorized into incidence angle categories.

When rain is encountered, the mean and standard deviations of the reference σ^0 values are retrieved from the spatial and temporal surface reference data sets. To determine which reference measurement is to be used, the algorithm checks whether Nt samples are needed to be considered a valid reference estimate for the temporal and spatial reference data sets, respectively. If neither condition is satisfied, no estimate of the PIA is made and the flags are set accordingly. If only one condition is met, then the surface reference data which corresponds to this is used. If both conditions are satisfied, the surface reference data is taken from that set which has a smaller standard deviation. If a valid surface data set exists, then the 2-way path attenuation (PIA) is estimated from the following equation:

$$PIA = \left\langle \sigma^0(reference\ value) \right\rangle - \sigma^0(in\ rain) \tag{2.5}$$

where σ^0(in rain) is the value of the normalized radar surface cross section over the rain volume of interest and $(\sigma^0(refrence\ value))$ is the mean value obtained from either the temporal or spatial reference data sets. To obtain information as to the reliability of this PIA estimate we consider the difference between the PIA, as derived in Equation 2.5, and the standard deviation as calculated from the no-rain σ^0 values and stored in the reference data set. The reliability factor of the PIA estimate is obtained by using:

$$RelabFcator = PIA/std(reference\ value) \tag{2.6}$$

When this quantity is large, the reliability is considered high and conversely. The following data used from 2A21 PR reflectivity in this research:

2.4.3.1 Sigma Zero

Normalized backscattering radar cross-section of the surface (dB) for the 49 angles bins in the radar scan.

2.4.3.2 Incidence Angle

Incidence angle with respect to nadir (in degree); pitch/roll correction is included.

2.4.3.3 PIA

Estimated 2-way path attenuation in (dB) where:

$$PIA = 2\int_0^{rs} k(s)ds \tag{2.7}$$

where $k(s)$ is the attenuation coefficient in dB/km and the integral runs from storm top to the surface.

2.4.4 Level-2A Product (2A23)

The main objectives of the 2A23 data product are as follows:

- Detection of bright band (BB) and determination of the height of BB and its strength when BB exists.
- Classification of rain type into the following three categories: stratiform, convective, and other.
- Detection of shallow isolated (a kind of warm rain).
- Output of Rain/No-rain flag.
- Computation of the estimated height of freezing level.
- Output of the height of storm top.

The following data used from 2A23 PR reflectivity in this research:

2.4.4.1 Bright Band (BB) detection

The major conditions for the existence of BB are as follows:

1. Height of BB (HBB) must be close to the height of freezing (freezH) within ± 2 km.
2. BB has a clear peak.
3. HBB must be close to each other (within ± 0.65 km at most in one vertical plane with 49 angles bins of data).
4. Reflectivity (Z) at height above HBB by 0.5 km or higher must be smaller than the Z at least by 2 dB. In other words, Z must be decayed appreciably at height above HBB.

5. When Z at HBB exceeds 42 dBZ, and the peak is not sharp enough, the standard deviation of Z below HBB in the range from HBB - 0.5 km down to the clutter free height is smaller than 2 dB.

6. Below HBB, Z in the range from HBB - 0.5 km to HBB -1.0 km must be smaller than the Z at HBB at least by 1 dB.

The above conditions for BB are sufficient when HBB is found in the range of freezH ±1.5 km. However, when HBB is found in the height range outside of freezH ±1.5 km but in the expanded height range of ±2.5 km, further conditions are imposed on the detection of BB to avoid false BB peaks.

2.4.4.2 Rain Type

2A23 uses two different methods for classifying rain type; one is the vertical profile method (V-method) and the other is the horizontal pattern method (H-method). Both methods classify rain into three categories: stratiform, convective, and other.

2.4.4.3 Rain Type classification by V-method

Outline of the V-method is as follows:

1. When BB exists, rain is basically classified as stratiform except when $Z_{max} > Z_{BB}$ and $Z_{max} > 42$ dBZ, where Z_{BB} is the Z factor at the BB peak and the Z_{max} is the maximum value of Z in the rain region, rain type is classified as convective even though BB clearly exists.

2. When BB is not detected, and the maximum value of Z at a given angle bin exceeds 39 dBZ, rain type for this angle bin is classified as convective.

3. Other type is defined as not-stratiform and not-convective. This means that there exists appreciable radar echo but it is not strong enough to be convective and also BB is not detected.

The other type of rain consists of the following cases: cloud, actually stratiform but BB fails, ambiguous because radar echo is not strong enough to be convective, and finally simply noise.

2.4.4.4 Rain Type classification by H-method

The horizontal pattern method (H-method) also classifies rain into three categories: stratiform, convective, and other, but with the definitions of these being different from those of the V-method. The H-method is based on the University of Washington convective/stratiform separation method, which examines the horizontal pattern of Z at a given height; where Z has a 2 km horizontal resolution. In 2A23, the following modifications are made:

- instead of examining a horizontal pattern of Z at a given height, a horizontal pattern of Z_{max} is examined; here Z_{max} is the maximum of Z along the range for each antenna scan angle below freezing height (-1 km margin).
- Parameters are changed so that they may be suitable for the TRMM data with 4.3 km horizontal resolution. Choice of parameters was made before the launch of the TRMM using test Ground Validation (GV) data in such a way that a 4.3 km resolution produces almost the same result as that with a 2 km resolution data.
- Other type of rain is introduced to handle noise.

In the H-method, detection of convective rain is made first. If one of the following conditions is satisfied at a pixel, which corresponds to the angle bin data being considered, it is judged that the pixel is a convective center:

- Z_{max} exceeds 40 dBZ.
- Z_{max} stands out against the background area.

Rain type for a convective center is convective, and rain type for the pixels nearest to the convective center is also convective. If rain type is not convective and if the rain echo is certain to exist, then rain type is stratiform. Rain type by the H-method is "'other"' if the radar echo below the freezing height (-1 km margin) at a given angle bin is possibly noise. This means that the other type by the H-method includes the case of noise and cloud.

2.4.4.5 Unification of Rain Type

The unified rain type is expressed by 2 digits. The first digit indicates the rain type (1:stratiform, 2:convective, 3:other) and the last digit indicates a level of confidence, which decreases as the number increases. Table 2.5 shows the unified rain type. Rain types by V-method and H-method can be reconstructed from the unified rain type (Table 2.6).

2.4.5 Level-2A Product (2A25)

The main objectives of 2A25 are to correct for the rain attenuation in measured radar reflectivity and to estimate the instantaneous three-dimensional distribution of rain from the TRMM precipitation radar (PR) data. The estimates of attenuation-corrected radar reflectivity factor and rainfall rate are given at each resolution cell of the PR radar. The estimated near surface rain rate and average rainfall rate between the two altitudes (2 and 4 km) are also calculated for each beam position.

2A25 basically uses a hybrid of the Hitschfeld-Bordan method and the surface reference method to estimate the vertical true radar reflectivity (Z) profile. More details on the Hitschfeld-Bordan method and the surface reference method for correction reflectivity will be given in Chapter 3. Since radar echoes from the near surface are contaminated by the mainlobe clutter, the rain estimate at the lowest

value	rain type
10	stratiform certain (BB exist)
11	stratiform certain (BB exist)
12	probably stratiform
13	maybe stratiform
14	maybe stratiform or maybe transition or something else
15	maybe stratiform
20	convective certain (no BB)
21	convective certain
22	convective certain
23	probably convective (BB exists)
24	maybe convective
25	maybe convective
26	convective
27	convective
28	convective
29	convective
30	other
31	other

Table 2.5: Unified Rain Type.

V-method	H-method	Unified Type
stratiform	stratiform	stratiform
stratiform	other	stratiform
other	stratiform	stratiform
stratiform (BB certain)	convective	stratiform
convective	convective	convective
other	convective	convective
convective	other	convective
convective	stratiform	convective
stratiform (BB not certain)	convective	convective
other	other	other

Table 2.6: Reconstructed Unified Rain Type.

point in the clutter-free region is given in the near-surface rainfall rate for each angle bin.

The major input data to 2A25 are the measured radar reflectivity factor Z_m, the apparent decrease of the surface cross section ($\Delta\sigma^0$) by the attenuation due to rain, its reliability, the rain type and the miscellaneous height information. The algorithm first defines the region for processing; it processes only the data between the rain top and the lowest height above the surface that is free from the surface clutter. The bright-band (BB) height and the climatological freezing height are used to define the regions of liquid (water), solid (ice), and the mixed phase of precipitation particles. The initial values of the coefficients in the k-Z ($k = \alpha Z^{\beta}$) and Z-R ($R = aZ^{b}$) relationships at different altitudes are accordingly defined. The following data used from 2A25 PR reflectivity in this research:

2.4.5.1 Corrected Z Factor

This is the attenuation corrected Z-factor at 13.8 GHz at the radar ranges gates from 0 to 20 km. It ranges from 0.1 to 80 dBZ and is multiplied by 100. If the input radar reflectivity factor (Z_m) is below the noise level, the corrected Z factor is set to 0.

2.5 Data Alignment

The size of 1C21 data per scan is 49 rays and 140 bins. On the other hand, 2A25 data size per scan is 49 rays and 80 bins. Thus, in order to eleminate the difference in size of 1C21 and 2A25, data alignment is needed. To obtain the ellipsoid bin number of 2A25, the following equation is used.

$$2A25\ Ellipsoid = (Bin\ Ellipsoid - Ray\ Start)/2 \tag{2.8}$$

Chapter 3

ATTENUATION CORRECTION BACKGROUND AND THEORETICAL MODELS

3.1 Introduction

It is well known that precipitation can greatly affect the propagation of radio waves at frequencies above 3 GHz in various ways and that these effects must be taken into account in the design of radio frequency (RF) links as well as sensor systems such as radar. Among these effects, the most serious is precipitation-induced attenuation. Therefore, attenuation of microwaves indicates the decrease in power of the electromagnetic wave as it propagates. When an electromagnetic wave propagates through the atmosphere, it is scattered or absorbed by particles in the atmosphere and therefore, the wave is attenuated and this attenuation is called extinction. In other words, the sum of the total scattering and absorption cross section is called extinction cross section.

$$\sigma_{ext} = \sigma_s + \sigma_a \tag{3.1}$$

where σ_s is the total scattering cross section and σ_a is the total absorption cross section. Due to this attenuation, the other end receives a weaker wave than the

original. The absorption and scattering of electromagnetic waves due to precipitation has been studied since the early 1940s nearly coincidental with the beginning of radar (Bringi and Chandrasekar, 2001). In general, the attenuation of radio waves increases with radar reflectivity. Even at a relatively low frequency such as 3 GHz (S-band), attenuation effects can be significant when the propagation path passes through multiple precipitation cells of high intensity.

Recently higher frequency bands, such as Ka-band, are getting more attention for remote sensing applications and satellite communication because of the need for larger bandwidth and lower cost. However, radio wave propagation is much more susceptible to precipitation attenuation at higher frequencies. Rain, clouds, and gaseous absorption by oxygen and water vapor can easily affect the signal and must be considered. Rain can produce attenuation of the order 20-30 dB (in 20-30 GHz range). Thus estimations of attenuation and intrinsic reflectivity are some of the most important issues for space borne radar operations.

This chapter describes attenuation correction used in TRMM (Ku-band) algorithm and frequency scaling of attenuation (Ka-band) and theoretical computation of attenuation in precipitation.

3.2 Attenuation Correction

Attenuation is produced by various obstacles such as atmospheric gas, clouds and precipitation. The total specific attenuation k [dB/km] can be expressed as:

$$k = k_g + k_c + k_p \tag{3.2}$$

where k_g, k_c and k_p are the specific attenuation in dB/km for gas, clouds and precipitation, respectively. Among the three, k_p dominates in the presence of precipitation.

In the past few decades several methods of attenuation estimation from radar return have been proposed. Iguchi, et al. (2000) describes the attenuation correction method for TRMM standard algorithm. It is based on a hybrid of the surface reference method from Iguchi and Meneghini (1994) and the Hitschfeld-Bordan method (1954). The corrected reflectivity factor or true effective reflectivity factor Z_e [dBZ] ($Z = mm^6m^{-3}$) in TRMM 2A25 data is obtained by this algorithm. Attenuation correction estimates Z_e at 13.8 GHz at each radar resolution cell from the vertical profiles of measured reflectivity factor Z_m [dBZ] in 1C-21 data. When there is attenuation, the radar equation becomes:

$$P_r(r) = \frac{C\,|K|}{r^2} \cdot Z_m(r) \tag{3.3}$$

where

$$Z_m(r) = Z(r) exp\left[-0.2ln10 \int_r^0 k(s)ds\right] \tag{3.4}$$

and

$$K = \frac{m^2 - 1}{m^2 + 2} \tag{3.5}$$

where $P_r(r)$ is the received power, r is the range from the radar, C is the radar constant, m is the complex index of refraction of the precipitation particles, $k(r)$ is the specific attenuation [dB/km](or attenuation coefficients), and the quantity $\int_0^r k(s)d(s)$ the attenuation. The attenuation to the surface is $\int_0^{r_s} k(s)d(s)$ where r_s

is the range to the surface ans is called the "Path Integrated Attenuation" (PIA). The quantity $exp\left[-0.2ln10\int_0^r k(s)d(s)\right]$ is called the "attenuation factor".

If C, m, and r are known, the measured reflectivity $Z_m(r)$ can be calculated from the measured received power $P_r(r)$. To calculate the rainfall profile $R(r)$, we are required to have the true reflectivity (corrected reflectivity) $Z(r)$ or the specific attenuation $k(r)$. When the attenuation is negligible, $Z(r) = Z_m(r)$. We need to solve Equation (3.4) for the unknown functions $Z(r)$ and $k(r)$ for a given function $Z_m(r)$. This problem is obviously ill posed and cannot be solved uniquely unless some relation exists between $Z(r)$ and $k(r)$. One such solution derived by Hitschfeld and Bordan (1954) with a power-law relation ($k = \alpha Z^\beta$), gives a reasonable estimate if the attenuation effect is small. When the attenuation is large, however, the Hitschfeld-Bordan solution can become unstable. To avoid this instability problem, several methods have been proposed (Iguchi and Meneghini, 1994; Marzoug and Amayence, 1994; Marzoug and Amayence, 1991; Kozu and Nakamura, 1991a and 1991b; Meneghini, 1978; Meneghini et al., 1983; and Menghini and Nakamura, 1990).

3.3 Surface Reference Technique

The surface reference technique estimates the PIA through rain from the decrease in the surface return. In particular, an estimate of the attenuation factor at $r = r_s$ is obtained from the ratio of the surface return power measured in rain to that measured in adjacent rain-free areas:

$$\hat{A}(r_s s) = \frac{P_r\left[r_s; rain\right]}{P_r\left[r_s; no\ rain\right]} \tag{3.6}$$

An estimate of the PIA, which follows directly from $\hat{A}(r_s)$, is then used to constrain the Hitschfeld-Bordan solution. If k is related to Z by $k = \alpha Z^\beta$ and β is

constant in range, then Equation 3.4 can be written as a differential equation in the following way:

$$\frac{du}{dr} + u\beta\frac{d}{dr}lnZ_m + q\alpha = 0 \tag{3.7}$$

where $u = Z^{-\beta}$ and $q = 0.2\beta ln10$. A general solution to this equation is:

$$Z(r) = Z_m(r)\left[C_1 - qS(r)\right]^{-1/\beta} \tag{3.8}$$

where C_1 is an arbitrary constant, and $S(r)$ is defined by:

$$S(r) = \int_0^r \alpha(s)Z_m^{\beta}(s)ds \tag{3.9}$$

If the initial condition is given as:

$$Z(r) = Z_m(r) \quad at\ r = 0 \tag{3.10}$$

then C_1 becomes 1 and this corresponds to the Hitschfeld-Bordan solution:

$$Z_{HB}(r) = Z_m(r)\left[1 - qS(r)\right]^{-1/\beta} \tag{3.11}$$

If, instead, the final condition on $Z(r)$ is given at $r = r_s$, the following condition

must be satisfied by C_1:

$$C_1 = \left[\frac{Z_m(r_s)}{Z(r_s)}\right]^{\beta} + qS(r_s) \tag{3.12}$$

By substituting Equation 5.1 into Equation 3.8, we get the final Z:

$$Z_{fv} = Z_m(r)\left\{\left[\frac{Z_m(r_s)}{Z(r_s)}\right]^{\beta} + q\left[S(r_s) - S(r)\right]\right\}^{-1/\beta} \tag{3.13}$$

If we define A_s by:

$$A_s = exp\left(-0.2ln10\int_0^{r_s} kds\right) \tag{3.14}$$

then,

$$\frac{Z_m(r_s)}{Z(r_s)} = A_s \tag{3.15}$$

and the solution can be written as:

$$Z_{fv}(r) = Z_m(r)\left\{A_s^{\beta} + q\left[S(r_s) - S(r)\right]\right\}^{-1/\beta} \tag{3.16}$$

and this method is called the "final value method". The final value method uses the PIA as the single condition to choose the solution. Unlike the forward solution of the Hitschfeld-Bordan, this solution is stable. Since this solution is solved backward

from the surface, it depends only on the measured $Z_m(r)$ between the point of interest and the surface. The values of $Z_m(r)$ above the range r do not affect the solution. This is the advantage of the final value method since it is not easy to model the $k - Z$ relation appropriately at high altitudes where the phase and size distribution of precipitating particles are not known.

Since the integration constant C_1 is adjusted to satisfy the surface condition, the solution does not satisfy the natural initial condition given in Equation 3.10. In order to satisfy both initial and PIA conditions, it is necessary to introduce an adjustable parameter. Different surface reference methods adjust different model parameters so that the total attenuation calculated from the Hitschfeld-Bordan solution with the adjusted parameters equals the PIA. Let introduce a correction factor defined by:

$$\epsilon = \frac{1 - A_s^{\beta}}{qS(r_s)} \tag{3.17}$$

If the model parameters α and β accurately represent the $k - Z$ relationship and if there is no error in the radar calibration or the PIA estimate, then ϵ becomes unity. This is the case when the total attenuation is equal to the attenuation calculated from the retrieved $Z(r)$ with an assumed $k - Z$ relationship.

The α adjustment method adjusts the coefficient α by a factor of ϵ and makes the two attenuations equal. The corrected $Z(r)$ is then given by:

$$\begin{aligned} Z_\alpha(r) &= Z_m(r)\left[1 - \epsilon q S(r)\right]^{-1/\beta} \\ &= Z_m\left\{A_s^{\beta} + \epsilon q\left|S(r_s) - S(r)\right|\right\}^{-1/\beta} \end{aligned} \tag{3.18}$$

This solution is expressed in two different forms in order for the easy comparison

with the Hitschfeld-Bordan solution (Equation 5.2) and with the final value solution (Equation 3.16), respectively (Iguchi and Meneghini, 1994). The equivalence of these two forms can be easily verified using the relation in Equation 3.17.

The radar constant adjustment method (Meneghini et. al., 1983; and, Menghini and Nakamura, 1990) adjusts the radar constant C and makes the two attenuations equal. The corrected $Z(r)$ is given by:

$$\begin{aligned} Z_C(r) &= \epsilon^{1/\beta} Z_m(r) \left[1 - \epsilon q S(r)\right]^{-1/\beta} \\ &= Z_m \left\{ \frac{A_s^\beta}{\epsilon} + q \left[S(r_s) - S(r)\right] \right\}^{-1/\beta} \end{aligned} \tag{3.19}$$

It is easy to see from Equations (5.2), (3.16), (3.18), and (3.19) that $Z_C(r) = \epsilon^{1/\beta} Z_a(r)$ and that the following inequalities hold:

$$\begin{aligned} &if\ \epsilon > 1 \ \Rightarrow Z_C(r) > Z_{fv}(r) > Z_a(r) > Z_{HB}(r) \\ &if\ \epsilon = 1 \ \Rightarrow Z_C(r) = Z_{fv}(r) = Z_a(r) = Z_{HB}(r) \\ &if\ \epsilon < 1 \ \Rightarrow Z_C(r) < Z_{fv}(r) < Z_a(r) < Z_{HB}(r) \end{aligned} \tag{3.20}$$

3.4 PR Attenuation Correction

Iguchi et al.(2000) describes the attenuation correction method for TRMM standard algorithm. It is based on a hybrid of the surface reference method from Iguchi-Meneghini (1994) and the Hitschfeld-Bordan method (1954). The corrected reflectivity factor or true effective reflectivity factor Z_e [dBZ] ($Z = mm^6 mm^{-3}$) in TRMM 2A25 data is obtained by this algorithm. Attenuation correction estimates

Z_e at 13.8 GHz at each radar resolution cell from the vertical profiles of measured reflectivity factor Z_m [dBZ] in 1C-21 data.

The Hitschfeld-Bordan method uses the k-Z_e relationship $k = \alpha Z_e^{\beta}$. The coefficient α in the k-Z_e relationship is adjusted in such a way that the path-integrated attenuation (PIA) estimated from the measured Z_m profile by the Hitschfeld-Bordan method matches the estimate of PIA from the surface reference. α values may vary depending on temperature as well as the parameter N_w described in the next section. β is uniform within the radar resolution cell, the observed radar reflectivity factor $Z_m(r)$ and the true effective radar reflectivity factor $Z_e(r)$ are related through:

$$\begin{aligned} Z_m(r) &= Z_e(r)A(r) \\ &= Z_e(r)exp\left[-0.2ln(10)\int_0^r k(s)ds\right], \end{aligned} \tag{3.21}$$

where $A(r)$ is the attenuation factor from the radar to range r, and $k(r)$ is the specific attenuation or attenuation coefficient expressed in decibels per kilometer. Given an estimate of the attenuation factor $A(r)$, one can calculate $Z_e(r)$ from measured $Z_m(r)$ by $Z_e(r) = Z_m(r)/A(r)$.

If k is related to Z_e by a power law $k = \alpha Z_e^{\beta}$, then Equation 3.21 can be solved for Z_e and the solution becomes:

$$Z_e(r) = \frac{Z_m(r)}{A_{HB}(r)} \tag{3.22}$$

where $A_{HB}(r)$ is given by:

$$A_{HB}(r) = \left[1 - q\beta\int_0^r \alpha(s)Z_m^{\beta}(s)ds\right]^{1/\beta} \tag{3.23}$$

With $q = 0.2\ln(10)$ (Iguchi and Meneghini 1994). Equation 3.23 is equivalent to the Hitschfeld-Bordan solution for the attenuation correction (Hitschfeld and Bordan 1954).

Let PIA denote the two-way attenuation to the surface ($r = r_s$) expressed in units of decibels, that is,

$$\begin{aligned} PIA[dB] &= -10\log_{10} A(r_s) \\ &= -10\log_{10}\left[\frac{Z_m(r_s)}{Z_e(r_s)}\right] \\ &= 10\log_{10}[Z_e(r_s)] - 10\log_{10}[Z_m(r_s)] \end{aligned} \tag{3.24}$$

or

$$10\log_{10}[Z_m(r_s)] = 10\log_{10}[Z_e(r_s)] - PIA \tag{3.25}$$

then, the Hitschfeld-Bordan estimate of PIA becomes

$$PIA_{HB} = -10\log_{10} A_{HB}(r_s) = -\frac{10}{\beta}\log_{10}(1-\zeta) \tag{3.26}$$

Here, ζ is defined as:

$$\zeta = q\beta\int_0^{r_s} \alpha(s) Z_m^{\beta}(s) ds \tag{3.27}$$

The surface reference technique also gives an independent estimate of PIA (Meneghini et al. 2000). This PIA is denoted by PIA_{SR}. This technique assumes that the

decrease of the apparent surface cross section is caused by the propagation loss of radar signal by rain:

$$PIA_{SR} = \Delta\sigma^0 = \left\langle \sigma^0_{no-rain} \right\rangle - \sigma^0_{rain} \tag{3.28}$$

The objective here is to find the best estimate of PIA, denoted by PIA_e, from ζ and $\Delta\sigma^0$. Once the estimate of PIA_e is obtained, an attenuation correction factor ϵ is introduced in such a way that the modified HitschfeldBordan estimate gives the same path attenuation as PIA_e:

$$PIA_e = -\frac{10}{\beta}\log_{10}(1-\epsilon\zeta). \tag{3.29}$$

With this ϵ, the attenuation-corrected Z_e can be calculated at all ranges by (Iguchi and Meneghini, 1994)

$$Z_e(r) = \frac{Z_m(r)}{\left[1 - \epsilon q\beta \int_0^r \alpha(s) Z_m^\beta(s) ds\right]^{1/\beta}} \tag{3.30}$$

Because multiplying ζ by ϵ is equivalent to adjusting α, this is an α-adjustment method. If the surface reference $\Delta\sigma^0$ is taken to be exact and if we set $PIA_e = PIA_{SR} = \Delta\sigma^0$, the attenuation correction factor is given by:

$$\epsilon = \epsilon_s = \frac{1 - 10^{\beta\Delta\sigma^0/10}}{\zeta}. \tag{3.31}$$

3.5 Theoretical Computation of Attenuation in Precipitation

The absorption and scattering of electromagnetic waves in precipitation are responsible for the attenuation. The sum of the total scattering and absorption cross section is called the extinction cross section σ_{ext}. For frequencies corresponding to Rayleigh scattering, the absorption cross section of a spherical drop is proportional to its volume, and it dominates the extinction cross section. The specific attenuation of a propagation wave through hydrometeors can be expressed as:

$$A = 4.343 \times 10^3 \int \sigma_{ext}(D)N(D)dD \quad dBkm^{-1} \tag{3.32}$$

where $N(D)dD$ is the number of particles per unit volume with sizes in the interval D to $D+dD$ and given in the unit of m^{-3} while σ_{ext} is given in m^2. For raindrops, Equation 3.32 can be parameterized up to 15 GHz as:

$$A = 4.343 \times 10^3 C_\lambda \int D^4(D)N(D)dD \quad dBkm^{-1} \tag{3.33}$$

where the coefficient C_λ is dependent on wavelength. It is also a function of temperature. If the intrinsic radar reflectivity at a range r from the radar is $Z(r)$, then the measured reflectivity ($Z_m(r)$) is reduced to attenuation and can be expressed as:

$$Z_m(r) = Z(r)exp\left[-4\int_0^r K_{im}(r)dr\right] \tag{3.34}$$

Where K_{im} is the imaginary part of effective propagation constant K_{eff}. K_{im} is in

units of m^{-1} and r in m. Both $Z(r)$ and $K_m(r)$ are described by the hydrometeor size distribution. If the path length r is in (km) and specific attenuation is defined in $dBkm^{-1}$, then it can be shown that $A = 8.686 \times 10^3 K_m$ and Equation 5.6 reduces to:

$$\begin{aligned} 10log_{10}[Z_m(r)] &= 10log_{10}[Z_h(r)] - 2\int_0^r A(r)dr \\ &\cong 10log_{10}[Z_h(r)] - 2\sum(A(r)\Delta r) \end{aligned} \tag{3.35}$$

The intrinsic radar reflectivity is defined as:

$$Z = \frac{\lambda^4}{\pi |K|} \int \sigma(D)N(D)d(D) \tag{3.36}$$

where $\sigma(D)$ is the backscatter cross section, λ is the wavelength, and $|K| = \left|\frac{\epsilon_r - 1}{\epsilon_r + 2}\right|^2$.

3.5.1 Microphysical Model of Precipitation

The raindrop size distribution (RSD) plays an important role in determining some of the radar parameters, such as the reflectivity factor, the differential reflectivity, the attenuation characteristics of various hydrometers in precipitation and the specific differential phase (Bringi and Chandrasekar, 2001). In the Rayleigh scattering region, the attenuation is proportional to the product of the volume and the imaginary part of the complex dielectric constant of the hydrometeor. The dielectric constant changes with wavelength and temperature. The most widely used shape to represent the RSD is the gamma distribution (Ulbrich, 1983):

$$N(D) = N_o D^{\mu} exp(-\Lambda D) \quad mm^{-1}m^{-3} \tag{3.37}$$

where $N(D)$ $(mm^{-3}m^{-1})$ is the distribution of raindrop per diameter interval D (mm) N_o $(mm^{-3}m^{-1})$ is termed the intercept parameter, μ is the rate of curve, and Λ (mm^{-1}) is the slope parameter. The gamma size distribution can be written in classical form as:

$$N(D) = n_c f_D(D) \tag{3.38}$$

where n_c is the number concentration, and $f(D)$ is the probability density function describing the size distribution. The median volume diameter D_0 (mm) is defined such that precipitation particles up to size D_0 contribute to half the mass content. The volume weighted mean diameter D_m $[mm]$ (generally referred to as the mean volume diameter) can be defined as the ratio of the fourth to the third moments of the distribution:

$$D_m = \frac{\int_0^\infty N(D)D^4 dD}{\int_0^\infty N(D)D^3 dD} \tag{3.39}$$

And for a Gamma distribution, Ulbrich (1983)

$$D_m = D_0 \frac{(4+\mu)}{(3.67+\mu)} \tag{3.40}$$

Ulbrich (1983) has shown that a gamma model for Equation 5.8 can adequately describe much of the natural variability in the hydrometeor size distribution. In order to compare the size distribution of hydrometeors under widely varying precipitation rates the concept of scaling drop size has been used by several authors

(Sekhon and Srivastava, 1971; Willis, 1984; and, Testud et al., 2001). A general expression of the normalization of the distribution is:

$$N(D) = N_w F(D/D_m) \tag{3.41}$$

and

$$F(X) = \frac{\Gamma(4)}{3.67^4} \frac{(3.67+\mu)^{4+\mu}}{\Gamma(4+\mu)} X^{\mu} exp[-(3.67+\mu)X] \tag{3.42}$$

where N_w $(mm^{-1}m^{-3})$ is the scaling parameter to normalize $F(D/D_m)$. Here, $F(X)$ denotes the normalized distribution describing the intrinsic shape of the distribution (noting that $X = D/D_m$), and X is a dimensionless quantity. The corresponding normalized (scaled) $N(D)$ can be expressed as:

$$N(D) = N_w f(\mu) \left(\frac{D}{D_o}\right)^{\mu} exp(-\Lambda\mu) \tag{3.43}$$

μ, D_o, and Λ are related to each other as:

$$\Lambda = \frac{3.67+\mu}{D_o} \tag{3.44}$$

Thus the three critical parameters of the hydrometeor size distribution namely μ, D_o, and N_w control the nature of hydrometeor size distribution, and varying them over a wide range of naturally observed values yields a physically realistic simulation of derived parameters such as radar reflectivity and attenuation.

3.5.2 Simulation Results

The simulations are used to study the attenuation and reflectivity through various hydrometeor particles such as rain, graupel, aggregate, and snow. The variability of the parameters used in the simulation in this research is shown in Table 3.1 while Table 3.2 shows the densities and water ratio of graupel. Essentially the shape parameter, μ, of the distribution is changed between -1 to 4 for rain, whereas it is kept zero as for all ice particles (implying exponential distribution). These ranges are chosen from a wide variety of published observations of raindrop size distributions (Pruppacher and Klett, 1997).

Hydrometeor Type	$D_0(mm)$	$N_w(mm^{-1}m^{-3})$	μ
Rain	$0.5 \leq D_0 \leq 2.5$	$3.0 \leq logN_w \leq 5.0$	$-1.0 \leq \mu \leq 4.0$
Wet Graupel	$1.0 \leq D_0 \leq 3.0$	$2.0 \leq logN_w \leq 4.0$	0
Aggregate	$0.5 \leq D_0 \leq 2.0$	$2.0 \leq logN_w \leq 4.0$	0
Snow	$0.5 \leq D_0 \leq 2.5$	$2.0 \leq logN_w \leq 4.0$	0

Table 3.1: RSD Parameters.

Hydrometeor Type	**Density**	**Water Ratio**
Rain	1.0	-
Wet Graupel	0.4	0.17
Aggregate	[0.1,0.5]	-
Snow	0.1	-

Table 3.2: Densities and Water Ratios.

For this research, 1000 samples of each type of hydrometeor mentioned above are generated. After generating distribution parameter samples for each hydrometeor type, the reflectivity factor and the specific attenuations k are computed with the parameters by using Equation 3.45 and 3.32, respectively, at 13.8 GHz (Ku-band), 28 GHz, and 35 GHz (Ka-band).

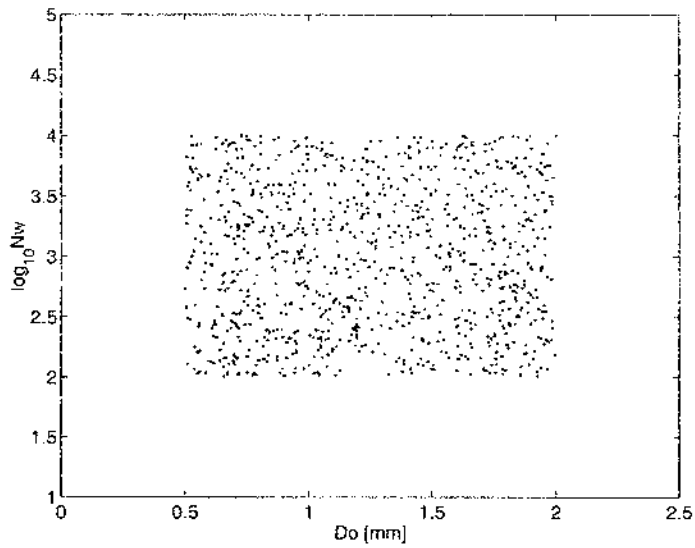

Figure 3.1: Aggregate D_0 vs $log_{10}Nw$.

$$Z = \frac{\lambda^4}{\pi^5 |K_p|^2} \int_D \sigma_b(D) N(D) dD \tag{3.45}$$

where $\sigma_b(D)$ is backscatter cross section and $|K_p|^2$ is the dielectric factors of the scattering particle and defined as:

$$|K_p|^2 = \left| \frac{\epsilon_p - 1}{\epsilon_p + 2} \right|^2 \tag{3.46}$$

where ϵ_p is the relative permittivity. Figures 3.1, 3.2, and 3.3 show D_0 vs $log_{10}Nw$ for aggregate, wet graupel, and rain, respectively while Figure 3.4 shows D_0 vs μ for rain.

Table 3.3 provides an itemized list of the figures of the scatter plot of attenuation versus reflectivity at 13.8 GHz (Ku-band), 28.0 GHz, and 35.0 GHz (Ka-band) for different categories of hydrometeor types. Here, four categories for hydrometeors are used, namely aggregates with densities from 0.1 to 0.5, wet graupel with

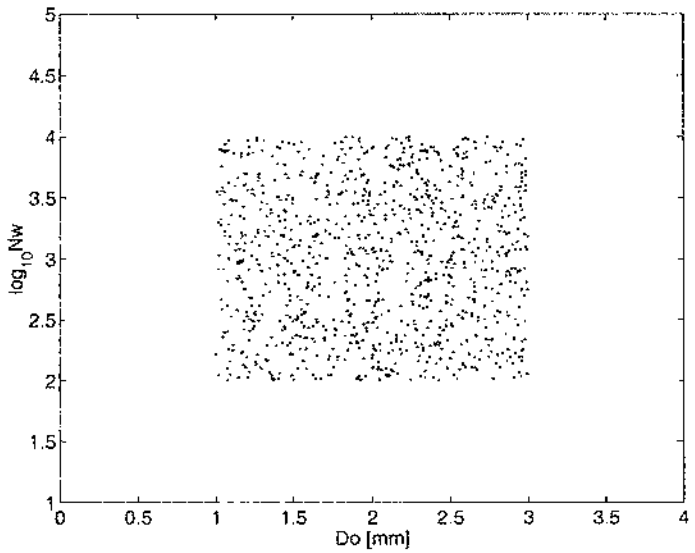

Figure 3.2: Wet graupel D_0 vs $log_{10}Nw$.

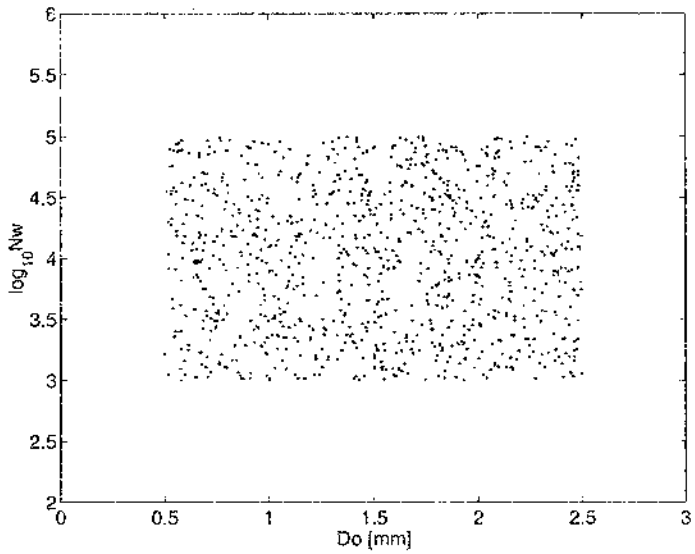

Figure 3.3: Rain D_0 vs $log_{10}Nw$.

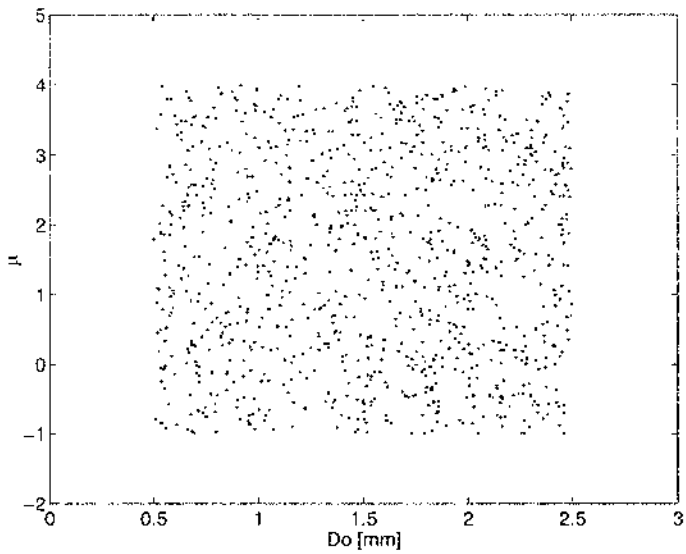

Figure 3.4: Rain D_0 vs μ.

0.4 density, snow with 0.5 density, and finally rain. In these figures the circle shows the result of scatter of attenuation vs. reflectivity while the solid line shows the result of fitting when the $k = \alpha Z^{\beta}$ model is used.

Figure Number	Title Description
Figure 3.5	aggregate with 0.1 density at 13.8 GHz
Figure 3.6	aggregate with 0.1 density at 28.0 GHz
Figure 3.7	aggregate with 0.1 density at 35.0 GHz
Figure 3.8	aggregate with 0.2 density at 13.8 GHz
Figure 3.9	aggregate with 0.2 density at 28.0 GHz
Figure 3.10	aggregate with 0.2 density at 35.0 GHz
Figure 3.11	aggregate with 0.3 density at 13.8 GHz
Figure 3.12	aggregate with 0.3 density at 28.0 GHz
Figure 3.13	aggregate with 0.3 density at 35.0 GHz
Figure 3.14	aggregate with 0.4 density at 13.8 GHz
Figure 3.15	aggregate with 0.4 density at 28.0 GHz
Figure 3.16	aggregate with 0.4 density at 35.0 GHz
Figure 3.17	aggregate with 0.5 density at 13.8 GHz
Figure 3.18	aggregate with 0.5 density at 28.0 GHz
Figure 3.19	aggregate with 0.5 density at 35.0 GHz
Figure 3.20	wet graupel with 0.4 density at 13.8 GHz
Figure 3.21	wet graupel with 0.4 density at 28.0 GHz
Figure 3.22	wet graupel with 0.4 density at 35.0 GHz
Figure 3.23	snow with 0.1 density at 13.8 GHz
Figure 3.24	snow with 0.1 density at 28.0 GHz
Figure 3.25	snow with 0.1 density at 35.0 GHz
Figure 3.26	rain with 1.0 density at 13.8 GHz
Figure 3.27	rain with 1.0 density at 28.0 GHz
Figure 3.28	rain with 1.0 density at 35.0 GHz

Table 3.3: Figure Number List of Scatter Plot of Attenuation vs. Reflectivity.

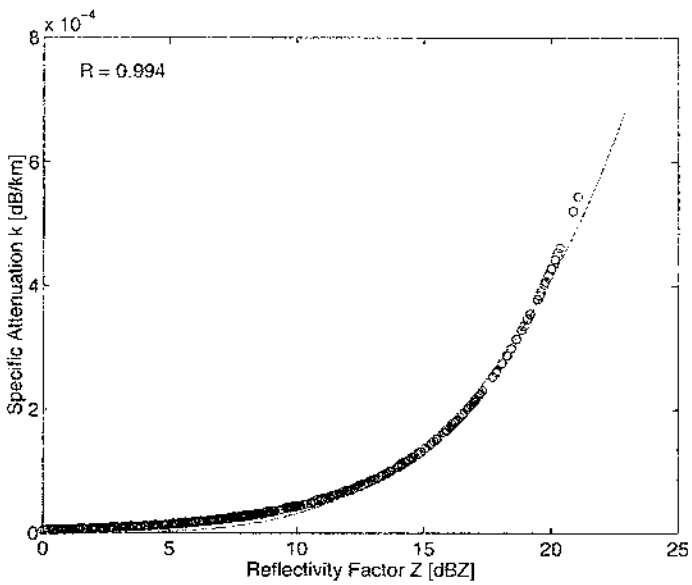

Figure 3.5: Scatter plot of specific attenuation vs. reflectivity for aggregate with density 0.1 at 13.8 GHz.

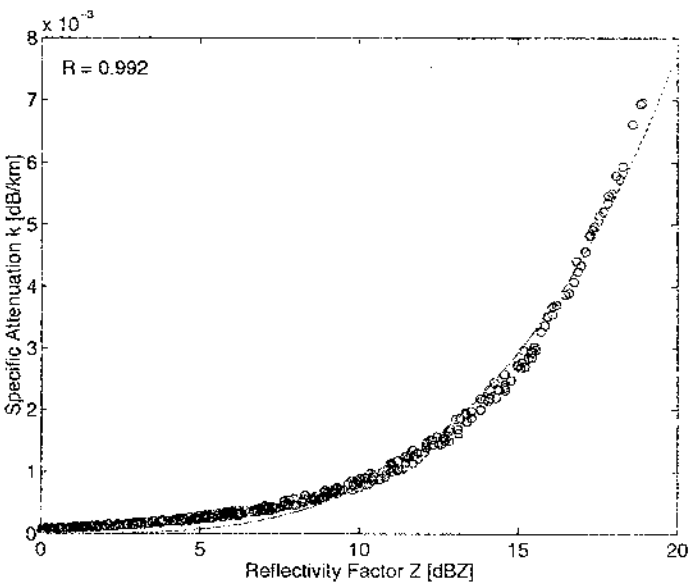

Figure 3.6: Scatter plot of specific attenuation vs. reflectivity for aggregate with density 0.1 at 28.0 GHz.

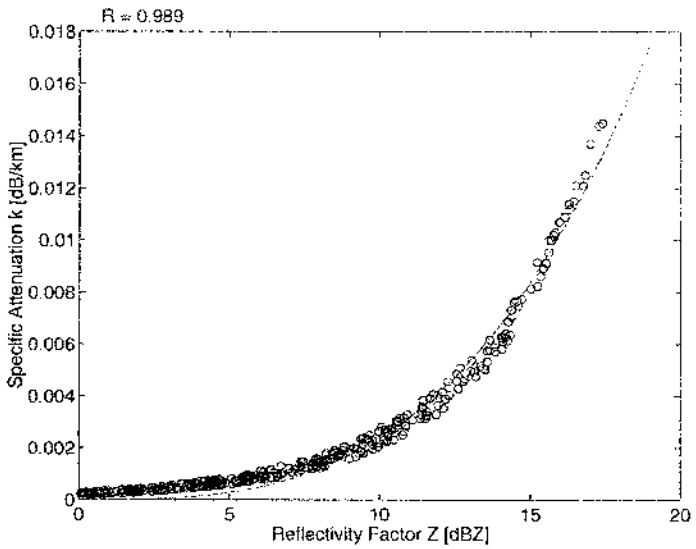

Figure 3.7: Scatter plot of specific attenuation vs. reflectivity for aggregate with density 0.1 at 35.0 GHz.

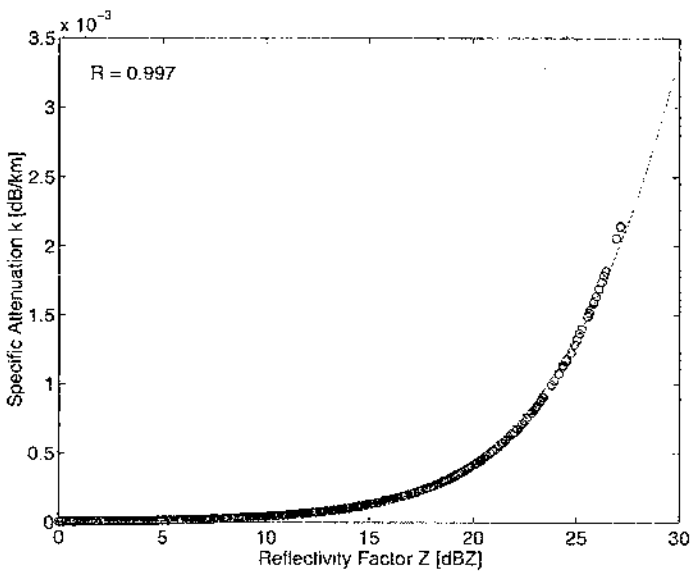

Figure 3.8: Scatter plot of specific attenuation vs. reflectivity for aggregate with density 0.2 at 13.8 GHz.

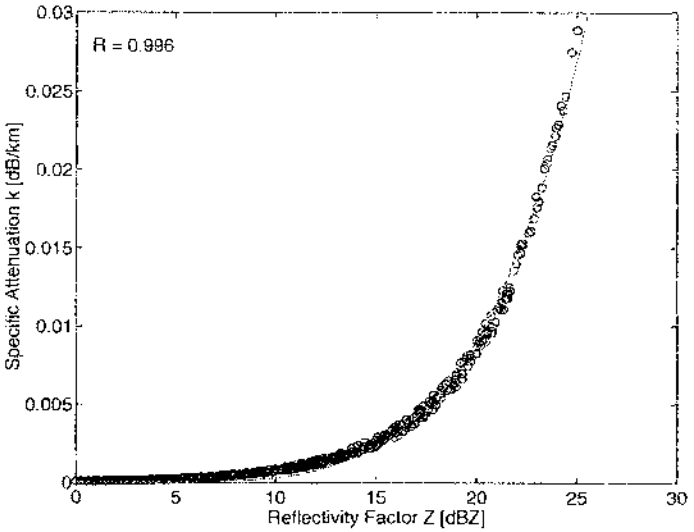

Figure 3.9: Scatter plot of specific attenuation vs. reflectivity for aggregate with density 0.2 at 28.0 GHz.

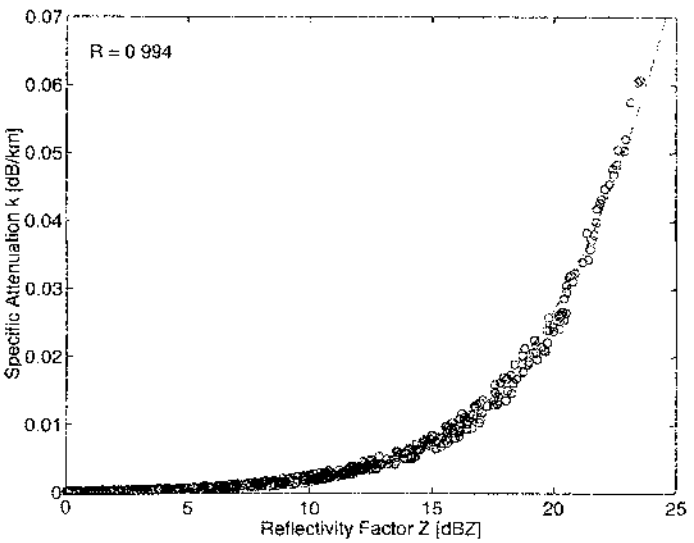

Figure 3.10: Scatter plot of specific attenuation vs. reflectivity for aggregate with density 0.2 at 35 GHz.

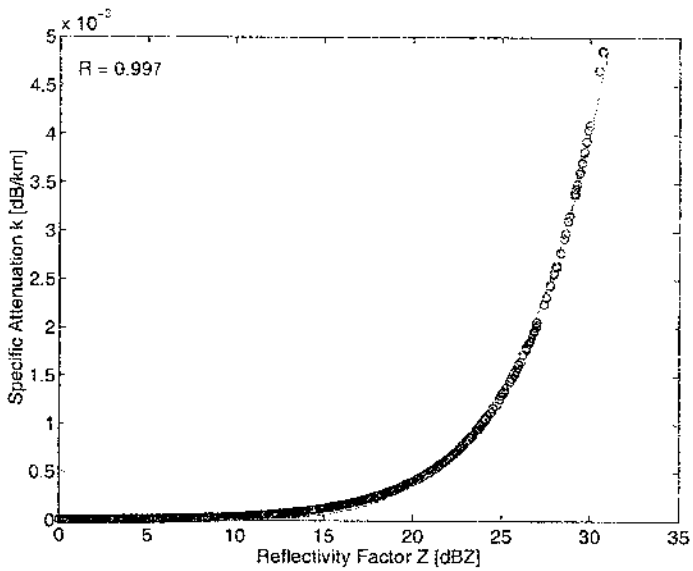

Figure 3.11: Scatter plot of specific attenuation vs. reflectivity for aggregate with density 0.3 at 13.8 GHz.

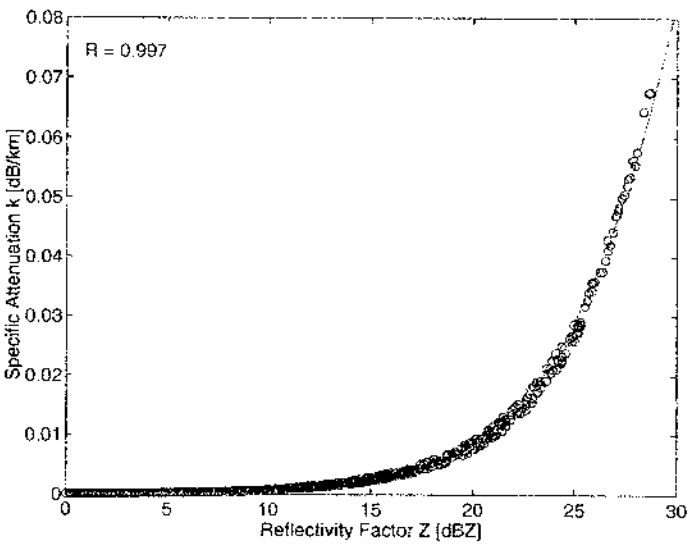

Figure 3.12: Scatter plot of specific attenuation vs. reflectivity for aggregate with density 0.3 at 28.0 GHz.

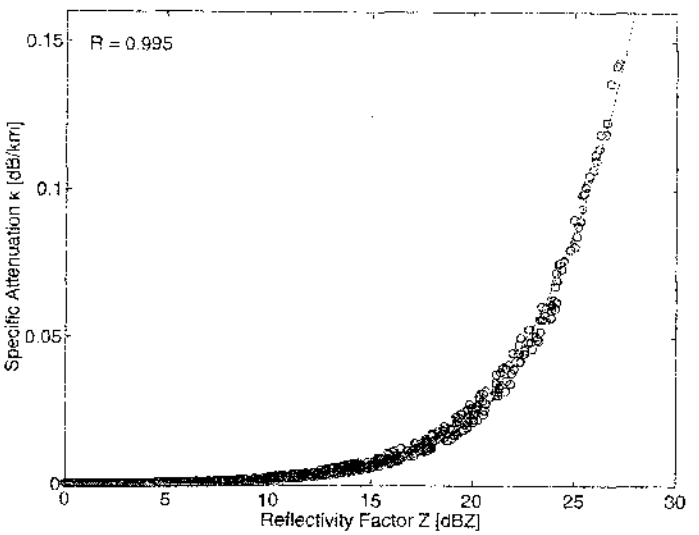

Figure 3.13: Scatter plot of specific attenuation vs. reflectivity for aggregate with density 0.3 at 35.0 GHz.

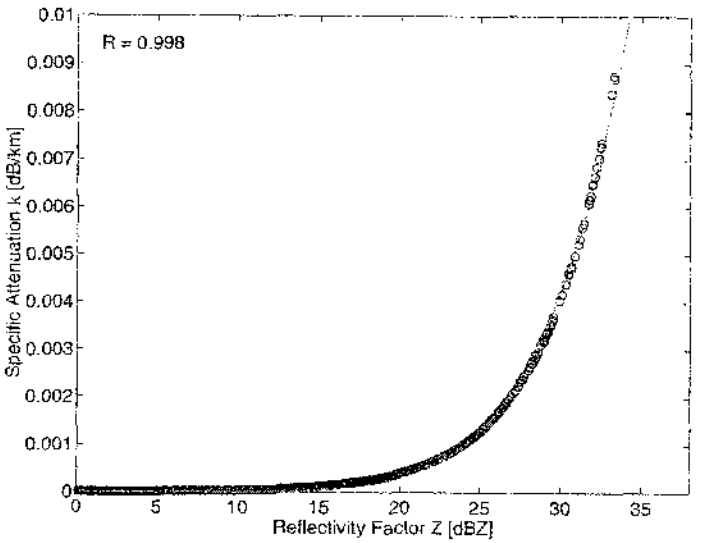

Figure 3.14: Scatter plot of specific attenuation vs. reflectivity for aggregate with density 0.4 at 13.8 GHz.

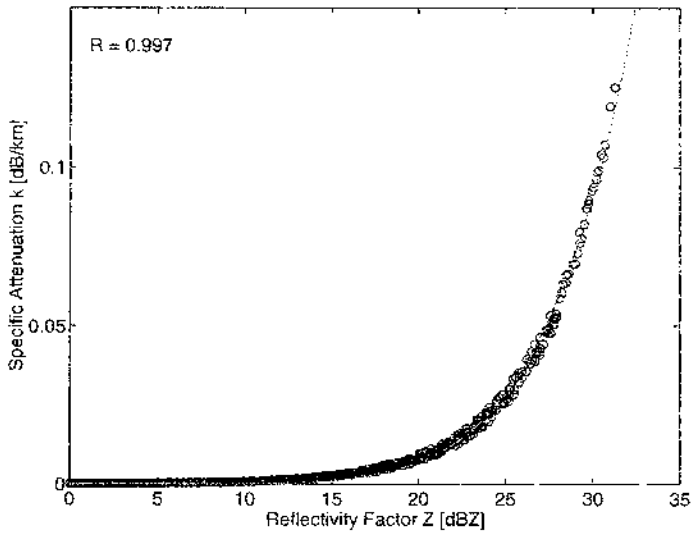

Figure 3.15: Scatter plot of specific attenuation vs. reflectivity for aggregate with density 0.4 at 28.0 GHz.

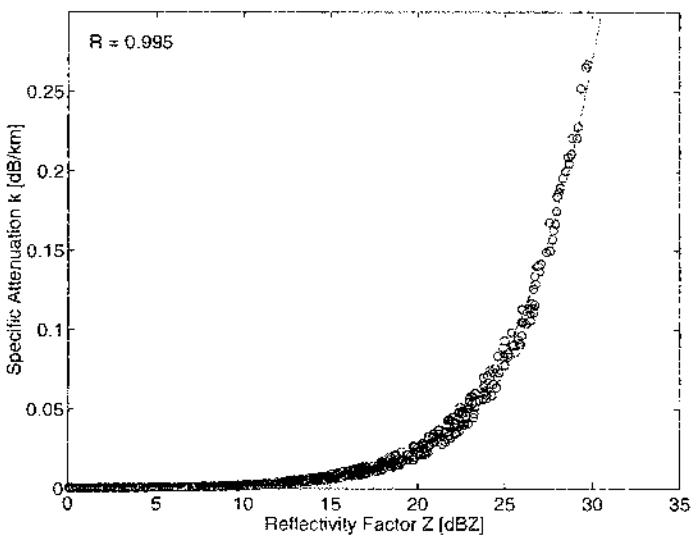

Figure 3.16: Scatter plot of specific attenuation vs. reflectivity for aggregate with density 0.4 at 35.0 GHz.

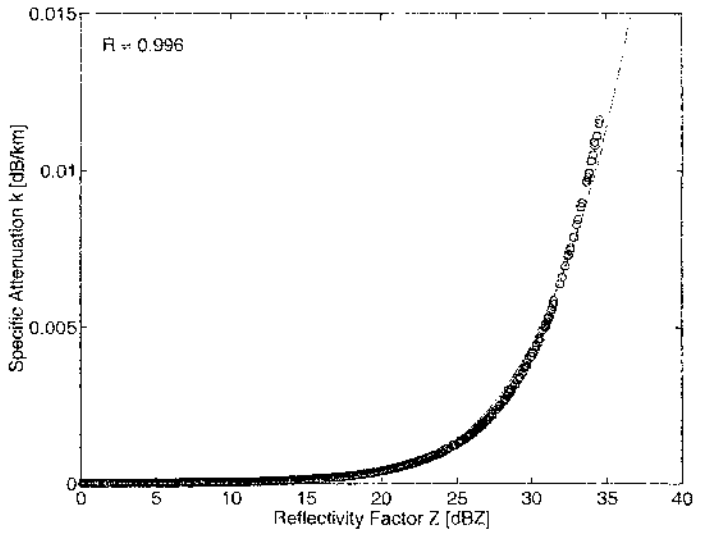

Figure 3.17: Scatter plot of specific attenuation vs. reflectivity for aggregate with density 0.5 at 13.8 GHz.

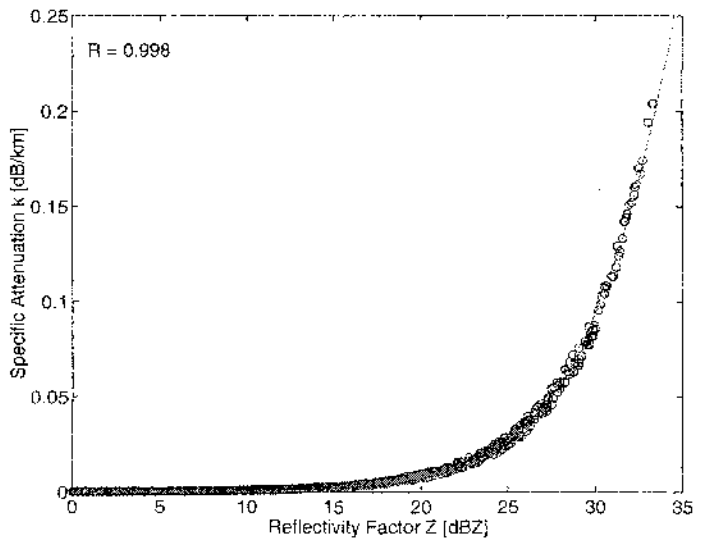

Figure 3.18: Scatter plot of specific attenuation vs. reflectivity for aggregate with density 0.5 at 28.0 GHz.

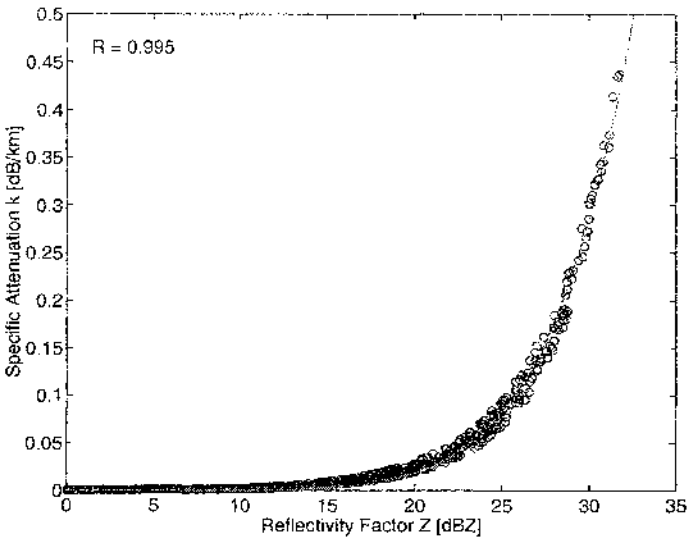

Figure 3.19: Scatter plot of specific attenuation vs. reflectivity for aggregate with density 0.5 at 35.0 GHz.

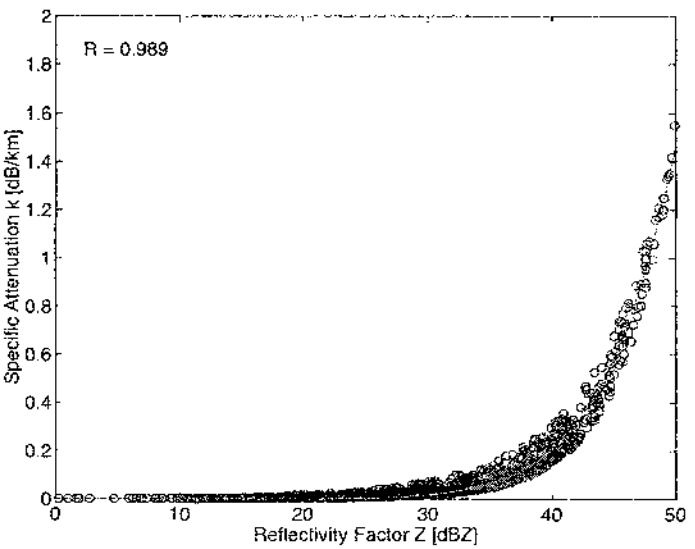

Figure 3.20: Scatter plot of specific attenuation vs. reflectivity for wet graupel with density 0.4 at 13.8 GHz.

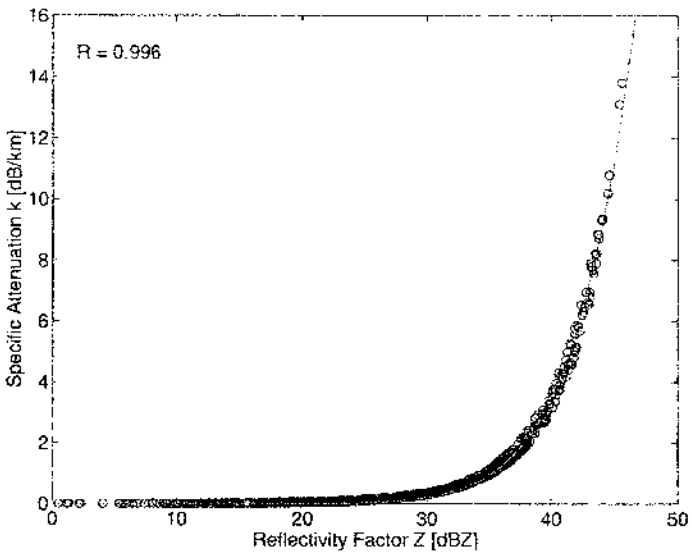

Figure 3.21: Scatter plot of specific attenuation vs. reflectivity for wet graupel with density 0.4 at 28.0 GHz.

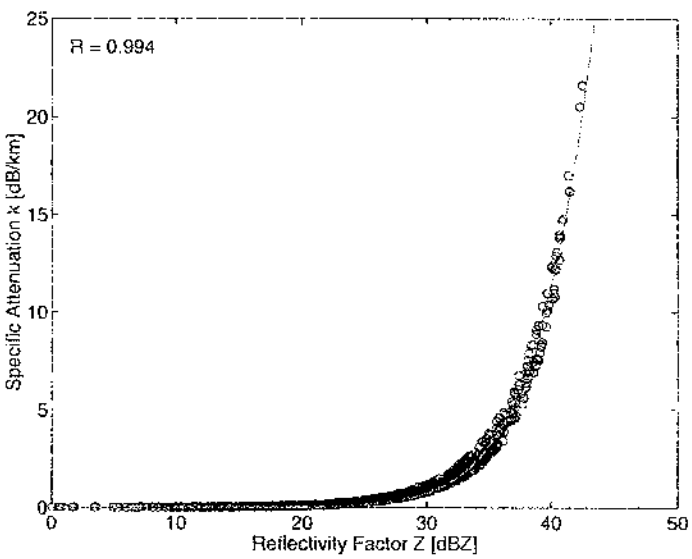

Figure 3.22: Scatter plot of specific attenuation vs. reflectivity for wet graupel with density 0.4 at 35.0 GHz.

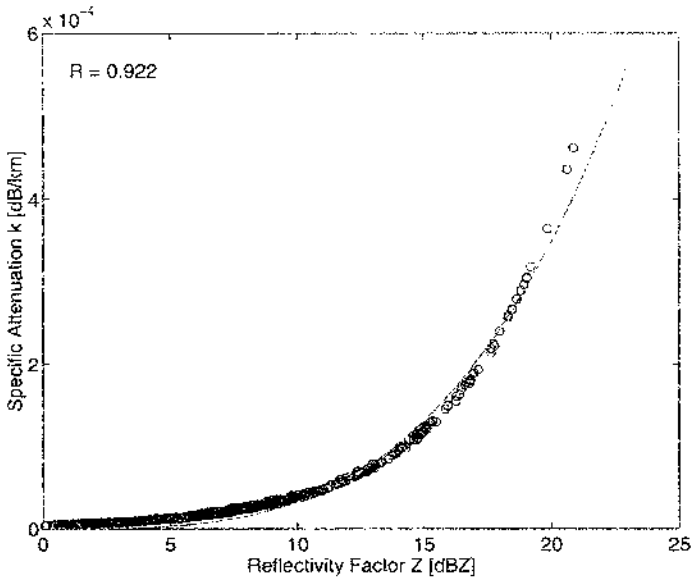

Figure 3.23: Scatter plot of specific attenuation vs. reflectivity for snow with density 0.1 at 13.8 GHz.

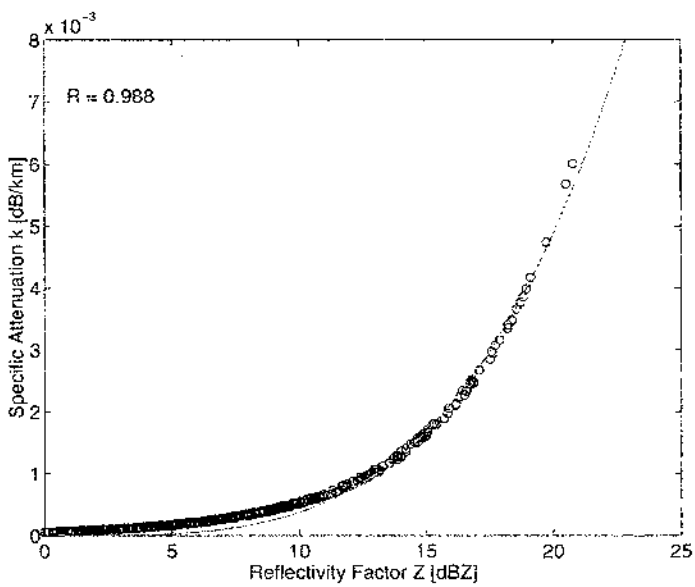

Figure 3.24: Scatter plot of specific attenuation vs. reflectivity for snow with density 0.1 at 28.0 GHz.

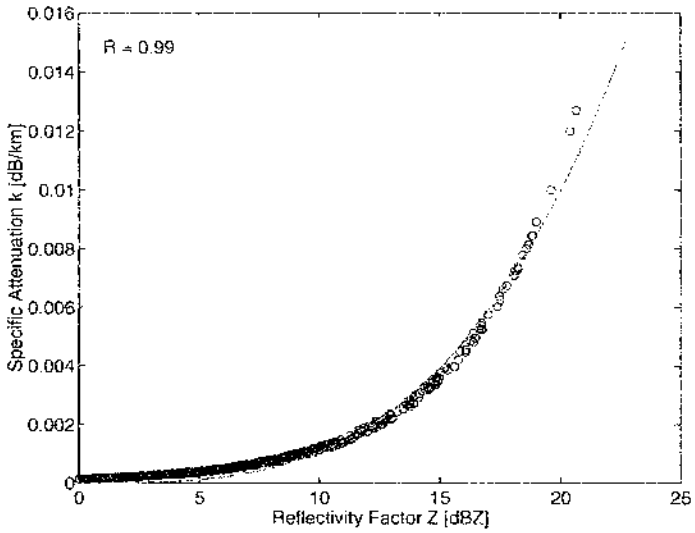

Figure 3.25: Scatter plot of specific attenuation vs. reflectivity for snow with density 0.1 at 35.0 GHz.

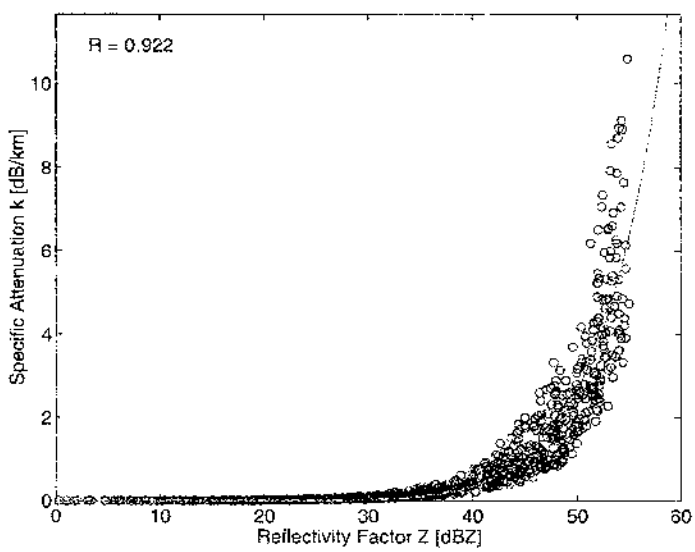

Figure 3.26: Scatter plot of specific attenuation vs. reflectivity for rain with density 1.0 at 13.8 GHz.

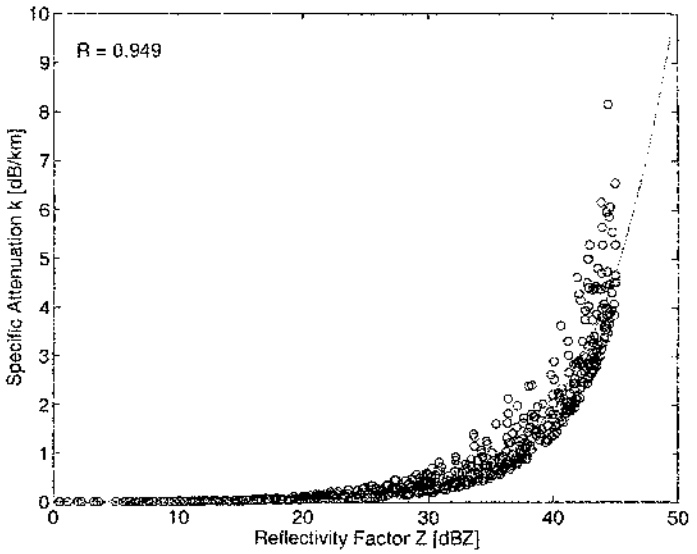

Figure 3.27: Scatter plot of specific attenuation vs. reflectivity for rain with density 1.0 at 28.0 GHz.

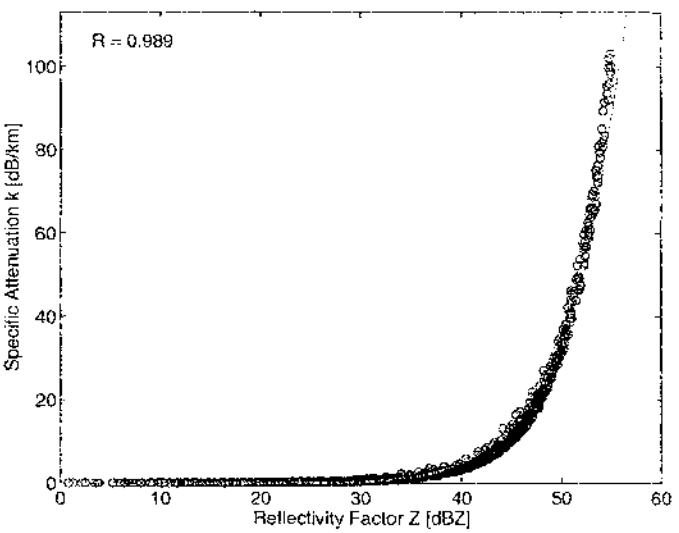

Figure 3.28: Scatter plot of specific attenuation vs. reflectivity for rain with density 1.0 at 35.0 GHz.

Table 3.4 shows the parameterization of the relation between specific attenuation and reflectivity of the form $k = \alpha Z^{\beta}$ for different types of hydrometeors.

Hydrometeor Type	13.8 GHz		28.0 GHz		35.0 GHz	
	α	β	α	β	α	β
Aggregate with 0.1 density	4.44E-06	0.995	7.40E-05	1.045	1.90E-04	1.075
Aggregate with 0.2 density	4.08E-06	1.002	6.90E-05	1.048	1.78E-04	1.079
Aggregate with 0.3 density	2.90E-06	1.051	6.62E-05	1.049	1.60E-04	1.080
Aggregate with 0.4 density	3.90E-06	1.007	6.43E-05	1.052	1.51E-04	1.090
Aggregate with 0.5 density	4.08E-06	1.002	6.24E-05	1.055	1.70E-04	1.079
Wet graupel with 0.4 density	7.70E-05	0.895	1.90E-04	1.063	1.30E-04	1.163
Snow with 0.1 density	3.93E-06	0.991	5.60E-05	0.978	1.27E-04	0.969
Rain with 1.0 density	1.32E-04	0.834	3.02E-04	0.938	7.20E-04	0.920

Table 3.4: Parameter of $k = \alpha Z^{\beta}$ for Aggregate, Wet graupel, Snow and Rain.

3.6 Frequency Scaling of Attenuation

The specific attenuations at two different frequencies $f1$ and $f2$ can be approximated as:

$$k_{f2} = a k_{f1} \tag{3.47}$$

where a is constant. Thus, in a region of uniform k, the ratio of PIA_{f1} and PIA_{f2} can be written as:

$$\frac{PIA_{f_2}(r)}{PIA_{f_1}(r)} = \frac{2\int_0^r k_{f_2}(s)ds}{2\int_0^r k_{f_1}(s)ds} \approx a \tag{3.48}$$

or

$$PIA_{f_2}(r) \approx a \cdot PIA_{f_1}(r) \tag{3.49}$$

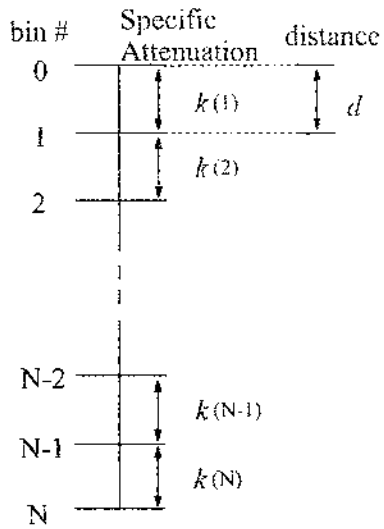

Figure 3.29: Specific attenuation layout.

now $\int_0^r k(s)ds$ can be approximated as

$$\int_0^r k(s)ds \approx \sum_{i=1}^{n} k(i)d \tag{3.50}$$

where n is bin number and d $[km]$ is the distance between bins. In the TRMM system. d is 0.25 km and N is 79 (Figure 3.29). Thus, PIA at bin number n is:

$$PIA(n) \approx 2d\sum_{i=1}^{n} k(i) \tag{3.51}$$

From Equation 3.49 and Equation 3.51:

$$\begin{aligned} PIA_{f_2}(n) &\approx a \cdot PIA_{f_1}(n) \\ &\approx 2ad\sum_{i=1}^{n} k_{f_1}(i). \end{aligned} \tag{3.52}$$

The actual atmosphere consists of multi-layer media (aggregate, graupel, rain etc.). When radar propagates through M-layers, Equation 3.52 becomes:

$$\begin{aligned} PIA_{f_2}(n) &\approx 2a_1 d \sum_{i=1}^{n_1} k_{f_1}(i) + 2a_2 d \sum_{i=n_1+1}^{n_2} k_{f_1}(i) \\ &\quad \cdots + 2a_M d \sum_{i=n_{M-1}+1}^{n} k_{f_1}(i) \\ &\approx 2d \sum_{m=1}^{M} a_m \left\{ \sum_{i=n_{m-1}+1}^{n_m} k_{f_1}(i) \right\} \end{aligned} \tag{3.53}$$

where a_m is the coefficient of Equation 3.49 for m-th layer and n_m is the bin number between mth and m+1th layers. From Equation 3.51 specific attenuation $k(n)$ is obtained by:

$$\begin{aligned} k(n) &= \sum_{i=1}^{n} k(i) - \sum_{i=1}^{n-1} k(i) \\ &= \frac{PIA(n)}{2d} - \frac{PIA(n-1)}{2d} \\ &= \frac{PIA(n) - PIA(n-1)}{2d} \end{aligned} \tag{3.54}$$

Finally,

$$\begin{aligned} PIA_{f_2}(n) &\approx 2d \sum_{m=1}^{M} a_m \left[\sum_{i=n_{m-1}+1}^{n_m} k_{f_1}(i) \right] \\ &\approx \sum_{m=1}^{M} a_m \left[\sum_{i=n_{m-1}+1}^{n_m} \{ PIA_{f_1}(i) - PIA_{f_1}(i-1) \} \right]. \end{aligned} \tag{3.55}$$

Table 3.5 provides an itemized list of the figures of the scatter plot of specific attenuation through aggregate, wet graupel, snow, and rain at 13.8 GHz, 28.0 GHz and 35.0 GHz. In these figures the circle shows the result of scatter while the solid line shows the result of linearly fitting.

Figure Number	**Title Deiscription**
Figure 3.30	aggregate with 0.1 density at 13.8 and 28.0 GHz
Figure 3.31	aggregate with 0.1 density at 13.8 and 35.0 GHz
Figure 3.32	aggregate with 0.2 density at 13.8 and 28.0 GHz
Figure 3.33	aggregate with 0.2 density at 13.8 and 35.0 GHz
Figure 3.34	aggregate with 0.3 density at 13.8 and 28.0 GHz
Figure 3.35	aggregate with 0.3 density at 13.8 and 35.0 GHz
Figure 3.36	aggregate with 0.4 density at 13.8 and 28.0 GHz
Figure 3.37	aggregate with 0.4 density at 13.8 and 35.0 GHz
Figure 3.38	aggregate with 0.5 density at 13.8 and 28.0 GHz
Figure 3.39	aggregate with 0.5 density at 13.8 and 35.0 GHz
Figure 3.40	wet graupel at 13.8 and 28.0 GHz
Figure 3.41	wet graupel at 13.8 and 35.0 GHz
Figure 3.42	snow at 13.8 and 28.0 GHz
Figure 3.43	snow at 13.8 and 35.0 GHz
Figure 3.44	rain at 13.8 and 28.0 GHz
Figure 3.45	rain at 13.8 and 35.0 GHz

Table 3.5: Figure Number List of Scatter Plot of Attenuation.

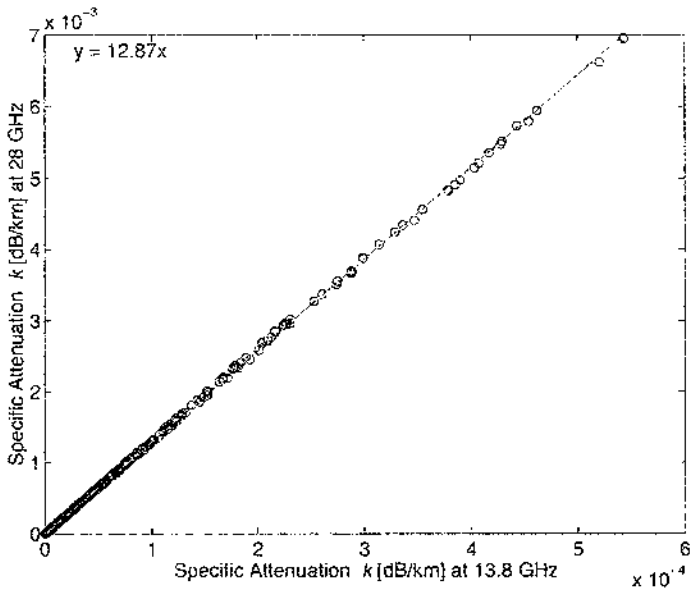

Figure 3.30: Scatter plot of specific attenuation for aggregate with density 0.1 at 13.8 and 28.0 GHz.

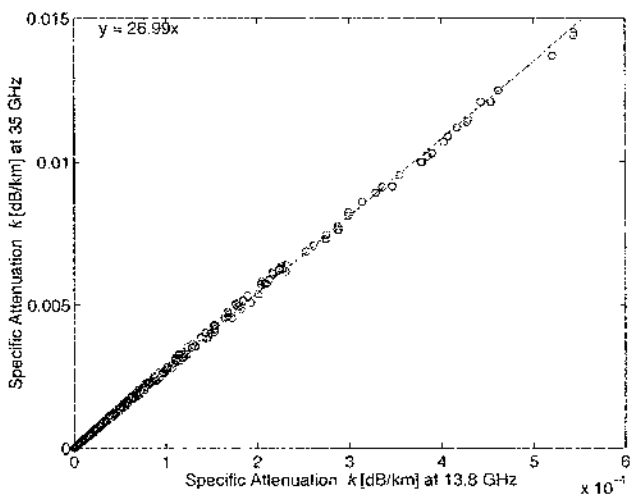

Figure 3.31: Scatter plot of specific attenuation for aggregate with density 0.1 at 13.8 and 35.0 GHz.

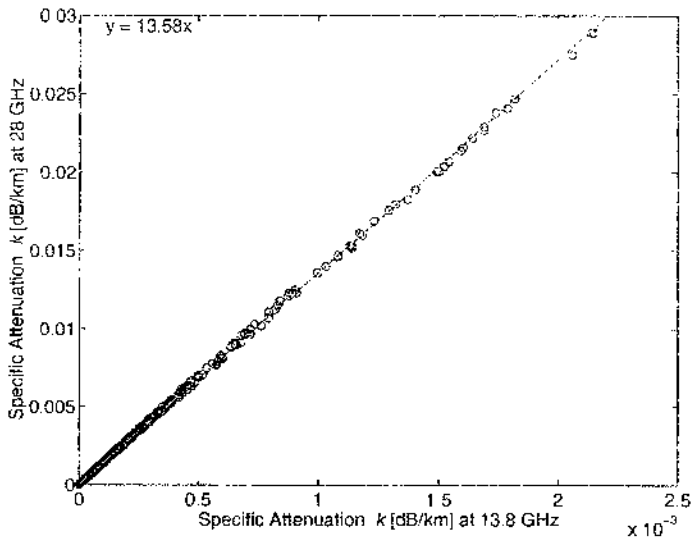

Figure 3.32: Scatter plot of specific attenuation for aggregate with density 0.2 at 13.8 and 28.0 GHz.

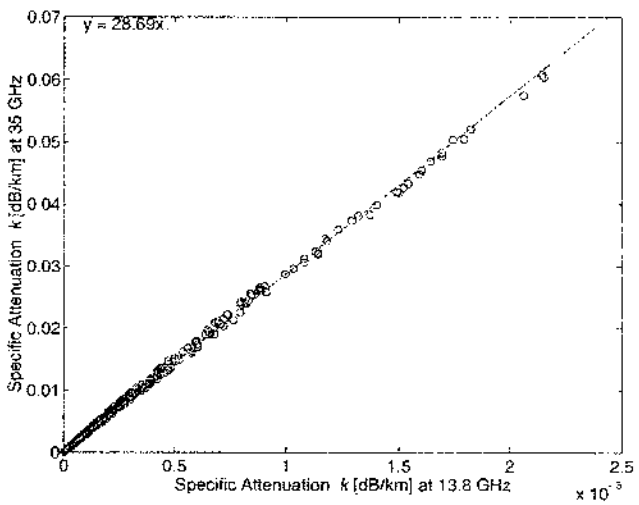

Figure 3.33: Scatter plot of specific attenuation for aggregate with density 0.2 at 13.8 and 35.0 GHz.

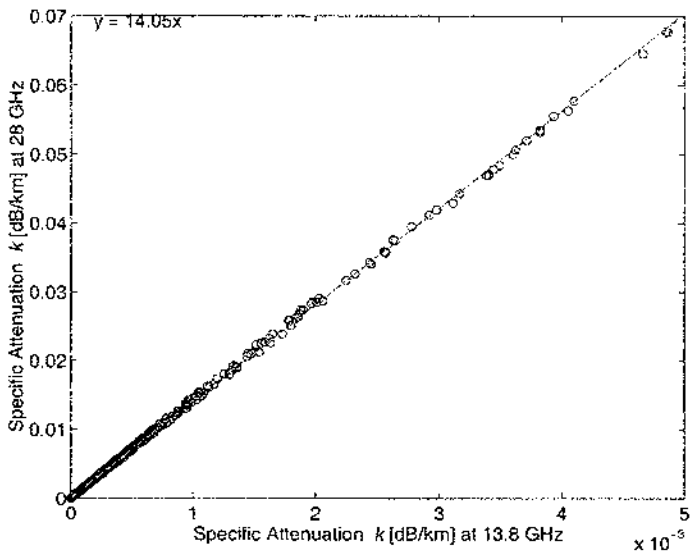

Figure 3.34: Scatter plot of specific attenuation for aggregate with density 0.3 at 13.8 and 28.0 GHz.

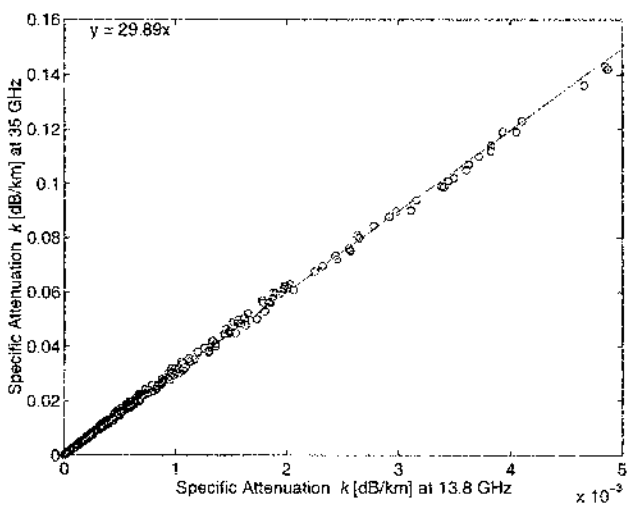

Figure 3.35: Scatter plot of specific attenuation for aggregate with density 0.3 at 13.8 and 35.0 GHz.

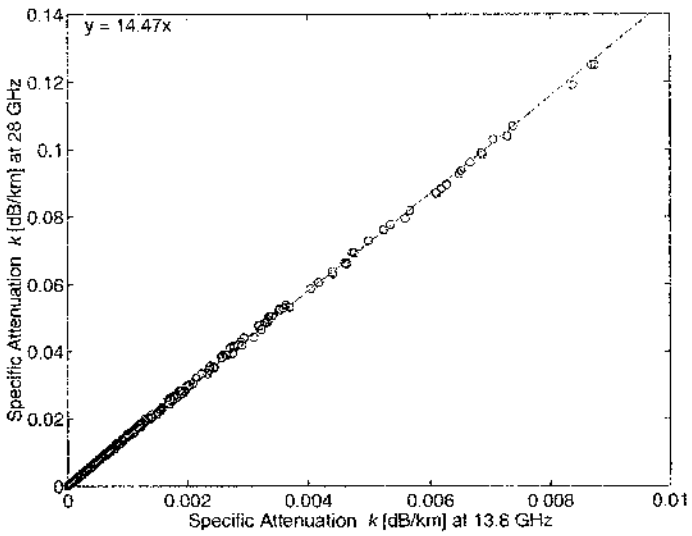

Figure 3.36: Scatter plot of specific attenuation for aggregate with density 0.4 at 13.8 and 28.0 GHz.

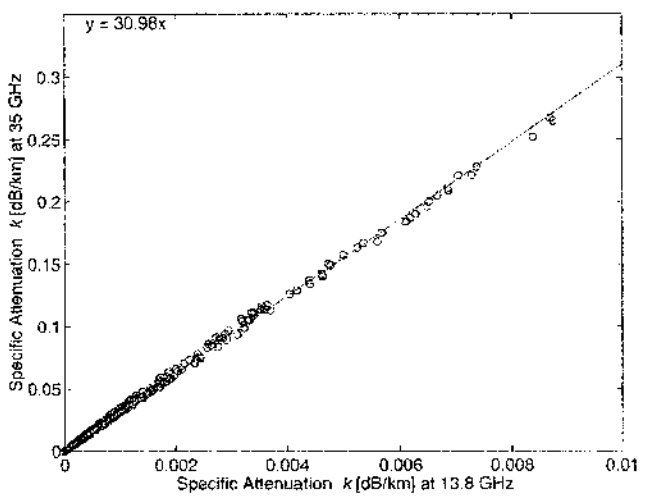

Figure 3.37: Scatter plot of specific attenuation for aggregate with density 0.4 at 13.8 and 35.0 GHz.

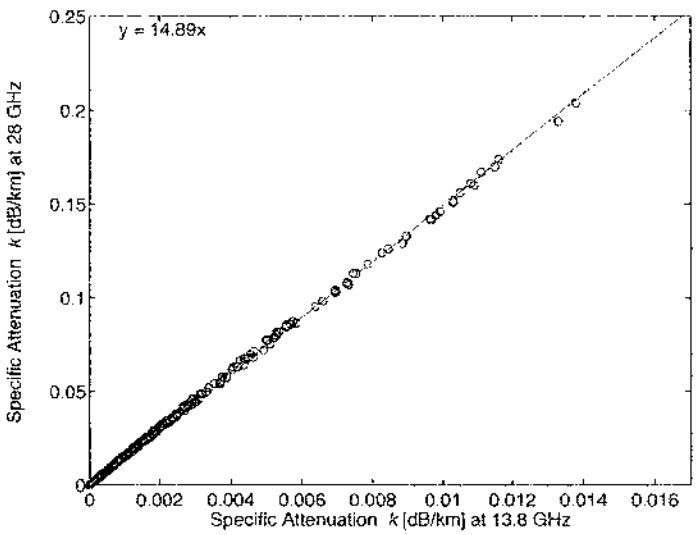

Figure 3.38: Scatter plot of specific attenuation for aggregate with density 0.5 at 13.8 and 28.0 GHz.

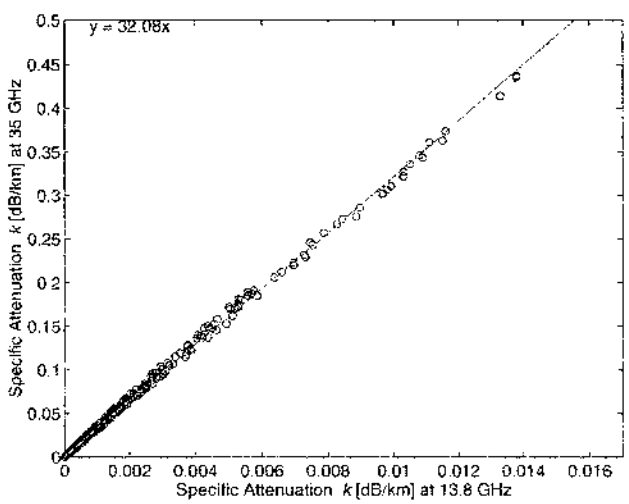

Figure 3.39: Scatter plot of specific attenuation for aggregate with density 0.5 at 13.8 and 35.0 GHz.

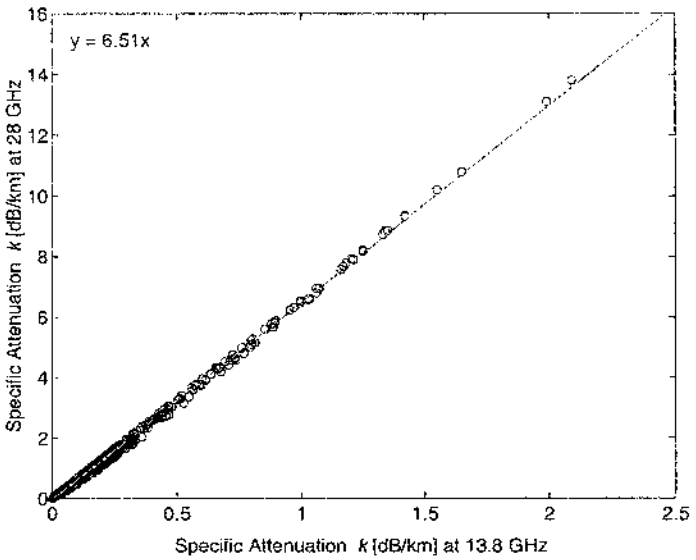

Figure 3.40: Scatter plot of specific attenuation for wet graupel at 13.8 and 28.0 GHz.

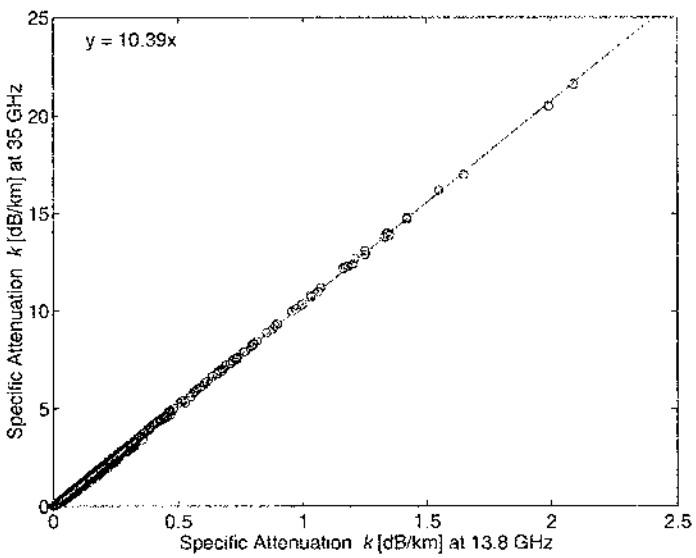

Figure 3.41: Scatter plot of specific attenuation for wet graupel at 13.8 and 35.0 GHz.

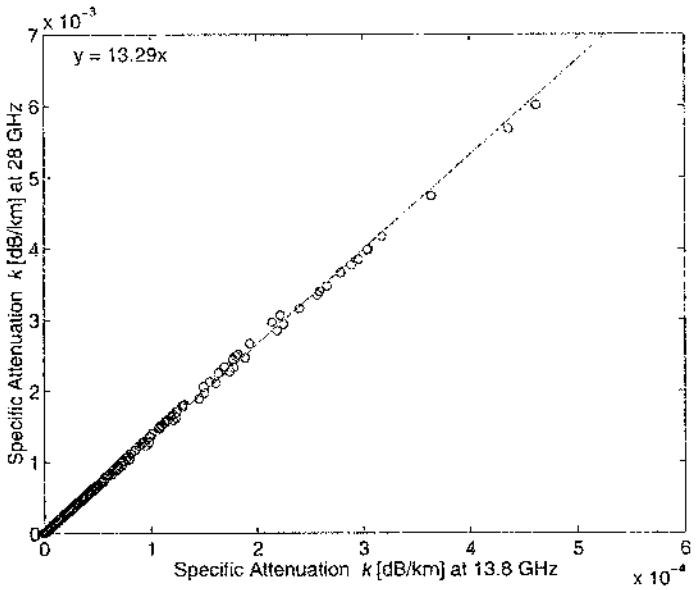

Figure 3.42: Scatter plot of specific attenuation for snow at 13.8 and 28.0 GHz.

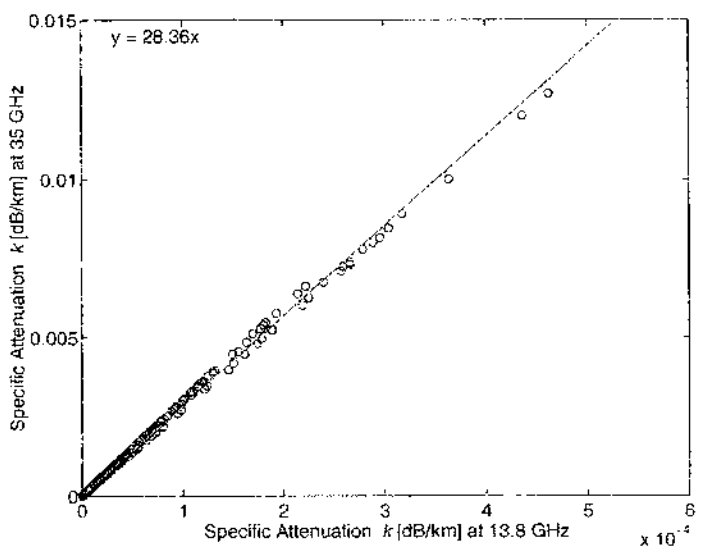

Figure 3.43: Scatter plot of specific attenuation for snow at 13.8 and 35.0 GHz.

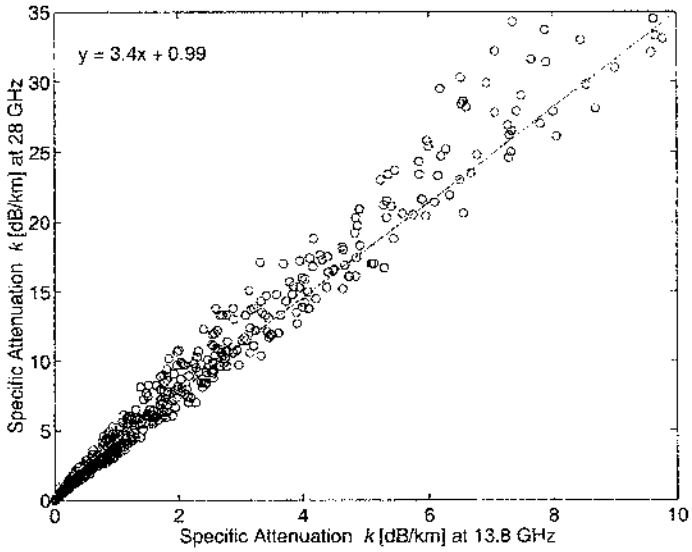

Figure 3.44: Scatter plot of specific attenuation for rain at 13.8 and 28.0 GHz.

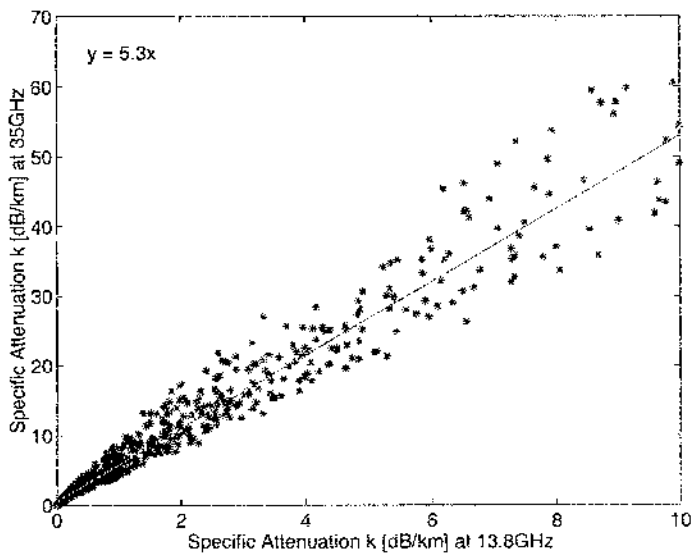

Figure 3.45: Scatter plot of specific attenuation for rain at 13.8 and 35.0 GHz.

Table 5.3 shows the attenuation relationship between 13.8 GHz (Ku-band),28.0 GHz, and 35 GHz (Ka-band).

Hydrometeor Type	**13.8 and 28.0**	**13.8 and 35.0**
Aggregate with 0.1 density	12.87	26.98
Aggregate with 0.2 density	13.58	28.69
Aggregate with 0.3 density	14.05	29.89
Aggregate with 0.4 density	14.47	30.97
Aggregate with 0.5 density	14.50	32.08
Wet graupel with 0.4 density	6.51	10.39
Snow with 0.1 density	13.28	28.36
Rain with 1.0 density	3.39	5.31

Table 3.6: Parameter of $k(Ka) = ck(Ku)$ for Aggregate, Wet graupel, Snow and Rain.

Table 3.7 provides an itemized list of the figures of the scatter plot of reflectivity through aggregate, wet graupel, snow, and rain at 13.8 GHz, 28.0 GHz and 13.8 GHz, 35.0 GHz. In these figures the circle shows the result of scatter while the solid line shows the result of fitting these figures.

Figure Number	Title Description
Figure 3.46	aggregate with 0.1 density at 13.8 and 28.0 GHz
Figure 3.47	aggregate with 0.1 density at 13.8 and 35.0 GHz
Figure 3.48	aggregate with 0.2 density at 13.8 and 28.0 GHz
Figure 3.49	aggregate with 0.2 density at 13.8 and 35.0 GHz
Figure 3.50	aggregate with 0.3 density at 13.8 and 28.0 GHz
Figure 3.51	aggregate with 0.3 density at 13.8 and 35.0 GHz
Figure 3.52	aggregate with 0.4 density at 13.8 and 28.0 GHz
Figure 3.53	aggregate with 0.4 density at 13.8 and 35.0 GHz
Figure 3.54	aggregate with 0.5 density at 13.8 and 28.0 GHz
Figure 3.55	aggregate with 0.5 density at 13.8 and 35.0 GHz
Figure 3.56	wet graupel at 13.8 and 28.0 GHz
Figure 3.57	wet graupel at 13.8 and 35.0 GHz
Figure 3.58	snow at 13.8 and 28.0 GHz
Figure 3.59	snow at 13.8 and 35.0 GHz
Figure 3.60	rain at 13.8 and 28.0 GHz
Figure 3.61	rain at 13.8 and 35.0 GHz

Table 3.7: Figure Number List of Scatter Plot of Reflectivity.

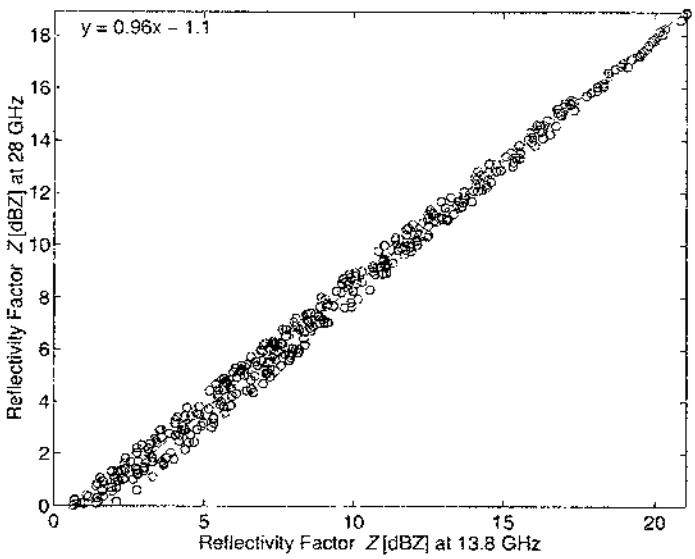

Figure 3.46: Scatter plot of reflectivity for aggregate with density 0.1 at 13.8 and 28.0 GHz.

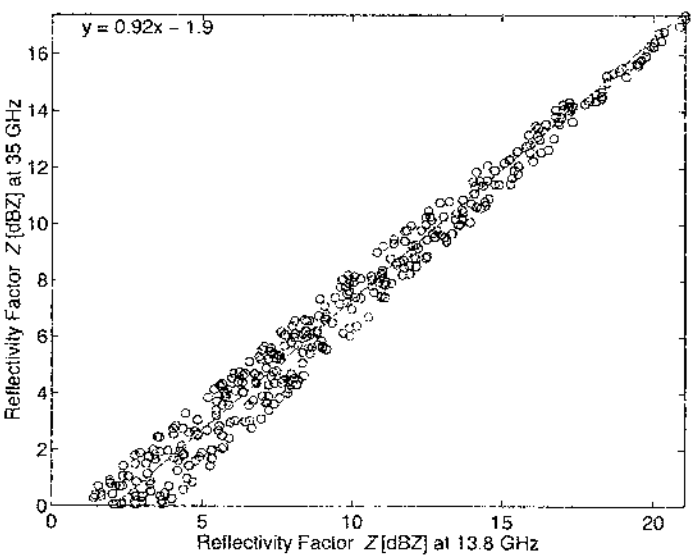

Figure 3.47: Scatter plot of reflectivity for aggregate with density 0.1 at 13.8 and 35.0 GHz.

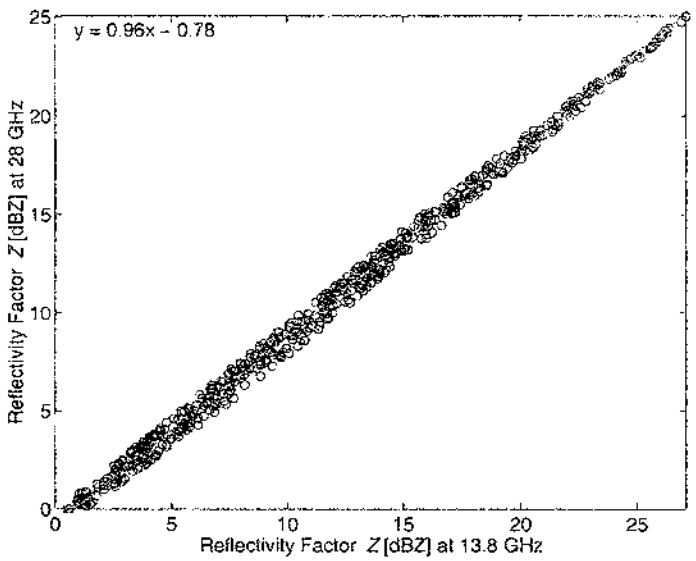

Figure 3.48: Scatter plot of reflectivity for aggregate with density 0.2 at 13.8 and 28.0 GHz.

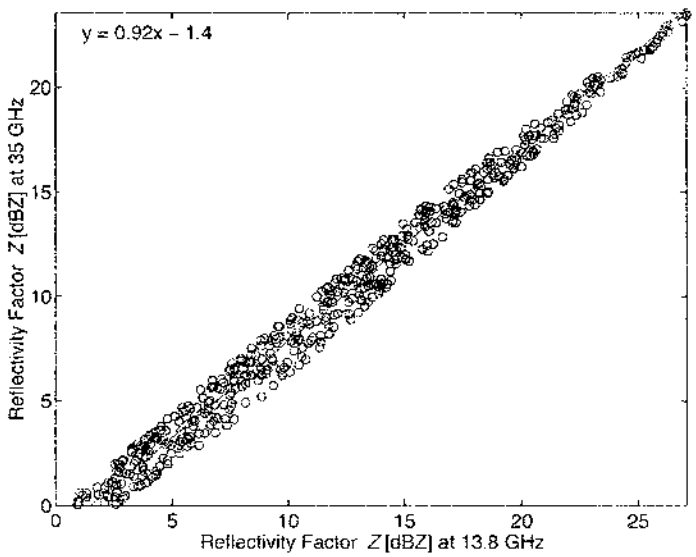

Figure 3.49: Scatter plot of reflectivity for aggregate with density 0.2 at 13.8 and 35.0 GHz.

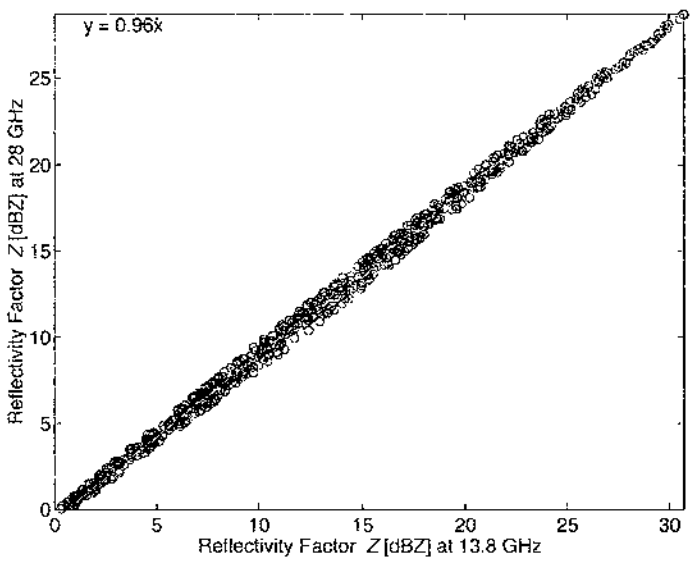

Figure 3.50: Scatter plot of reflectivity for aggregate with density 0.3 at 13.8 and 28.0 GHz.

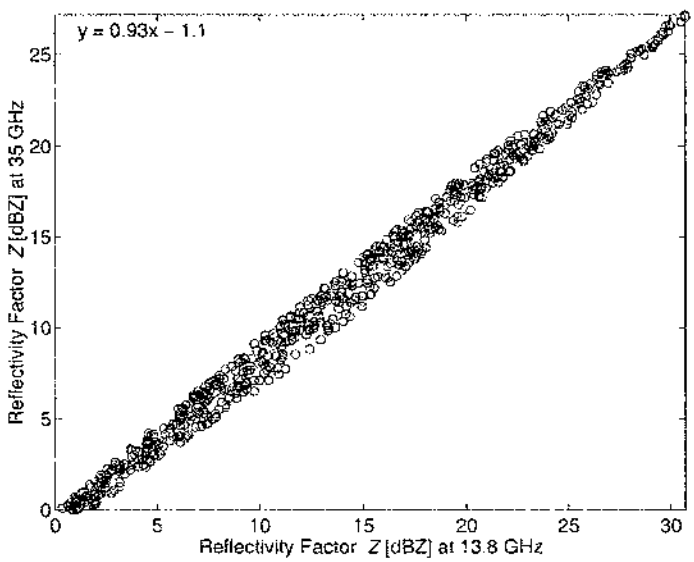

Figure 3.51: Scatter plot of reflectivity for aggregate with density 0.3 at 13.8 and 35.0 GHz.

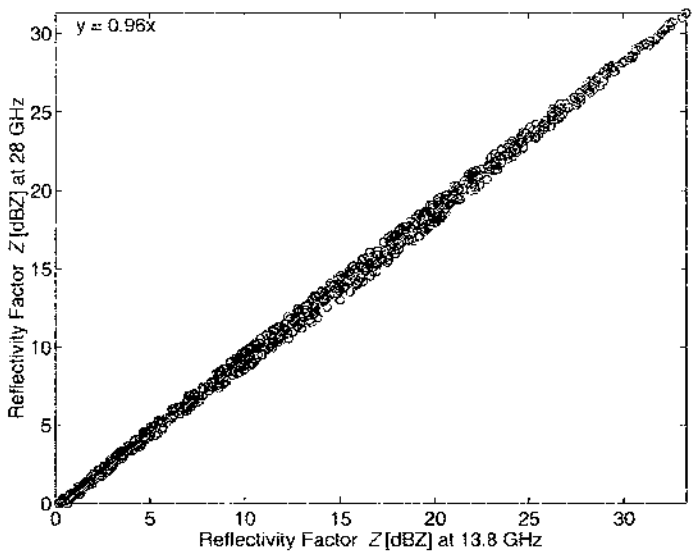

Figure 3.52: Scatter plot of reflectivity for aggregate with density 0.4 at 13.8 and 28.0 GHz.

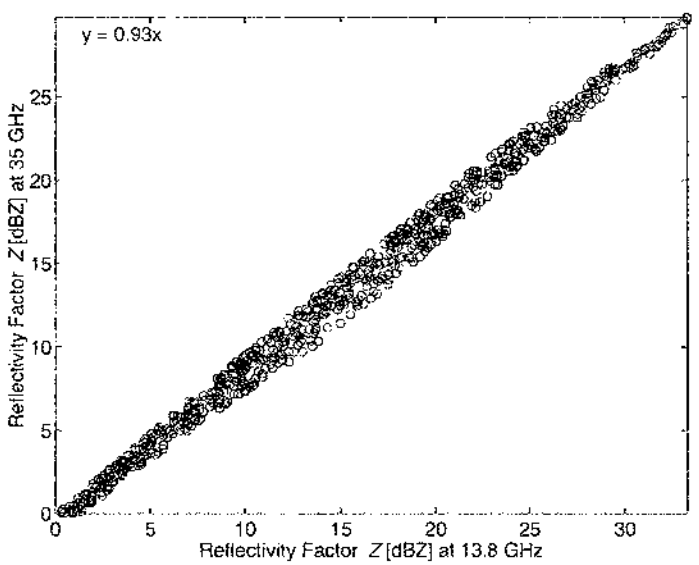

Figure 3.53: Scatter plot of reflectivity for aggregate with density 0.4 at 13.8 and 35.0 GHz.

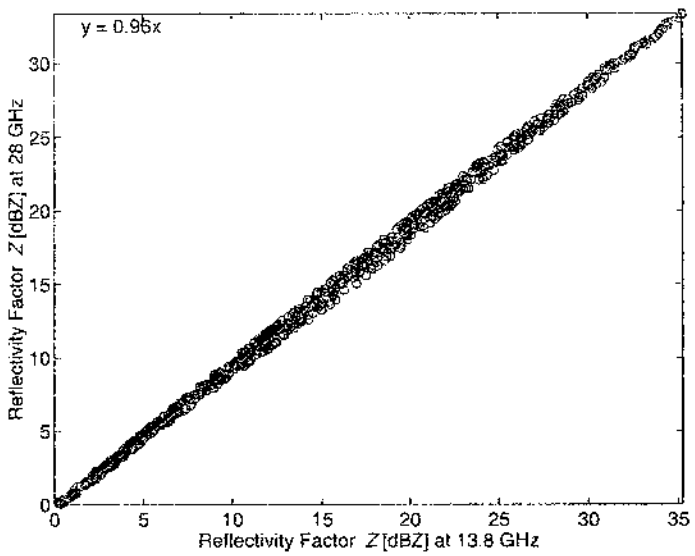

Figure 3.54: Scatter plot of reflectivity for aggregate with density 0.5 at 13.8 and 28.0 GHz.

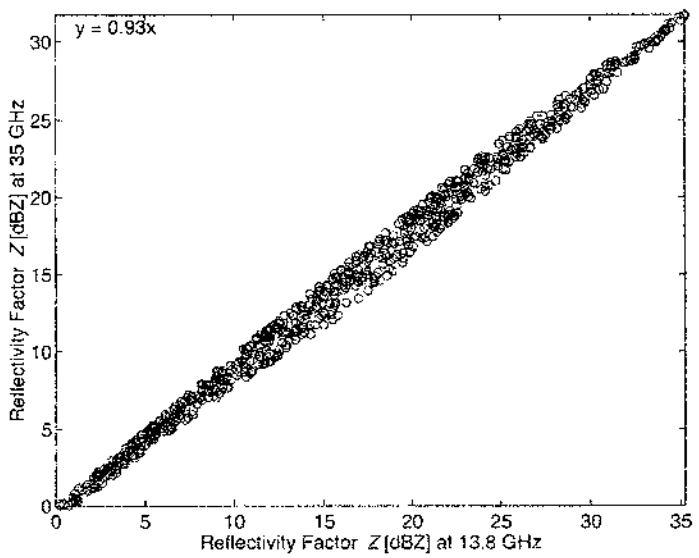

Figure 3.55: Scatter plot of reflectivity for aggregate with density 0.5 at 13.8 and 35.0 GHz.

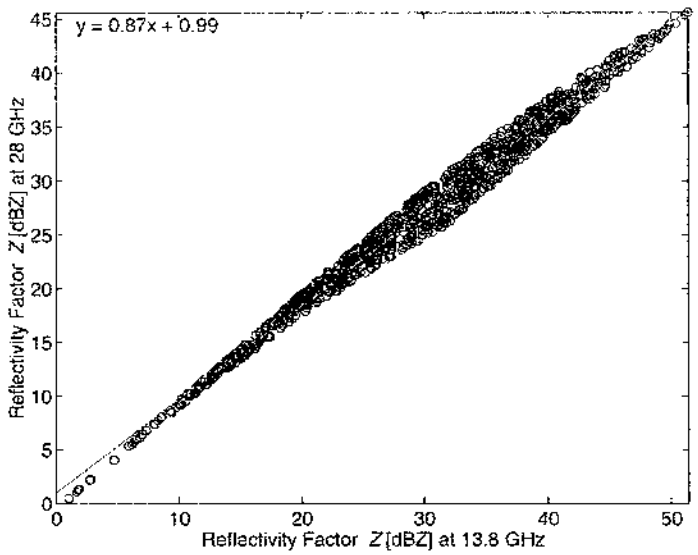

Figure 3.56: Scatter plot of reflectivity for wet graupel at 13.8 and 28.0 GHz.

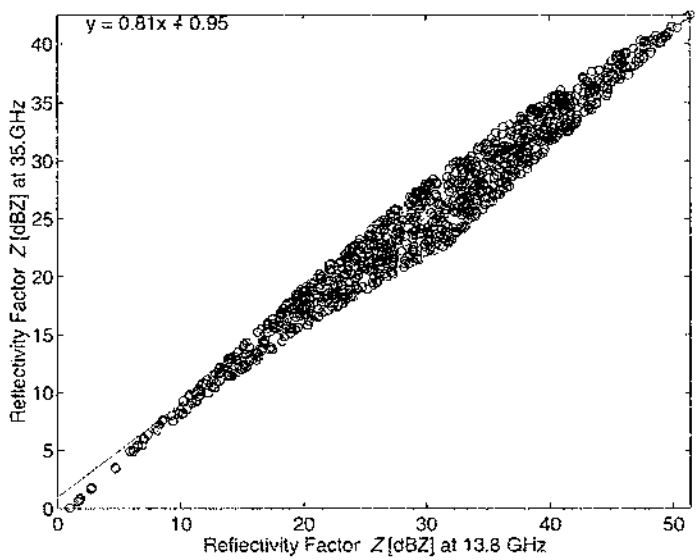

Figure 3.57: Scatter plot of reflectivity for wet graupel at 13.8 and 35.0 GHz.

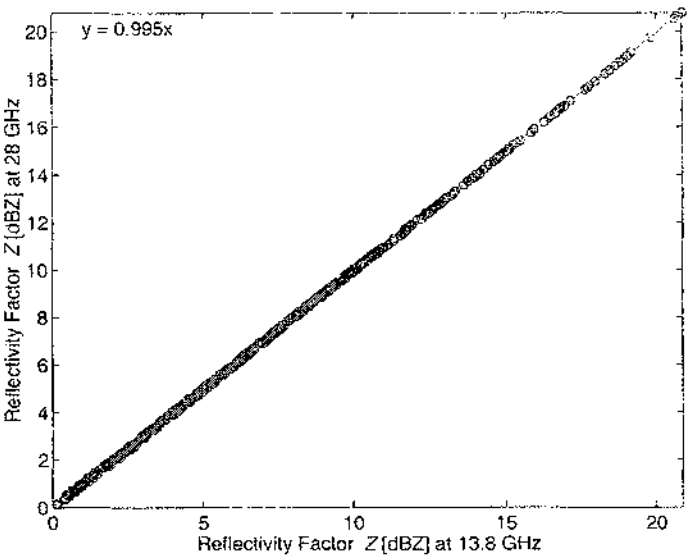

Figure 3.58: Scatter plot of reflectivity for snow at 13.8 and 28.0 GHz.

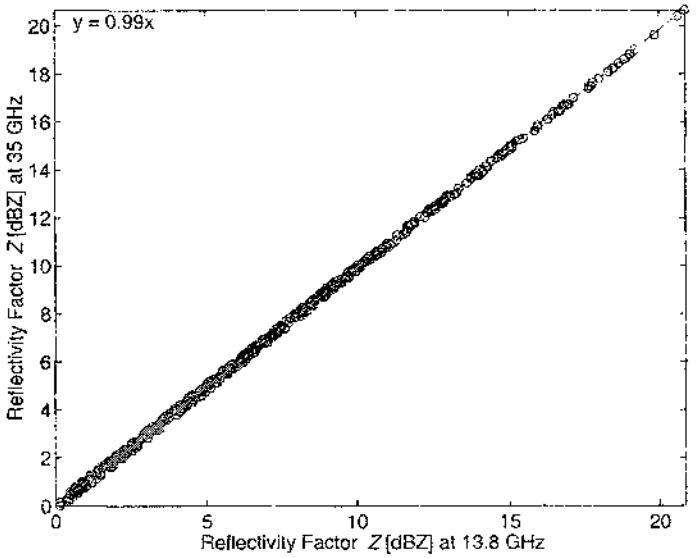

Figure 3.59: Scatter plot of reflectivity for snow at 13.8 and 35.0 GHz.

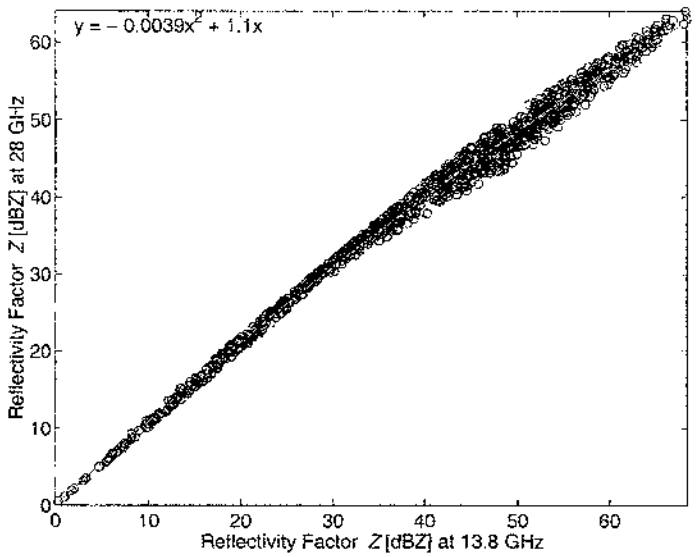

Figure 3.60: Scatter plot of reflectivity for rain at 13.8 and 28.0 GHz.

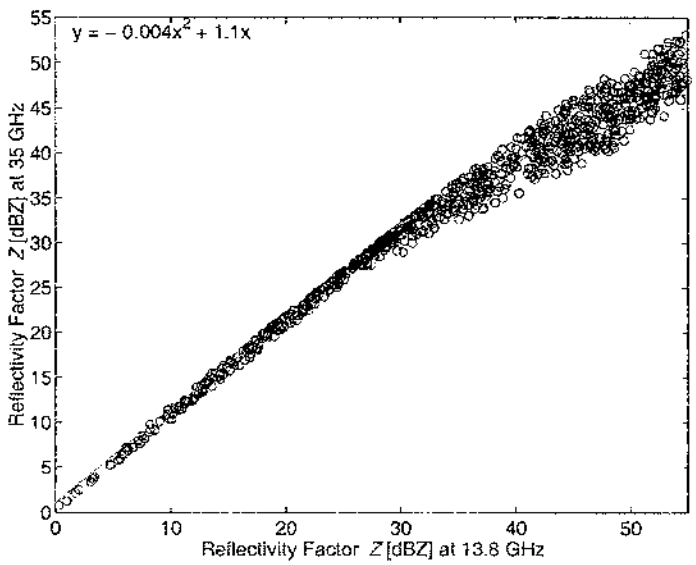

Figure 3.61: Scatter plot of reflectivity for rain at 13.8 and 35.0 GHz.

Table 3.8 shows the reflectivity relationship between 13.8 GHz (Ku-band),28.0 GHz. and 35 GHz (Ka-band).

Hydrometeor Type	**13.8 GHz and 28.0**	**13.8 and 35.0**
Aggregate with 0.1 density	0.96	0.92
Aggregate with 0.2 density	0.96	0.92
Aggregate with 0.3 density	0.96	0.93
Aggregate with 0.4 density	0.96	0.93
Aggregate with 0.5 density	0.96	0.93
Wet graupel with 0.4 density	0.87	0.81
Snow with 0.1 density	0.99	0.99
Rain with 1.0 density	$-0.0039x^2 + 1.1$	$-0.004x^2 + 1.1$

Table 3.8: Parameter of $Z(Ka) = cZ(Ku)$ for Aggregate, Wet graupel, Snow and Rain.

The results from Figures 3.30 to 3.45 show that the specific attenuation at Ka and Ku band frequencies are nearly linearly related. Therefore, the same relationship holds for cumulative attenuation also. For results from Figures 3.46 to 3.61 a linear fit is made to the reflectivities for aggregate, wet graupel, and snow while a second order polynomial fit is made for rain.

Chapter 4

GLOBAL MAP OF ATTENUATION AND REFLECTIVITY

4.1 Introduction

This chapter describes the microphysical model, which was developed in order to estimate the attenuation as well as the observed reflectivity pattern at Ka band. This chapter also presents the results of attenuation map computation over the globe. With the methodology described in chapter 3, the basic concept of attenuation mapping is shown by using vertical profiles. Finally, global maps (horizontal sections) of cumulative attenuations, reflectivities and reflectivity ratios are presented.

4.2 Microphysical Model

In order to estimate the attenuation as well as the observed reflectivity pattern at Ka-band the following microphysical model was developed. While this model may not provide an accurate description of the space-time microphysical structure of precipitation, it is sufficient for studying the bulk of attenuation properties. The 2A23 PR data product classifies precipitation into 2 main categories: stratiform and convective as mentioned in Chapter 2. Therefore, the microphysical model which is developed here is also classified into two models: namely convective and stratiform.

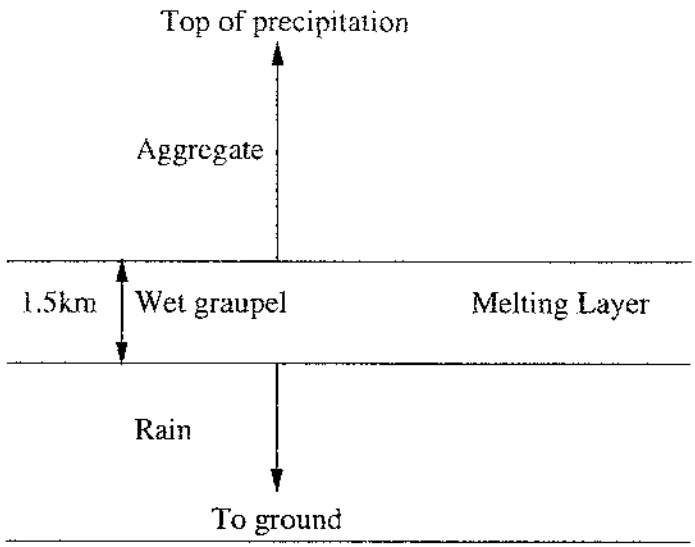

Figure 4.1: Microphysical model of convective precipitation.

4.2.1 Convective Model

Figure 4.1 shows the schematic of the microphysical model for convective precipitation. The microphysical convective model is based on the following:

- Region below the melting layer is rain.
- Region above the melting layer is aggregate with densities from 0.1 to 0.4.
- Region in the melting layer is wet graupel with 0.4 density.
- The thickness of the melting layer is 1.5 km.
- The middle of the melting layer is located at the estimated freezing height ($0^{o}C$).

4.2.2 Stratiform Model

Figure 4.2 shows the schematic of the microphysical model for stratiform precipitation. The microphysical stratiform model is based on the following:

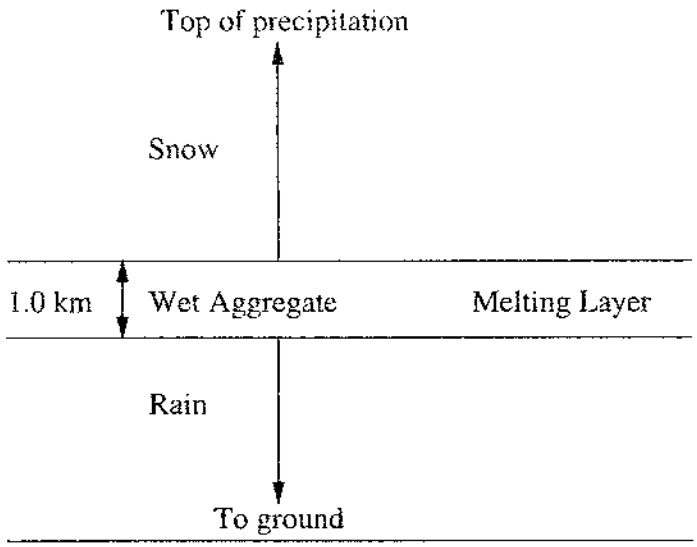

Figure 4.2: Microphysical model of stratiform precipitation.

- Region below the melting layer is rain.
- Region above the melting layer is snow with 0.1 density.
- Region in the melting layer is wet aggregate with 0.5 density.
- The thickness of the melting layer is 1.0 km.
- The middle of the melting layer is located at the center of the estimated bright band (BB).

4.3 Vertical Profile of Attenuation

The earth's surface produces a strong echo compared to those of the precipitation scatters, especially close to ground. This problem is more pronounced at off-nadir angles in comparison to nadir angles. In order to ensure that surface clutter does not contaminate the data that is used in this research, a surface clutter free region ("clutter free certain" according to TRMM PR documentation (TRMM, 2000)) is determined and only data in clutter free regions are considered

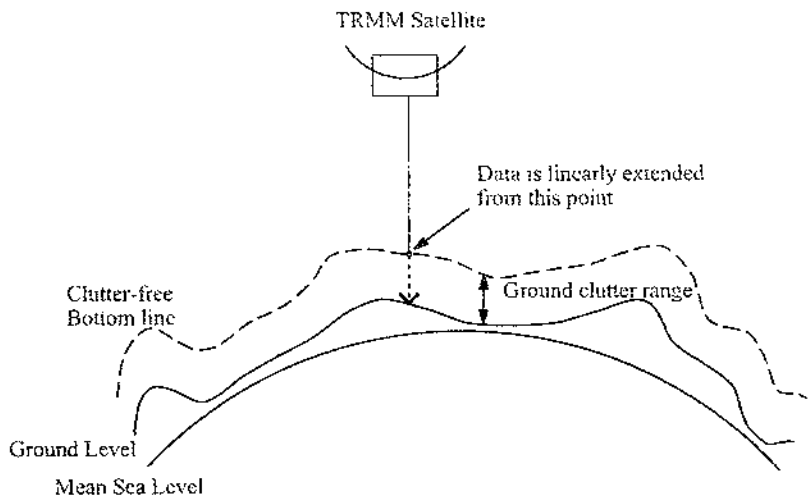

Figure 4.3: Schematic showing the variable clutter free region around the globe.

for analysis. Figure 4.3 shows the sketch of variable clutter free altitude as a function of position around the globe. The difference between measured reflectivity and attenuation corrected reflectivity at a specified range from the radar yields the cumulative attenuation on the earth-space path. The range profile of attenuation in TRMM is obtained as a combination of the HB algorithm and the surface reference technique as explained in Chapter 3.

A vertical profile of reflectivity is shown in Figure 4.4, for data taken over Melbourne, FL on August 13, 1998. Range bin 80 is mean sea level (MSL) for this data set. The distance between the consecutive bins is 250 m. Figure 4.5 shows the measured reflectivity Z_m [dBZ] (1C21 TRMM PR) and corrected reflectivity Z_e [dBZ] (2A25 TRMM PR) along ray number 42 of Figure 4.4. In this data set the clutter free height is estimated to be about 1.5 km altitude. Therefore, the measurements below this altitude are discarded; however, the data immediately above is linearly extrapolated down to the surface as shown in Figure 4.5. This vertical profile is classified as convective precipitation by the 2A23 data product; therefore, the convective microphysical model was applied to this profile. Figure

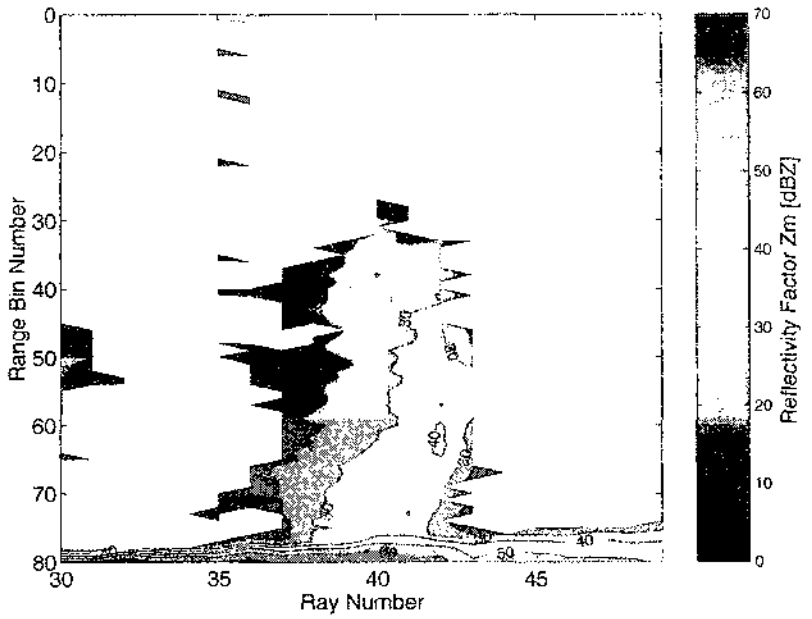

Figure 4.4: Storm over Melbourne, FL August 13, 1998 scan: 4085 22:30.

4.6 shows the path integrated attenuation at 13.8 GHz and the estimated path integrated attenuation at 35 GHz. The results of Figure 4.6 show cumulative attenuation of the order of 5 dB at 13.8 GHz and of the order of 35 dB at 35 GHz for the specific case presented here. Figure 4.7 shows estimated measured reflectivity at Ka-band for the data shown in Figure 4.4. It can be seen that the estimates of attenuation at 35 GHz are in the range of values reported in the literature (Pruppacher and Klett, 1997). In addition, the observed reflectivity at 35 GHz is severely attenuated due to the enhanced attenuation through rain and the melting layer at 35 GHz.

4.4 Monthly Maps of Global Attenuation at Ku- and Ka-Band

The procedure developed in this chapter is extended to observations around the globe using TRMM data and are presented as monthly maps here. In this

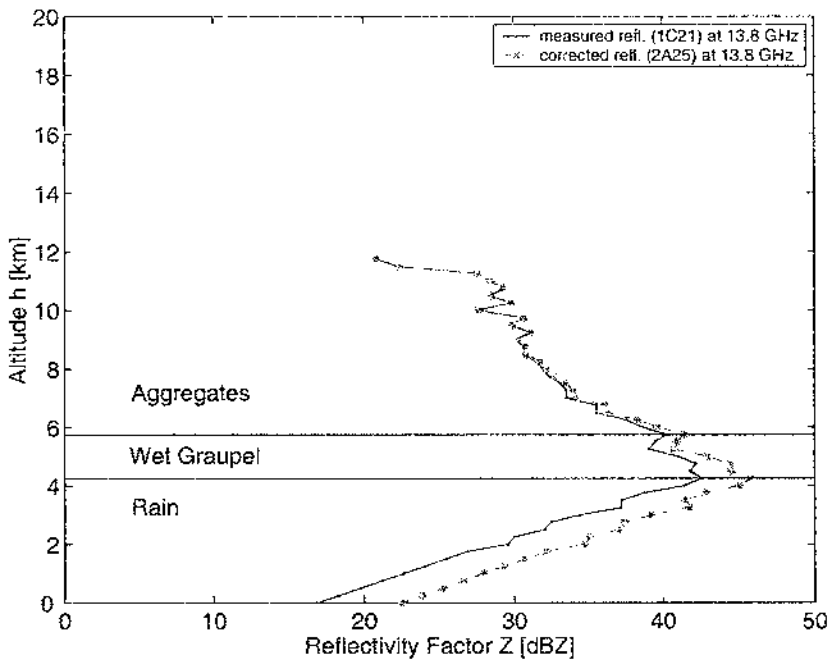

Figure 4.5: Reflectivity vs. altitude along ray 42 in Figure 4.4.

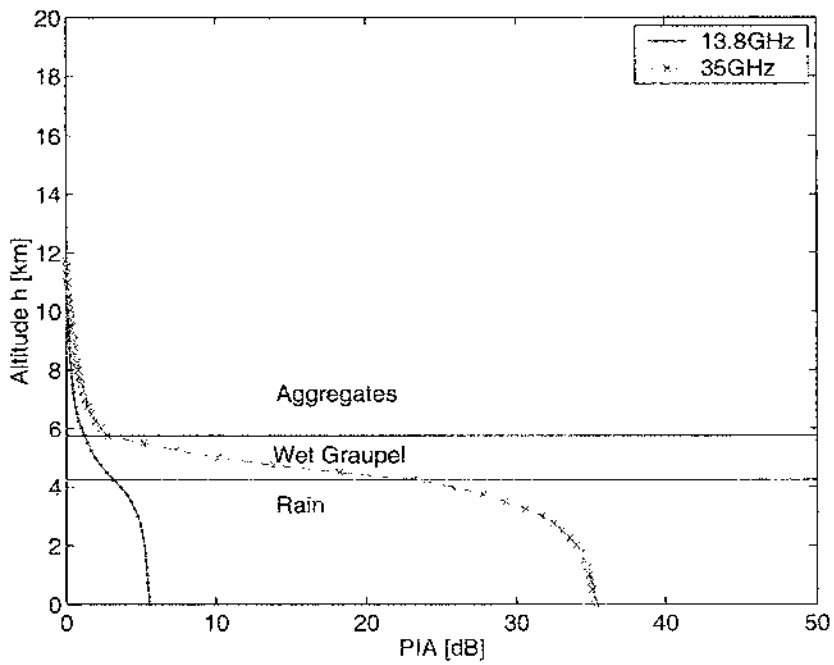

Figure 4.6: PIA vs altitude along ray 42 in Figure 4.4.

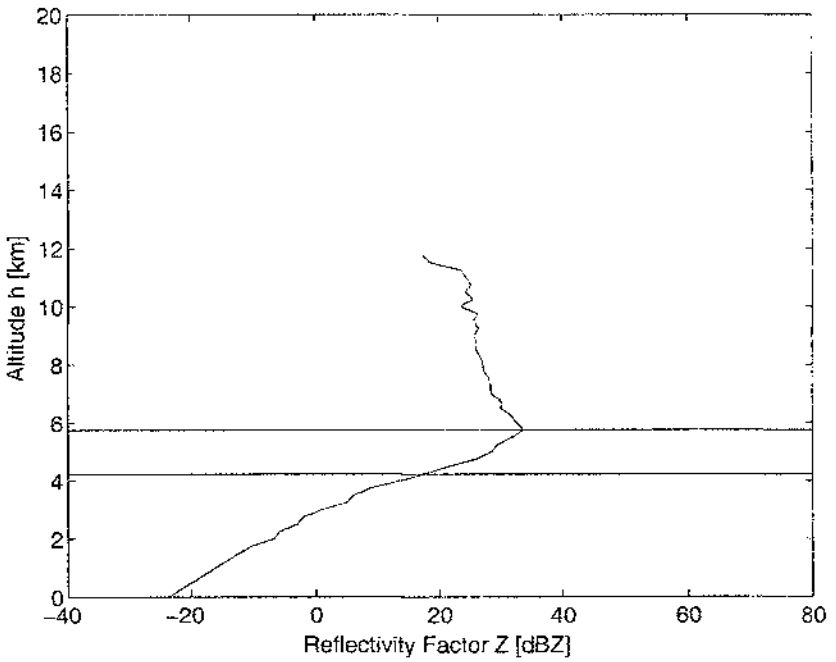

Figure 4.7: Measured reflectivity at 35 GHz vs. altitude along the beam shown in Figure 4.4.

section, TRMM PR observations data are used to develop monthly maps of attenuation at Ku- and Ka-bands. The maps at Ku-band are direct measurements whereas those at Ka-band are estimates based on the model developed in the previous section.

In the monthly map plots, the data area is from 35N to 35S and from 180W to 180E. So, the plots are restricted to the latitudes of $\pm 35^{o}$ coinciding with the coverage of TRMM. The color scales are adjusted to the full scale of each map. Each pixel in the plot is (0.5^{o} x 0.5^{o}) area and therefore of fairly high resolution. The resolution cells consist of 148 x 720 latitude-longitude elements. Attenuation data is allocated into a resolution cell specified by its geolocation data. Then all allocated data in the cell are accumulated and divided by the total number of data in the cell as the monthly average. On calculation, missing data are ignored

Figure Number	Title Description
Figure 4.8	Attenuation map at Ku-band for January 2000
Figure 4.9	Attenuation map at Ka-band for January 2000
Figure 4.10	Attenuation map at Ku-band for February 2000
Figure 4.11	Attenuation map at Ka-band for February 2000
Figure 4.12	Attenuation map at Ku-band for March 2000
Figure 4.13	Attenuation map at Ka-band for March 2000
Figure 4.14	Attenuation map at Ku-band for April 2000
Figure 4.15	Attenuation map at Ka-band for April 2000
Figure 4.16	Attenuation map at Ku-band for May 2000
Figure 4.17	Attenuation map at Ka-band for May 2000
Figure 4.18	Attenuation map at Ku-band for June 2000
Figure 4.19	Attenuation map at Ka-band for June 2000
Figure 4.20	Attenuation map at Ku-band for July 2000
Figure 4.21	Attenuation map at Ka-band for July 2000
Figure 4.22	Attenuation map at Ku-band for August 2000
Figure 4.23	Attenuation map at Ka-band for August 2000
Figure 4.24	Attenuation map at Ku-band for September 2000
Figure 4.25	Attenuation map at Ka-band for September 2000
Figure 4.26	Attenuation map at Ku-band for October 2000
Figure 4.27	Attenuation map at Ka-band for October 2000
Figure 4.28	Attenuation map at Ku-band for November 2000
Figure 4.29	Attenuation map at Ka-band for November 2000
Figure 4.30	Attenuation map at Ku-band for December 2000
Figure 4.31	Attenuation map at Ku-band for December 2000

Table 4.1: Figure Number List of Monthly Average PIA.

and not counted. The overlay shows the standard map of land/ocean boundaries. Table 4.1 provides an itemized list of figures.

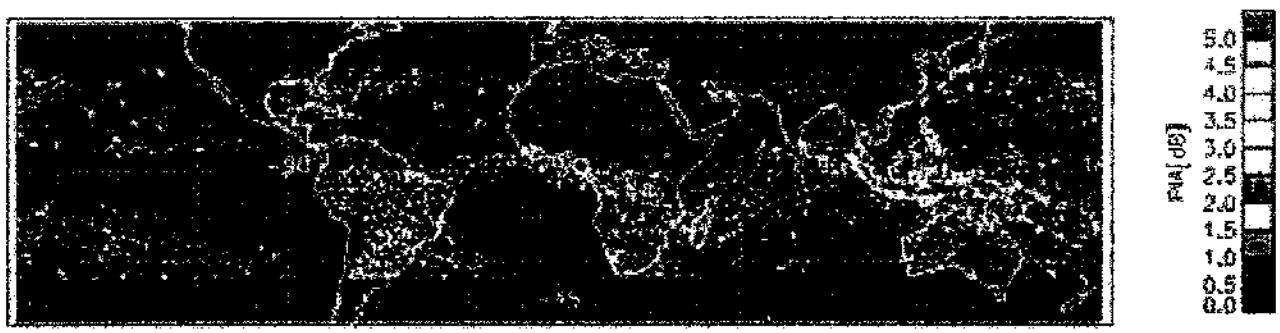

Figure 4.8: Attenuation map at Ku-band for January 2000.

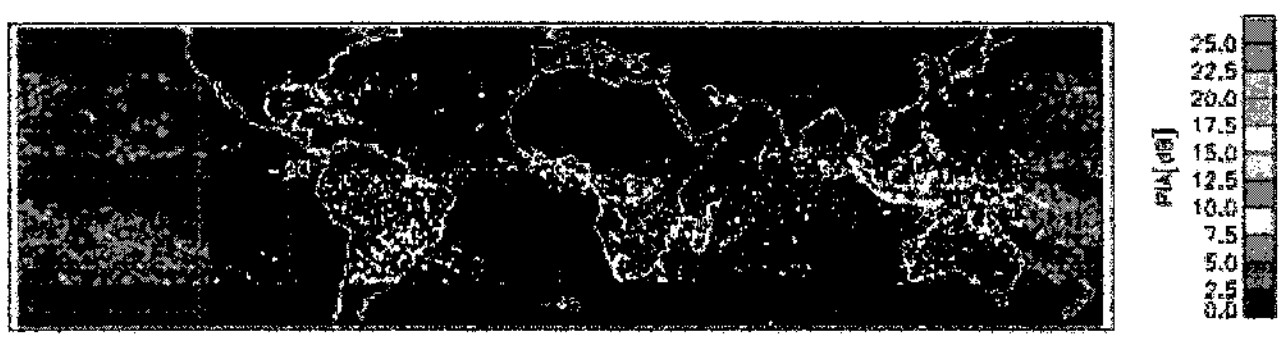

Figure 4.9: Attenuation map at Ka-band for January 2000.

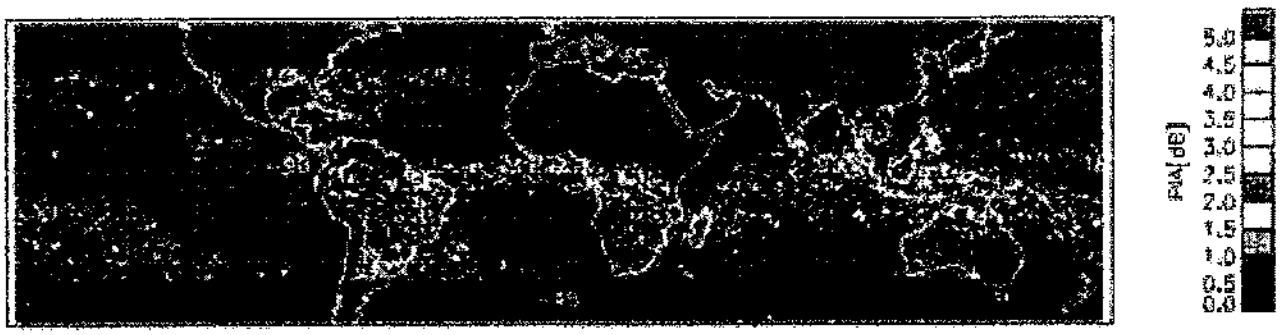

Figure 4.10: Attenuation map at Ku-band for February 2000.

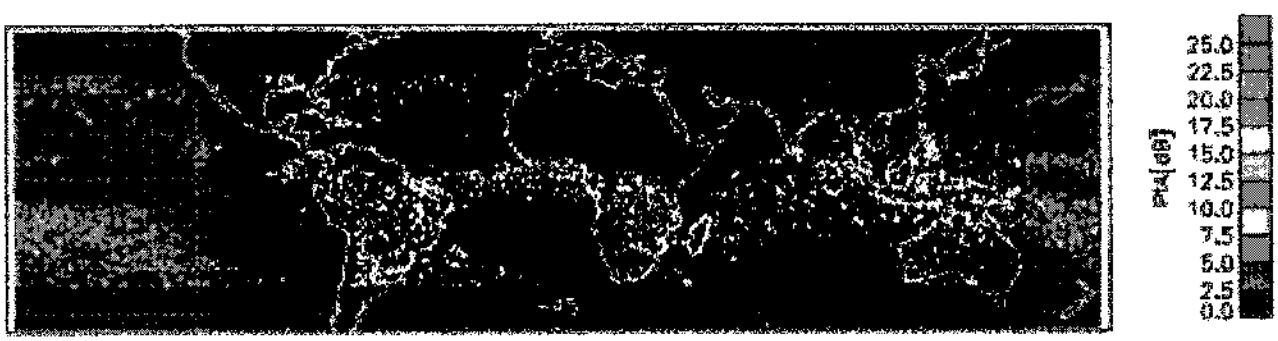

Figure 4.11: Attenuation map at Ka-band for February 2000.

Figure 4.12: Attenuation map at Ku-band for March 2000.

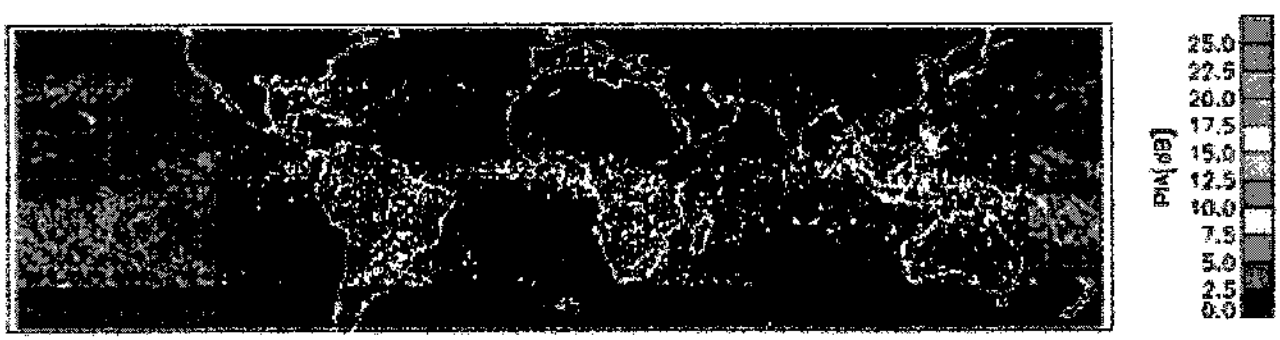

Figure 4.13: Attenuation map at Ka-band for March 2000.

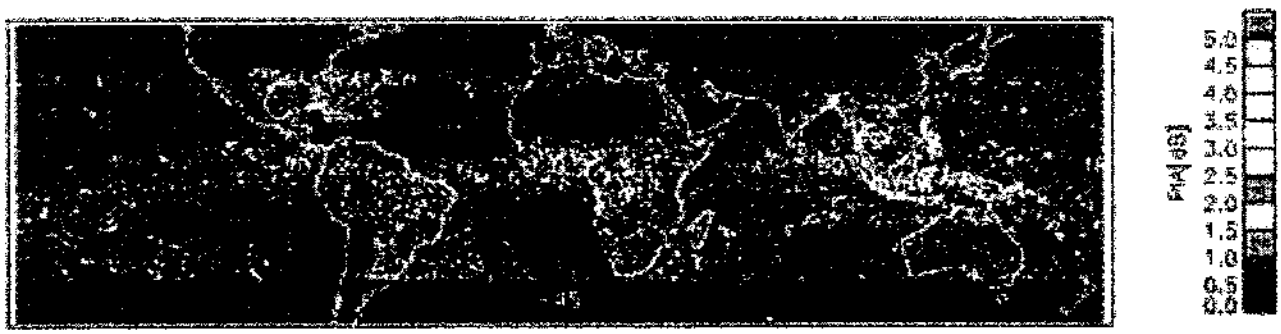

Figure 4.14: Attenuation map at Ku-band for April 2000.

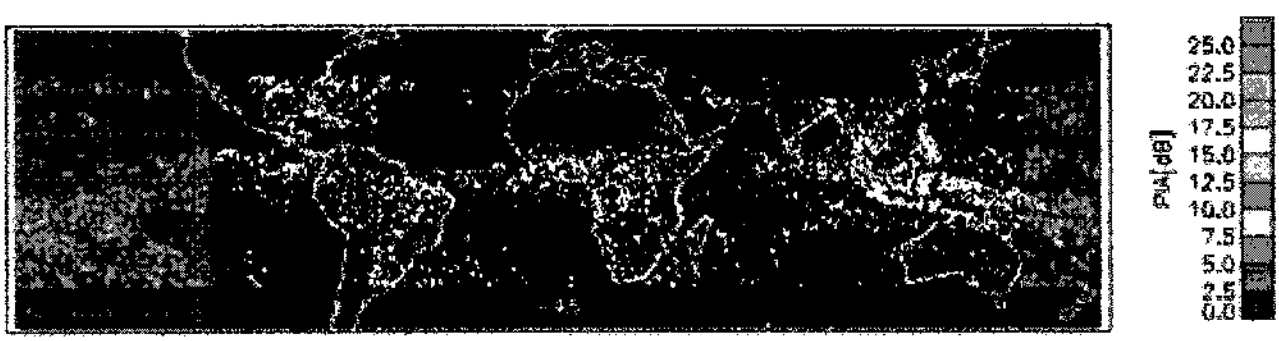

Figure 4.15: Attenuation map at Ka-band for April 2000.

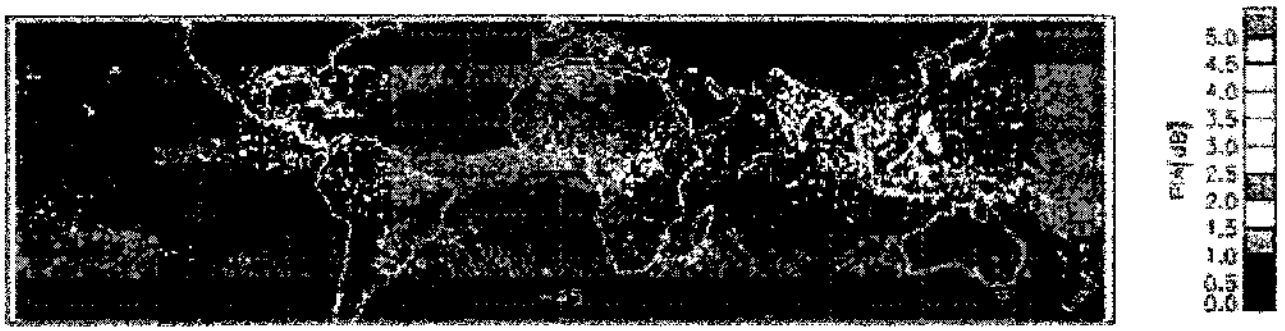

Figure 4.16: Attenuation map at Ku-band for May 2000.

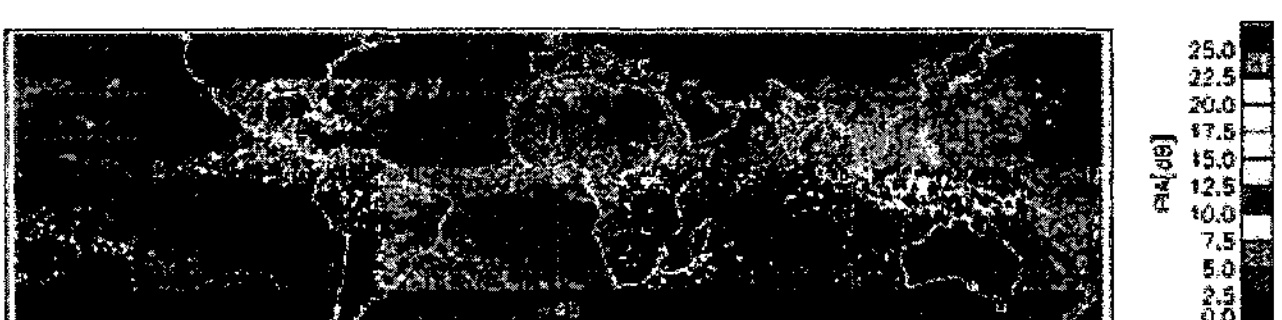

Figure 4.17: Attenuation map at Ka-band for May 2000.

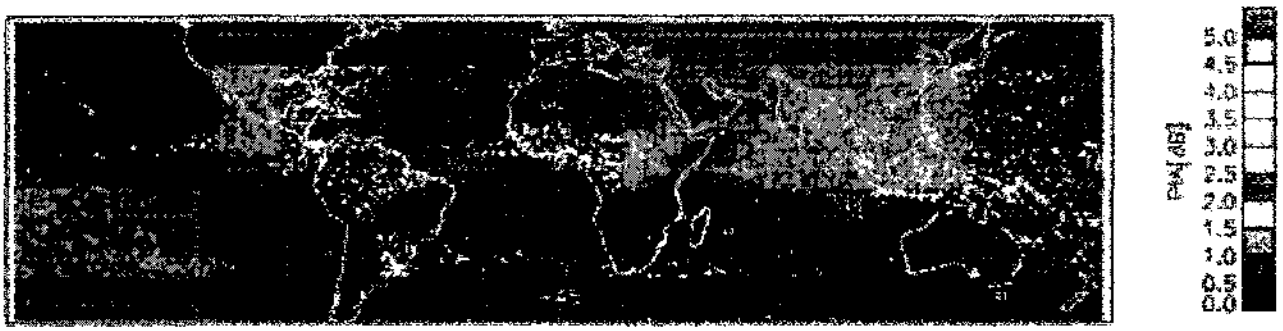

Figure 4.18: Attenuation map at Ku-band for June 2000.

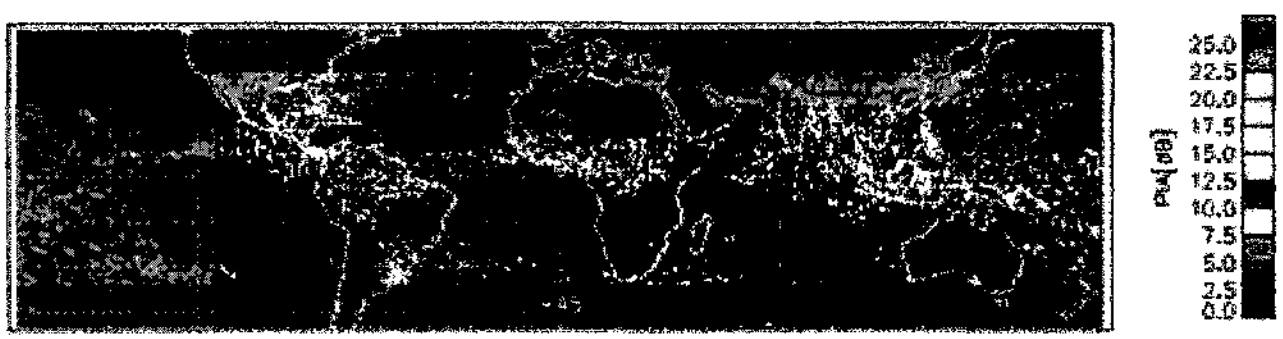

Figure 4.19: Attenuation map at Ka-band for June 2000.

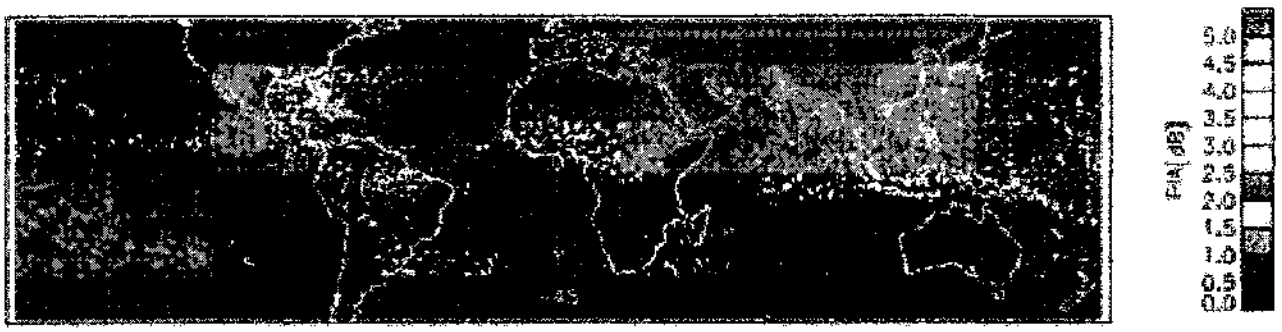

Figure 4.20: Attenuation map at Ku-band for July 2000.

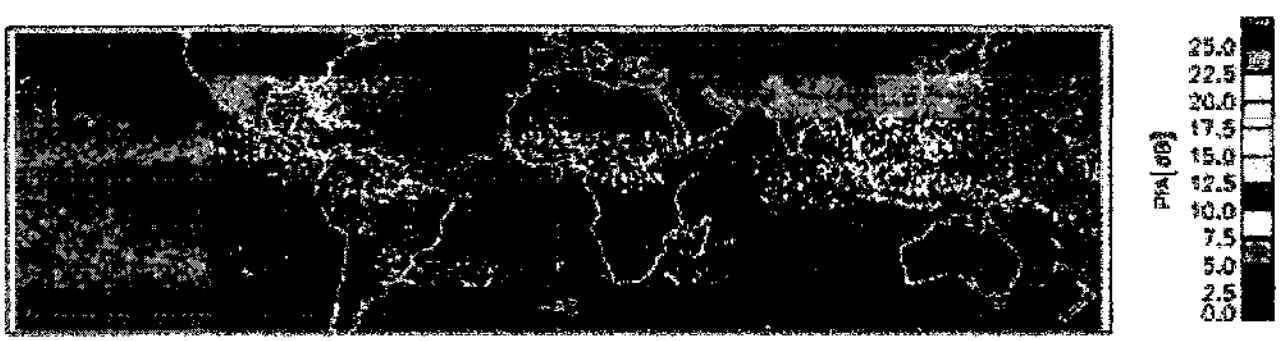

Figure 4.21: Attenuation map at Ka-band for July 2000.

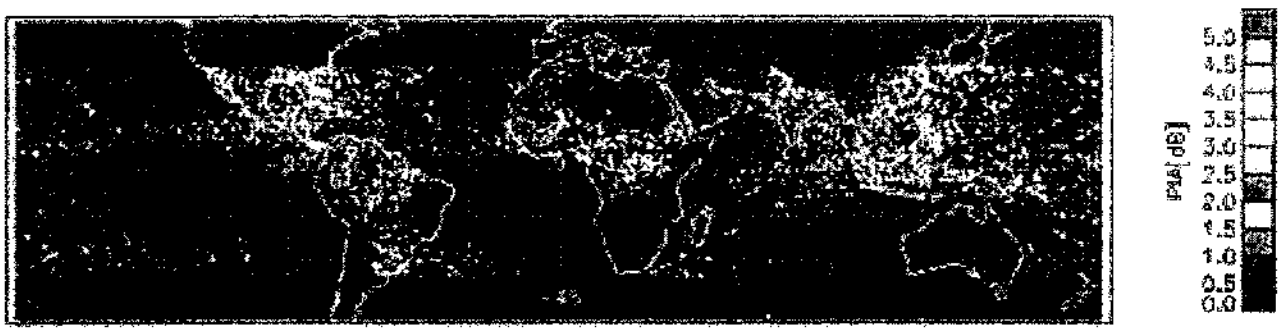

Figure 4.22: Attenuation map at Ku-band for August 2000.

Figure 4.23: Attenuation map at Ka-band for August 2000.

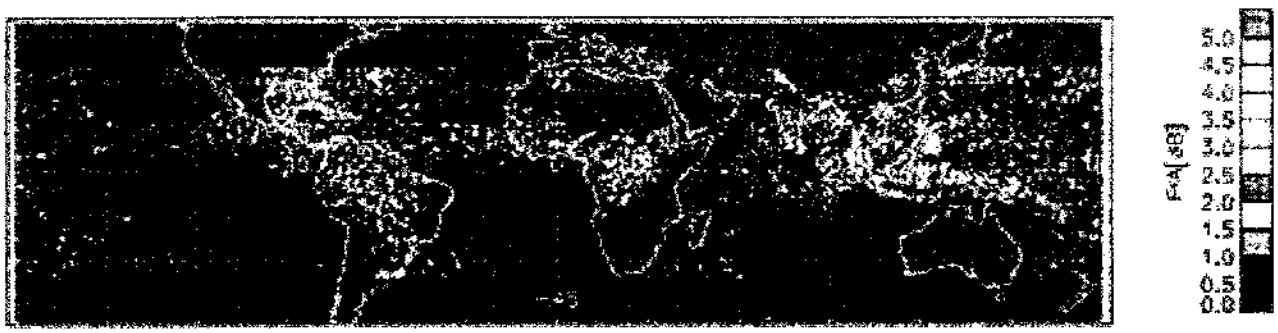

Figure 4.24: Attenuation map at Ku-band for September 2000.

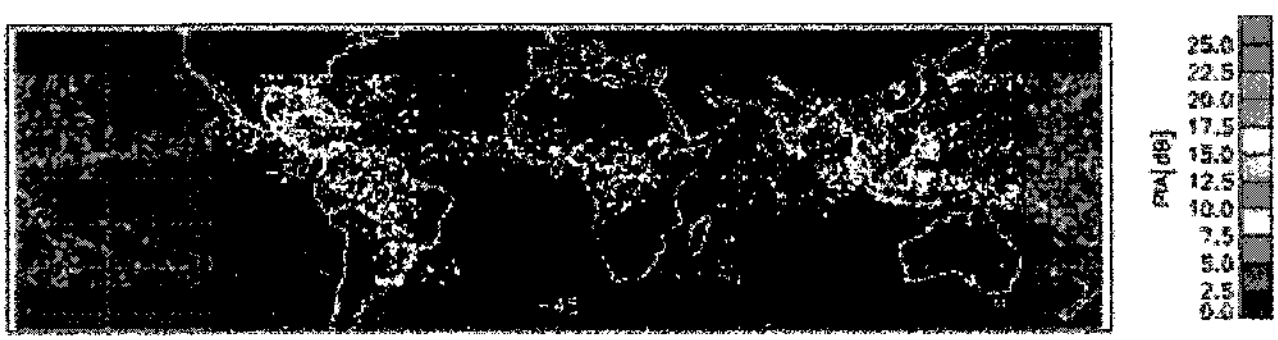

Figure 4.25: Attenuation map at Ka-band for September 2000.

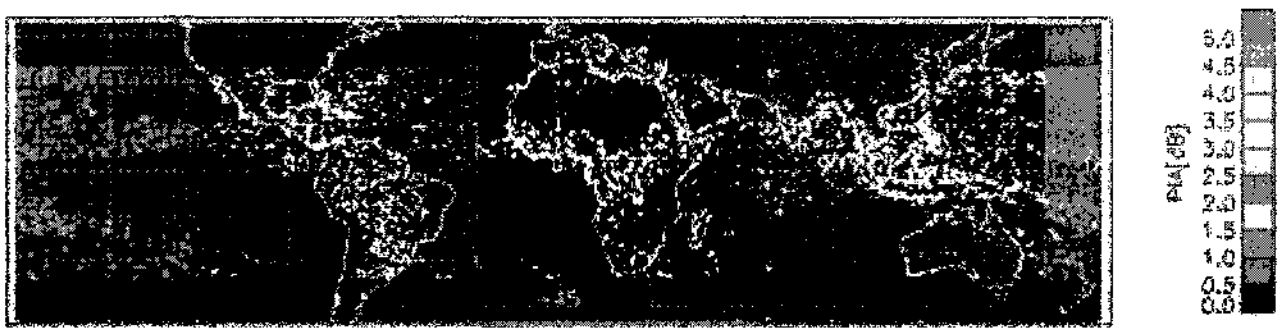

Figure 4.26: Attenuation map at Ku-band for October 2000.

Figure 4.27: Attenuation map at Ka-band for October 2000.

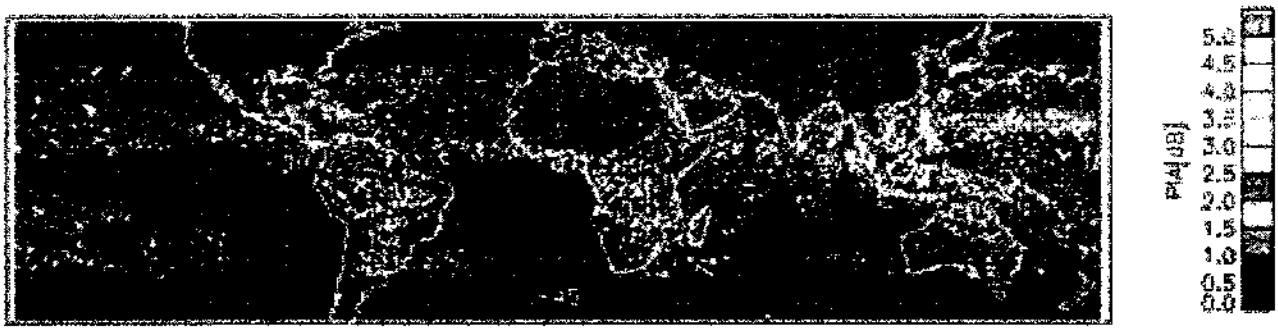

Figure 4.28: Attenuation map at Ku-band for November 2000.

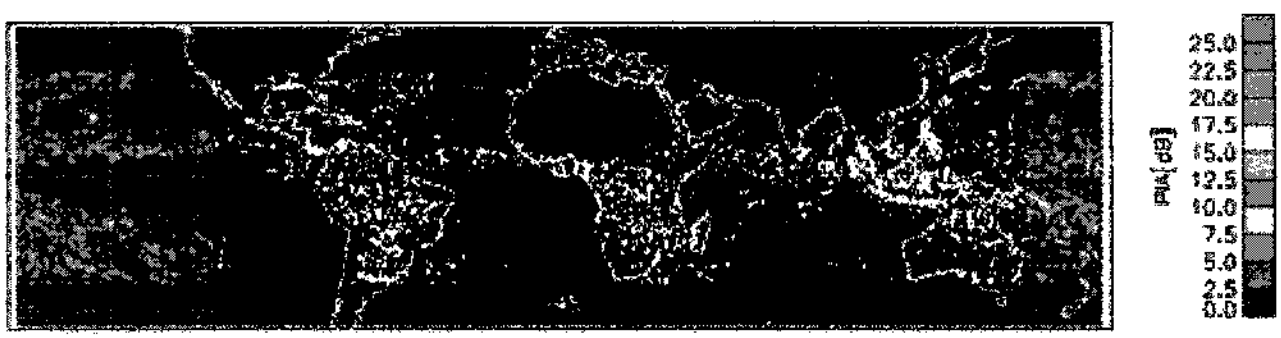

Figure 4.29: Attenuation map at Ka-band for November 2000.

Figure 4.30: Attenuation map at Ku-band for December 2000.

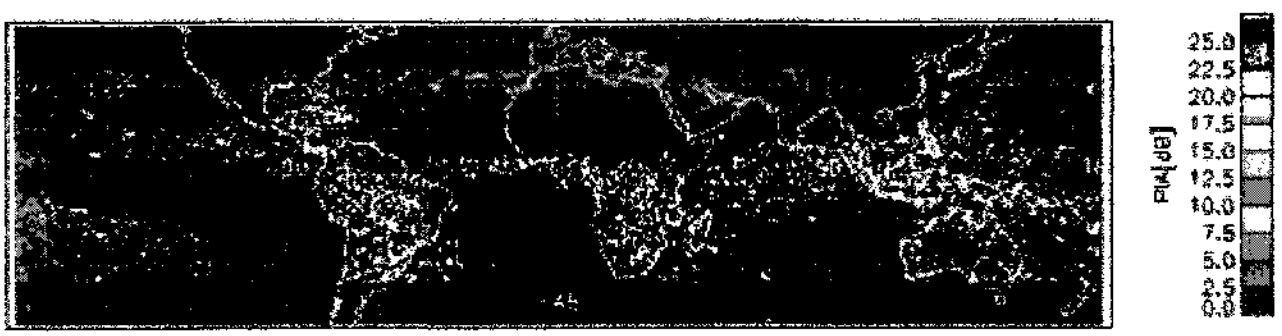

Figure 4.31: Attenuation map at Ka-band for December 2000.

Some features are obvious from these figures. For example, from Figures 4.8 and 4.9 we can see that the southern hemisphere experienced large attenuation in January compared to the northern hemisphere, because of the seasonal nature of precipitation. In addition, the attenuation over the land surface is on average much larger that that of the ocean, except in the inter-tropical convergent zone. The results of Figures 4.8 and 4.9 show that the attenuation at the surface averaged over (0.5^o x 0.5^o) area can be of the order of 30 dB at Ka-band. It should be noted that within the (0.5^o x 0.5^o) area the Ka-band attenuation could peak higher than the average value. Figures 4.12 and 4.13 show similar maps for March, 2000, which is spring time in the northern hemisphere and fall in the southern hemisphere. The results of Figures 4.12 and 4.13 show an increase in attenuation in the lower latitude over North America while the Amazon and Central Africa remain active. Figures 4.20 and 4.21 show the attenuation maps of Ku-and Ka-band for the month of July (summer time in the northern hemisphere). Figures 4.20 and 4.21 show expected contrast with the attenuation maps of January, 2000.

The next important application of the analysis developed here is the feasibility of using 35 GHz radar for global precipitation measurement purposes, in a dual-frequency mode of operation.

4.5 Monthly Maps of Global Reflectivity at Ku- and Ka-Band

Among the various technologies considered for space borne observation of precipitation observation, dual-frequency at Ku- and Ka-band provide the great promise of being able to yield better rainfall estimates as well as deriving the vertical structure of the drop size distribution parameters (Meneghini and Kozu, 1990). Several airborne experiments have validated the potential of the dual-frequency technique. It is obvious from the attenuation maps shown in the previous section that the cumulative attenuation along a path can exceed many tens of dB

at 35 GHz. The space-borne weather radar design for TRMM has a noise floor such that the minimum detectable reflectivity factor in precipitation is about 17 dBZ. Similar considerations can also be assumed for Ka-band. In order to utilize the dual-frequency radar observations at 14 and 35 GHz for precipitation estimation (as well as RSD retrieval), it is important the 35 GHz radar returns stay above the noise floor. For quantitative applications such as RSD retrieval, a reflectivity level of 3 dB above the noise floor (20 dBZ) can be assumed as this threshold. The results of Chapter 3 showed that the reflectivity at Ka-band could be different from the Ku-band, especially at intense precipitation. In addition, the observed reflectivity Z_m is reduced due to attenuation. Using a combination of parameterization for Ka-band reflectivity and attenuation, maps of "observed" reflectivity at Ka-band can be created. Cross validation of TRMM observed reflectivities with ground based radar indicate that only about 2% to 3% under estimate the precipitation intensity due to the lower limit of 17 dBZ (Bolen and Chandrasekar, 2000). However, that is definitely not going to be the case for Ka-band observation.

In this section, global maps of reflectivity as observed in year 2000 are presented. For each month, four maps are presented: measured reflectivity (1C21) at 13.8 GHz and its mapped reflectivity at 35 GHz, also the corrected reflectivity (2A25) at 13.8 GHz, and its mapped reflectivity at 35 GHz. The same mapping algorithm in the previous section for attenuation is used to obtain the global maps of reflectivity, except that the monthly average is at 2 km above mean sea level. Table 4.2 provides an itemized list of the figures of monthly average 1C21 reflectivity at Ku- and Ka-band while Table 4.3 provides an itemized list of the figures of monthly average 2A25 reflectivity at Ku- and Ka-band.

Figure Number	Title Description
Figure 4.32	1C21 reflectivity map at Ku-band for January 2000
Figure 4.33	1C21 reflectivity map at Ka-band for January 2000
Figure 4.34	1C21 reflectivity map at Ku-band for February 2000
Figure 4.35	1C21 reflectivity map at Ka-band for February 2000
Figure 4.36	1C21 reflectivity map at Ku-band for March 2000
Figure 4.37	1C21 reflectivity map at Ka-band for March 2000
Figure 4.38	1C21 reflectivity map at Ku-band for April 2000
Figure 4.39	1C21 reflectivity map at Ka-band for April 2000
Figure 4.40	1C21 reflectivity map at Ku-band for May 2000
Figure 4.41	1C21 reflectivity map at Ka-band for May 2000
Figure 4.42	1C21 reflectivity map at Ku-band for June 2000
Figure 4.43	1C21 reflectivity map at Ka-band for June 2000
Figure 4.44	1C21 reflectivity map at Ku-band for July 2000
Figure 4.45	1C21 reflectivity map at Ka-band for July 2000
Figure 4.46	1C21 reflectivity map at Ku-band for August 2000
Figure 4.47	1C21 reflectivity map at Ka-band for August 2000
Figure 4.48	1C21 reflectivity map at Ku-band for September 2000
Figure 4.49	1C21 reflectivity map at Ka-band for September 2000
Figure 4.50	1C21 reflectivity map at Ku-band for October 2000
Figure 4.51	1C21 reflectivity map at Ka-band for October 2000
Figure 4.52	1C21 reflectivity map at Ku-band for November 2000
Figure 4.53	1C21 reflectivity map at Ka-band for November 2000
Figure 4.54	1C21 reflectivity map at Ku-band for December 2000
Figure 4.55	1C21 reflectivity map at Ka-band for December 2000

Table 4.2: Figure Number List of Monthly Average 1C21 Reflectivity at Ku- and Ka-band.

Figure Number	Title Description
Figure 4.56	2A25 reflectivity map at Ku-band for January 2000
Figure 4.57	2A25 reflectivity map at Ka-band for January 2000
Figure 4.58	2A25 reflectivity map at Ku-band for February 2000
Figure 4.59	2A25 reflectivity map at Ka-band for February 2000
Figure 4.60	2A25 reflectivity map at Ku-band for March 2000
Figure 4.61	2A25 reflectivity map at Ka-band for March 2000
Figure 4.62	2A25 reflectivity map at Ku-band for April 2000
Figure 4.63	2A25 reflectivity map at Ka-band for April 2000
Figure 4.64	2A25 reflectivity map at Ku-band for May 2000
Figure 4.65	2A25 reflectivity map at Ka-band for May 2000
Figure 4.66	2A25 reflectivity map at Ku-band for June 2000
Figure 4.67	2A25 reflectivity map at Ka-band for June 2000
Figure 4.68	2A25 reflectivity map at Ku-band for July 2000
Figure 4.69	2A25 reflectivity map at Ka-band for July 2000
Figure 4.70	2A25 reflectivity map at Ku-band for August 2000
Figure 4.71	2A25 reflectivity map at Ka-band for August 2000
Figure 4.72	2A25 reflectivity map at Ku-band for September 2000
Figure 4.73	2A25 reflectivity map at Ka-band for September 2000
Figure 4.74	2A25 reflectivity map at Ku-band for October 2000
Figure 4.75	2A25 reflectivity map at Ka-band for October 2000
Figure 4.76	2A25 reflectivity map at Ku-band for November 2000
Figure 4.77	2A25 reflectivity map at Ka-band for November 2000
Figure 4.78	2A25 reflectivity map at Ku-band for December 2000
Figure 4.79	2A25 reflectivity map at Ka-band for December 2000

Table 4.3: Figure Number List of Monthly Average 2A25 Reflectivity at Ku- and Ka-band.

Figure 4.32: 1C21 reflectivity map at 13.8 GHz for January 2000.

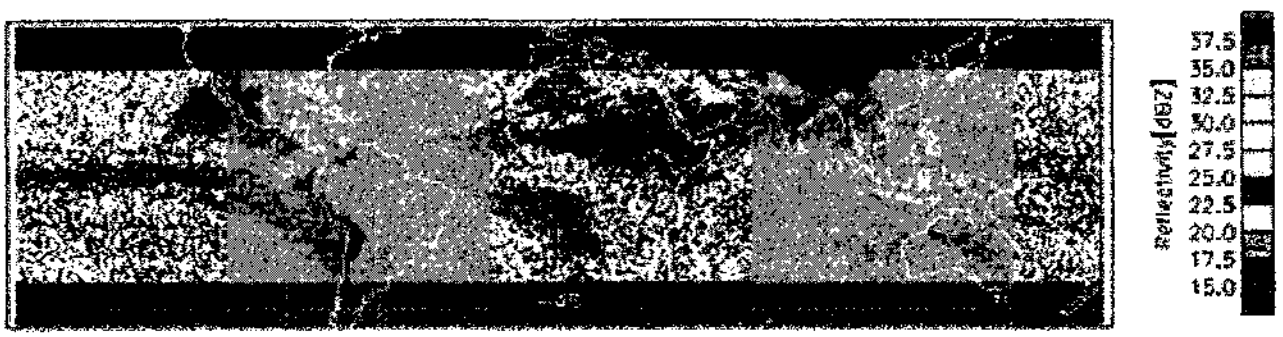

Figure 4.33: 1C21 reflectivity map at 35.0 GHz for January 2000.

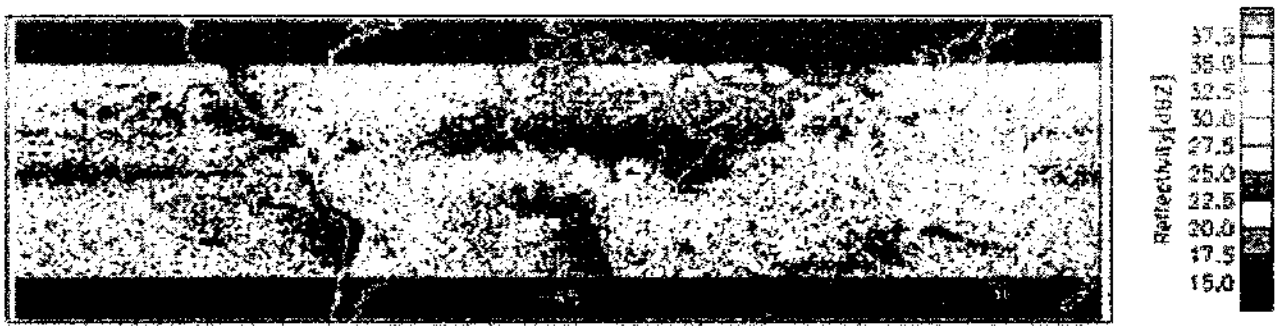

Figure 4.34: 1C21 reflectivity map at 13.8 GHz for February 2000.

Figure 4.35: 1C21 reflectivity map at 35.0 GHz for February 2000.

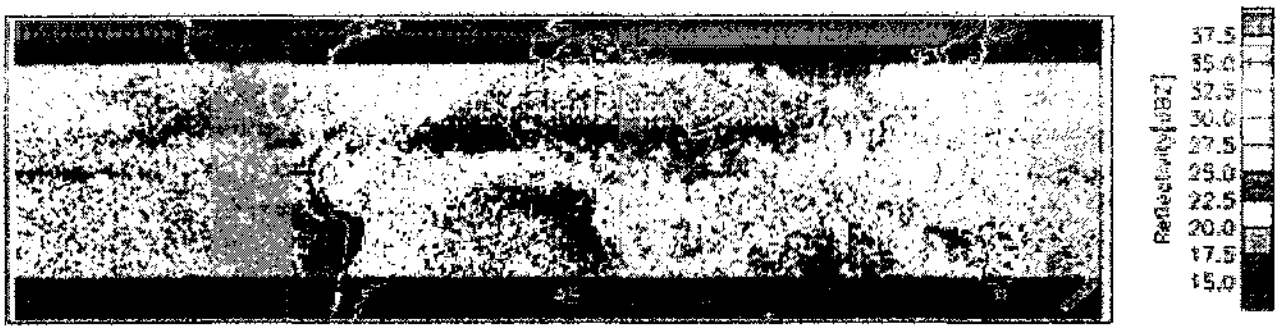

Figure 4.36: 1C21 reflectivity map at 13.8 GHz for March 2000.

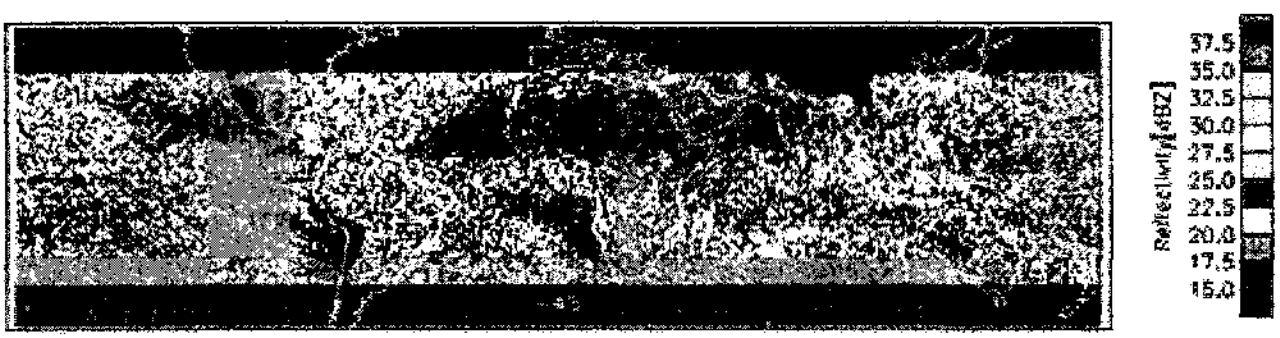

Figure 4.37: 1C21 reflectivity map at 35.0 GHz for March 2000.

Figure 4.38: 1C21 reflectivity map at 13.8 GHz for April 2000.

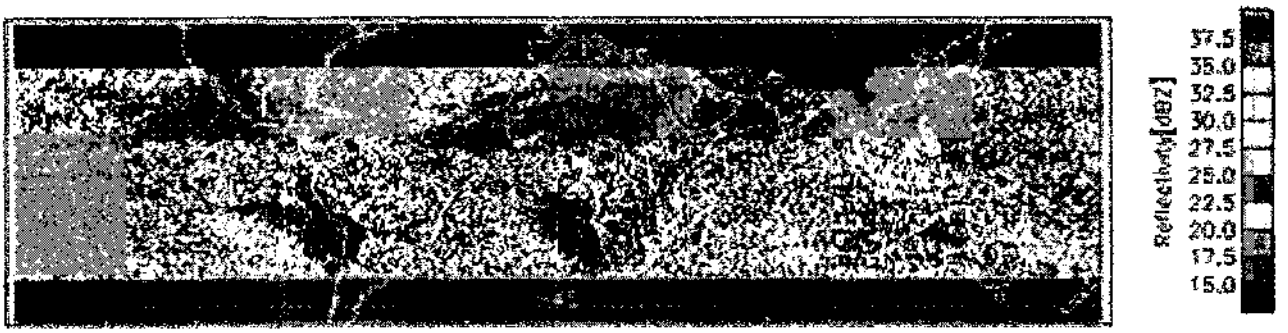

Figure 4.39: 1C21 reflectivity map at 35.0 GHz for April 2000.

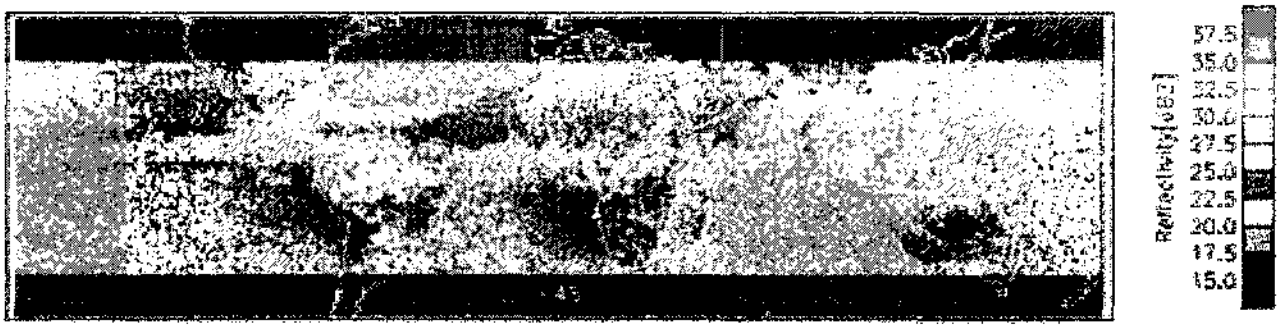

Figure 4.40: 1C21 reflectivity map at 13.8 GHz for May 2000.

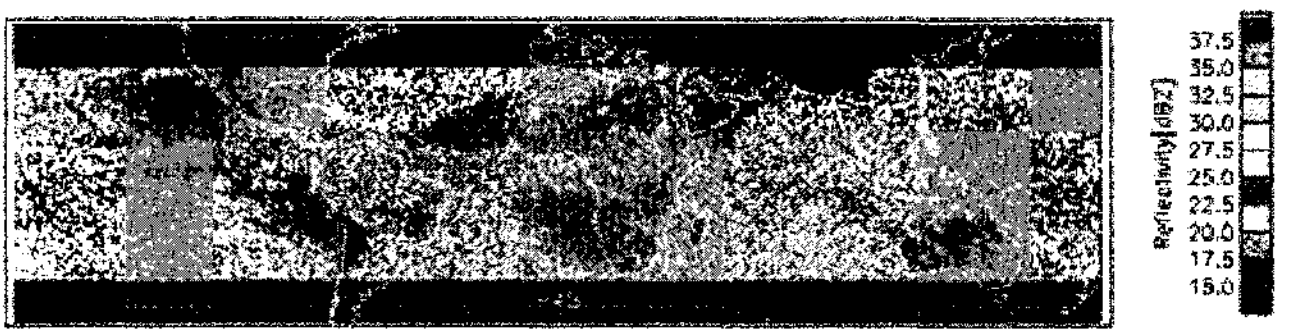

Figure 4.41: 1C21 reflectivity map at 35.0 GHz for May 2000.

Figure 4.42: 1C21 reflectivity map at 13.8 GHz for June 2000.

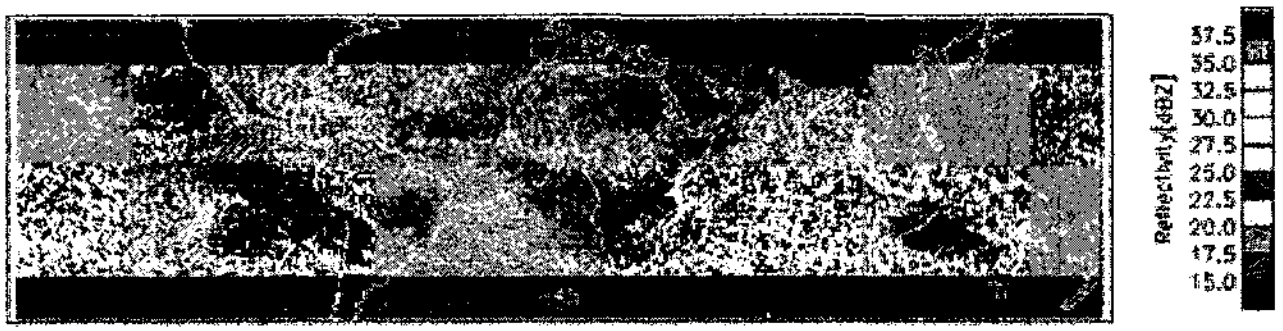

Figure 4.43: 1C21 reflectivity map at 35.0 GHz for June 2000.

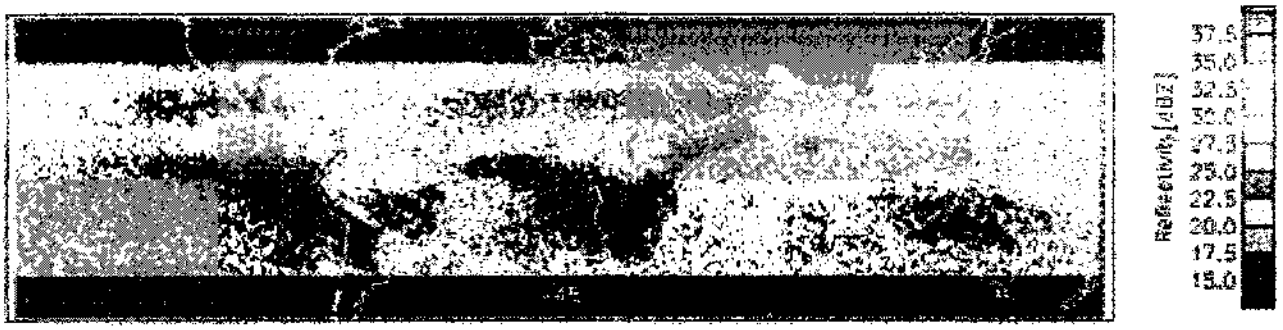

Figure 4.44: 1C21 reflectivity map at 13.8 GHz for July 2000.

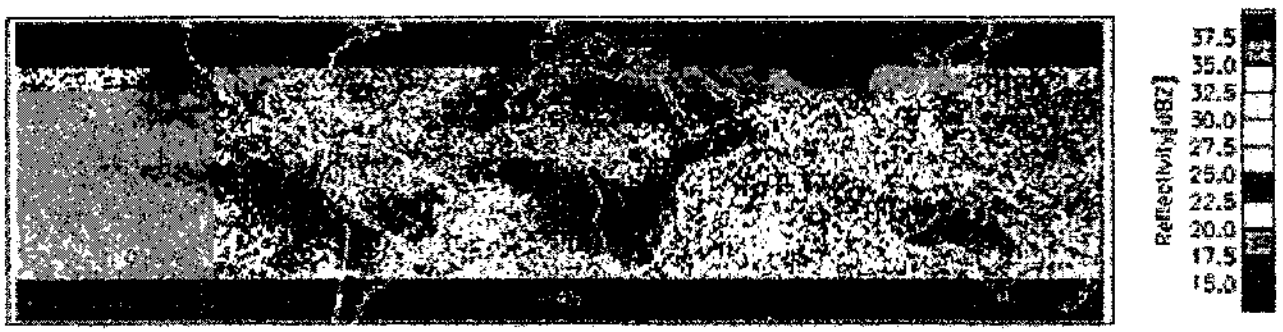

Figure 4.45: 1C21 reflectivity map at 35.0 GHz for July 2000.

Figure 4.46: 1C21 reflectivity map at 13.8 GHz for August 2000.

Figure 4.47: 1C21 reflectivity map at 35.0 GHz for August 2000.

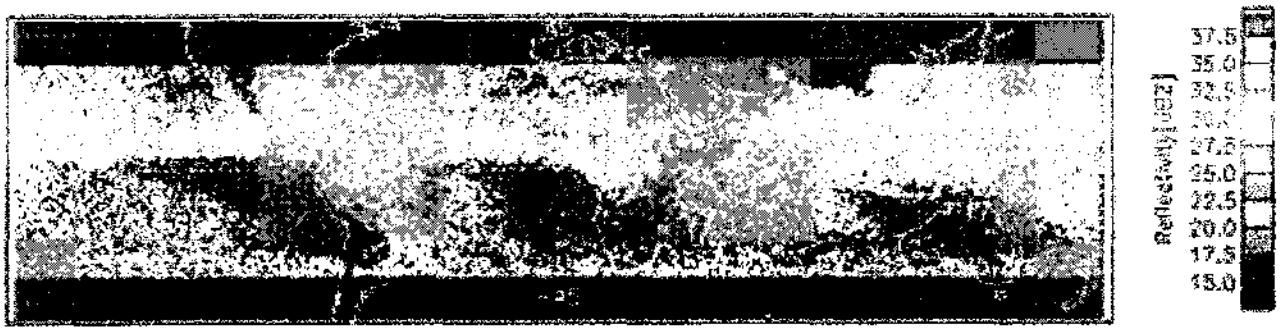

Figure 4.48: 1C21 reflectivity map at 13.8 GHz for September 2000.

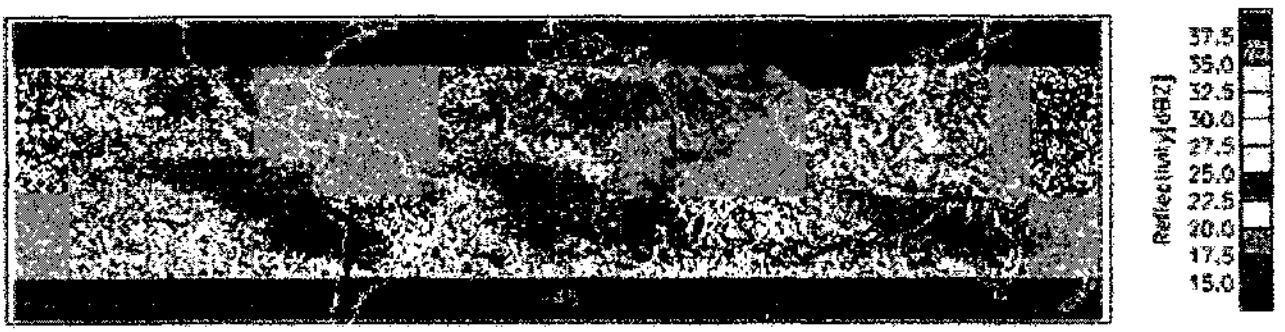

Figure 4.49: 1C21 reflectivity map at 35.0 GHz for September 2000.

Figure 4.50: 1C21 reflectivity map at 13.8 GHz for October 2000.

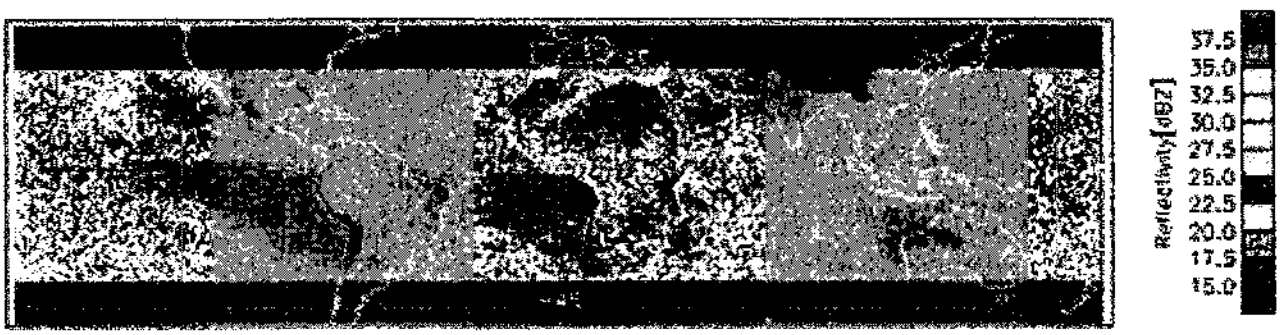

Figure 4.51: 1C21 reflectivity map at 35.0 GHz for October 2000.

Figure 4.52: 1C21 reflectivity map at 13.8 GHz for November 2000.

Figure 4.53: 1C21 reflectivity map at 35.0 GHz for November 2000.

Figure 4.54: 1C21 reflectivity map at 13.8 GHz for December 2000.

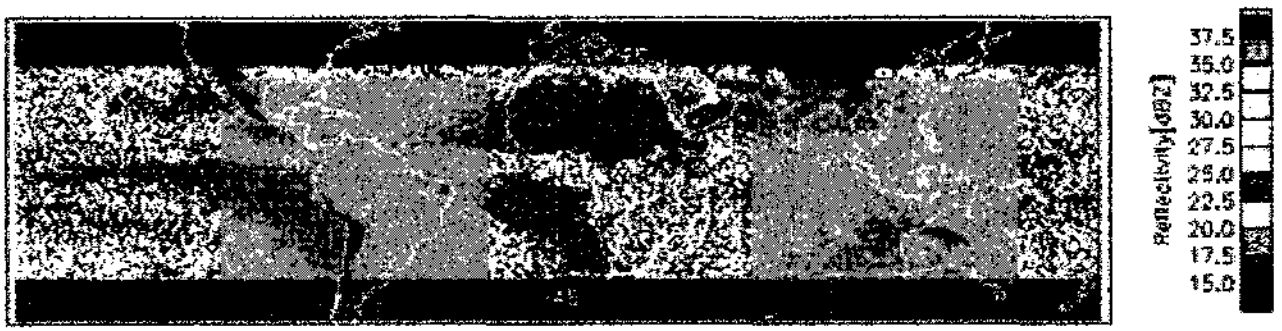

Figure 4.55: 1C21 reflectivity map at 35.0 GHz for December 2000.

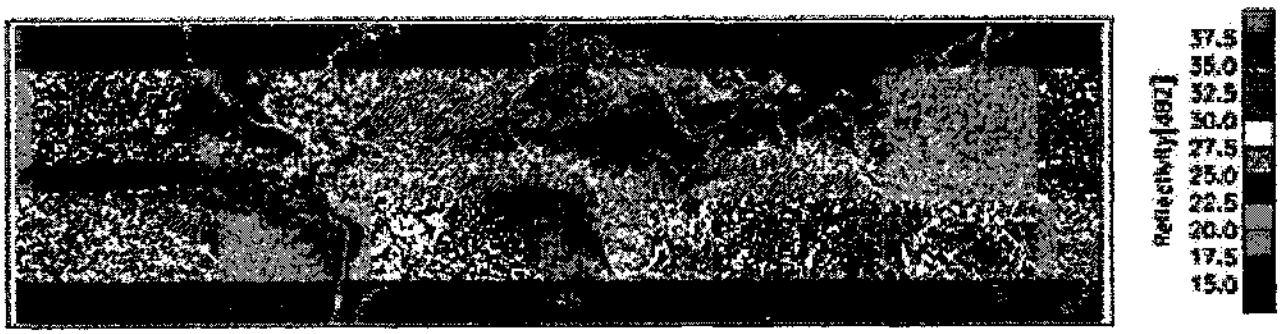

Figure 4.56: 2A25 reflectivity map at 13.8 GHz for January 2000.

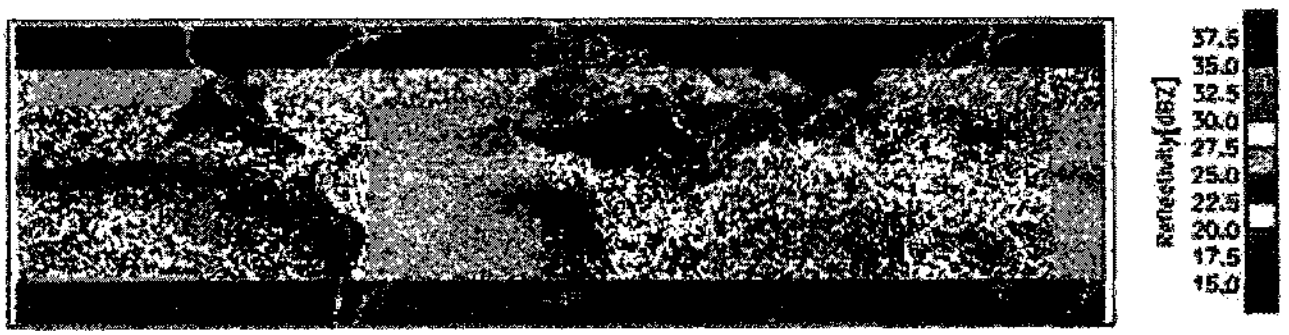

Figure 4.57: 2A25 reflectivity map at 35.0 GHz for January 2000.

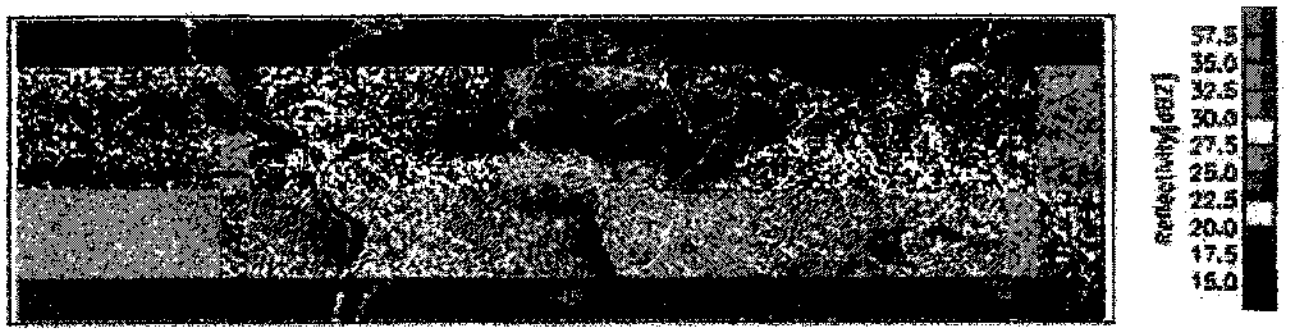

Figure 4.58: 2A25 reflectivity map at 13.8 GHz for February 2000.

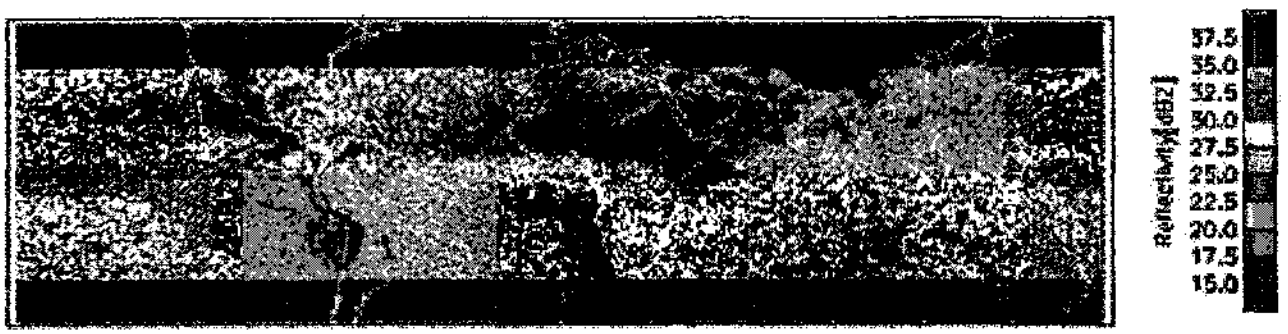

Figure 4.59: 2A25 reflectivity map at 35.0 GHz for February 2000.

Figure 4.60: 2A25 reflectivity map at 13.8 GHz for March 2000.

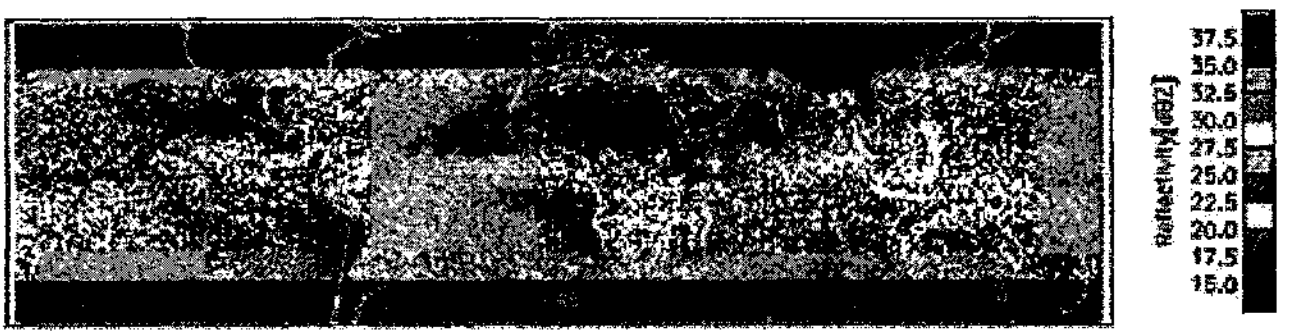

Figure 4.61: 2A25 reflectivity map at 35.0 GHz for March 2000.

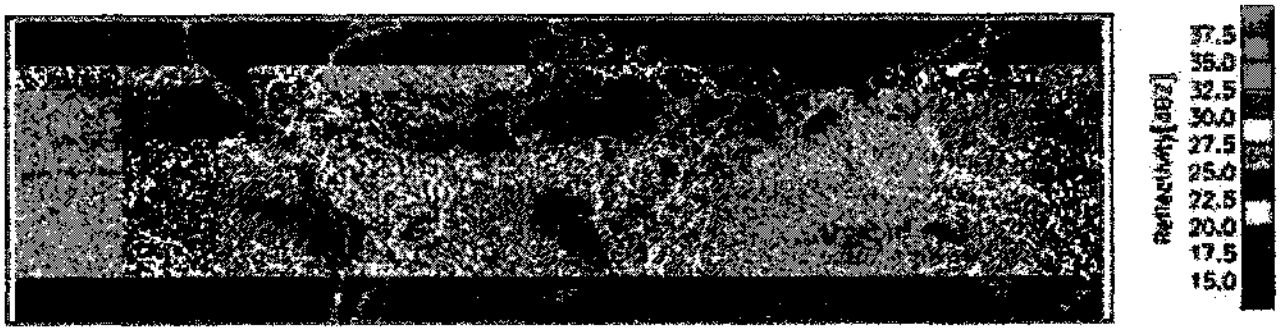

Figure 4.62: 2A25 reflectivity map at 13.8 GHz for April 2000.

Figure 4.63: 2A25 reflectivity map at 35.0 GHz for April 2000.

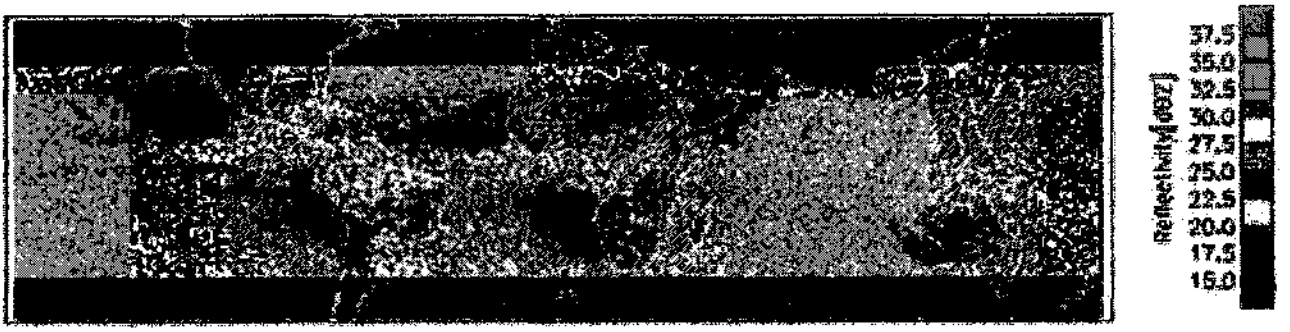

Figure 4.64: 2A25 reflectivity map at 13.8 GHz for May 2000.

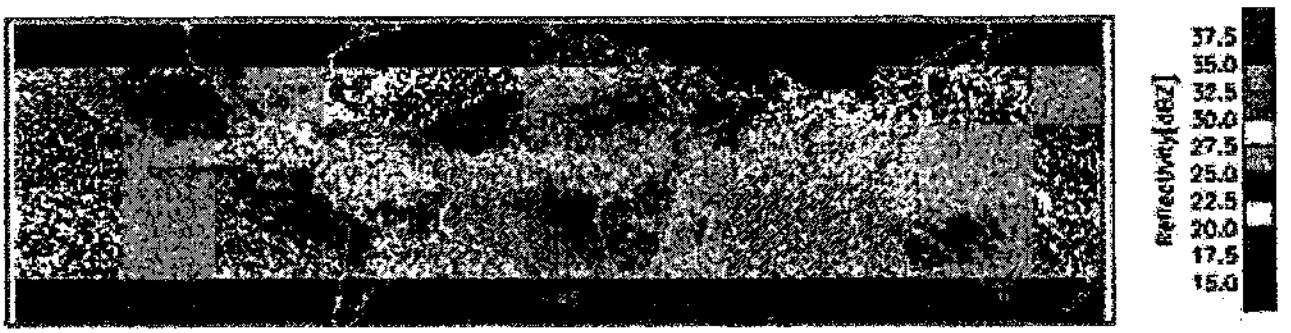

Figure 4.65: 2A25 reflectivity map at 35.0 GHz for May 2000.

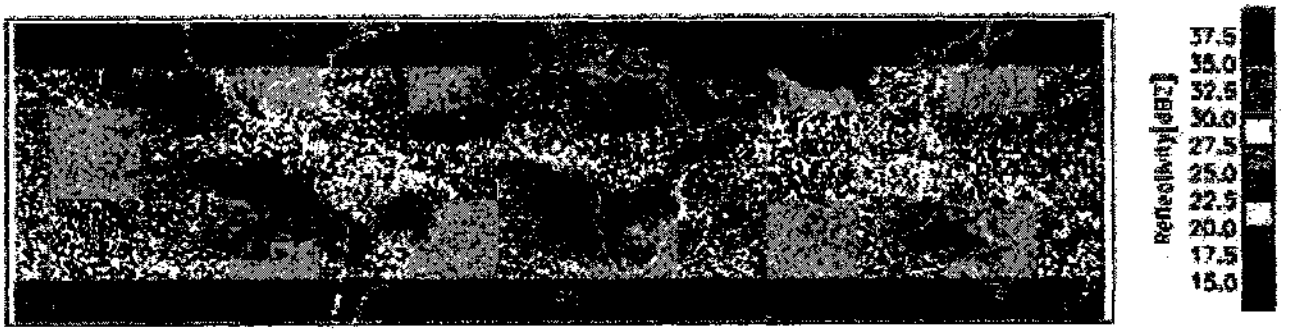

Figure 4.66: 2A25 reflectivity map at 13.8 GHz for June 2000.

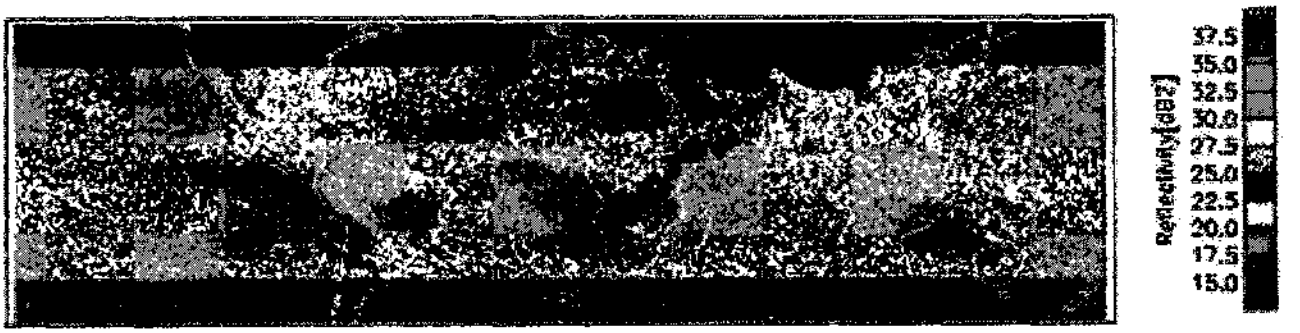

Figure 4.67: 2A25 reflectivity map at 35.0 GHz for June 2000.

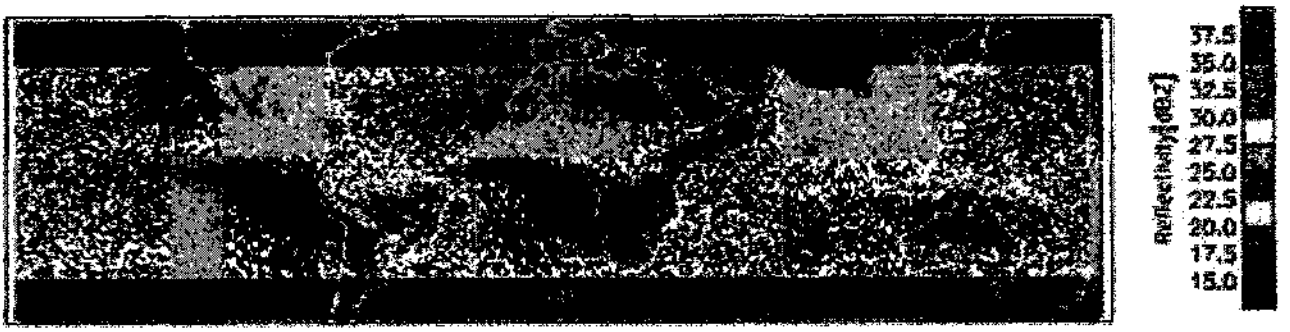

Figure 4.68: 2A25 reflectivity map at 13.8 GHz for July 2000.

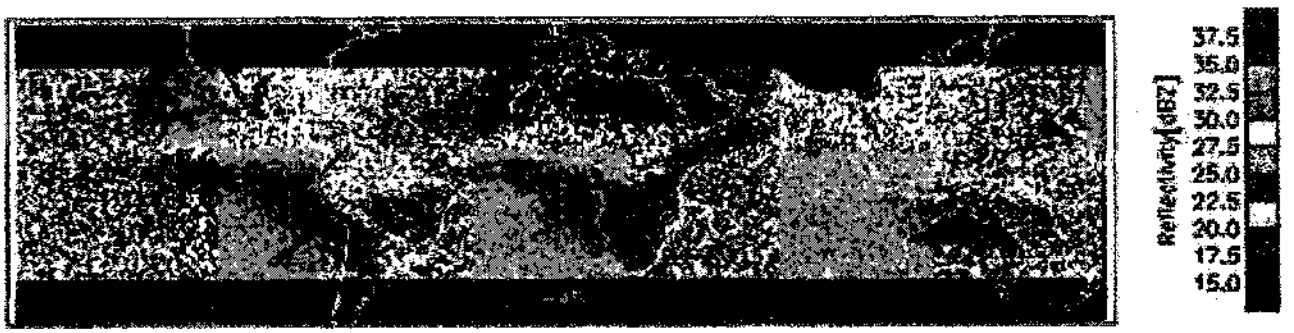

Figure 4.69: 2A25 reflectivity map at 35.0 GHz for July 2000.

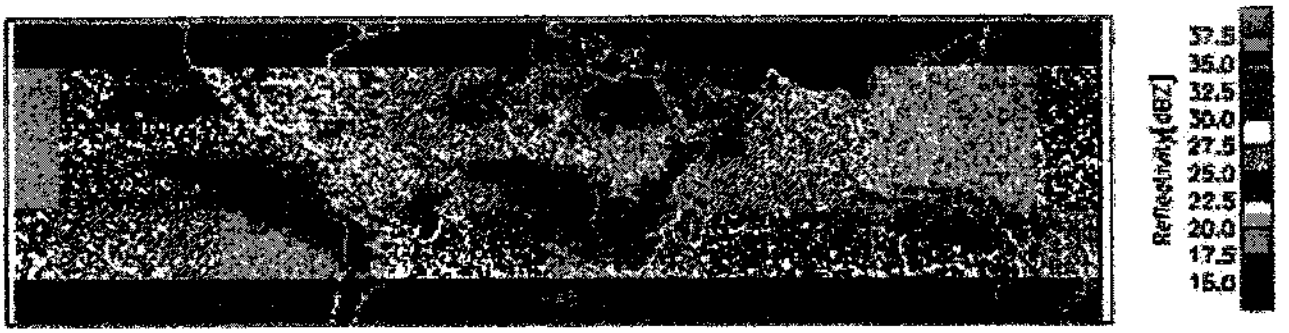

Figure 4.70: 2A25 reflectivity map at 13.8 GHz for August 2000.

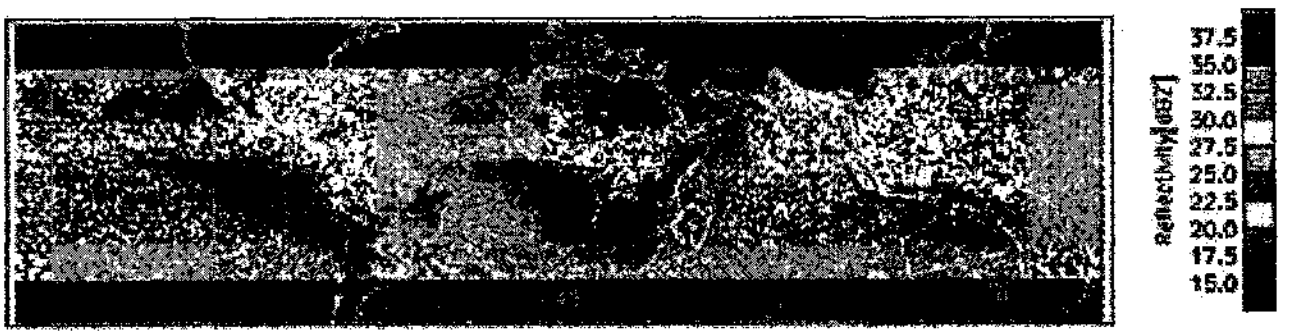

Figure 4.71: 2A25 reflectivity map at 35.0 GHz for August 2000.

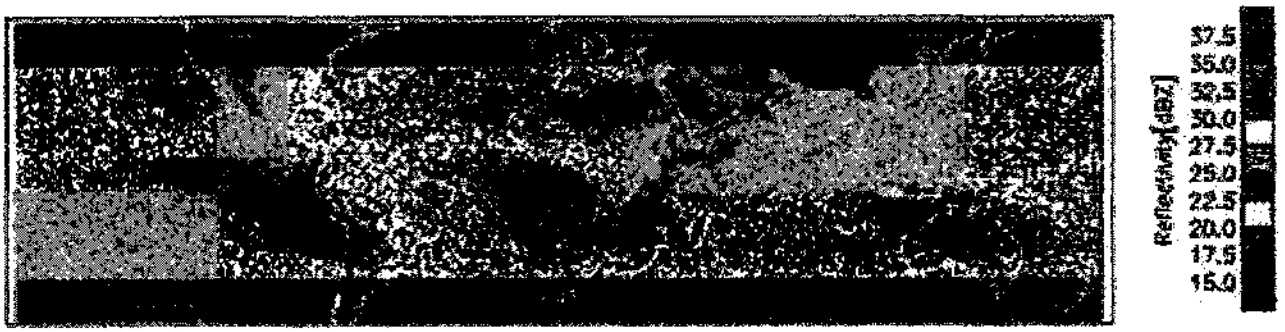

Figure 4.72: 2A25 reflectivity map at 13.8 GHz for September 2000.

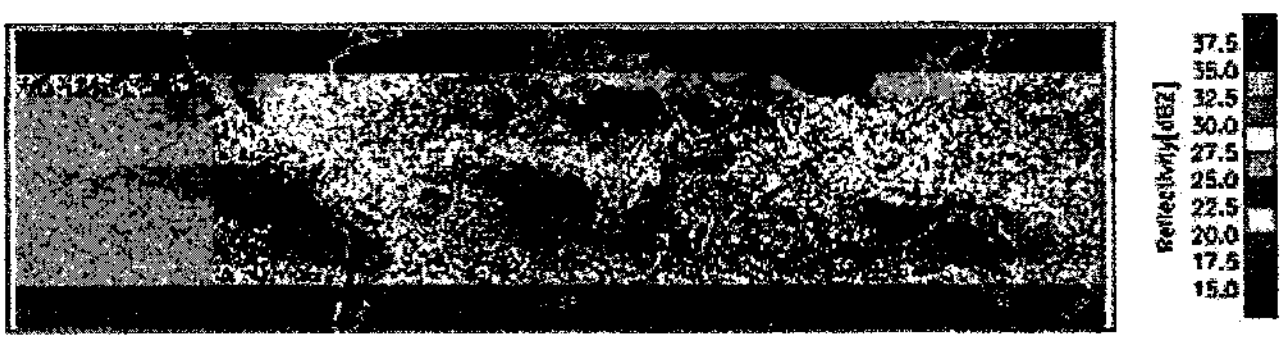

Figure 4.73: 2A25 reflectivity map at 35.0 GHz for September 2000.

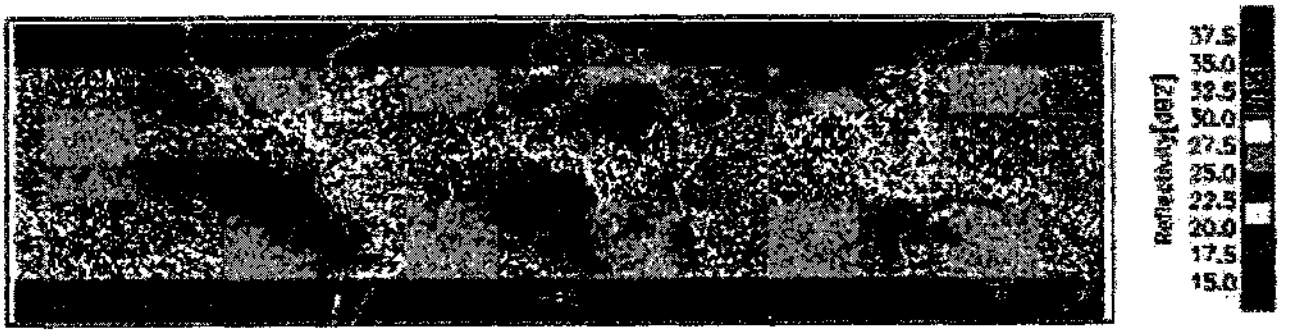

Figure 4.74: 2A25 reflectivity map at 13.8 GHz for October 2000.

Figure 4.75: 2A25 reflectivity map at 35.0 GHz for October 2000.

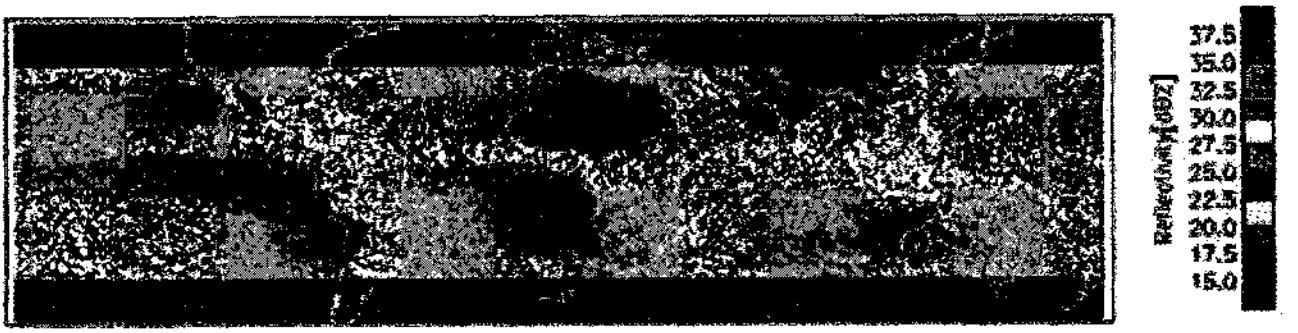

Figure 4.76: 2A25 reflectivity map at 13.8 GHz for November 2000.

Figure 4.77: 2A25 reflectivity map at 35.0 GHz for November 2000.

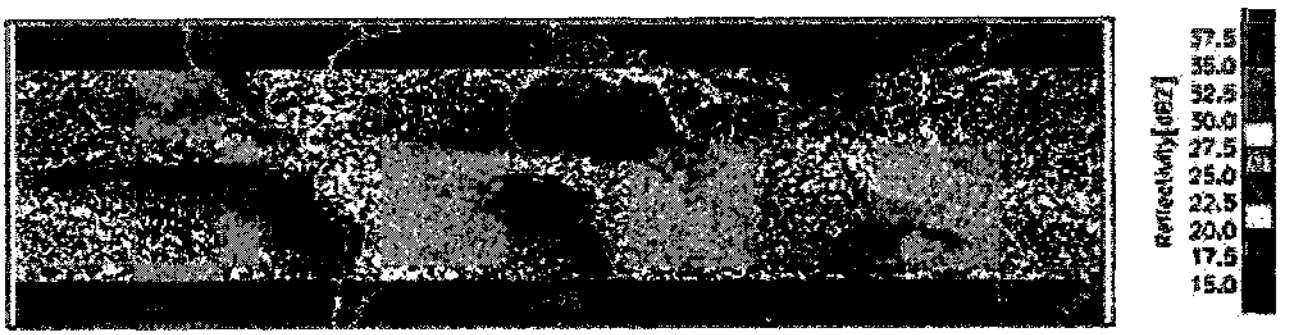

Figure 4.78: 2A25 reflectivity map at 13.8 GHz for December 2000.

Figure 4.79: 2A25 reflectivity map at 35.0 GHz for December 2000.

4.6 Global Map of Missed Data at Ka-band

In order to provide a quantitative measure of missed precipitation observation, monthly maps of the percentage of missed precipitation at Ka-band, under the condition that it is observed at Ku-band, are constructed. In this section, global maps of percentage of missing reflectivity at Ka-band are presented. For each month there are three maps. The first map shows the percentage of the observed reflectivity $\geq$ 20 dBZ at Ku- and Ka-band. The second map shows similar results when the observed reflectivity at Ku-band is $\geq$ 20 dBZ and at Ka-band is $<$ 20 dBZ. The last map shows the percentage of missing reflectivity at Ka-band given it is observed at Ku-band. The data are presented as monthly averages at 2 km above the mean sea level. The same mapping algorithm in the previous sections is used to obtain the global maps missing data at Ka-band. Table 5.2 provides an itemized list of the figures.

Figure	Title Description
Figure 4.80	Jan.:Percentage of reflectivity ≥ 20 at Ku- and Ka-band
Figure 4.81	Jan.:Percentage of reflectivity $\geq 20dBZ$ at Ku- and $< 20dBZ$ at Ka-band
Figure 4.82	Jan.:Percentage of missing reflectivity at Ka-band
Figure 4.83	Feb.:Percentage of reflectivity ≥ 20 at Ku- and Ka-band
Figure 4.84	Feb.:Percentage of reflectivity $\geq 20dBZ$ at Ku- and $< 20dBZ$ at Ka-band
Figure 4.85	Feb.:Percentage of missing reflectivity at Ka-band
Figure 4.86	Mar.:Percentage of reflectivity ≥ 20 at Ku- and Ka-band
Figure 4.87	Mar.:Percentage of reflectivity $\geq 20dBZ$ at Ku- and $< 20dBZ$ at Ka-band
Figure 4.88	Mar.:Percentage of missing reflectivity at Ka-band
Figure 4.89	Apr.:Percentage of reflectivity ≥ 20 at Ku- and Ka-band
Figure 4.90	Apr.:Percentage of reflectivity $\geq 20dBZ$ at Ku- and $< 20dBZ$ at Ka-band
Figure 4.91	Apr.:Percentage of missing reflectivity at Ka-band
Figure 4.92	May:Percentage of reflectivity ≥ 20 at Ku- and Ka-band
Figure 4.93	May:Percentage of reflectivity $\geq 20dBZ$ at Ku- and $< 20dBZ$ at Ka-band
Figure 4.94	May:Percentage of missing reflectivity at Ka-band
Figure 4.95	Jun.:Percentage of reflectivity ≥ 20 at Ku- and Ka-band
Figure 4.96	Jun.:Percentage of reflectivity $\geq 20dBZ$ at Ku- and $< 20dBZ$ at Ka-band
Figure 4.97	Jun.:Percentage of missing reflectivity at Ka-band
Figure 4.101	Jul.:Percentage of reflectivity ≥ 20 at Ku- and Ka-band
Figure 4.102	Jul.:Percentage of reflectivity $\geq 20dBZ$ at Ku- and $< 20dBZ$ at Ka-band
Figure 4.103	Jul.:Percentage of missing reflectivity at Ka-band
Figure ??	Aug.:Percentage of reflectivity ≥ 20 at Ku- and Ka-band
Figure ??	Aug.:Percentage of reflectivity $\geq 20dBZ$ at Ku- and $< 20dBZ$ at Ka-band
Figure ??	Aug.:Percentage of missing reflectivity at Ka-band
Figure 4.104	Sep.:Percentage of reflectivity ≥ 20 at Ku- and Ka-band
Figure 4.105	Sep.:Percentage of reflectivity $\geq 20dBZ$ at Ku- and $< 20dBZ$ at Ka-band
Figure 4.106	Sep.:Percentage of missing reflectivity at Ka-band
Figure 4.107	Oct.:Percentage of reflectivity ≥ 20 at Ku- and Ka-band
Figure 4.108	Oct.:Percentage of reflectivity $\geq 20dBZ$ at Ku- and $< 20dBZ$ at Ka-band
Figure 4.109	Oct.:Percentage of missing reflectivity at Ka-band
Figure 4.110	Nov.:Percentage of reflectivity ≥ 20 at Ku- and Ka-band
Figure 4.111	Nov.:Percentage of reflectivity $\geq 20dBZ$ at Ku- and $< 20dBZ$ at Ka-band
Figure 4.112	Nov.:Percentage of missing reflectivity at Ka-band
Figure 4.113	Dec.:Percentage of reflectivity ≥ 20 at Ku- and Ka-band
Figure 4.114	Dec.:Percentage of reflectivity $\geq 20dBZ$ at Ku- and $< 20dBZ$ at Ka-band
Figure 4.115	Dec.:Percentage of missing reflectivity at Ka-band

Table 4.4: Figure Number List of Monthly Percentage of Missing Reflectivity at Ka-band.

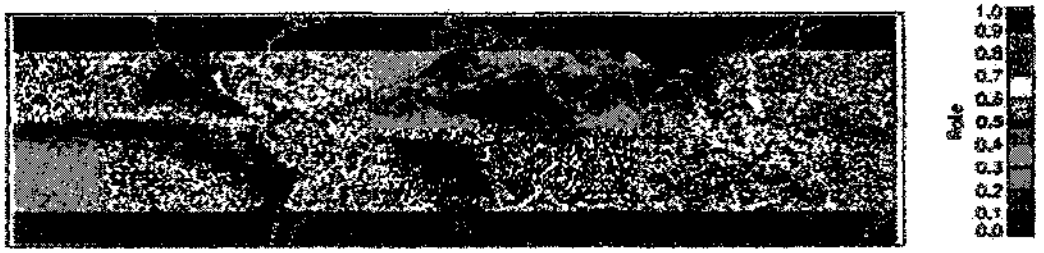

Figure 4.80: Percentage of reflectivity $\geq$ 20 at Ku- and Ka-band for January 2000.

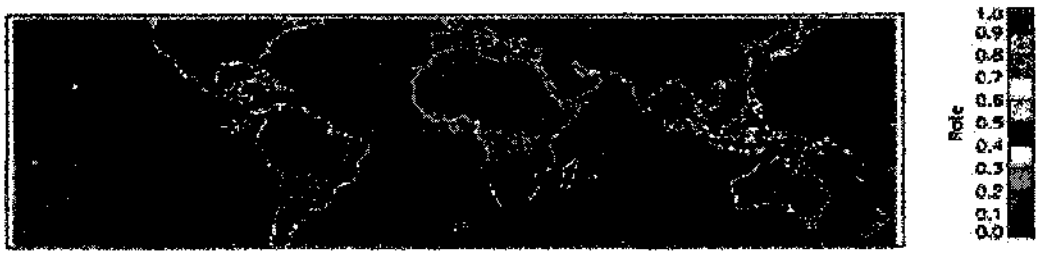

Figure 4.81: Percentage of reflectivity $\geq$ 20 dBZ at Ku-band and $<$ 20 dBZ at Ka-band for January 2000.

Figure 4.82: Percentage of missing reflectivity at Ka-band for January 2000.

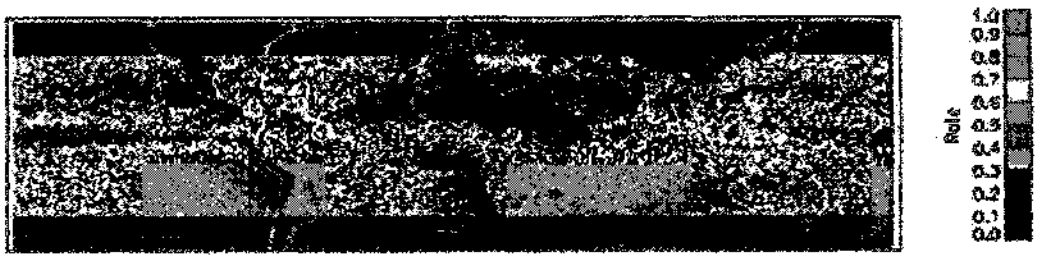

Figure 4.83: Percentage of reflectivity ≥ 20 at Ku- and Ka-band for February 2000.

Figure 4.84: Percentage of reflectivity ≥ 20 dBZ at Ku-band and < 20 dBZ at Ka-band for February 2000.

Figure 4.85: Percentage of missing reflectivity at Ka-band for February 2000.

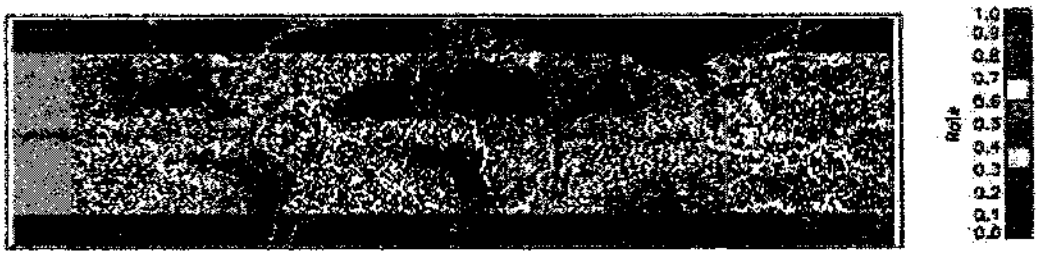

Figure 4.86: Percentage of reflectivity $\geq$ 20 at Ku- and Ka-band for March 2000.

Figure 4.87: Percentage of reflectivity $\geq$ 20 dBZ at Ku-band and $<$ 20 dBZ at Ka-band for March 2000.

Figure 4.88: Percentage of missing reflectivity at Ka-band for March 2000.

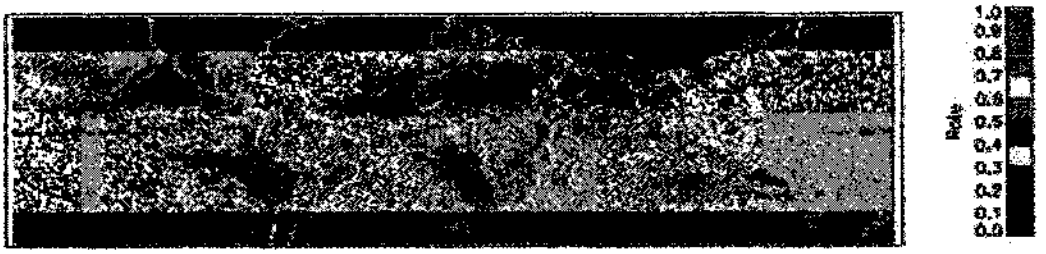

Figure 4.89: Percentage of reflectivity ≥ 20 at Ku- and Ka-band for April 2000.

Figure 4.90: Percentage of reflectivity ≥ 20 dBZ at Ku-band and < 20 dBZ at Ka-band for April 2000.

Figure 4.91: Percentage of missing reflectivity at Ka-band for April 2000.

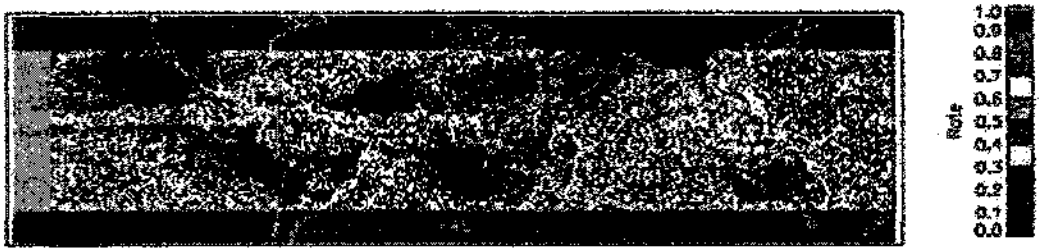

Figure 4.92: Percentage of reflectivity $\geq$ 20 at Ku- and Ka-band for May 2000.

Figure 4.93: Percentage of reflectivity $\geq$ 20 dBZ at Ku-band and $<$ 20 dBZ at Ka-band for May 2000.

Figure 4.94: Percentage of missing reflectivity at Ka-band for May 2000.

Figure 4.95: Percentage of reflectivity ≥ 20 at Ku- and Ka-band for June 2000.

Figure 4.96: Percentage of reflectivity ≥ 20 dBZ at Ku-band and < 20 dBZ at Ka-band for June 2000.

Figure 4.97: Percentage of missing reflectivity at Ka-band for June 2000.

Figure 4.98: Percentage of reflectivity ≥ 20 at Ku- and Ka-band for July 2000.

Figure 4.99: Percentage of reflectivity ≥ 20 dBZ at Ku-band and < 20 dBZ at Ka-band for July 2000.

Figure 4.100: Percentage of missing reflectivity at Ka-band for July 2000.

Figure 4.101: Percentage of reflectivity $\geq$ 20 at Ku- and Ka-band for August 2000.

Figure 4.102: Percentage of reflectivity $\geq$ 20 dBZ at Ku-band and $<$ 20 dBZ at Ka-band for August 2000.

Figure 4.103: Percentage of missing reflectivity at Ka-band for August 2000.

Figure 4.104: Percentage of reflectivity ≥ 20 at Ku- and Ka-band for Sep. 2000.

Figure 4.105: Percentage of reflectivity $\geq 20dBZ$ at Ku-band and $< 20dBZ$ at Ka-band for Sep. 2000.

Figure 4.106: Percentage of missing reflectivity at Ka-band for Sep. 2000.

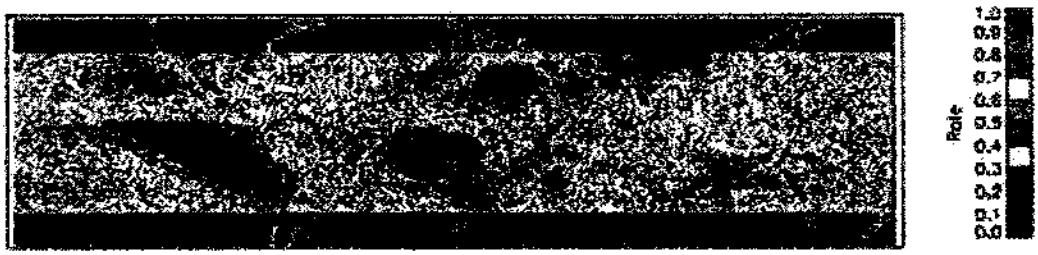

Figure 4.107: Percentage of reflectivity ≥ 20 at Ku- and Ka-band for Oct. 2000.

Figure 4.108: Percentage of reflectivity $\geq 20dBZ$ at Ku-band and $< 20dBZ$ at Ka-band for Oct. 2000.

Figure 4.109: Percentage of missing reflectivity at Ka-band for Oct. 2000.

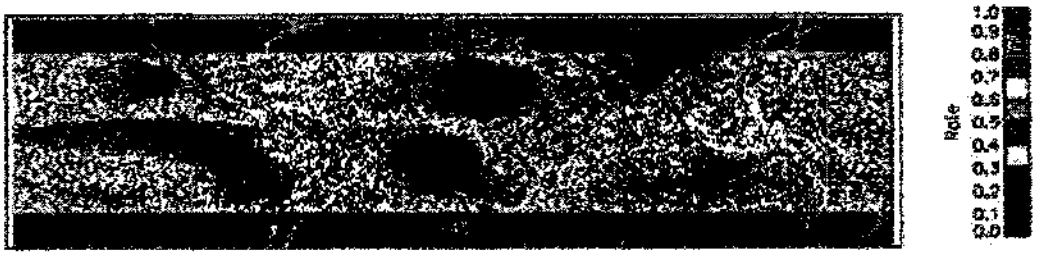

Figure 4.110: Percentage of reflectivity ≥ 20 at Ku- and Ka-band for Nov. 2000.

Figure 4.111: Percentage of reflectivity $\geq 20dBZ$ at Ku-band and $< 20dBZ$ at Ka-band for Nov. 2000.

Figure 4.112: Percentage of missing reflectivity at Ka-band for Nov. 2000.

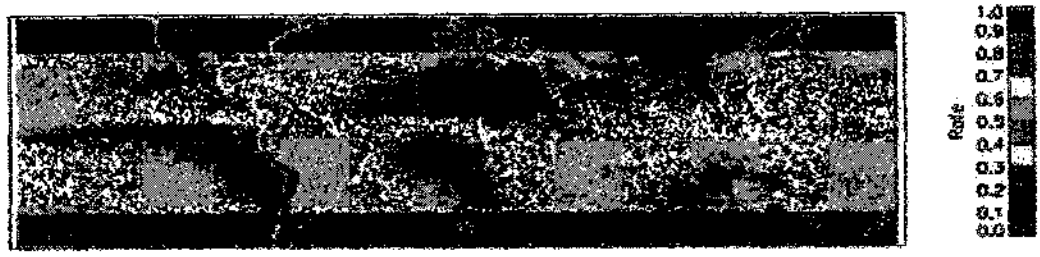

Figure 4.113: Percentage of reflectivity ≥ 20 at Ku- and Ka-band for Dec. 2000.

Figure 4.114: Percentage of reflectivity $\geq 20dBZ$ at Ku-band and $< 20dBZ$ at Ka-band for Dec. 2000.

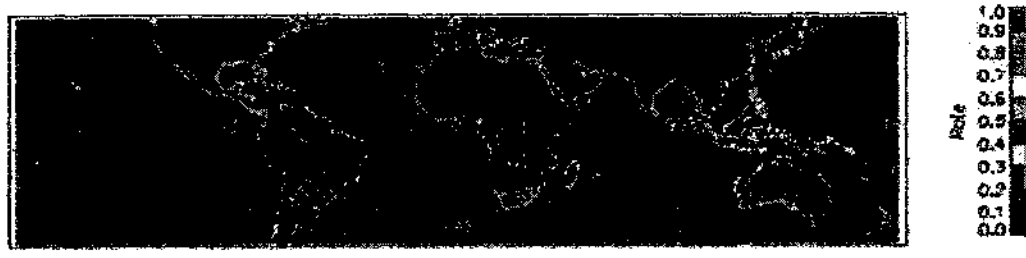

Figure 4.115: Percentage of missing reflectivity at Ka-band for Dec. 2000.

Chapter 5

ESTIMATION OF RAINDROP SIZE DISTRIBUTION

5.1 Introduction

The raindrop size distribution (RSD) model was described in Chapter 3. In order to compare the size distribution of hydrometeors under widely varying precipitation rates, the concept of scaling the drop size distribution and normalization has been used by several authors. A general expression of normalized distribution is

$$N(D) = N_w F(D/D_m) \tag{5.1}$$

where $N_w(mm^{-1}m^{-3})$ is the scaling parameter and $F(D/D_m)$ is the normalized function. The normalized/scaled Gamma RSD can be expressed as

$$N(D) = N_w f(\mu) \left(\frac{D}{D_0}\right)^{\mu} exp\,(-\Lambda D) \tag{5.2}$$

The normalized RSD can be used to relate any two moments of the RSD (Bringi and Chandrasekar, 2001). The concept of normalized Gamma RSD has been used by Bringi and Chadrasekar (2001) and Testud et al. (2001) to provide

a physical basis for the α adjustment method. This chapter develops an algorithm for estimating path integrated N_w and a profile of D_0 obtained using data from α adjustment method (Iguchi, 2000). Ground based polarimetric radar (GR) measurements can be used to estimate the parameters of Gamma RSD (Gorgucci, 2002), and comparison of RSD retrievals obtained from PR and GR data from several coincident overpasses are presented.

5.2 Estimation of Raindrop Size Distribution (RSD) Parameters from TRMM Measurements

The relationship between the specific attenuation and reflectivity can be approximated by a power law of the form,

$$k = \alpha Z^{\beta} \tag{5.3}$$

The α and β can vary depending on the RSD. Based on the concept of normalized RSD, the normalized attenuation and reflectivity can be related as (Bringi and Chandrasekar, 2001)

$$\left(\frac{k}{N_w}\right) = \tilde{\alpha}\left(\frac{Z}{N_w}\right)^{\beta} \tag{5.4}$$

Figure 5.1 shows a scatter plot of $log_{10}(k/N_w)$ versus $log_{10}(Z/N_w)$ for widely varying RSD parameters. It can be seen that $log_{10}(k/N_w)$ versus $log_{10}(Z/N_w)$ can be approximated by a straight line. Equation 5.4 can be rewritten as

$$k = \tilde{\alpha}(N_w)^{1-\beta} Z^{\beta} \tag{5.5}$$

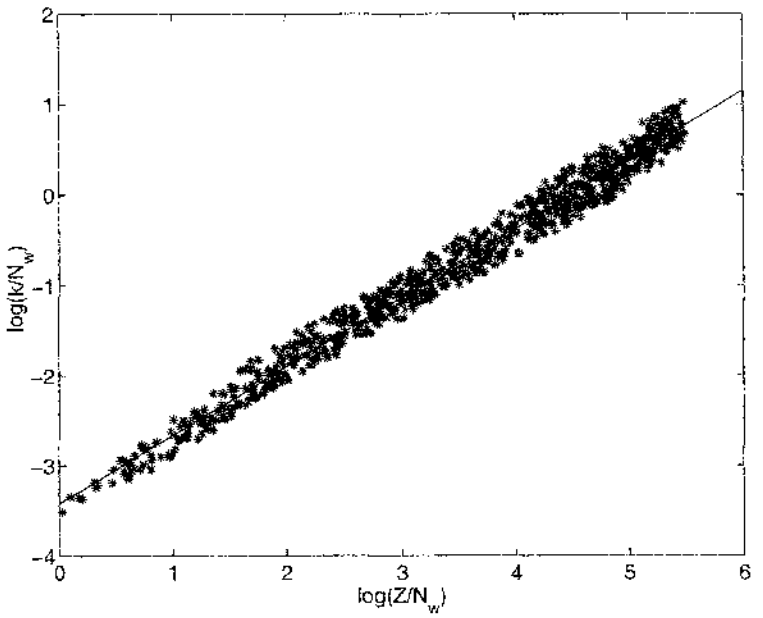

Figure 5.1: Scatter plot of k/N_w versus Z/N_w for widely varying RSD:3$\leq$ $log(N_w)$ $\leq$5, 0.5$\leq$ D_0 $\leq$ 2.5 and -1$\leq$ μ $\leq$ 4.

Equation 5.5 shows that changes in α can be attributed to changes in N_w (a path integrated value), where α and $\tilde{\alpha}$ are related by

$$\alpha = \tilde{\alpha}\,(N_w)^{1-\beta} \tag{5.6}$$

and

$$N_w = \left(\frac{\alpha}{\tilde{\alpha}}\right)^{\frac{1}{1-\beta}} \tag{5.7}$$

Equation 5.6 provides the physical basis for attributing changes in α to changes in N_w while keeping β fixed. TRMM program uses a combination of the α adjustment

procedure and Hitschfeld-Bordan algorithms (Hitschfeld, 1954) to determine the attenuation correction. The surface reference technique (SRT) is used to determine the path integrated attenuation [PIA]. Subsequently using the α adjustment procedure, the PIA is distributed along the path. However, when the surface reference is not reliable (due to fluctuation in the surface backscatter, σ^o), then the Hitschfeld-Bordan algorithm is used. TRMM uses a smooth transition between the two algorithms by performing attenuation correction as a weighted average of α adjustment and Hitschfeld-Bordan methods. The attenuation correction starts with an initial α_{ini} to estimate PIA. Subsequently, based on comparison with the surface reference technique, the α_{ini} is adjusted as

$$\alpha_{adj} = \alpha_{ini}\epsilon_o \tag{5.8}$$

where

$$\epsilon_o = 1 - \left[\frac{1-\epsilon_f}{W}\right] \tag{5.9}$$

ϵ_f is the final correction factor for SRT and W is the weight factor and these parameters are given in TRMM data (2A25). Once α_{adj} is calculated, then N_w can be retrieved from Equation 5.7. The median volume diameter, D_0, can be subsequently obtained as

$$D_0 = \left[\frac{Z}{N_w C}\right]^{\frac{1}{7}} \tag{5.10}$$

where C is given by

Parameter	Stratiform	Convective	Other
α_{ini}	2.85E-04	4.17E-04	4.17E-04
$\tilde{\alpha}$	4.50E-05	4.31E-05	4.31E-05
β	0.7923	0.7713	0.7713
μ	3	3	3

Table 5.1: Values of α_{ini}, $\tilde{\alpha}$, β, and μ.

$$C = \frac{f(\mu)\Gamma(7+\mu)}{(3.67+\mu)^{7+\mu}} \tag{5.11}$$

Table 5.1 shows the values of α_{ini}, $\tilde{\alpha}$, β, and μ used in this research as a function of precipitation type. Note that α_{ini} is given by Iguchi et al. (2000) for different precipitation types while $\tilde{\alpha}$ and β were calculated from the simulation.

5.3 Estimation of Raindrop Size Distribution (RSD) Parameters from Ground Radar Measurements

Determination of the RSD is of central importance in describing the properties of the rain medium. As mentioned before, radar measurements such as reflectivity (Z_h), differential reflectivity (Z_{dr}), and specific differential propagation phase (K_{dp}) are influenced by the underlying RSD and the mean shape of raindrops, and weight the RSD differently (Gorgucci et al. 2002). The radar measurements can be expressed in terms of RSD as follows:

$$Z_h = \frac{\lambda^4}{\pi^5 |k|^2} \int \sigma_h(D) N(D) dD \tag{5.12}$$

$$Z_{dr} = \frac{\int \sigma_h(D) N(D) dD}{\int \sigma_v(D) N(D) dD} \tag{5.13}$$

$$K_{dp} = \frac{180\lambda}{\pi} \Re \int [f_h(D) - f_v(D)] N(D) dD \tag{5.14}$$

$\sigma_{h,v}$ is the radar cross-section at horizontal and vertical polarization states, respectively, λ is the wavelength, and $k = (\epsilon_r - 1)/(\epsilon_r + 2)$ where ϵ_r is the dielectric constant of water. $\Re$ refers to the real part of a complex number and f_h and f_v are the forward scattering amplitudes at h and v polarization states, respectively.

With the Gamma RSD model, the median volume drop diameter (D_0), normalized intercept (N_w), and shaping parameter (μ) can be derived from polarimetric observations as (Gorgucci et al. 2002):

$$D_0 = a_1 Z_h^{b_1} (\xi_{dr})^{c_1} \tag{5.15}$$

where $\xi_{dr} = 10^{0.1 Z dr}$, $a_1 = 0.595\beta^{0.0353}$, $b_1 = 0.0242\beta^{-0.359}$, and $c_1 = 0.103\beta^{-0.91}$. in which the slope of the shape-size relationship (β) is given as $\beta = 2.08 Z_h^{-0.365} K_{dp}^{0.38} \xi_{dr}^{0.965}$.

$$log_{10}(N_w) = a_2 Z_h^{b2} (\xi_{dr})^{c_2} \tag{5.16}$$

where $a_2 = 3.12\beta^{0.0201}$, $b_2 = 0.176\beta^{0.376}$, and $c_2 = -0.101\beta^{-0.897}$.

$$\mu = \frac{a_3 D_0^{b_3}}{(\xi_{dr} - 1)} - c_3 (\xi dr)^{d_3} \tag{5.17}$$

where $a_3 = 200\beta^{1.89}$, $b_3 = 2.23\beta^{0.039}$, $c_3 = 3.16\beta^{-0.046}$, and $d_3 = 0.374\beta^{-0.355}$.

Equations (5.15-5.17) are valid for $Z_h \geq 35$ dBZ, $Z_{dr} \geq 0.2$ dB, $K_{dp} \geq 0.3\ ^{o}\ km^{-1}$, and rain rate $\leq 300\ mmhr^{-1}$.

At low rain rates, measurements of K_{dp} and sometimes Z_{dr} are noisy at long wavelengths (such as at S-band), which require some areal averaging to reduce measurement fluctuations. Bringi et al. (2002) extended the RSD estimates to lower rain rates for $Z_h \leq 35$ dBZ and $Z_{dr} \leq 0.2$ dB as follows:

$$D_0 = 1.68\,(\hat{\alpha})^{0.368}\,(Z_h)^{0.136} \tag{5.18}$$

where $\hat{\alpha} = \langle Z_{dr} \rangle \,/\, \langle Z_h^{0.37} \rangle$

$$N_w = (1.513/\hat{\gamma})^{7.35} \tag{5.19}$$

where $\hat{\gamma} = 1.68\,(\hat{\alpha})^{0.368}$. The RSD estimates lower rain rates for $Z_h \leq 35$ dBZ, and $Z_{dr} \geq 0.2$ dB as follows:

$$\begin{aligned} D_0 &= 1.68\,(Z_{dr})^{0.368}, \quad for \quad D_o \leq 1.5\,mm \\ &= 1.74\,(Z_{dr})^{0.536}, \quad for \quad D_o > 1.5\,mm \end{aligned} \tag{5.20}$$

$$N_w = \frac{21 Z_h}{D_0^{7.353}} \tag{5.21}$$

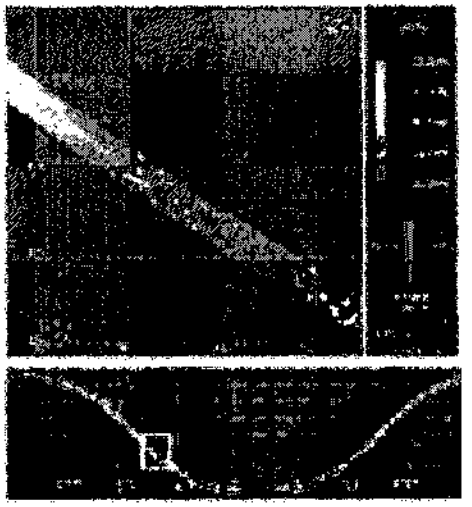

Figure 5.2: Location of case 1: Brazil 2/25/1999.

5.4 Data Analysis and Comparison Between PR and GR

RSD from ground radar (GR) observations can be obtained using the algorithms described by Gorgucci et al. (2002) and Bringi et al. (2002). The following compares RSD estimates obtained from GR and PR on simultaneous overpass cases. A total of about 32 overpass cases were studied from Brazil and Florida. Eight specific case studies are presented in detail.

5.4.1 Case 1: 25 February 1999

At this time the TRMM was over Brazil as it is shown in Figure 5.2. The cell analyzed here was part of wide spread precipitation occurring on that day and was perhaps in growth phase. Figures 5.3 and 5.4 show the estimates of N_w and D_0 from 2 to 4 km altitude from both radars. The results of Figure 5.3 show fairly good agreement between the RSD retrieved from TRMM PR and the ground radar based estimates.

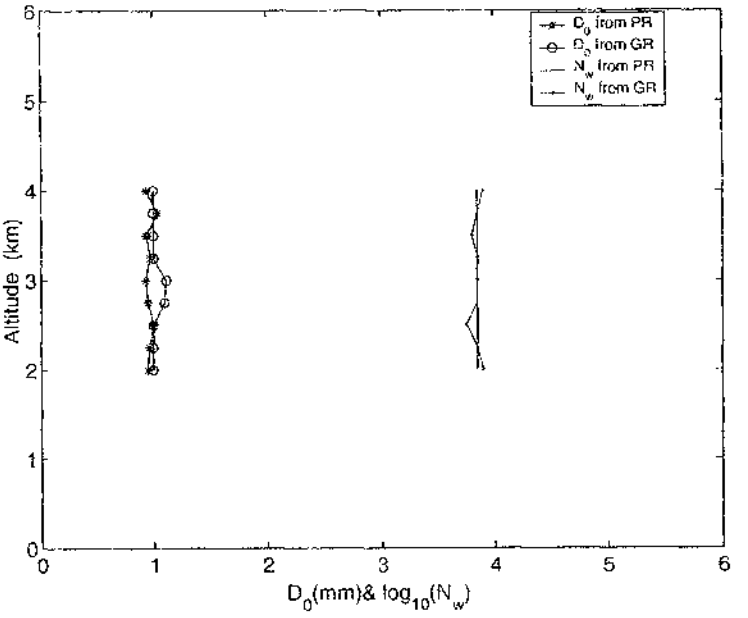

Figure 5.3: D_0 and N_w from PR and GR for case 1 (orbit 7174, scan 7376 and ray 29).

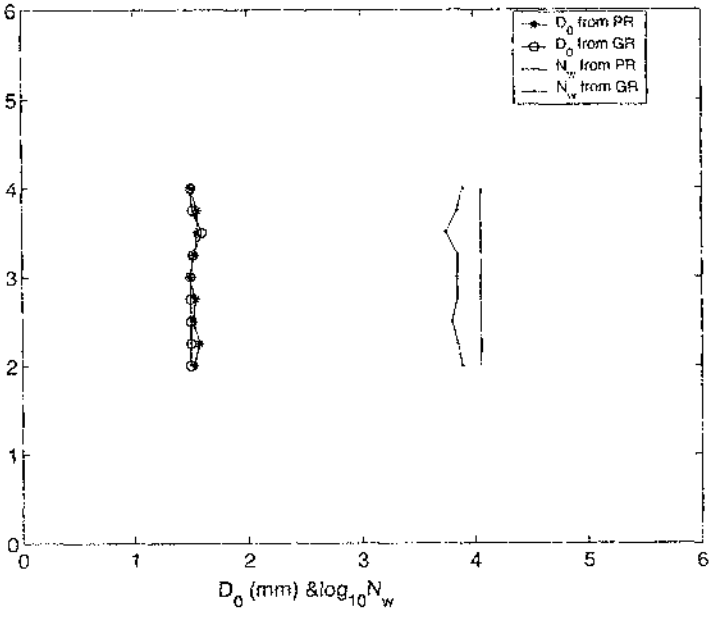

Figure 5.4: D_0 and N_w from PR and GR for case 1 (orbit 7174, scan 7359 and ray 13).

Figure 5.5: Location of case 2: Melbourne, Florida 8/13/1998.

5.4.2 Case 2: 13 August 1998

The cell analyzed here was part of a convective storm over Melbourne, Florida as it is shown in Figure 5.5. Figures 5.6 and 5.7 show the estimates of N_w and D_0 for altitudes between 2 to 4 km from both radars. The results of cross-validation in Figure 5.6 show fairly good agreement with the RSD parameters retrieved from TRMM PR and the ground radar based estimates.

5.4.3 Comparison Between PR and GR

A total of 16 ray profiles from Brazil (TRMM/LBA experiment) and 16 ray profiles from Florida (TRMM/TEFLUN experiment) were studied. Figure 5.8 and Figure 5.9 show scatter plot of N_w and D_0 obtained from PR and GR. It should be noted that N_w is a single path integrated from PR whereas D_0 is available as a profile.

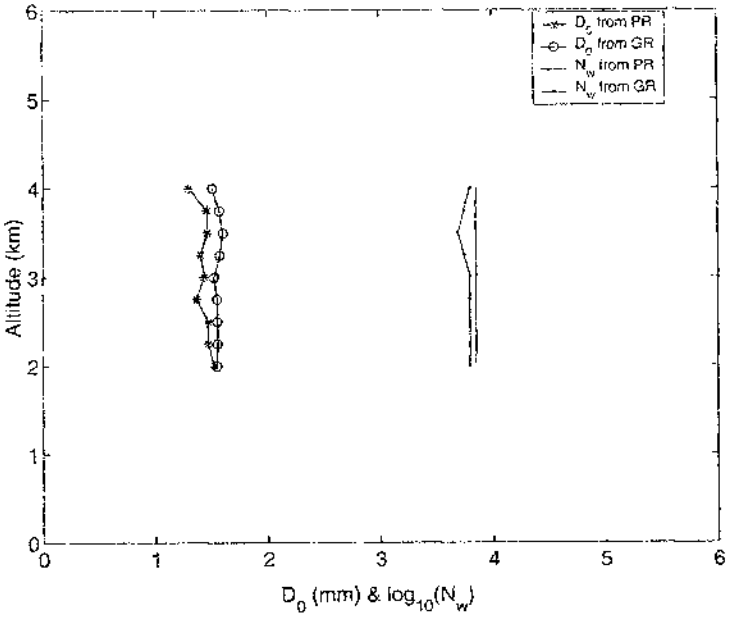

Figure 5.6: D_0 and N_w from PR and GR for case 2 (orbit 4085, scan 5419 and ray 38).

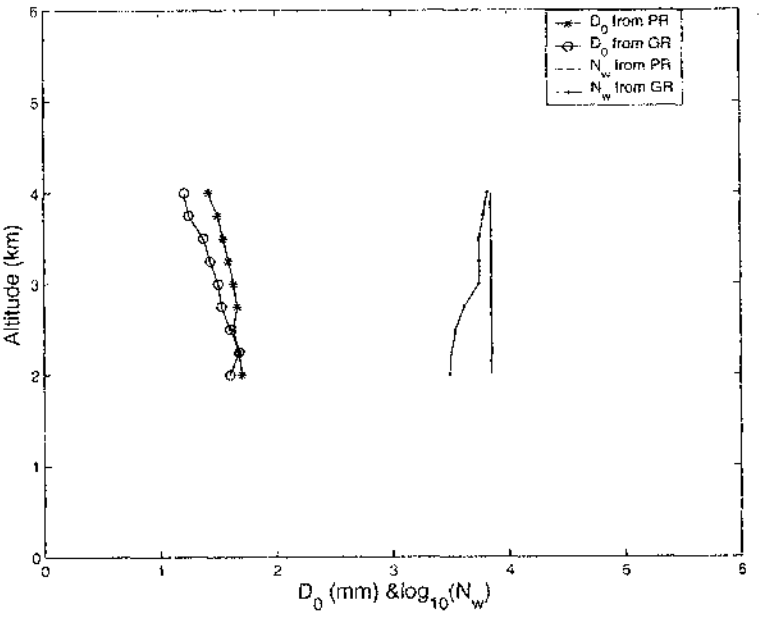

Figure 5.7: D_0 and N_w from PR and GR for case 2 (orbit 4085, scan 5420 and ray 39).

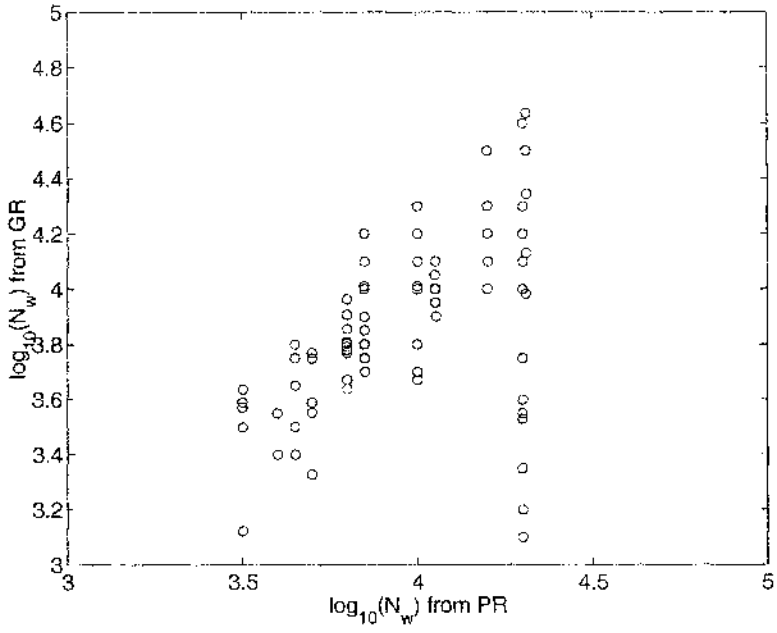

Figure 5.8: Scatter plot of N_w from PR and GR.

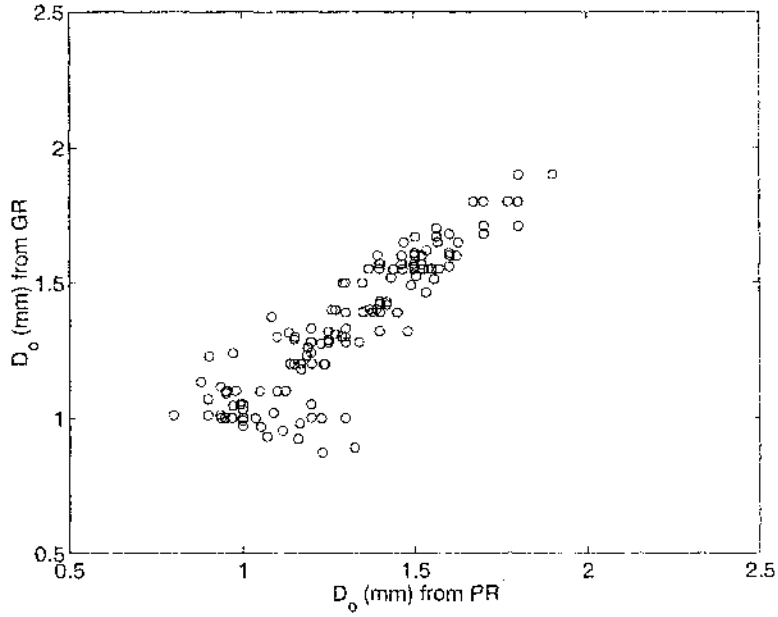

Figure 5.9: Scatter plot of D_0 from PR and GR.

5.5 Monthly Maps of RSD Parameters

TRMM PR observations are used to develop monthly maps of RSD parameters at Ku-bands. The map results for N_w and D_0 are estimates based on the model developed in section 5.2. Table 5.2 provides an itemized list of the figures of monthly average of N_w and monthly maximum of D_0 at altitude 2 km for the year 2000.

Figure Number	**Title Description**
Figure 5.10	Estimated N_w for January 2000
Figure 5.11	Estimated D_0 for January 2000
Figure 5.12	Estimated N_w for February 2000
Figure 5.13	Estimated D_0 for February 2000
Figure 5.14	Estimated N_w for March 2000
Figure 5.15	Estimated D_0 for March 2000
Figure 5.16	Estimated N_w for April 2000
Figure 5.17	Estimated D_0 for April 2000
Figure 5.18	Estimated N_w for May 2000
Figure 5.19	Estimated D_0 for May 2000
Figure 5.20	Estimated N_w for June 2000
Figure 5.21	Estimated D_0 for June 2000
Figure 5.22	Estimated N_w for July 2000
Figure 5.23	Estimated D_0 for July 2000
Figure 5.24	Estimated N_w for August 2000
Figure 5.25	Estimated D_0 for August 2000
Figure 5.26	Estimated N_w for September 2000
Figure 5.27	Estimated D_0 for September 2000
Figure 5.28	Estimated N_w for October 2000
Figure 5.29	Estimated D_0 for October 2000
Figure 5.30	Estimated N_w for November 2000
Figure 5.31	Estimated D_0 for November 2000
Figure 5.32	Estimated N_w for December 2000
Figure 5.33	Estimated D_0 for December 2000

Table 5.2: Figure Number List of Monthly Average N_w and Maximum D_0 for Cases Only When α Adjustment is Made.

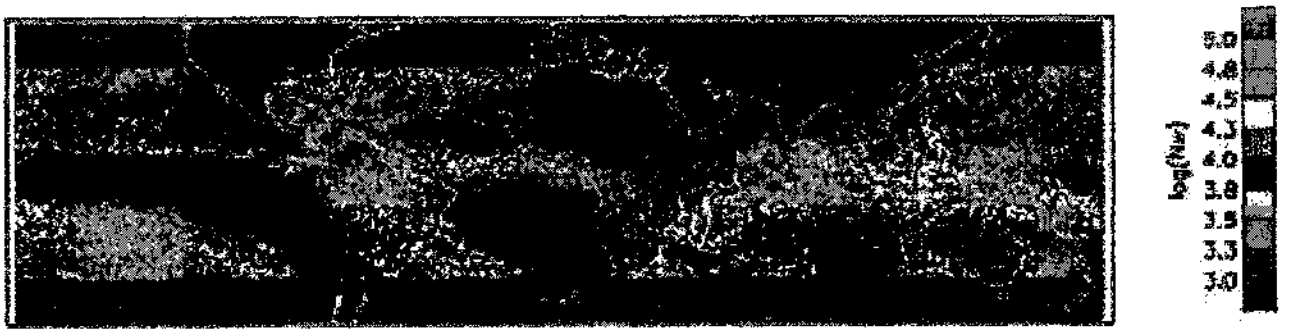

Figure 5.10: Estimated N_w for January 2000.

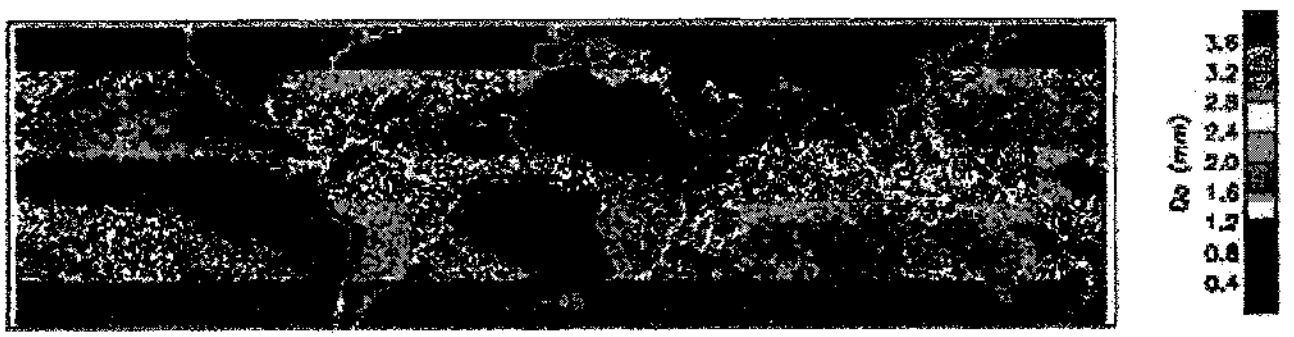

Figure 5.11: Estimated D_0 for January 2000.

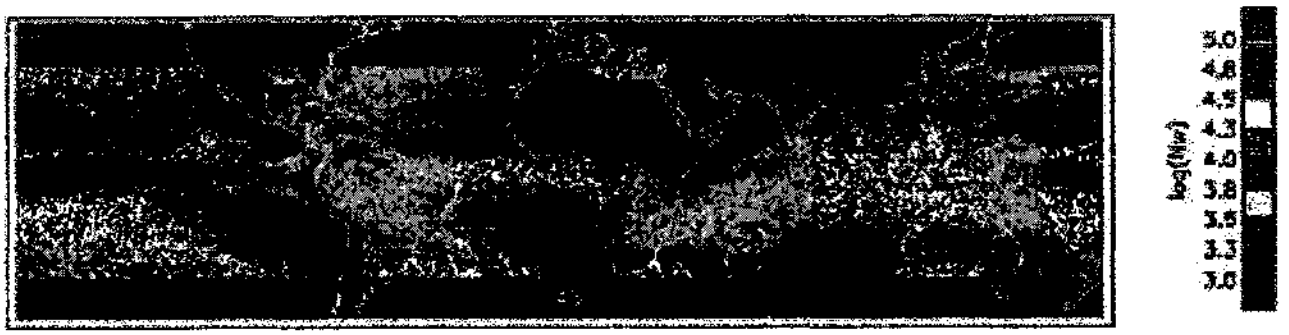

Figure 5.12: Estimated N_w for February 2000.

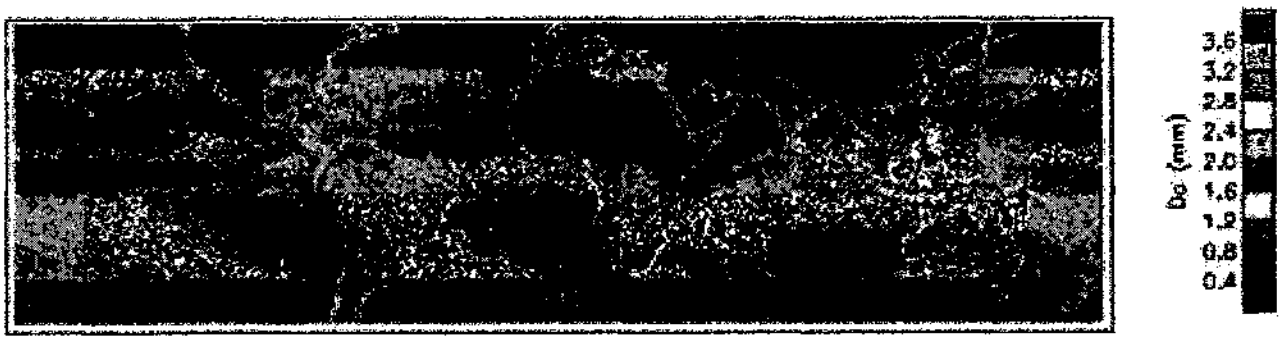

Figure 5.13: Estimated D_0 for February 2000.

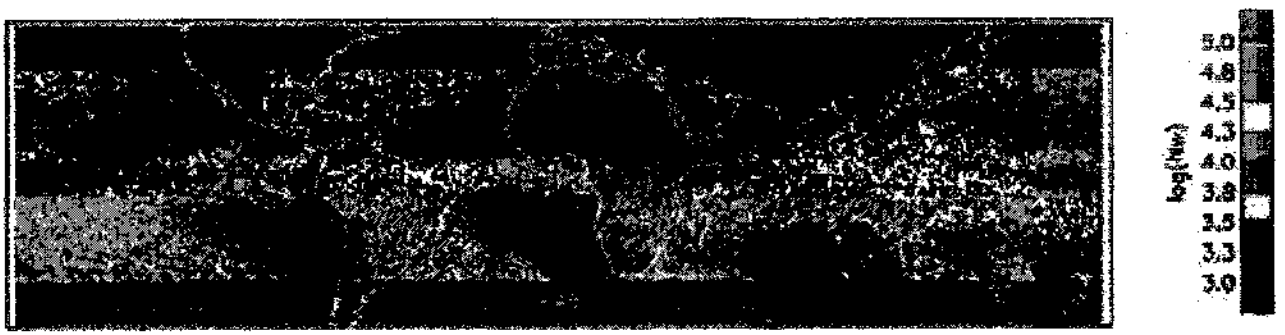

Figure 5.14: Estimated N_w for March 2000.

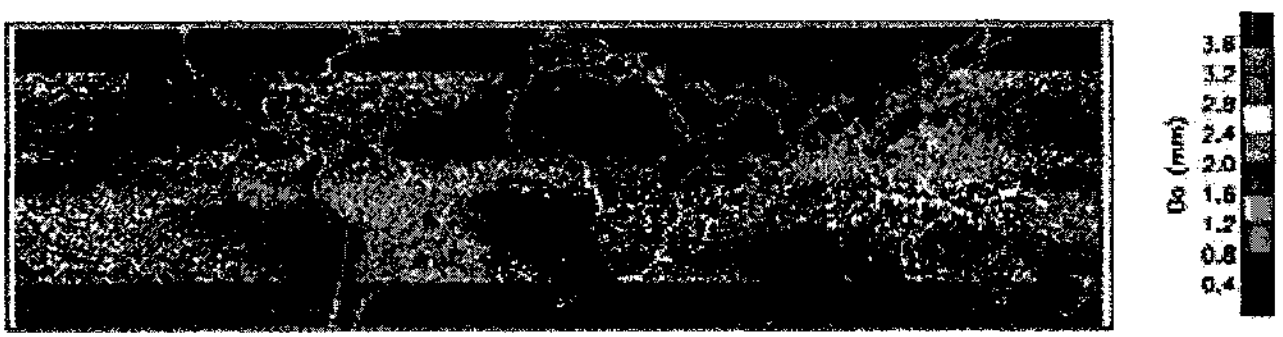

Figure 5.15: Estimated D_0 for March 2000.

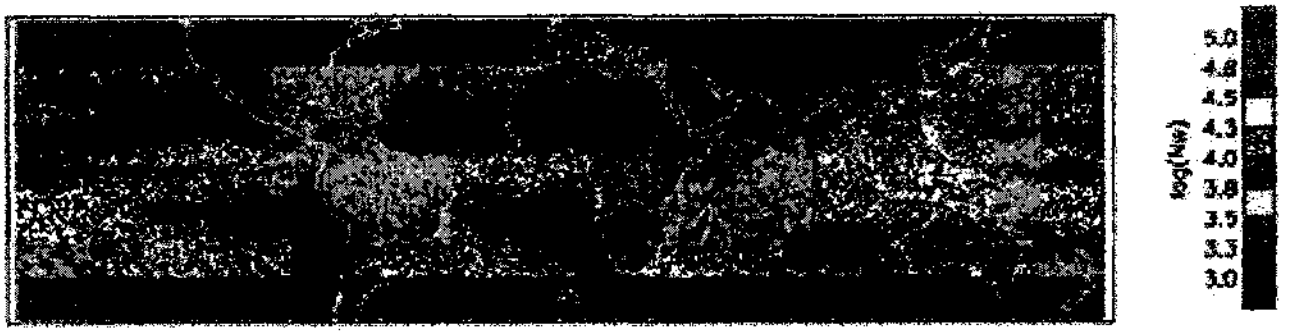

Figure 5.16: Estimated N_w for April 2000.

Figure 5.17: Estimated D_0 for April 2000.

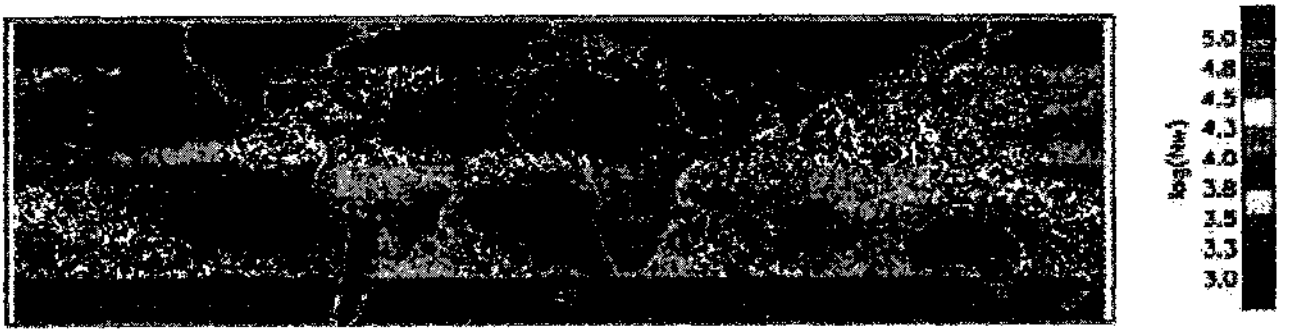

Figure 5.18: Estimated N_w for May 2000.

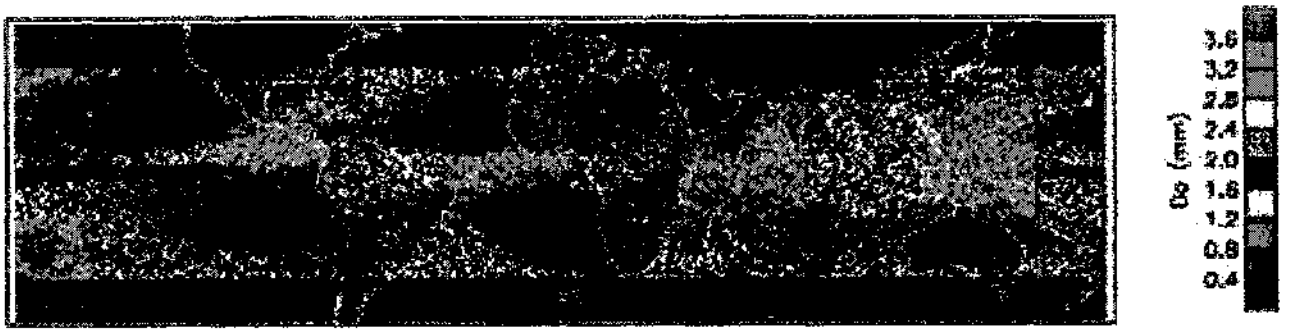

Figure 5.19: Estimated D_0 for May 2000.

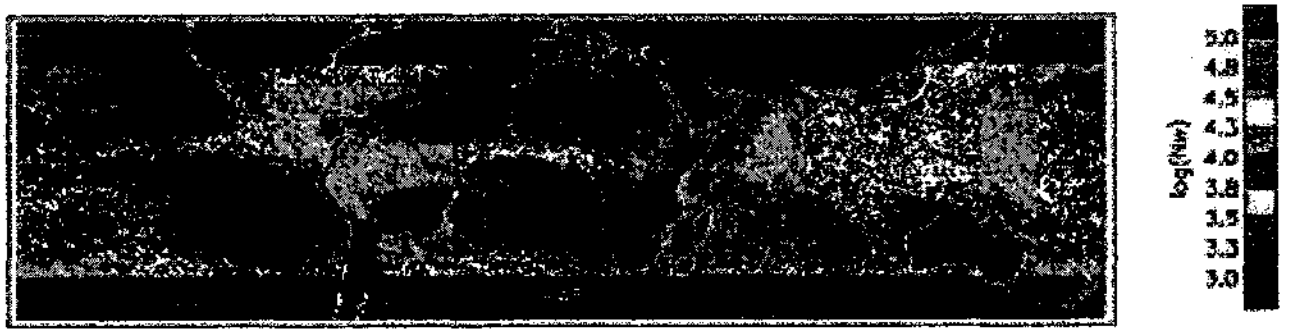

Figure 5.20: Estimated N_w for June 2000.

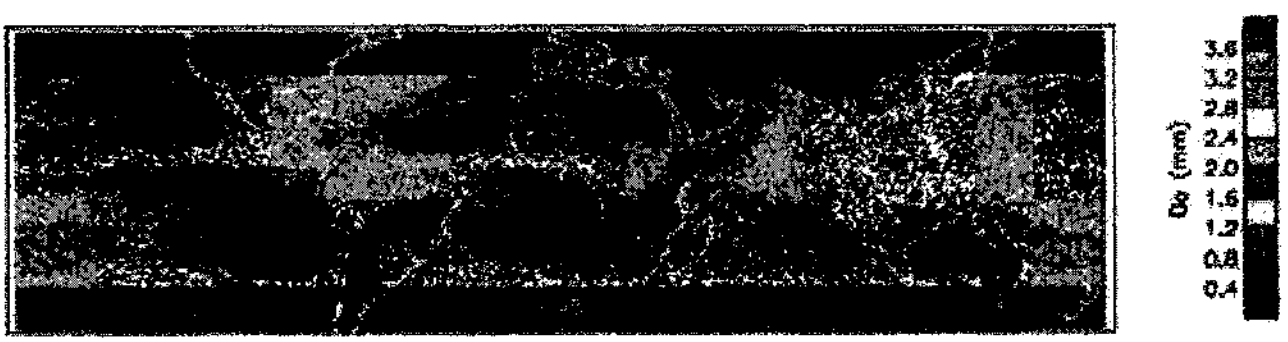

Figure 5.21: Estimated D_0 for June 2000.

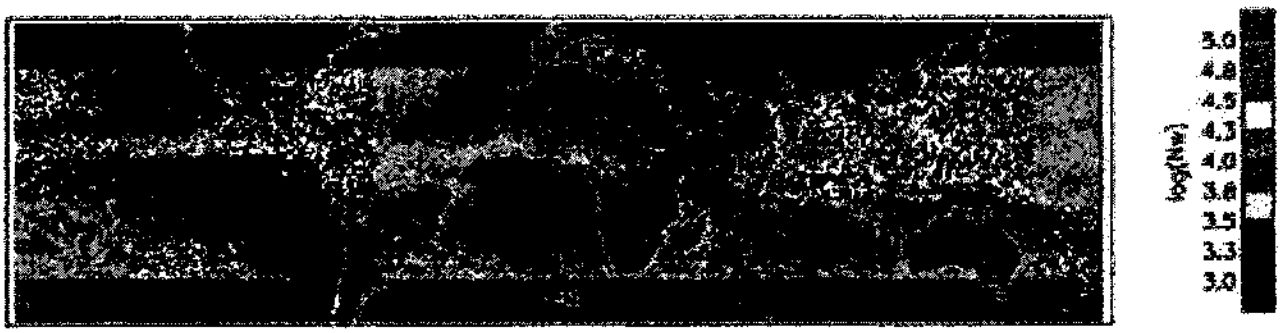

Figure 5.22: Estimated N_w for July 2000.

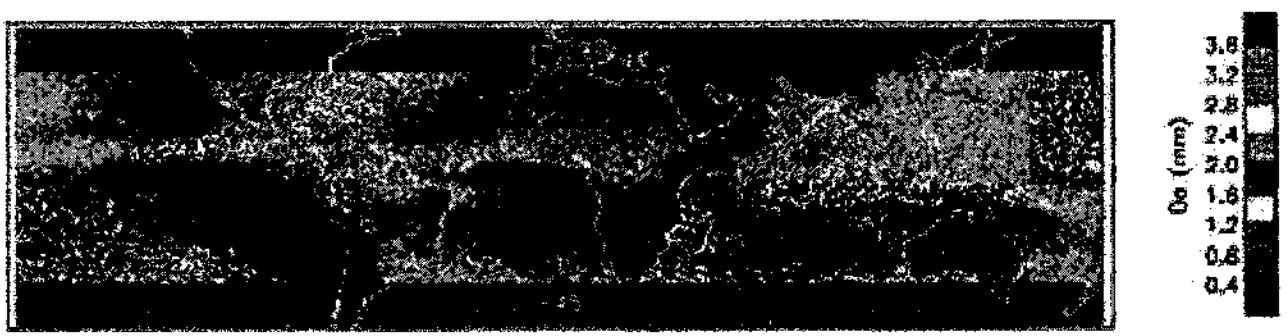

Figure 5.23: Estimated D_0 for July 2000.

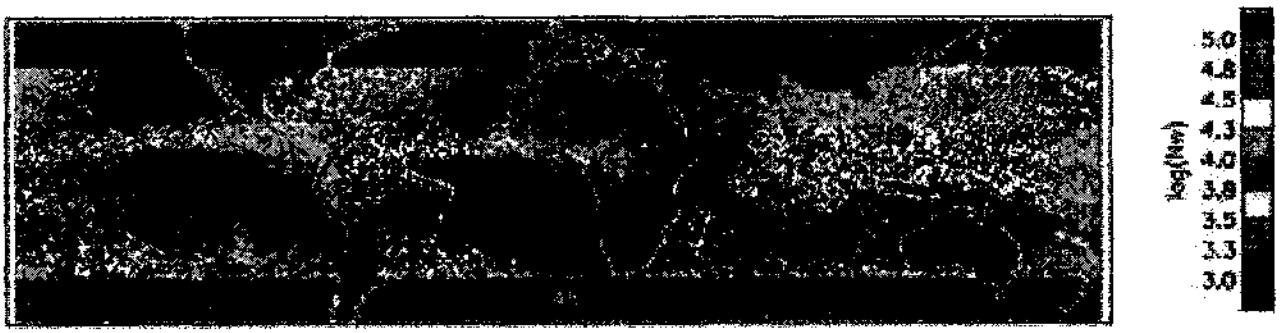

Figure 5.24: Estimated N_w for August 2000.

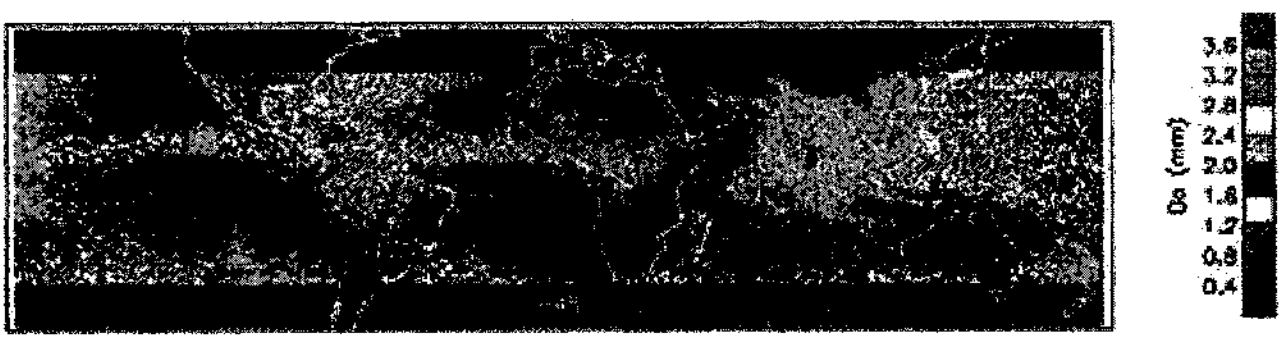

Figure 5.25: Estimated D_0 for August 2000.

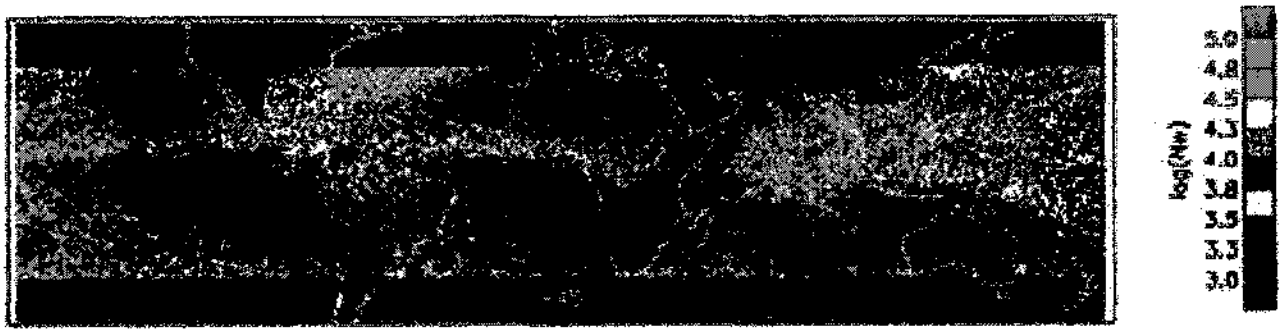

Figure 5.26: Estimated N_w for September 2000.

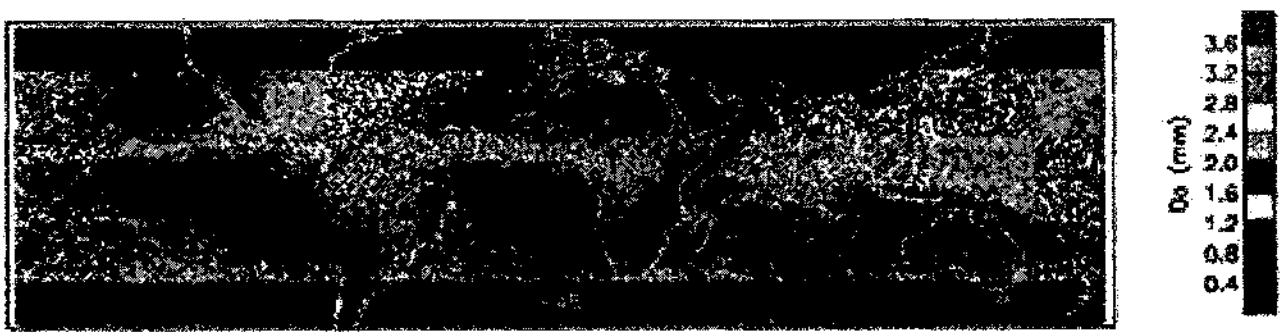

Figure 5.27: Estimated D_0 for September 2000.

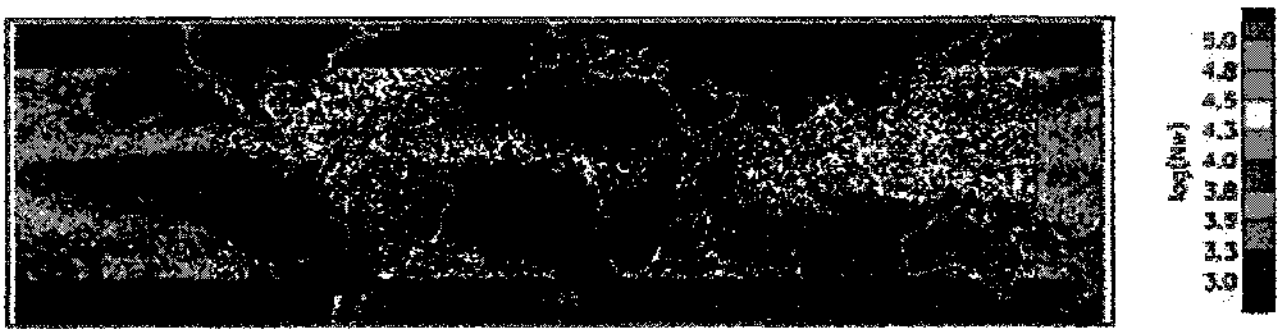

Figure 5.28: Estimated N_w for October 2000.

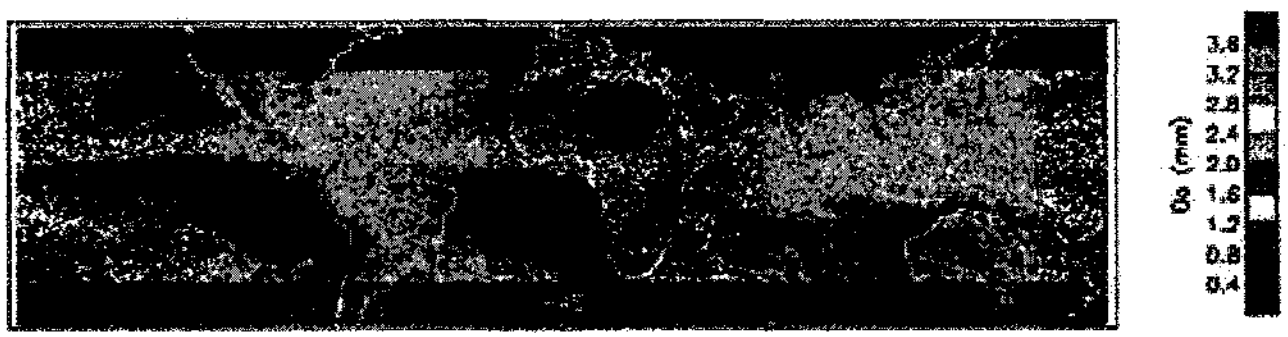

Figure 5.29: Estimated D_0 for October 2000.

Figure 5.30: Estimated N_w for November 2000.

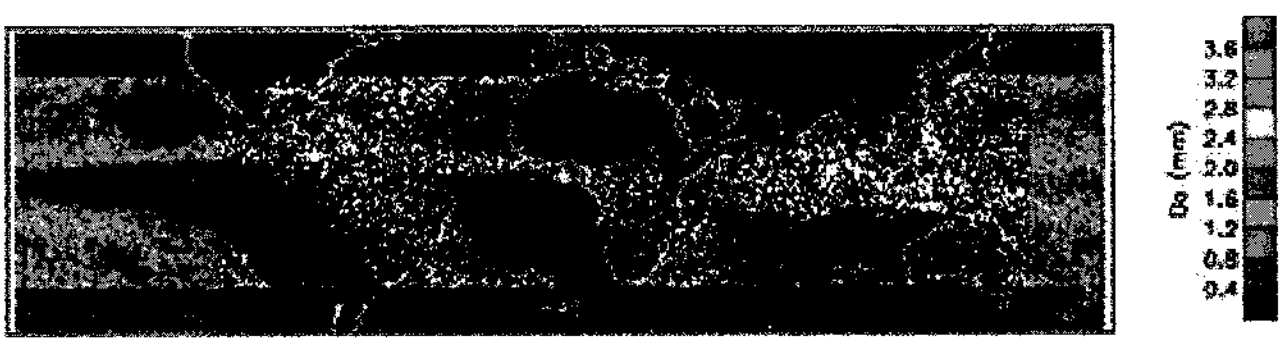

Figure 5.31: Estimated D_0 for November 2000.

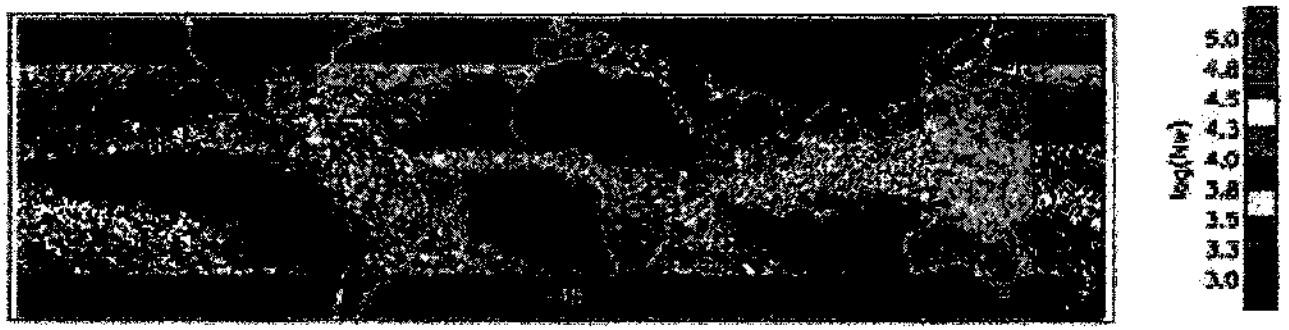

Figure 5.32: Estimated N_w for December 2000.

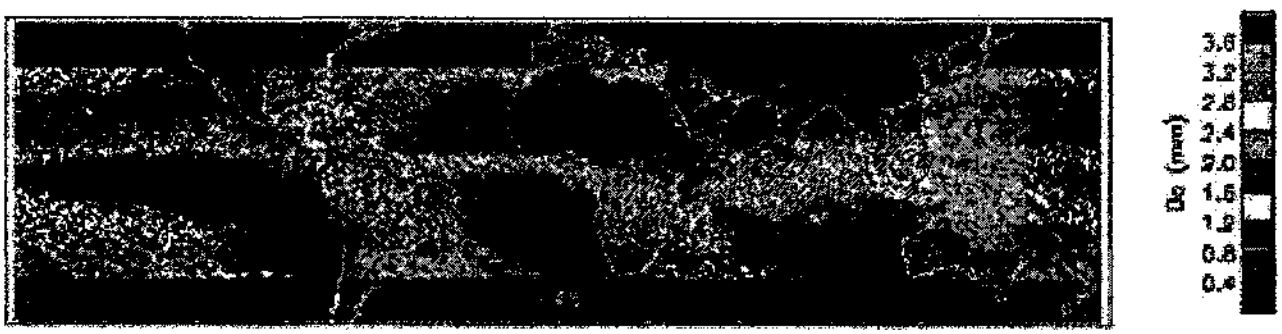

Figure 5.33: Estimated D_0 for December 2000.

The scales are adjusted to the full scale of each map. Each pixel in the plot is (0.5^o x 0.5^o) area and therefore of fairly high resolution. The overlay shows the standard map of land/ocean boundaries. The plots are restricted to the latitude of $\pm 35^o$ coinciding with the coverage of TRMM PR.

Note that these maps were generated only for α adjustment cases. However, when α adjustment is not reliable, an alternate estimate for N_w and D_0 was computed as

$$N_w = \left[\frac{\alpha_{ini}}{\tilde{\alpha}}\right]^{\frac{1}{1-\beta}} \tag{5.22}$$

The estimate provided for Equation 5.22 will be as accurate as the choice of α_{ini} for the specific storm. Table 5.3 provides an itemized list of the figures of monthly average of N_w and monthly maximum of D_0 at altitude 2 km for 2000 by using both Equations 5.7 and 5.22 for cases with α adjustment and without.

Figure Number	Title Description
Figure 5.34	Estimated N_w for January 2000
Figure 5.35	Estimated D_0 for January 2000
Figure 5.36	Percentage of α corrected for January 2000
Figure 5.37	Estimated N_w for February 2000
Figure 5.38	Estimated D_0 for February 2000
Figure 5.39	Percentage of α corrected for February 2000
Figure 5.40	Estimated N_w for March 2000
Figure 5.41	Estimated D_0 for March 2000
Figure 5.42	Percentage of α corrected for March 2000
Figure 5.43	Estimated N_w for April 2000
Figure 5.44	Estimated D_0 for April 2000
Figure 5.45	Percentage of α corrected for April 2000
Figure 5.46	Estimated N_w for May 2000
Figure 5.47	Estimated D_0 for May 2000
Figure 5.48	Percentage of α corrected for May 2000
Figure 5.49	Estimated N_w for June 2000
Figure 5.50	Estimated D_0 for June 2000
Figure 5.51	Percentage of α corrected for June 2000
Figure 5.52	Estimated N_w for July 2000
Figure 5.53	Estimated D_0 for July 2000
Figure 5.54	Percentage of α corrected for July 2000
Figure 5.55	Estimated N_w for August 2000
Figure 5.56	Estimated D_0 for August 2000
Figure 5.57	Percentage of α corrected for August 2000
Figure 5.58	Estimated N_w for September 2000
Figure 5.59	Estimated D_0 for September 2000
Figure 5.60	Percentage of α corrected for September 2000
Figure 5.61	Estimated N_w for October 2000
Figure 5.62	Estimated D_0 for October 2000
Figure 5.63	Percentage of α corrected for October 2000
Figure 5.64	Estimated N_w for November 2000
Figure 5.65	Estimated D_0 for November 2000
Figure 5.66	Percentage of α corrected for November 2000
Figure 5.67	Estimated N_w for December 2000
Figure 5.68	Estimated D_0 for December 2000
Figure 5.69	Percentage of α corrected for December 2000

Table 5.3: Figure Number List of Monthly Average N_w and Maximum D_0 for Cases with α Adjustment and Without.

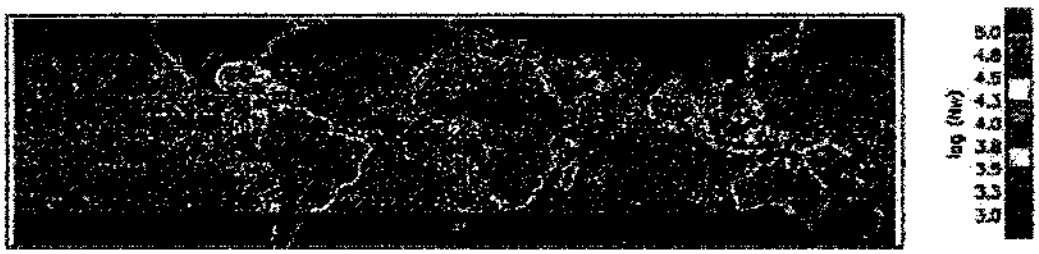

Figure 5.34: Estimated N_w for January 2000.

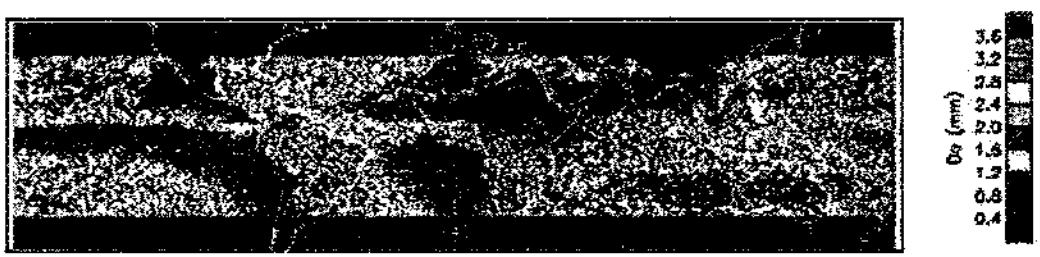

Figure 5.35: Estimated D_0 for January 2000.

Figure 5.36: Percentage of α corrected for January 2000.

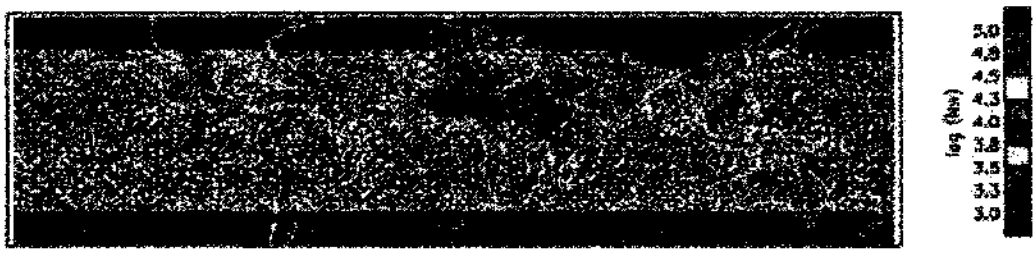

Figure 5.37: Estimated N_w for February 2000.

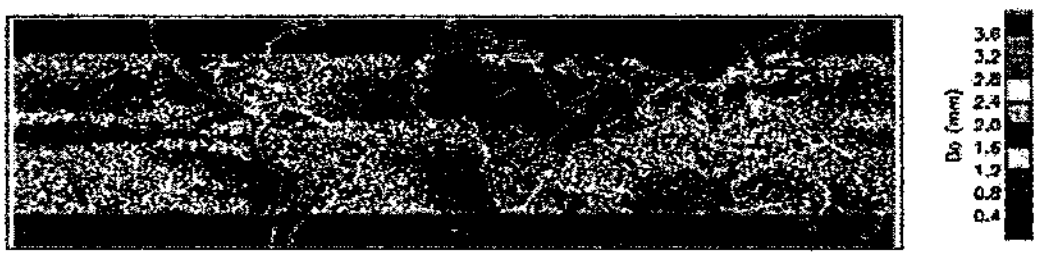

Figure 5.38: Estimated D_0 for February 2000.

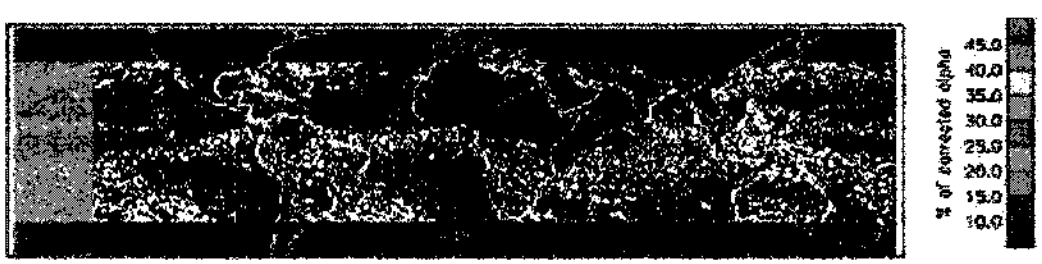

Figure 5.39: Percentage of α corrected for February 2000.

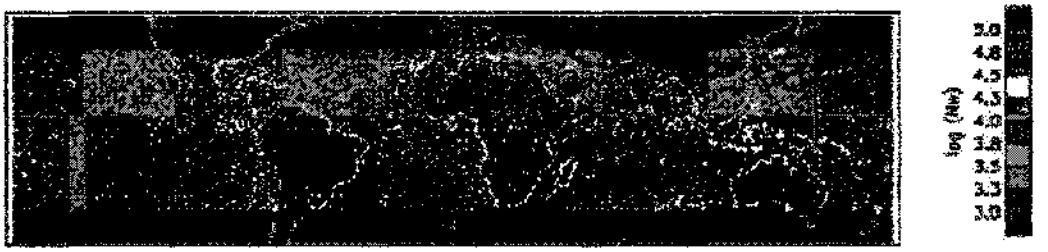

Figure 5.40: Estimated N_w for March 2000.

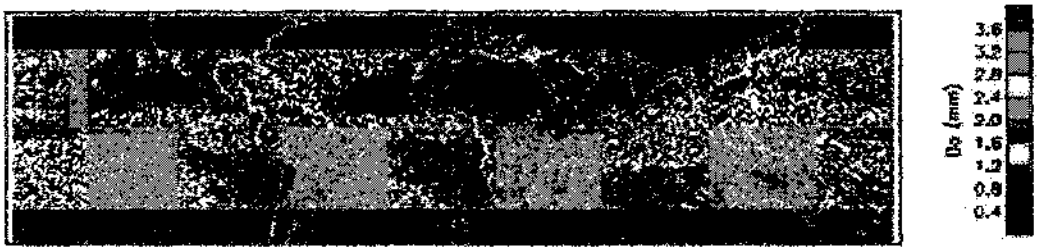

Figure 5.41: Estimated D_0 for March 2000.

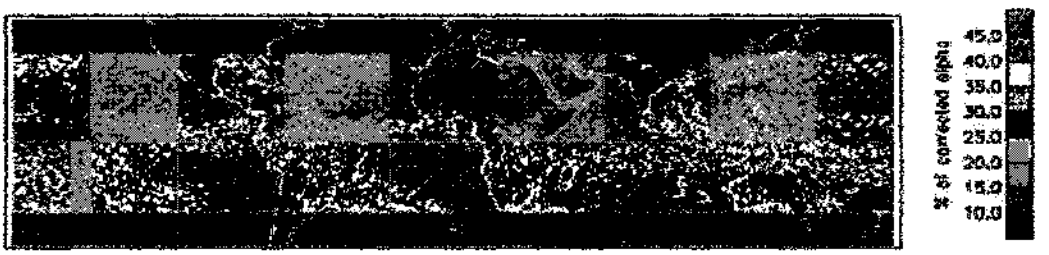

Figure 5.42: Percentage of α corrected for March 2000.

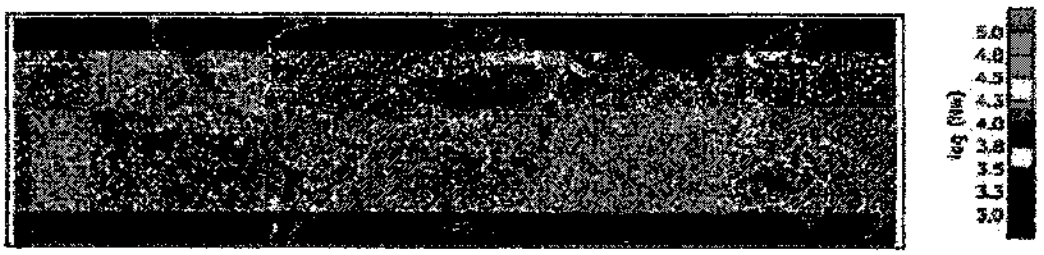

Figure 5.43: Estimated N_w for April 2000.

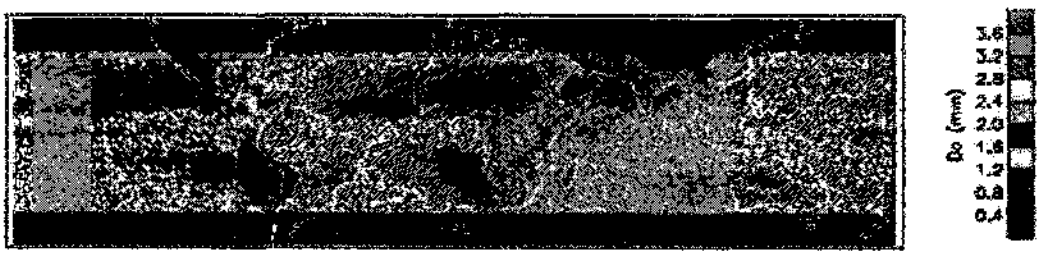

Figure 5.44: Estimated D_0 for April 2000.

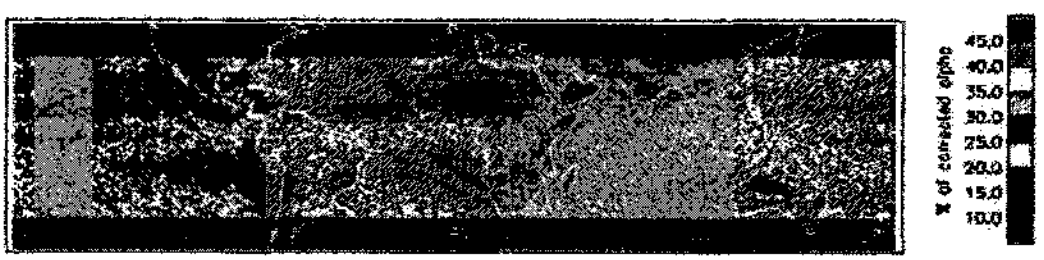

Figure 5.45: Percentage of α corrected for April 2000.

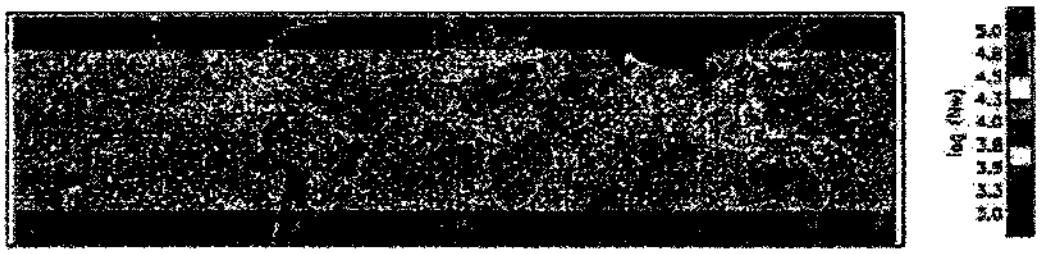

Figure 5.46: Estimated N_w for May 2000.

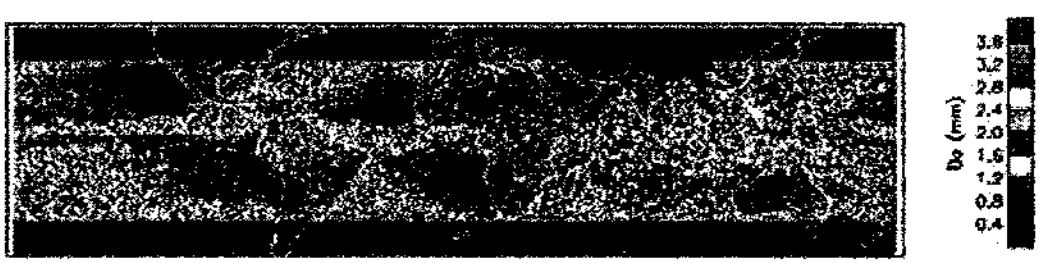

Figure 5.47: Estimated D_0 for May 2000.

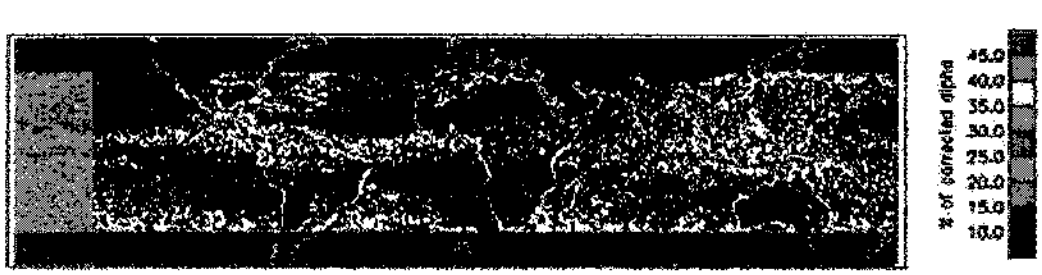

Figure 5.48: Percentage of α corrected for May 2000.

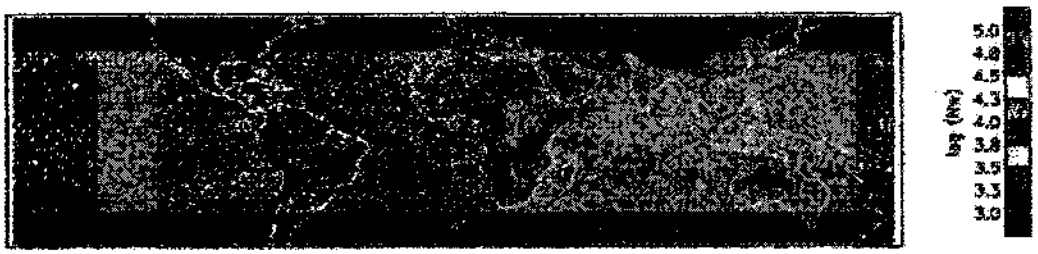

Figure 5.49: Estimated N_w for June 2000.

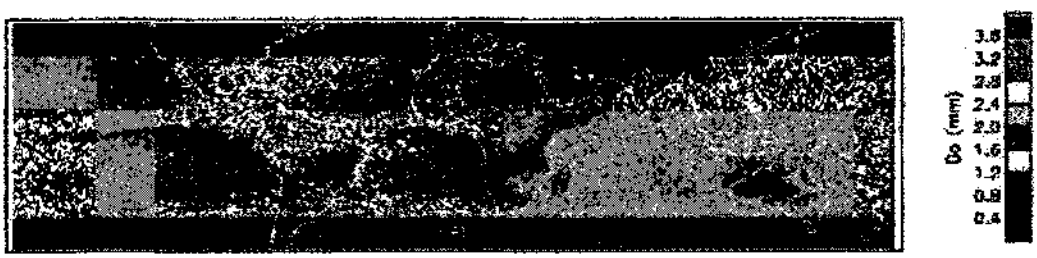

Figure 5.50: Estimated D_0 for June 2000.

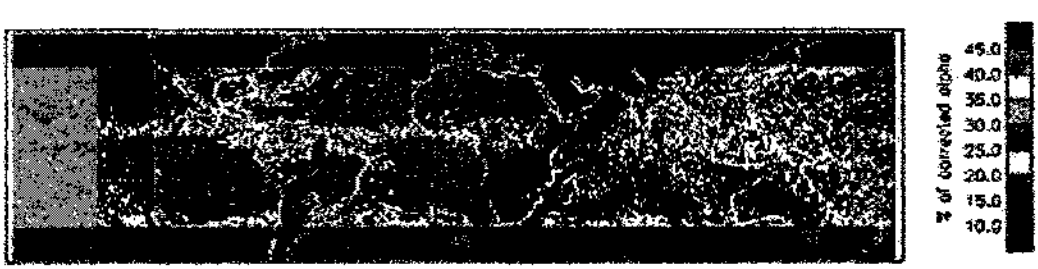

Figure 5.51: Percentage of α corrected for June 2000.

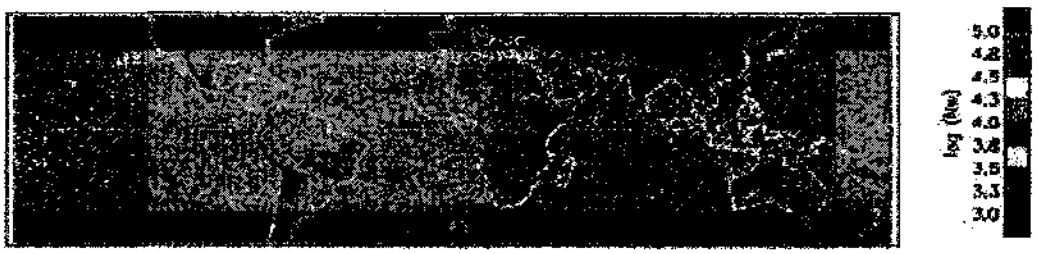

Figure 5.52: Estimated N_w for July 2000.

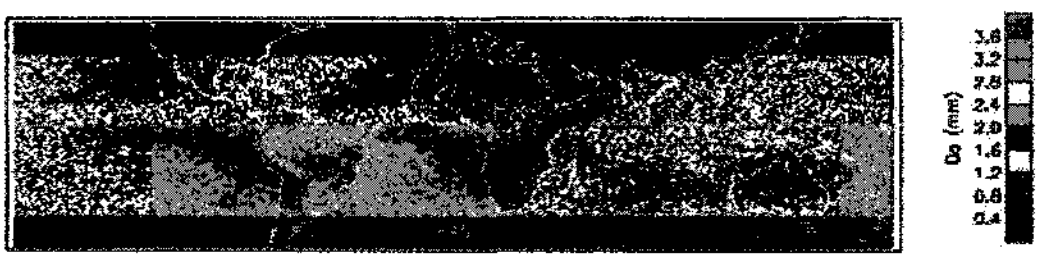

Figure 5.53: Estimated D_0 for July 2000.

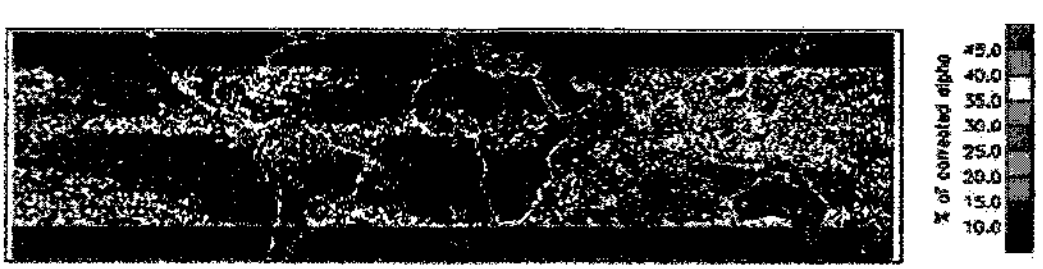

Figure 5.54: Percentage of α corrected for July 2000.

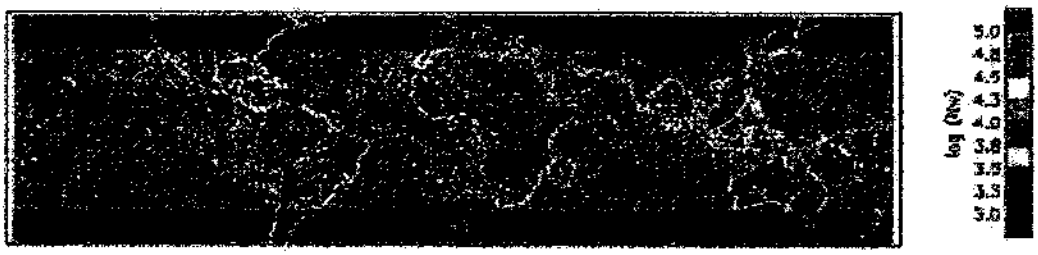

Figure 5.55: Estimated N_w for August 2000.

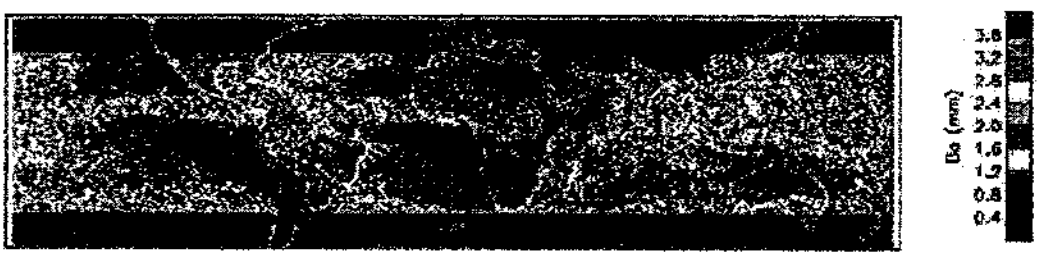

Figure 5.56: Estimated D_0 for August 2000.

Figure 5.57: Percentage of α corrected for August 2000.

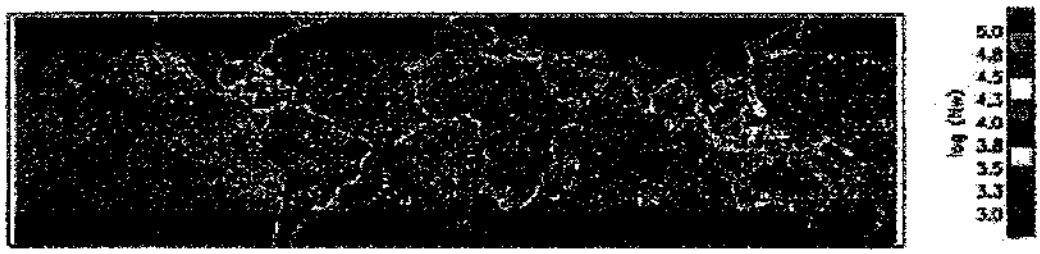

Figure 5.58: Estimated N_w for September 2000.

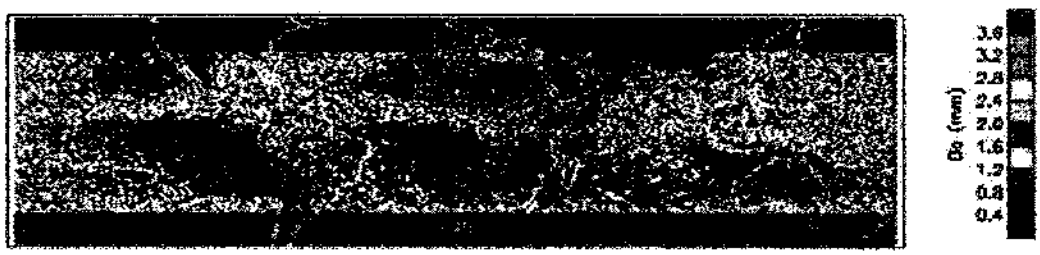

Figure 5.59: Estimated D_0 for September 2000.

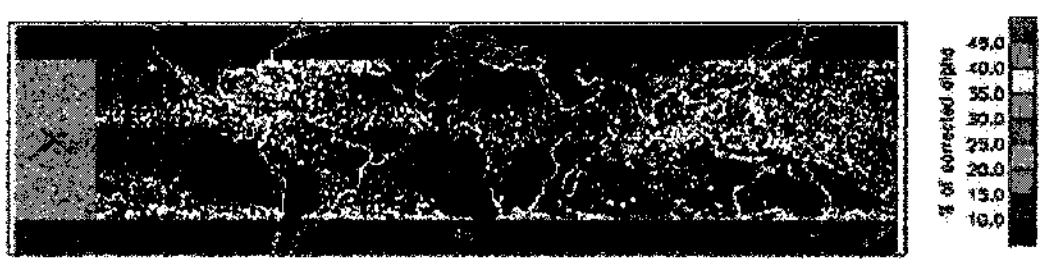

Figure 5.60: Percentage of α corrected for September 2000.

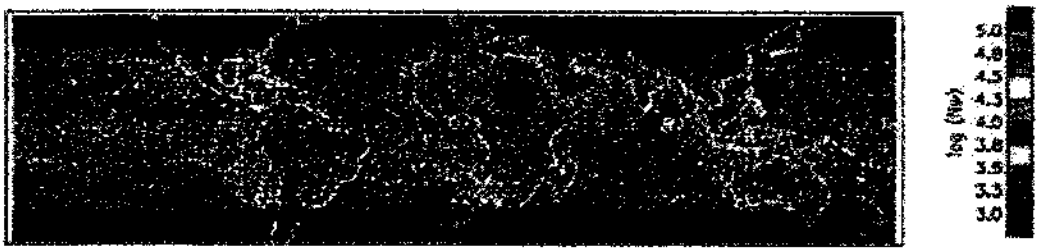

Figure 5.61: Estimated N_w for October 2000.

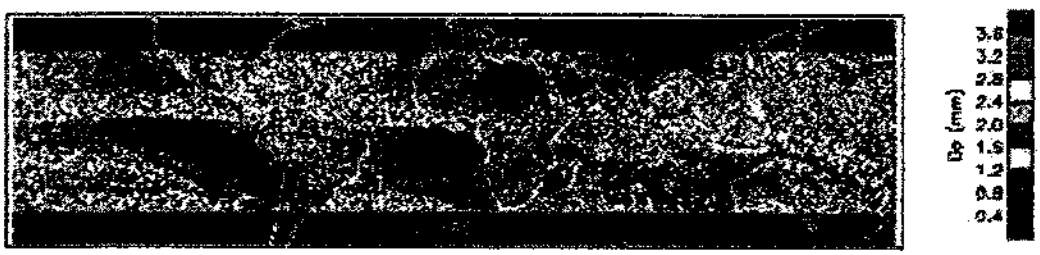

Figure 5.62: Estimated D_0 for October 2000.

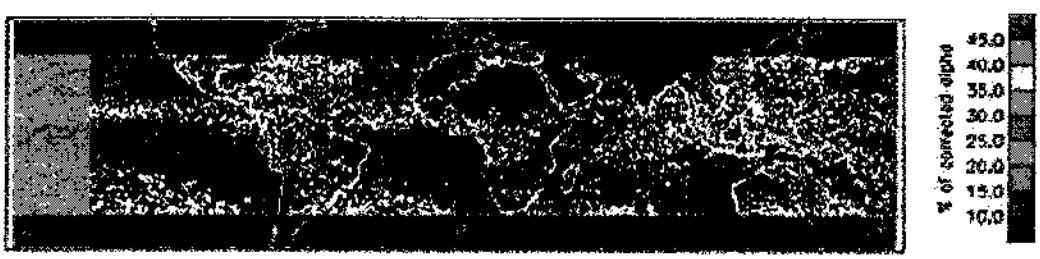

Figure 5.63: Percentage of α corrected for October 2000.

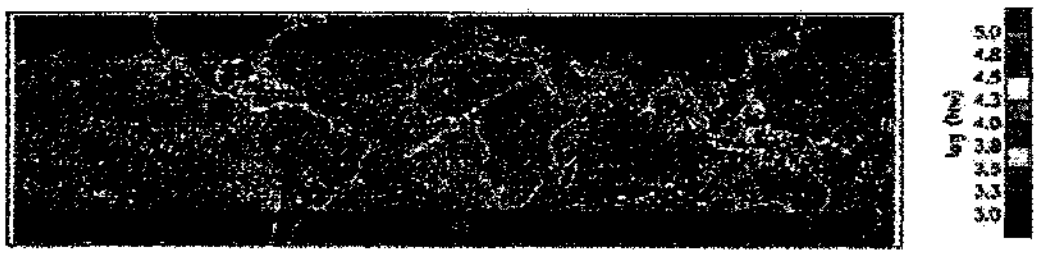

Figure 5.64: Estimated N_w for November 2000.

Figure 5.65: Estimated D_0 for November 2000.

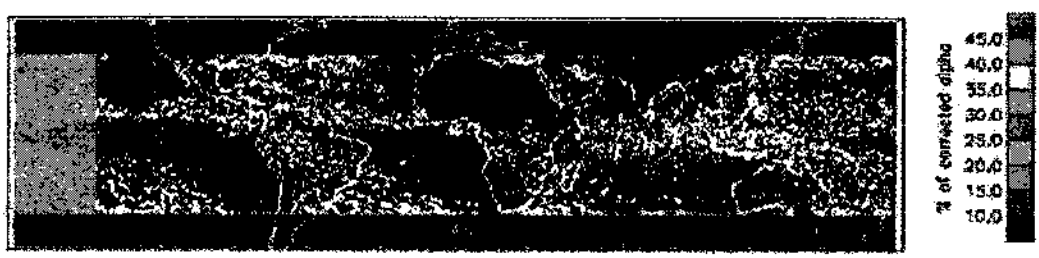

Figure 5.66: Percentage of α corrected for November 2000.

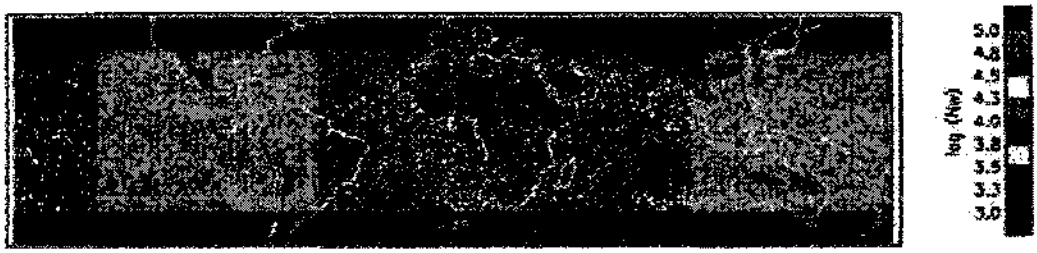

Figure 5.67: Estimated N_w for December 2000.

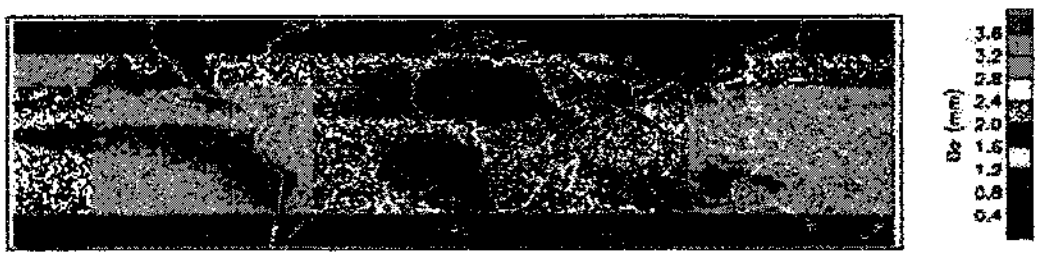

Figure 5.68: Estimated D_0 for December 2000.

Figure 5.69: Percentage of α corrected for December 2000.

5.6 Area Analysis

The algorithm, which was developed in this chapter, was used to estimate the RSD parameters for six different places for July 2000. Table 5.4 shows an itemized list of the location of these places, the scatter plots of D_0 versus N_w, and the histograms of D_0 and the N_w. Note that the analysis for each case was done within 300 km by using data from July 2000.

Figure Number	Title Description
Figure 5.70	Locations of case studies
Figure 5.71	Scatter plot of D_0 vs. N_w for case 1, only with α adjustment
Figure 5.72	Scatter plot of D_0 vs. N_w for case 1, with and without α adjustment
Figure 5.73	Histograms of D_0 and N_w for case 1, only with α adjustment
Figure 5.74	Histograms of D_0 and N_w for case 1, with and without α adjustment
Figure 5.75	Scatter plot of D_0 vs. N_w for case 2, only with α adjustment
Figure 5.76	Scatter plot of D_0 vs. N_w for case 2, with and without α adjustment
Figure 5.77	Histograms of D_0 and N_w for case 2, only with α adjustment
Figure 5.78	Histograms of D_0 and N_w for case 2, with and without α adjustment
Figure 5.79	Scatter plot of D_0 vs. N_w for case 3, only with α adjustment
Figure 5.80	Scatter plot of D_0 vs. N_w for case 3, with and without α adjustment
Figure 5.81	Histograms of D_0 and N_w for case 3, only with α adjustment
Figure 5.82	Histograms of D_0 and N_w for case 3, with and without α adjustment
Figure 5.83	Scatter plot of D_0 vs. N_w for case 4, only with α adjustment
Figure 5.84	Scatter plot of D_0 vs. N_w for case 4, with and without α adjustment
Figure 5.85	Histograms of D_0 and N_w for case 4, only with α adjustment
Figure 5.86	Histograms of D_0 and N_w for case 4, with and without α adjustment
Figure 5.87	Scatter plot of D_0 vs. N_w for case 5, only with α adjustment
Figure 5.88	Scatter plot of D_0 vs. N_w for case 5, with and without α adjustment
Figure 5.89	Histograms of D_0 and N_w for case 5, only with α adjustment
Figure 5.90	Histograms of D_0 and N_w for case 5, with and without α adjustment
Figure 5.91	Scatter plot of D_0 vs. N_w for case 6, only with α adjustment
Figure 5.92	Scatter plot of D_0 vs. N_w for case 6, with and without α adjustment
Figure 5.93	Histograms of D_0 and N_w for case 6, only with α adjustment
Figure 5.94	Histograms of D_0 and N_w for case 6, with and without α adjustment

Table 5.4: Figure Number List of Area Analysis of RSD.

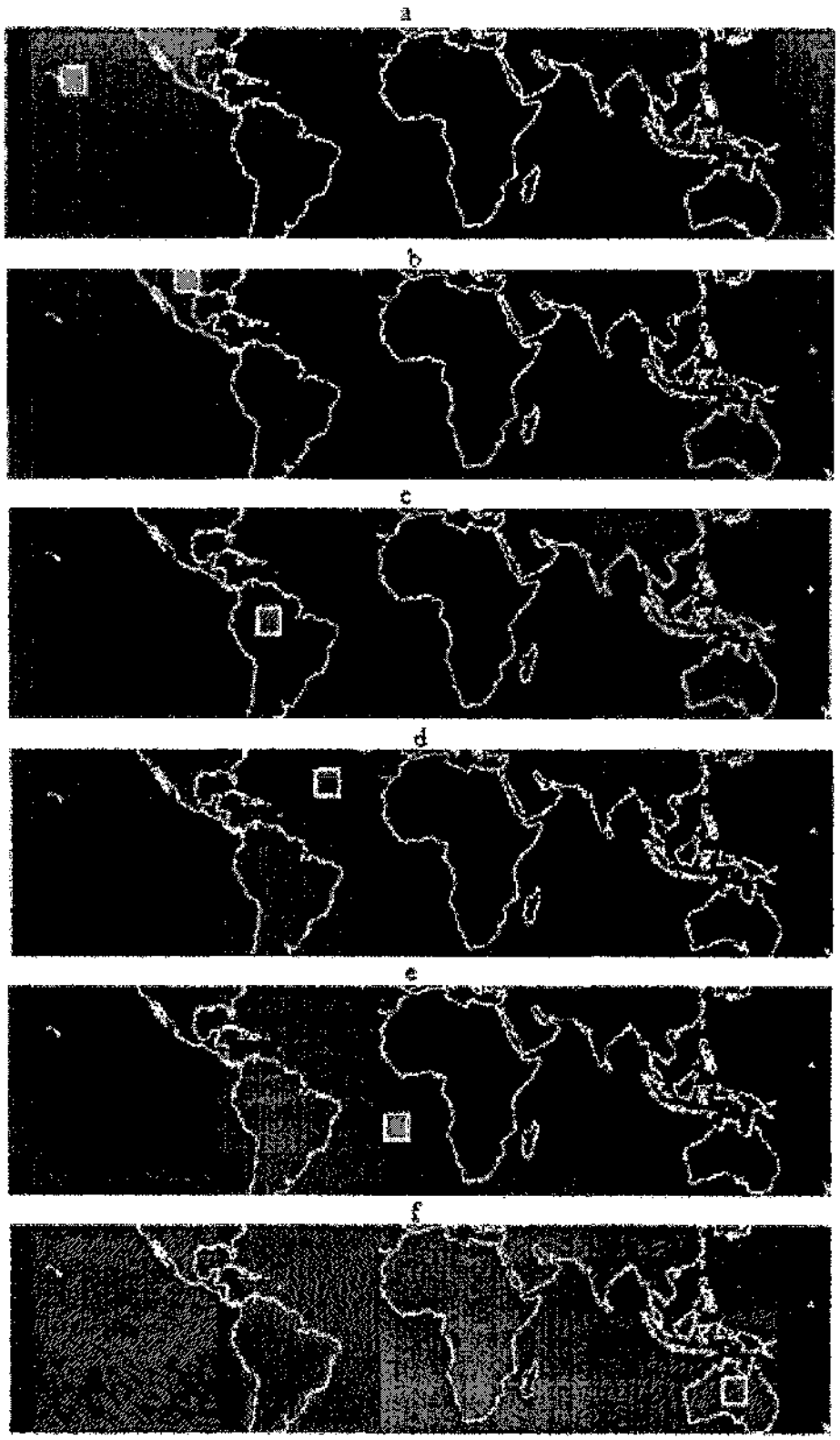

Figure 5.70: Location of case studies: a) Pacific Ocean, b) North America, c) South America, d)North Atlantic Ocean, e) South Atlantic Ocean and f)Australia.

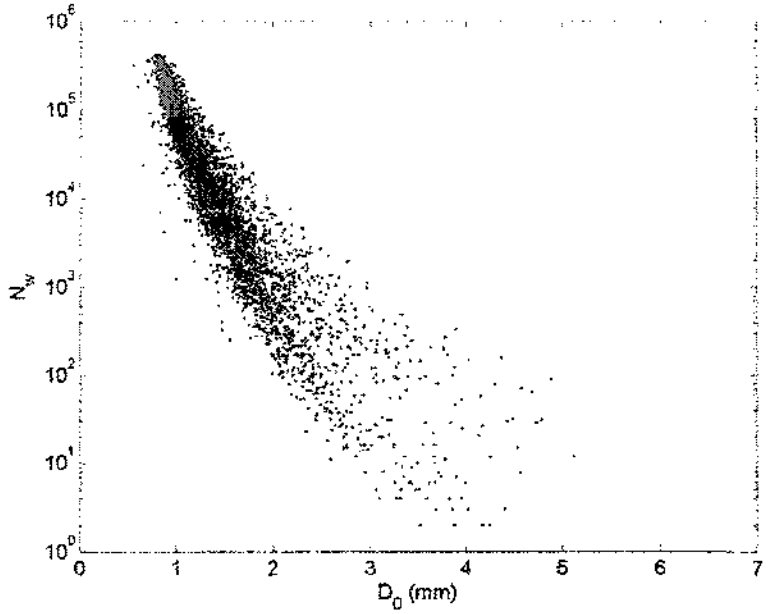

Figure 5.71: Scatter plot of D_0 vs. N_w for case 1, only with α adjustment.

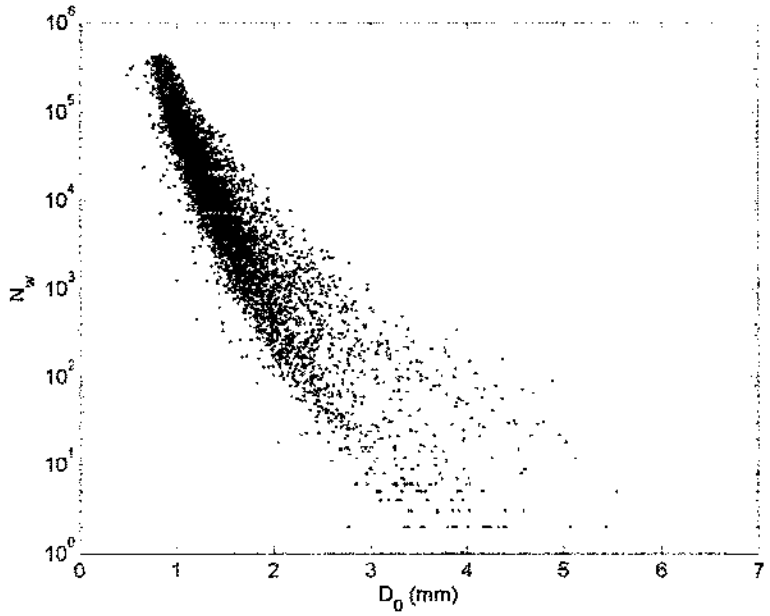

Figure 5.72: Scatter plot of D_0 vs. N_w for case 1, with and without α adjustment.

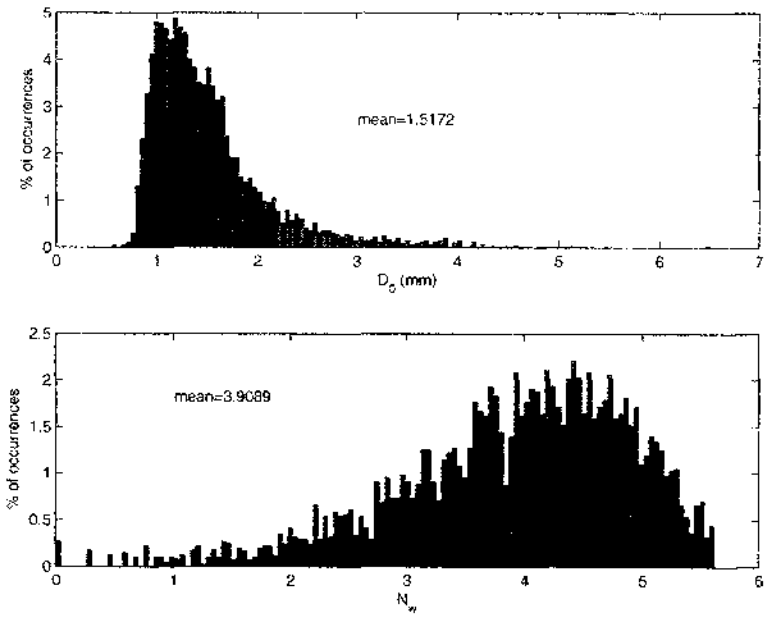

Figure 5.73: Histograms of D_0 and N_w for case 1, only with α adjustment.

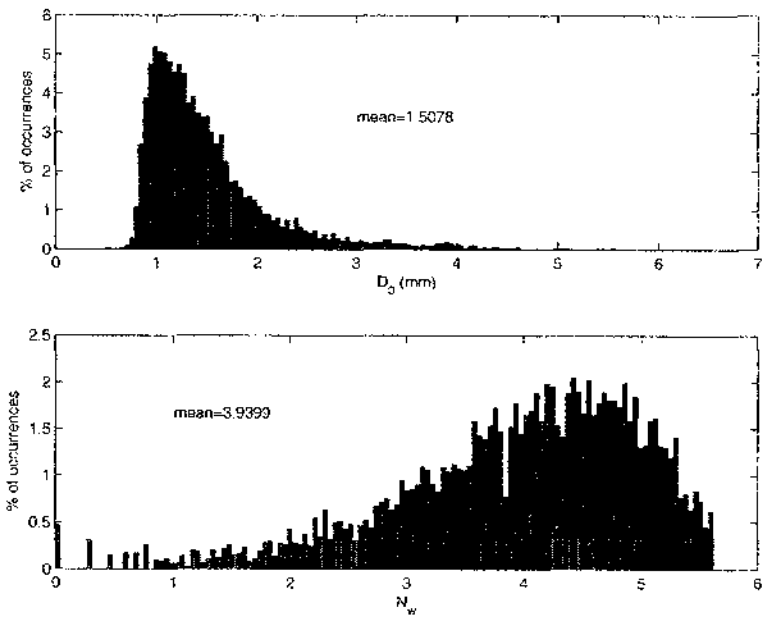

Figure 5.74: Histograms of D_0 and N_w for case 1, with and without α adjustment.

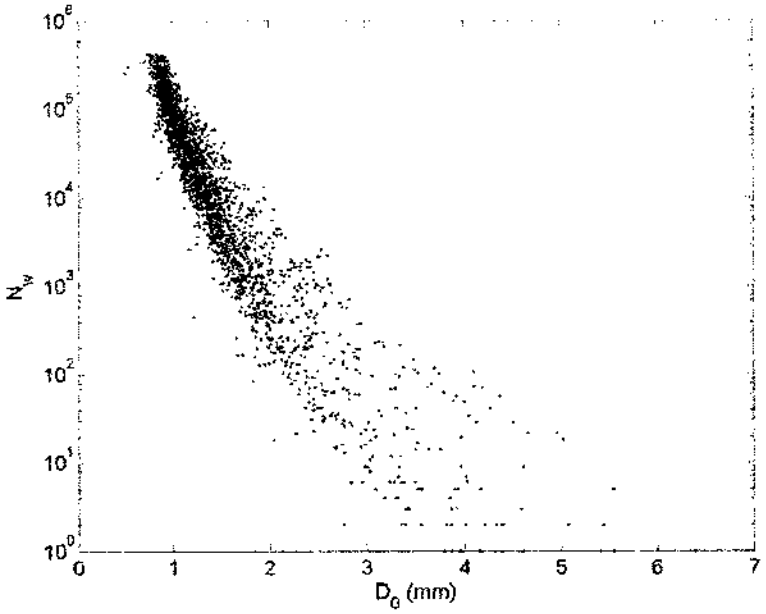

Figure 5.75: Scatter plot of D_0 vs. N_w for case 2, only with α adjustment.

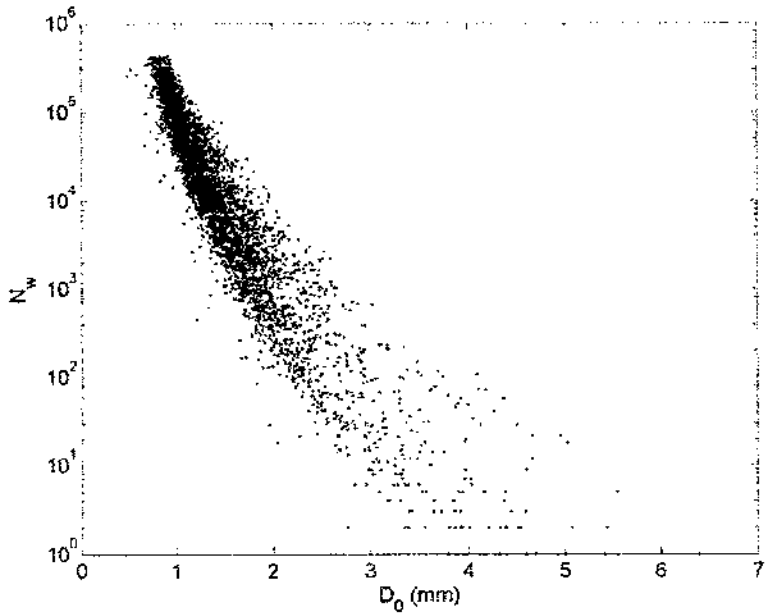

Figure 5.76: Scatter plot of D_0 vs. N_w for case 2, with and without α adjustment.

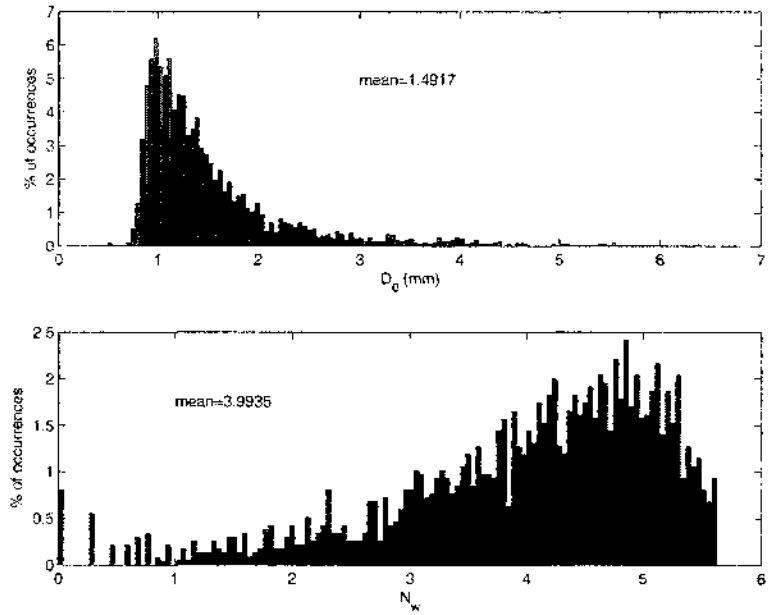

Figure 5.77: Histograms of D_0 and N_w for case 2, only with α adjustment.

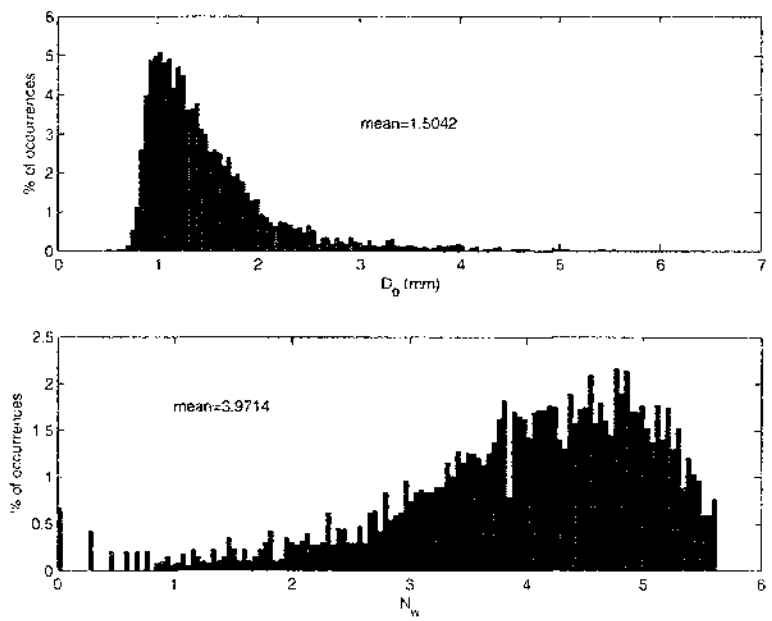

Figure 5.78: Histograms of D_0 and N_w for case 2, with and without α adjustment.

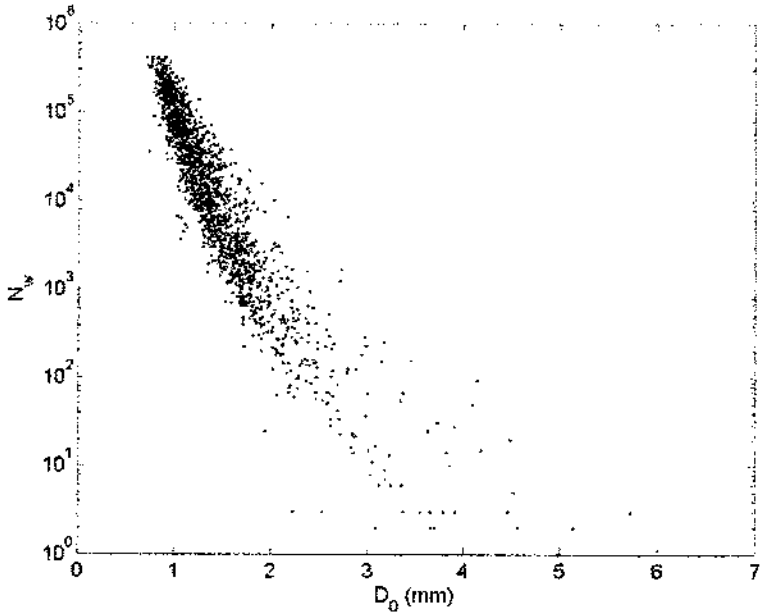

Figure 5.79: Scatter plot of D_0 vs. N_w for case 3, only with α adjustment.

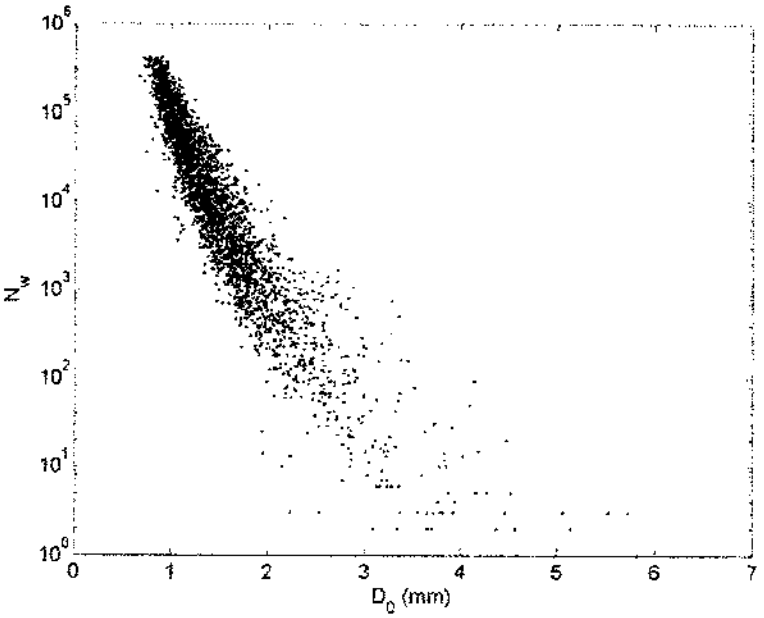

Figure 5.80: Scatter plot of D_0 vs. N_w for case 3, with and without α adjustment.

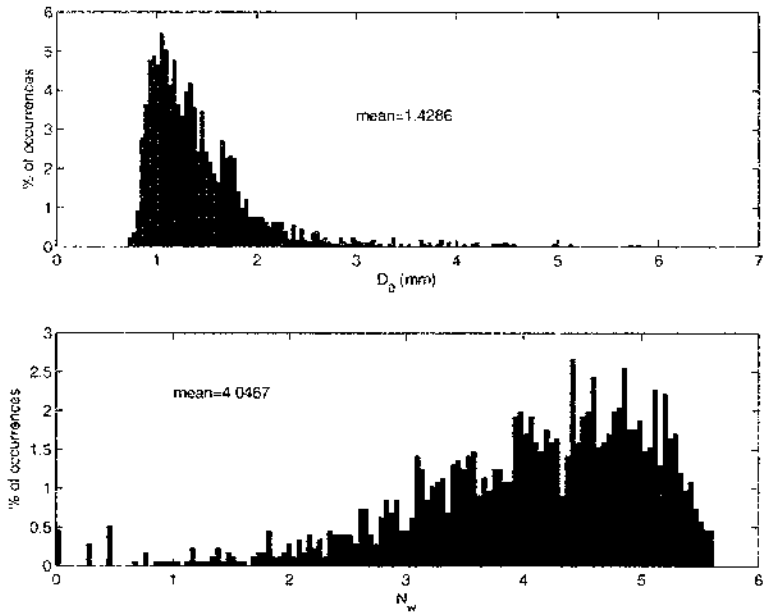

Figure 5.81: Histograms of D_0 and N_w for case 3, only with α adjustment.

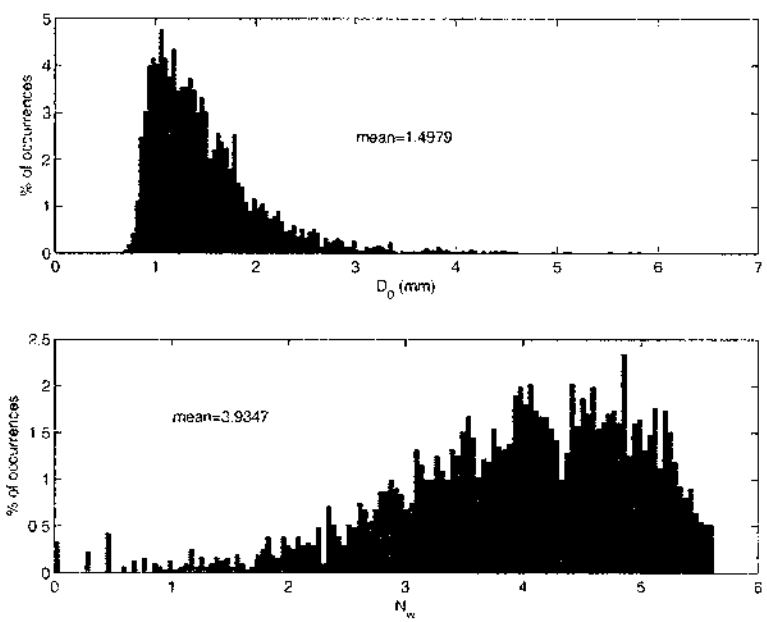

Figure 5.82: Histograms of D_0 and N_w for case 3, with and without α adjustment.

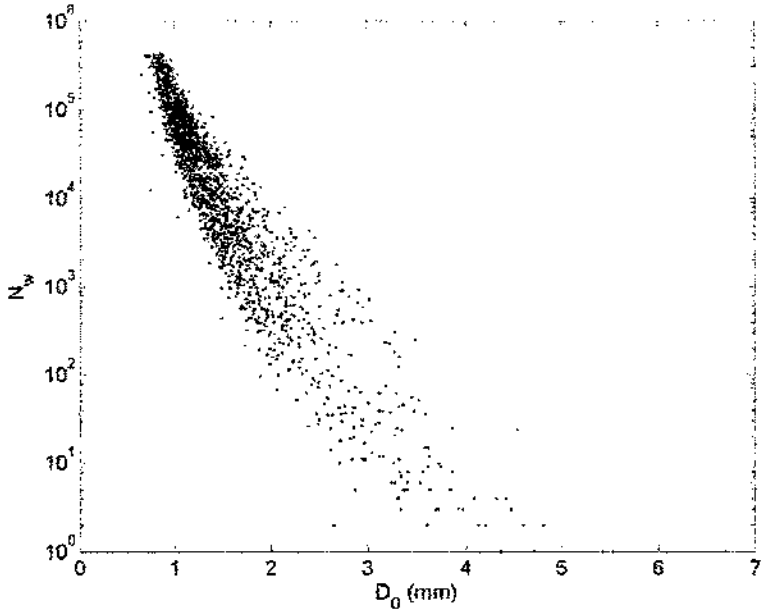

Figure 5.83: Scatter Plot of D_0 vs. N_w for case 4, only with α adjustment.

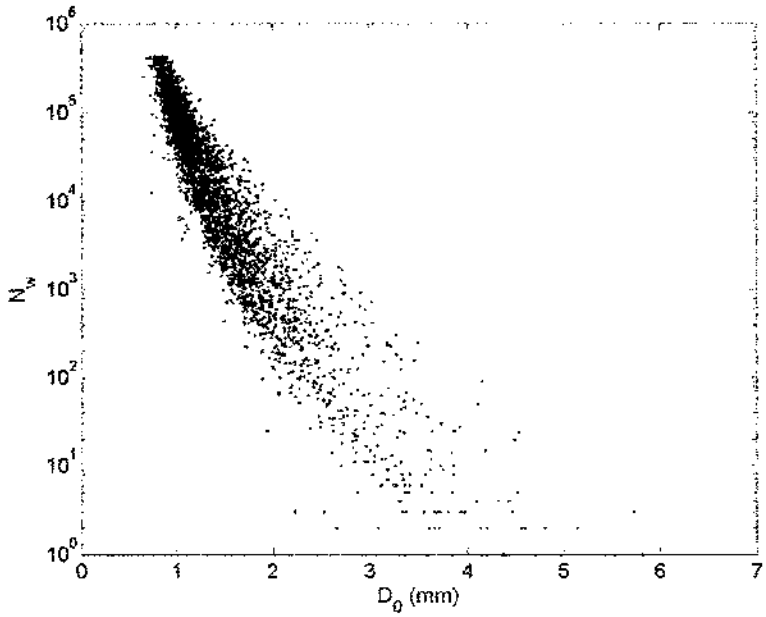

Figure 5.84: Scatter plot of D_0 vs. N_w for case 4, with and without α adjustment.

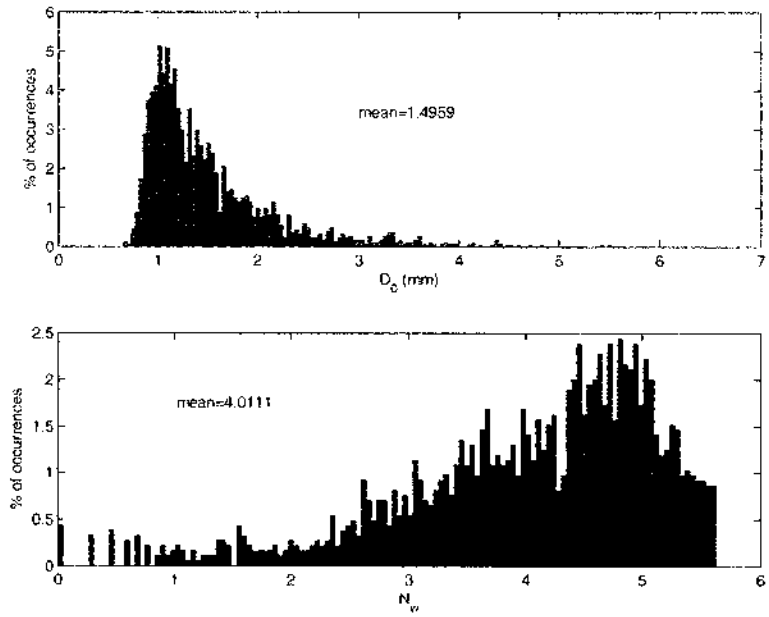

Figure 5.85: Histograms of D_0 and N_w for case 4, only with α adjustment.

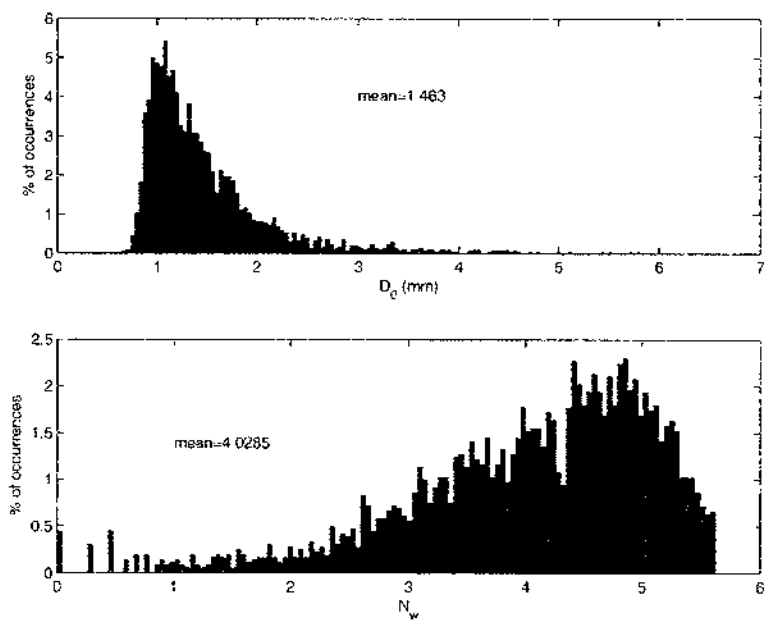

Figure 5.86: Histograms of D_0 and N_w for case 4, with and without α adjustment.

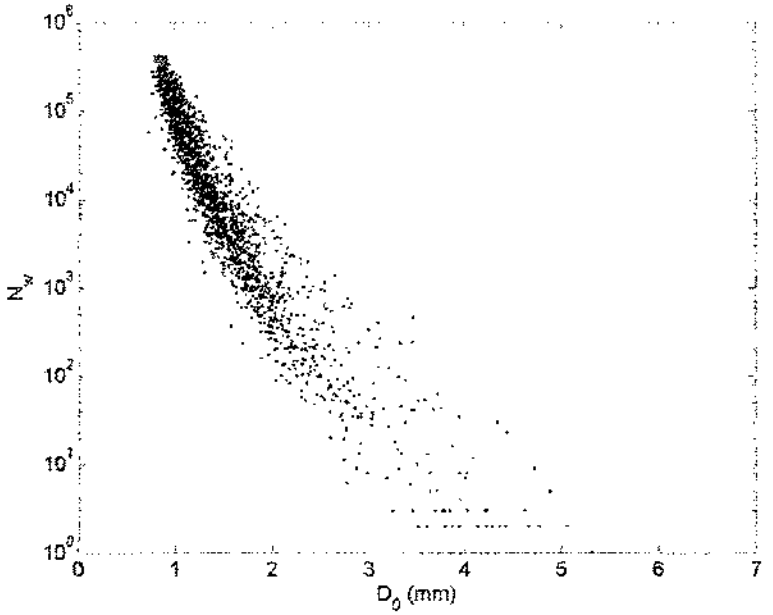

Figure 5.87: Scatter Plot of D_0 vs. N_w for case 5, only with α adjustment.

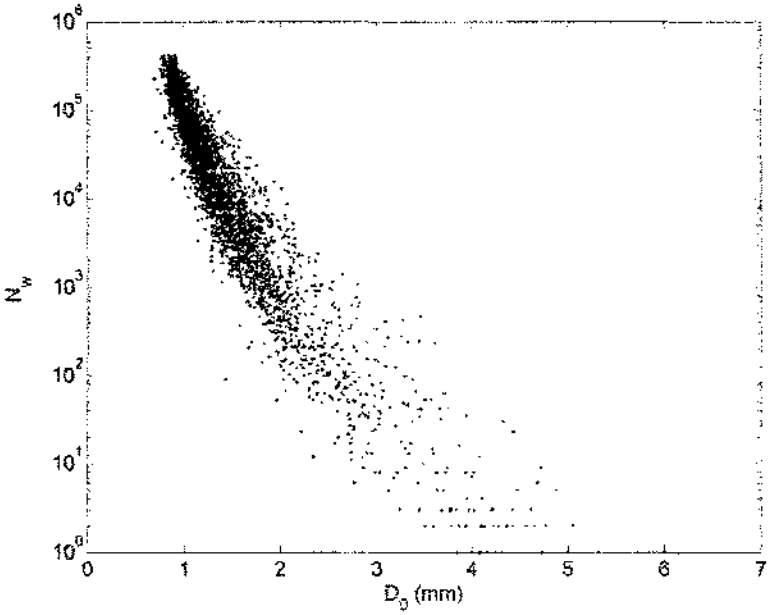

Figure 5.88: Scatter plot of D_0 vs. N_w for case 5, with and without α adjustment.

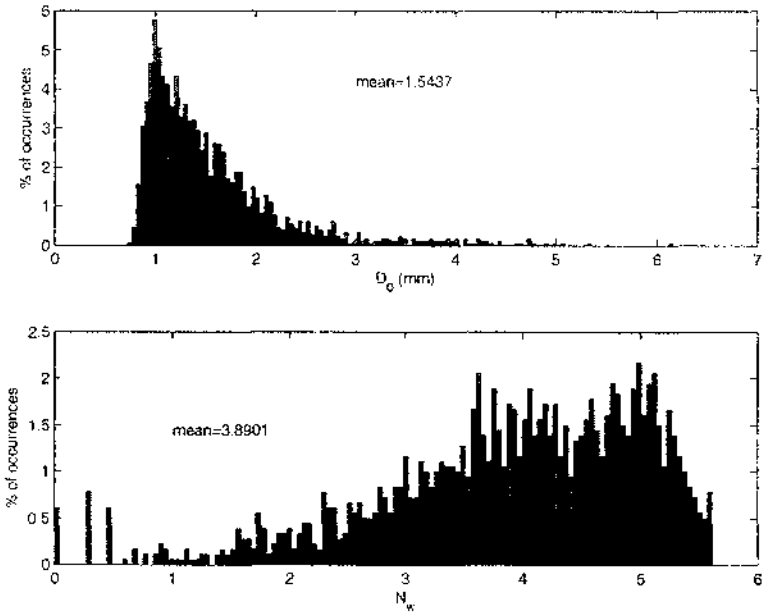

Figure 5.89: Histograms of D_0 and N_w for case 5, only with α adjustment.

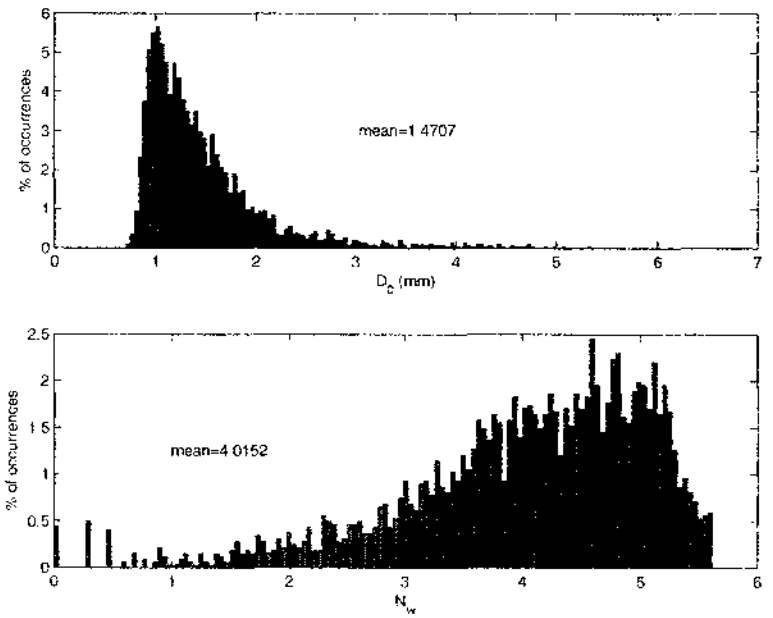

Figure 5.90: Histograms of D_0 and N_w for case 5, with and without α adjustment.

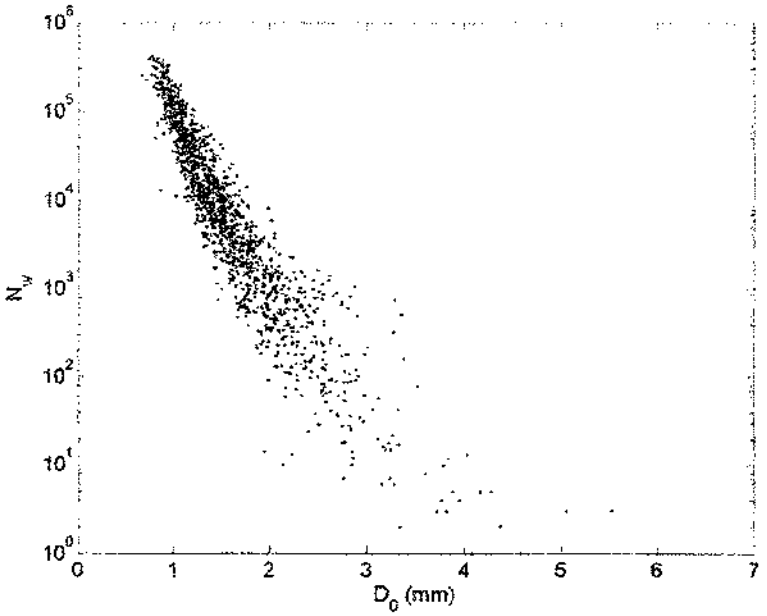

Figure 5.91: Scatter Plot of D_0 vs. N_w for case 6, only with α adjustment.

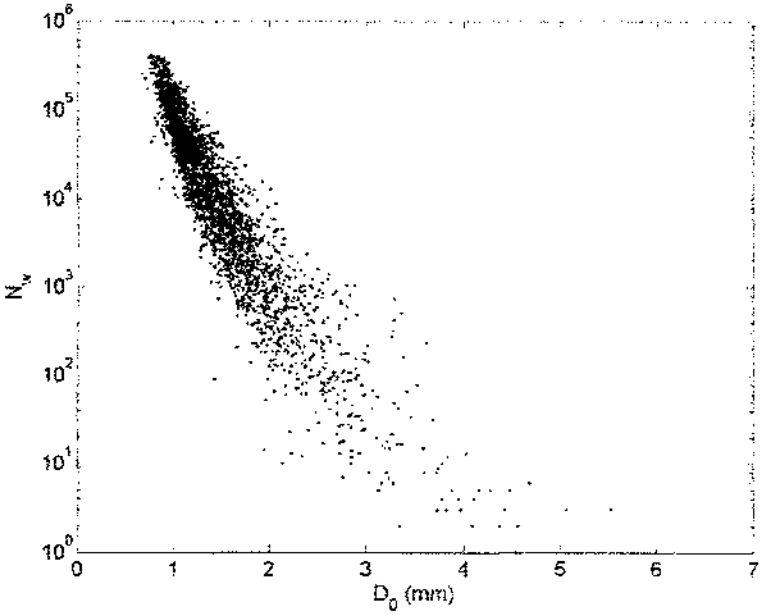

Figure 5.92: Scatter plot of D_0 vs. N_w for case 6, with and without α adjustment.

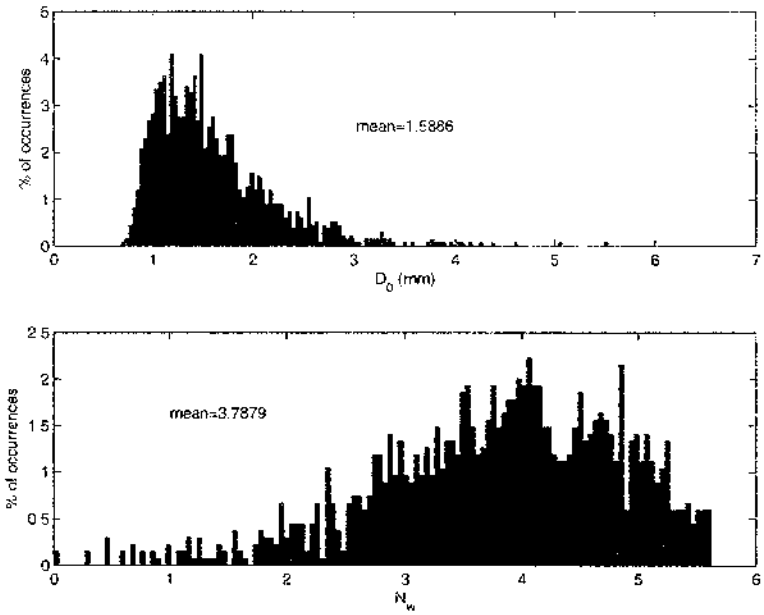

Figure 5.93: Histograms of D_0 and N_w for case 6, only with α adjustment.

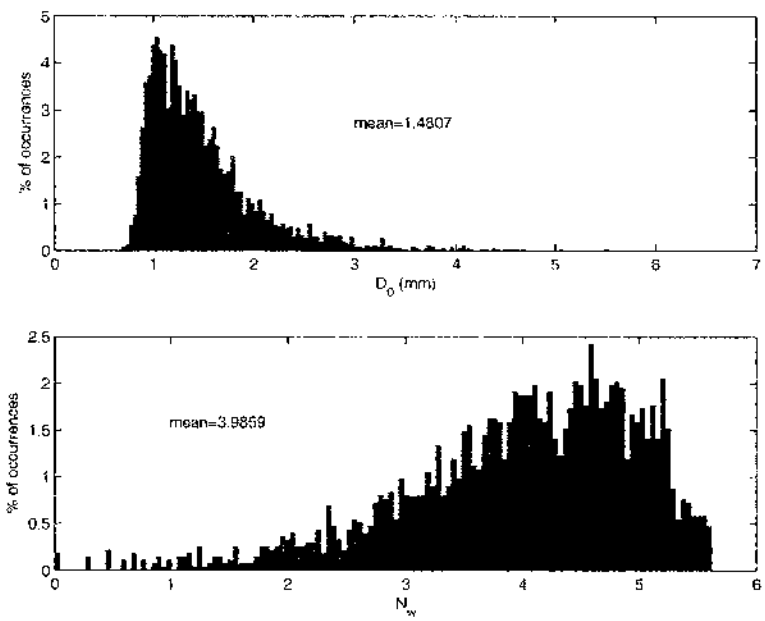

Figure 5.94: Histograms of D_0 and N_w for case 6, with and without α adjustment.

Chapter 6

EXAMINATION OF SURFACE CROSS SECTION STATISTICS OVER OCEAN AND LAND

6.1 Introduction

Weather radars that operate at frequencies higher than about 5 GHz can be affected adversely by rain attenuation. However, for spaceborne applications, where the size and mass of the antenna are limited, adequate spatial resolution can be obtained only by increasing the frequency. For the Tropical Rainfall Measuring Mission (TRMM) precipitation radar (PR), the use of 13.8-GHz radar frequency with a 2-m antenna size represents a compromise between the desire to minimize the antenna size and rain attenuation and maximize the spatial resolution. As demonstrated by Hitschfeld and Bordan (1954) in their classic study, estimates of rain rate from a single-attenuating wavelength radar are unstable when the path attenuation is large, unless the radar constant and the drop size distribution are known to a high degree of accuracy. Because these conditions are seldom met, an alternative strategy is needed to complement the Hitschfeld-Bordan method for moderate and high rain rates. One of the proposed ways of estimating attenuation is the surface reference technique (SRT).

In this chapter, the data from TRMM PR is used to study the statistical characteristics of the surface return (σ^0) as a function of the surface type (ocean/land) and incident angles during rain and rain-free times. Note that this work is further extended to the preliminary studies of Meneghini et al. (2000).

6.2 Background

Airborne meteorological radars typically operate at attenuating wavelengths. Correction for attenuation along the propagation path, therefore, is required to retrieve a reflectivity factor for accurate estimation of the rainfall rate. The surface reference technique (SRT) to correct the observed reflectivity for the effects of attenuation has been developed for down-looking radars (Meneghini et al.,1983). The SRT algorithm uses the radar cross section of the ocean surface as a means of estimating the path integrated attenuation. In the SRT, an initial value is determined for the radar cross section of a rain-free area in relatively close proximity to the rain cloud. During subsequent observations of precipitation, any decrease in the observed surface cross section from the reference value is assumed to be a result of the two-way attenuation along the propagation path (PIA). The PIA for each beam is then used as a limiting condition in an attenuation correction algorithm (Iguchi and Meneghini, 1994). A number of studies have evaluated the SRT with airborne radar observations (Meneghini et. al, 1992). In these studies, the SRT has been used on observations at a variety of incidence angles acquired during flights over the ocean. Development of the SRT has focused on cases over water because the ocean surface presents a well-known, and relatively constant, microwave reflection. In addition to airborne applications, the SRT is used for processing the reflectivity profiles from the spaceborne precipitation radar launched in 1998 on the Tropical Rainfall Measuring Mission (TRMM). The SRT has been developed over a number of years and extensively tested by airborne weather radar data (Durden and Haddad 1998; Fujita 1983; Iguchi and Meneghini 1994; Iguchi et al. 2000; Kozu and Nakamura 1991; Marecal et al. 1997; Marzoug and Amayenc 1994; Meneghini et al. 1983, 1992).

6.3 Surface Cross Section

The key parameter in the surface reference techniques (SRT) is the normalized surface scattering cross section, σ^0. This can be defined in terms of the surface return power P_s and the radar range to the surface r_s by the equation:

$$P_s = \left(C_s \sigma^0 r_s^{-2}\right) exp\left[-0.2 ln 10 \int_0^{r_s} k ds\right] \tag{6.1}$$

where in general, C_s is a function of the radar parameters, the range, and the incident angle (Meneghini and Kozu, 1990). The last term in Equation 6.1 represents the two-way path attenuation from the radar to the surface and k is the specific attenuation ($dB\ km^{-1}$) due to atmospheric gases, clouds, and precipitation.

As mentioned above, SRT estimates the PIA through rain from the decrease in the surface return. In particular, an estimate of the attenuation factor at $r = r_s$ is obtained from a ratio of the surface return power measured in rain to that measured in adjacent rain-free areas:

$$\hat{A}(r_s) = \frac{P_r\left(r_s; rain\right)}{P_r\left(r_s; no\ rain\right)} \tag{6.2}$$

In the presence of rain, the apparent normalized radar cross section (NRCS) of the surface (dB), $\sigma^0(R, \theta)$, is related to the NRCS that would exist in the absence of rain, $\sigma^0(NR, \theta)$, by:

$$\sigma^0(R, \theta) = \sigma^0(NR, \theta) - A + \epsilon \tag{6.3}$$

where the parameter ϵ is used to represent the change in the surface cross section caused by rain on the surface. The two-way path attenuation, A, is related to the specific attenuation, $k(dB\,km^{-1})$, and the extinction cross section, σ_{ext}, of the scatters by:

$$\begin{aligned} A &= 2\int k(s)ds \\ &= \int\int \sigma_{ext}(\lambda, D)N(D, s)dD\,ds \end{aligned} \tag{6.4}$$

where the integral over the slant range "s" runs from the radar to the surface, $N(D)$) is the drop size distribution, and D is the equivolume diameter.

Because the quantity $\sigma^0(NR, \theta)$ in Equation 6.3 is not measurable, it is replaced by a reference value, $\langle\sigma^0(NR, \theta)\rangle$, which leads to the attenuation estimate, $\hat{A}(r_s)$:

$$\hat{A}(r_s) = \left\langle\sigma^0(NR, \theta)\right\rangle - \sigma^0(R, \theta) \tag{6.5}$$

The only requirement made on the reference estimate $\langle\sigma^0(NR, \theta)\rangle$ is that it be obtained from an average over a rain-free area.

6.4 Data Analysis: σ^0 Over Ocean

The SRT is expected to work well with negligible error when the rain attenuation is much larger than the inherent variability of the NRCS of the surface (Meneghini et al., 2000). However, because NRCS varies with surface type, and incident angle, the characterization of σ^0 is not simple. In this section, data from

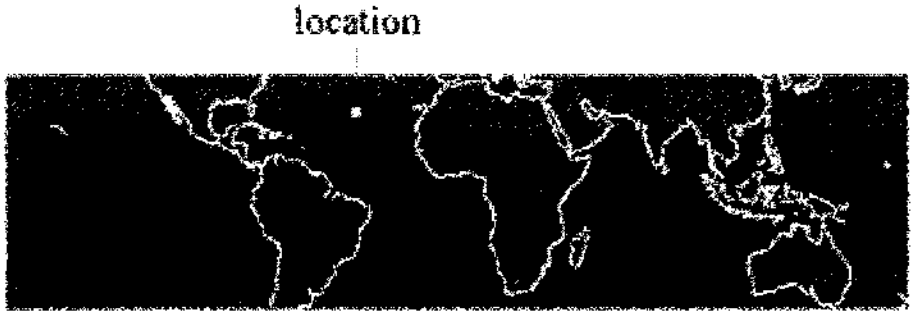

Figure 6.1: Location of case study 1: Atlantic Ocean, 25°N to 27°N and −41°E to −39°E .

the Tropical Rainfall Measuring Mission (TRMM) Precipitation Radar (PR) 2A21 are used to develop statistics of σ^0 over the ocean during the rain and in the absence of the rain.

6.4.1 Case Study 1: Area Analysis

In this case study, a 2^o area over the Atlantic Ocean was selected as an example of σ^0 over ocean during rain and rain free time. Figure 6.1 shows the location of this case study. The square box in Figure 6.1 represents 25°N to 27°N and −41°E to −39°E where the location that corresponds to the midpoint of this area is 26°N and −40°E. Tables 6.1 and 6.2 show the summary of data that was used in this case study for rain and rain-free cases, respectively.

Figures 6.2 and 6.3 show the histogram of σ^0 at nadir for a 2^o area over the Atlantic Ocean during rain and rain-free time, respectively. It is clear from these figures that the mean value of σ^0 for this specific location is 11.4 dB in the case of rain, while it is 12.24 dB for the rain-free case (there is $\approx$1 dB difference in σ^0 between rain and rain-free time). Also the standard deviation of σ^0 in the rain-free case is more stable compared to rain time (standard deviation of σ^0 for rain-free is 0.8877 dB while for rain is 1.4 dB).

Date	Orbit Number	Scan Number	R (mm/hr)
02/02/1999	6812	3569-3626	12
04/14/1999	7927	5582-5645	10.5
11/24/1999	11458	3506-3570	11
01/11/2000	12218	5545-5608	2.5
01/15/2000	12276	3487-3551	3.5
03/18/2000	13264	3550-3610	6.5
03/03/2001	18790	3575-3632	5
10/28/2001	22543	3538-3602	11
11/19/2001	22894	3573-3637	8

Table 6.1: Summary of Data Used in Case Study 1 for Rain Cases.

Date	Orbit Number	Scan Number
01/18/1999	6565	3544-3607
03/14/1999	7433	5548-5611
05/10/1999	8340	3517-3579
01/17/2000	12307	3553-3613
01/27/2000	12465	5560-5623
02/25/2000	12928	5527-5586
02/25/2001	18701	5561-5624
03/13/2001	18948	5576-5640
04/11/2001	19411	5541-5604

Table 6.2: Summary of Data Used in Case Study 1 for Rain-Free Cases.

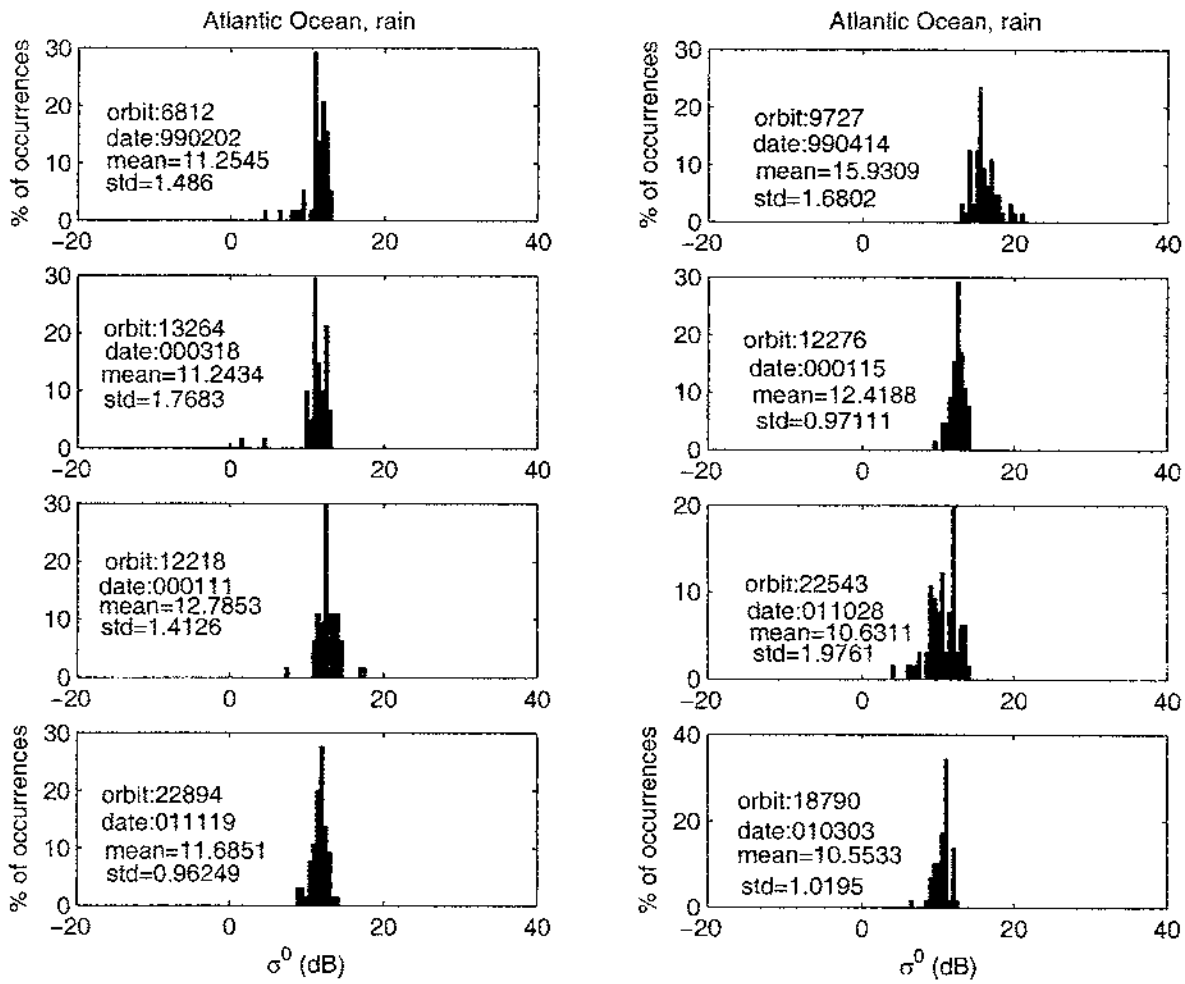

Figure 6.2: Histogram of σ^0 at nadir for the Atlantic Ocean 2° area: rain cases.

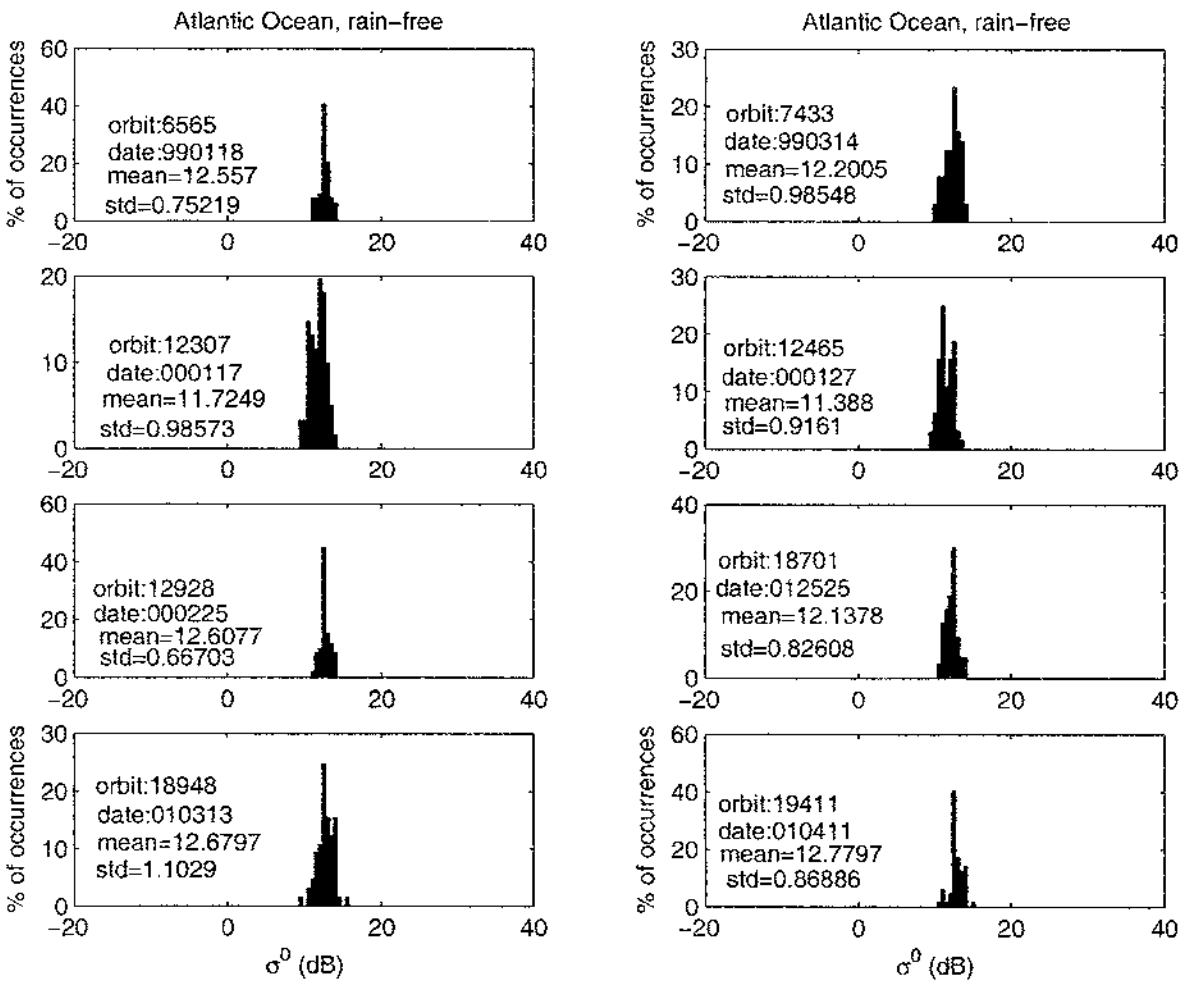

Figure 6.3: Histogram of σ^0 at nadir for the Atlantic Ocean 2^o area: rain-free cases.

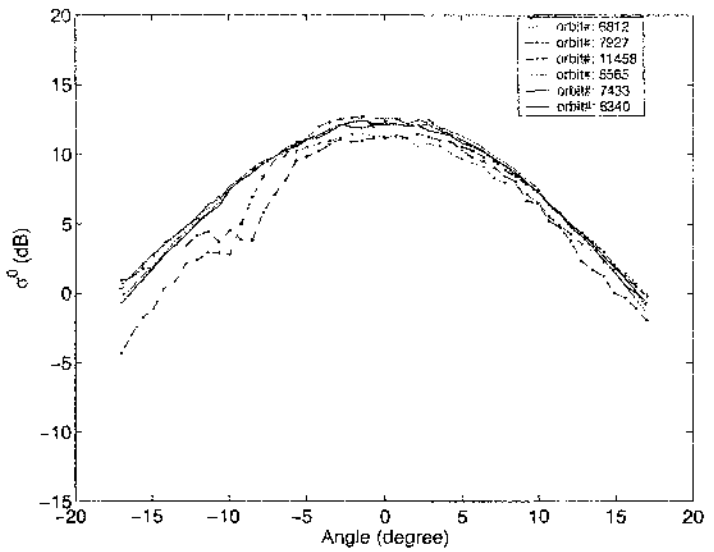

Figure 6.4: Mean of σ^0 as a function of incident angle for different orbits over the Atlantic Ocean for the year 1999; solid lines represent rain-free cases while dashed lines represent rain cases.

Figures 6.4 to 6.6 show the mean of σ^0 as a function of incident angle for different orbits for the location shown in Figure 6.1 for the years 1999, 2000, and 2001, respectively, while Figures 6.7 to 6.9 show the standard deviation of σ^0 as a function of incident angle for the year of 1999, 2000, and 2001, respectively.

We can conclude the following results from these figures:

- The maximum values of σ^0 always occurred at nadir.
- The maximum difference between σ^0 in the presence of rain and in its absence at nadir for the cases consider here is 2.3 dB.
- The standard deviation of σ^0 in the rain-free case is more stable compared to the rain case (Fiures 6.7-6.9).

Figures 6.10 and 6.11 show profiles of σ^0 during the rain-free and rain time over the location of Case Study 1, respectively. It is clear that σ^0 decreases in case of rain compared to rain-free time.

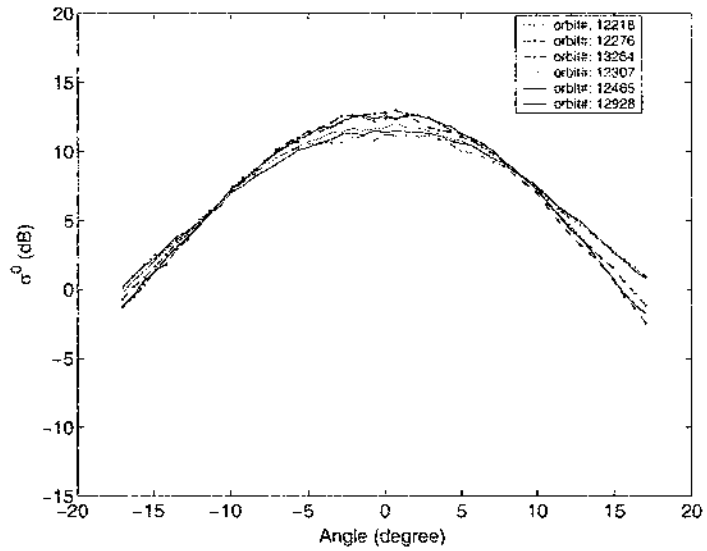

Figure 6.5: Mean of σ^0 as a function of incident angle for different orbits over the Atlantic Ocean for year 2000; solid lines represent rain-free cases while dashed lines represent rain cases.

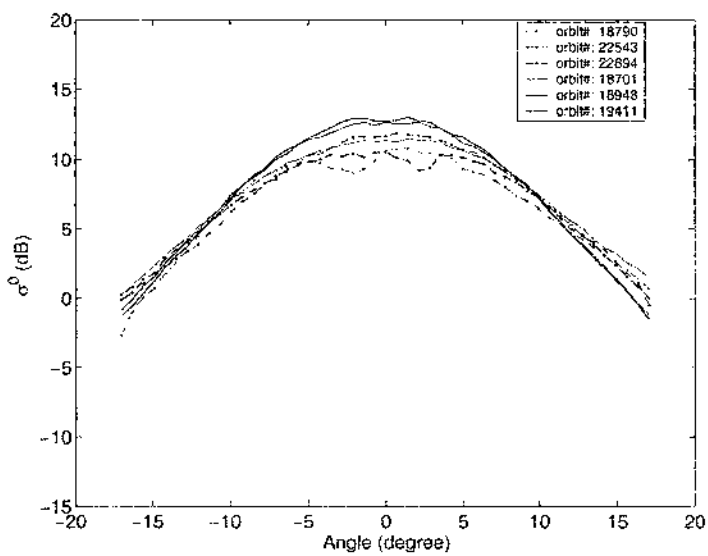

Figure 6.6: Mean of σ^0 as a function of incident angle for different orbits over the Atlantic Ocean for the year 2001; solid lines represent rain-free cases while dashed lines represent rain cases.

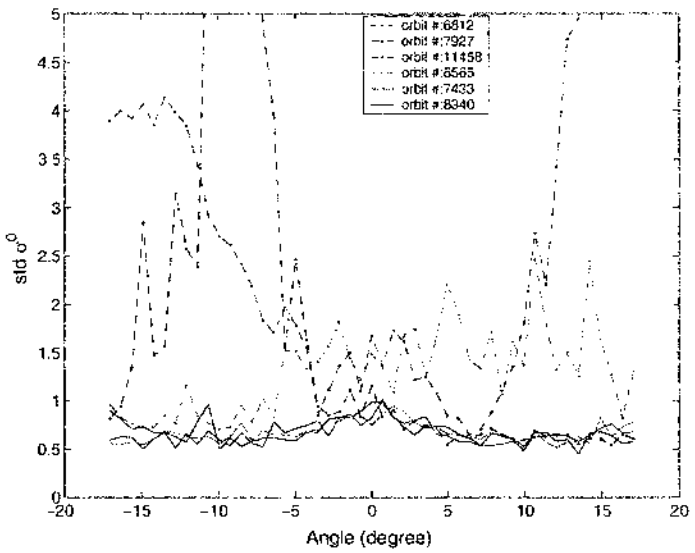

Figure 6.7: Standard deviation of σ^0 as a function of incident angle for different orbits over the Atlantic Ocean for the year 1999; solid lines represent rain-free cases while dashed lines represent rain cases.

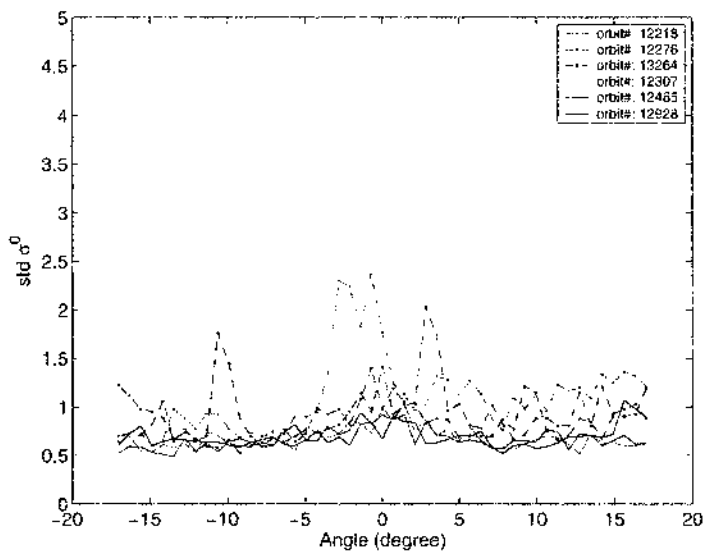

Figure 6.8: Standard deviation of σ^0 as a function of incident angle for different orbits over the Atlantic Ocean for the year 2000; solid lines represent free-rain cases while dashed lines represent rain cases.

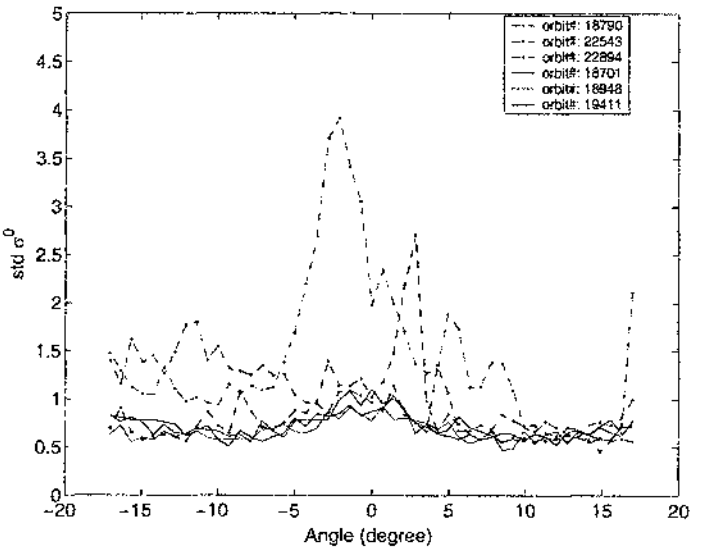

Figure 6.9: Standard deviation of σ^0 as a function of incident angle for different orbits over the Atlantic Ocean for the year 2001; solid lines represent rain-free cases while dashed lines represent rain cases.

Figure 6.10: σ^0 over the Atlantic Ocean during rain-free: Orbit 16027 on 9/9/2000.

Figure 6.11: σ^0 over the Atlantic Ocean during rain: Orbit 15425 on 8/2/2000.

6.4.2 Case Study 2: Orbit Analysis

In this case study, TRMM PR data was used to examine σ^0 within the whole orbit over the ocean during rain and rain-free time. Table 6.3 shows the summary of the data that was used for analysis in this case study.

Date	Orbit Number
01/18/1999	6565
01/17/2000	12307
03/18/2000	13264
10/28/2001	22543

Table 6.3: Summary of Data Used in Case Study 2.

Figure 6.12 shows the location of orbits for this case study. Figures 6.13 and 6.14 show the histogram of σ^0 at nadir over the ocean for different orbits during rain and rain-free time, respectively. It is clear from these figures that the mean value of σ^0 for these orbits is 11.86 dB in the case of rain, while it is 12.91 dB for rain-free cases (there is $\approx$1 dB difference in σ^0 between rain and rain-free time). The standard deviation of σ^0 in the cases of rain-free and rain are close to each other (standard deviation of σ^0 for rain-free is 1.89 dB, while for rain it is 1.93 dB).

Figure 6.15 shows the mean of σ^0 as a function of incident angles for different orbits over the ocean, while Figure 6.16 shows the the standard deviation of σ^0 as a function of incident angles. It is clear from these figures that the mean of σ^0 is maximum at the nadir and the difference during rain and rain-free is about 2.5 dB, while the standard deviation of σ^0 during the rain and rain-free time is minimum at the incident angle between -5^o to 5^o and maximum at $\pm 17^o$. From Figure 6.16 it is clear that over the ocean, the smallest standard deviations occur at incident angles 4.26^o during rain-free (a similar result was mentioned in Meneghini et al., 2000).

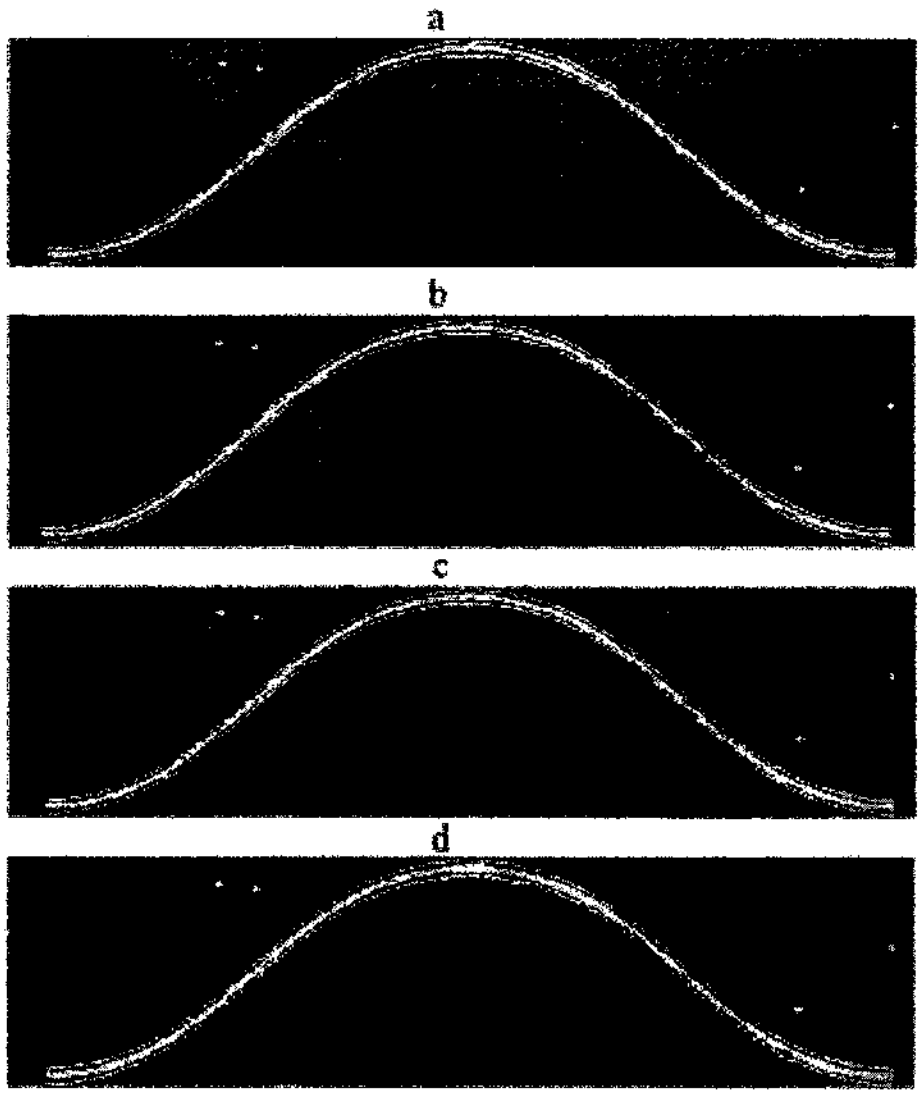

Figure 6.12: Location of orbits for Case Study 2: a) orbit no. 6565, b) orbit no. 12307, c) orbit no. 13264 and d) orbit no. 22543.

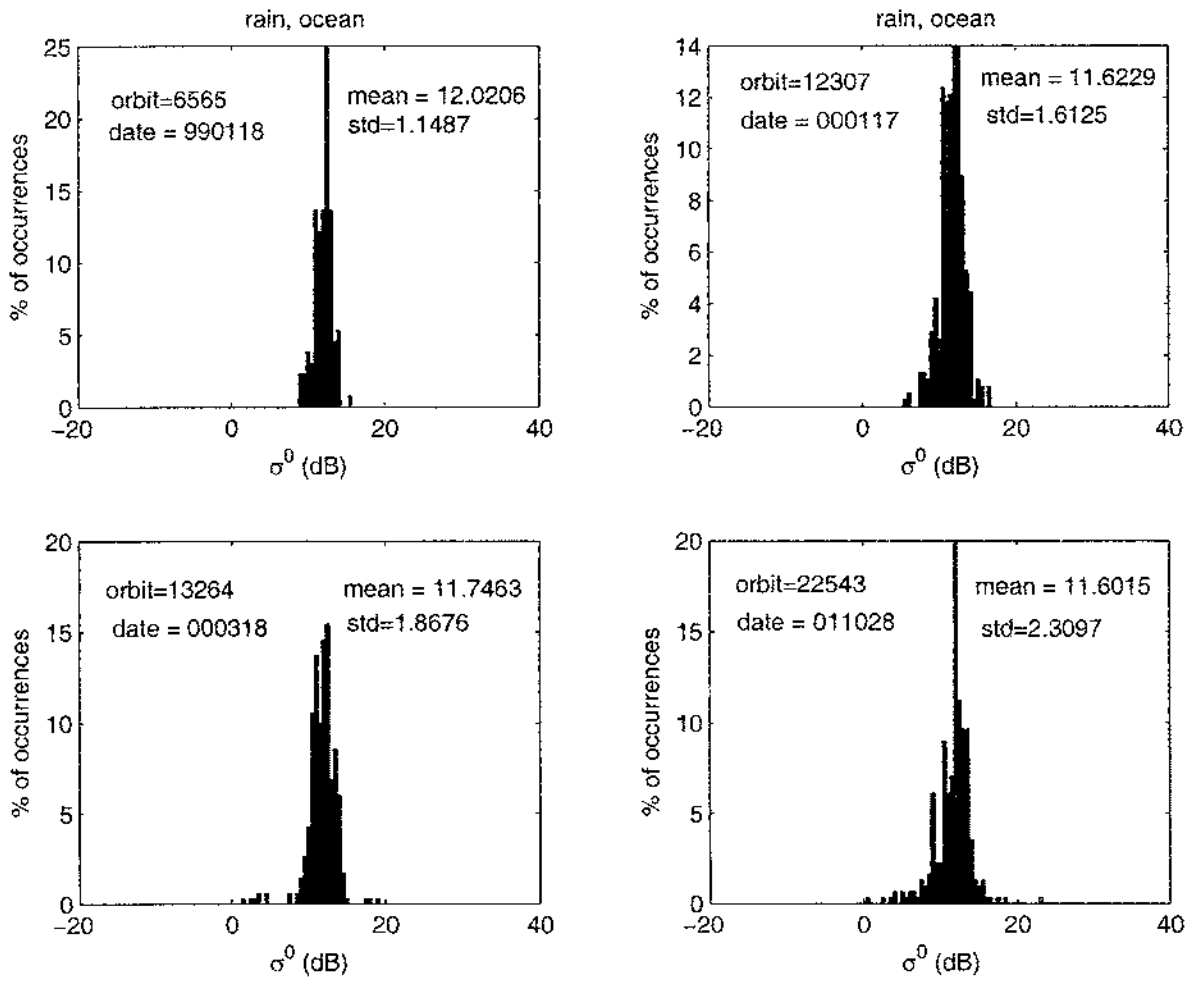

Figure 6.13: Histogram of σ^0 at nadir for orbit analysis: rain cases.

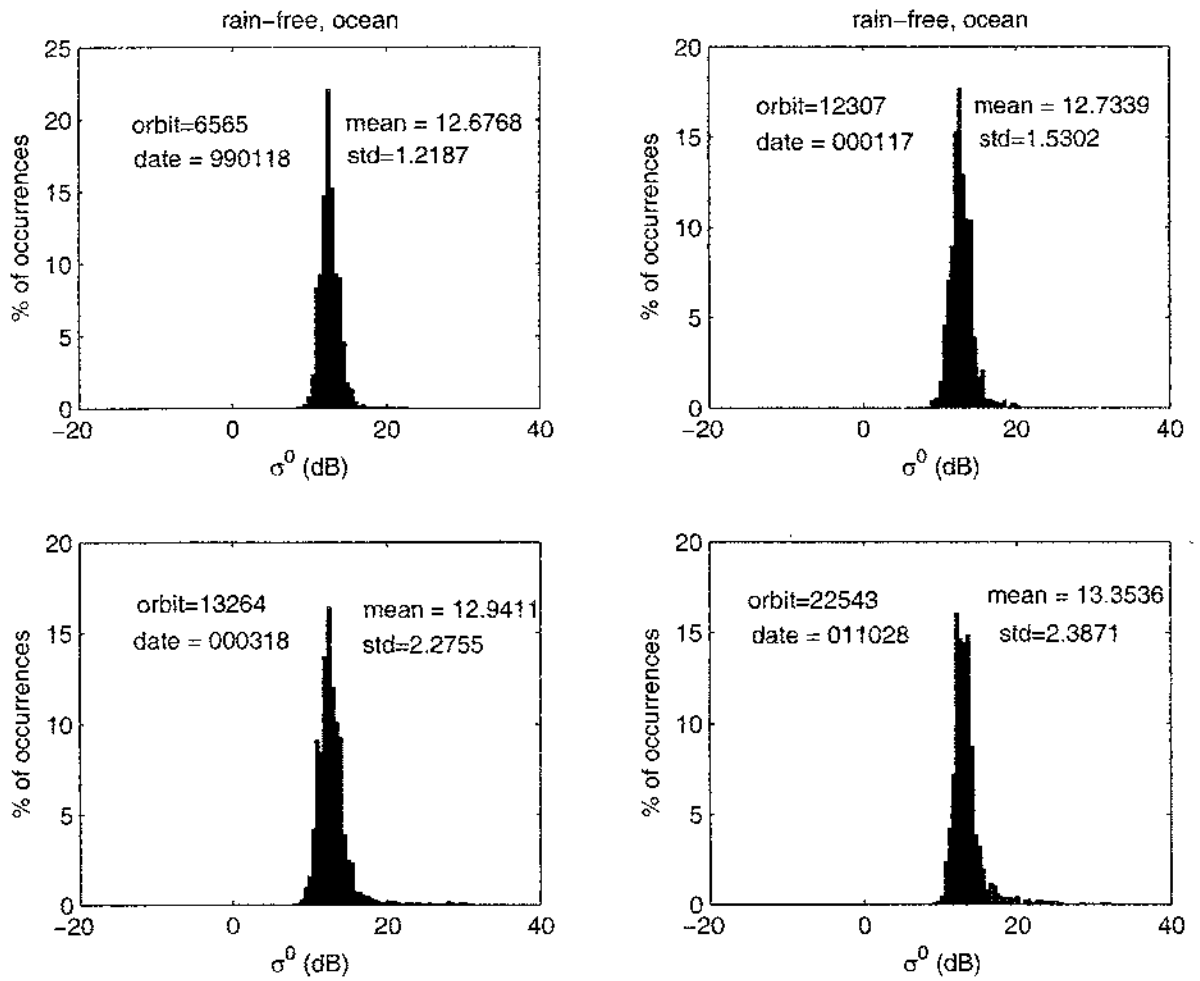

Figure 6.14: Histogram of σ^0 at nadir for orbit analysis: rain-free cases.

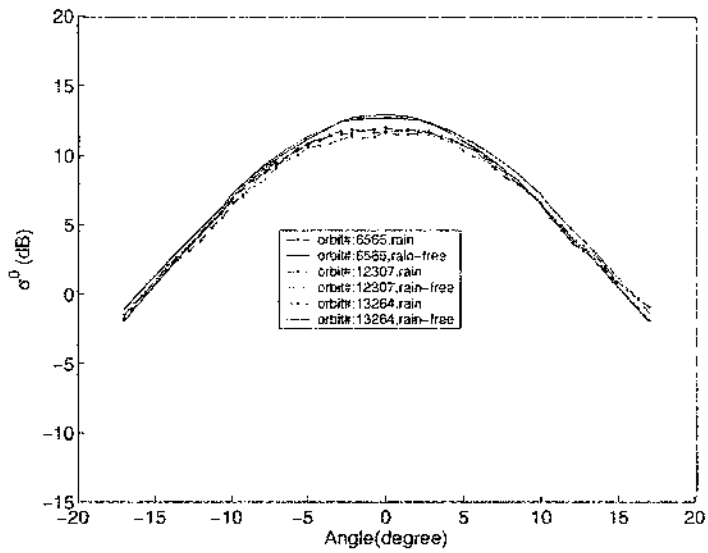

Figure 6.15: Mean of σ^0 as a function of incident angle for different orbits; solid lines represent rain-free cases while dashed lines represent rain cases.

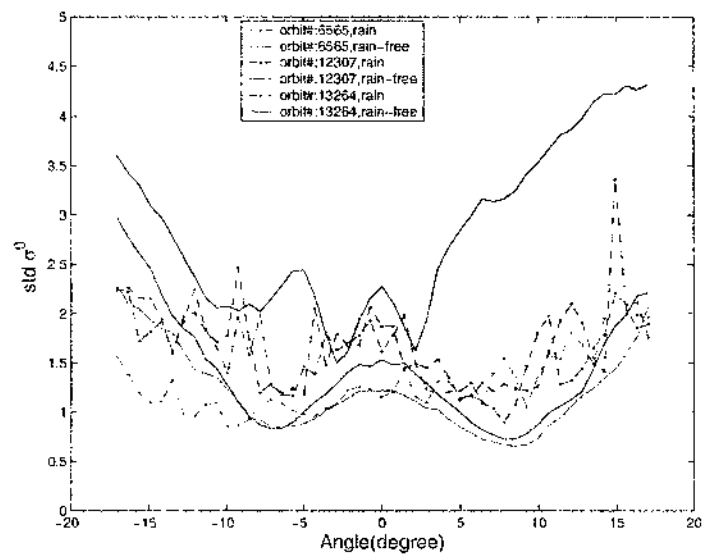

Figure 6.16: Standard deviation of σ^0 as a function of incident angle for different orbits; solid lines represent rain-free cases while dashed lines represent rain cases.

6.4.3 Case Study 3: σ^0 for the Ocean Before Crossing/After Crossing Land

In this case study, TRMM PR data was used to examine σ^0 over the ocean before and after the land during rain-free time. Table 6.4 shows the summary of the data used for analysis.

Date	Orbit	Scan before land	Scan after land
01/18/1999	6565	2152-2452	2759-3059
01/17/2000	12307	2157-2457	2761-3061
03/18/2000	13264	2155-2455	2760-3060
10/28/2001	22543	2166-2466	2778-3078

Table 6.4: Summary of Data Used in Case Study 3.

Figure 6.17 shows the location of this case study. Note that the square boxes in Figure 6.17 represent 300 scans. Figures 6.18 to 6.21 show the histogram of σ^0 at nadir over the ocean before and after crossing the land during rain-free time, while Figure 6.22 shows the histogram of σ^0 at nadir before and after the land when all four previous orbits are combined together. Figures 6.23 and 6.24 show the mean and the standard deviation of σ^0 as a function of incident angles over the ocean before and after crossing the land for the location shown in Figure 6.17. The following is clear from these figures:

- The mean value of σ^0 at nadir during rain-free over the ocean before crossing the land is always higher than after crossing the land (before the land is 13.8 dB, while after the land is 11.93 dB).
- The standard deviation of σ^0 at nadir over the ocean before and after crossing the land are similar (before crossing land is 1.524 dB, while after cossing land is 1.152 dB).

- The standard deviation of σ^0 at off-nadir before crossing the land is much higher compared to after crossing the land.
- The standard deviation of σ^0 does not change much as a function of incident angles after crossing the land, while it does change a lot before crossing the land.

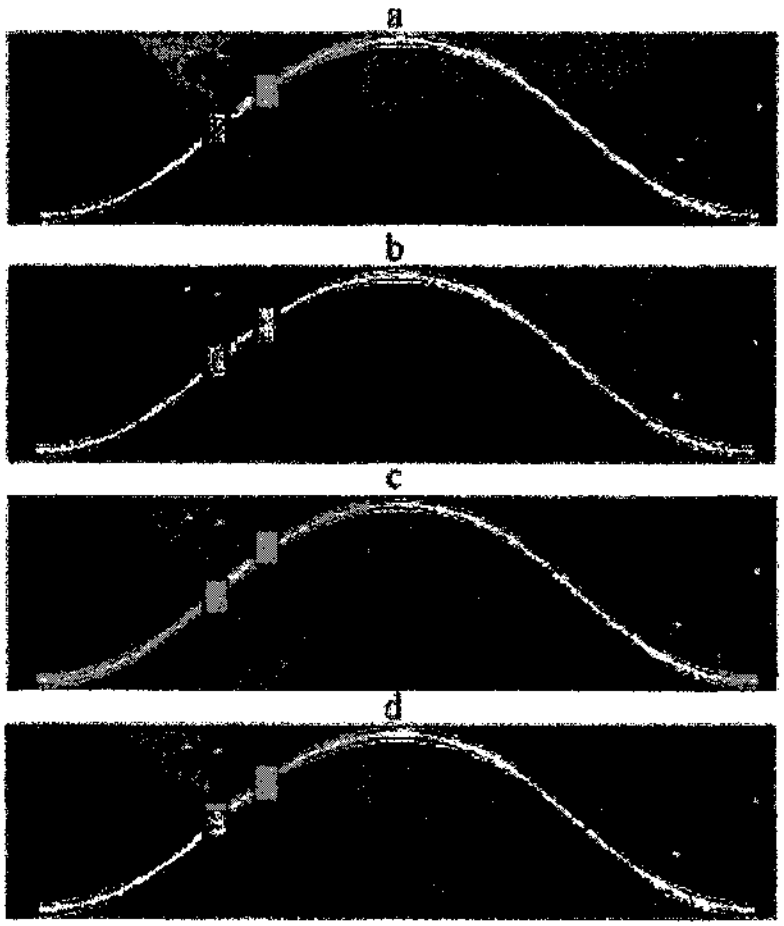

Figure 6.17: Location of Case Study 3: a) orbit no. 6565, b) orbit no. 12307, c) orbit no. 13264 and d) orbit no. 22543.

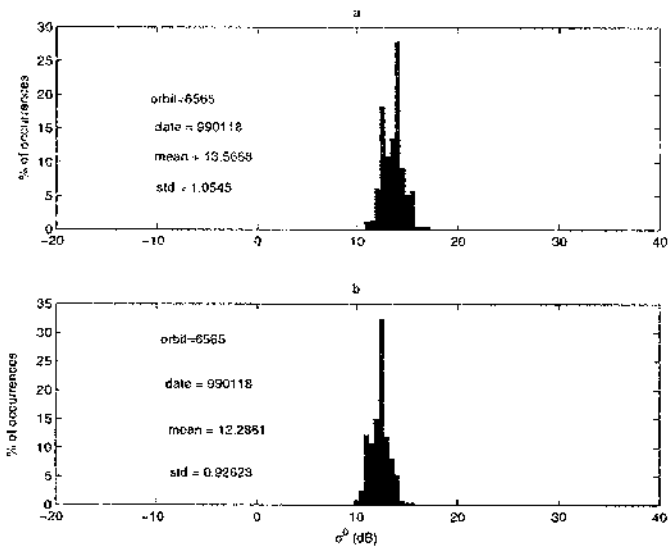

Figure 6.18: Histogram of σ^0 at nadir a) for the ocean before crossing the land and b) for the ocean after crossing the land, Orbit 6565, 08/18/1999.

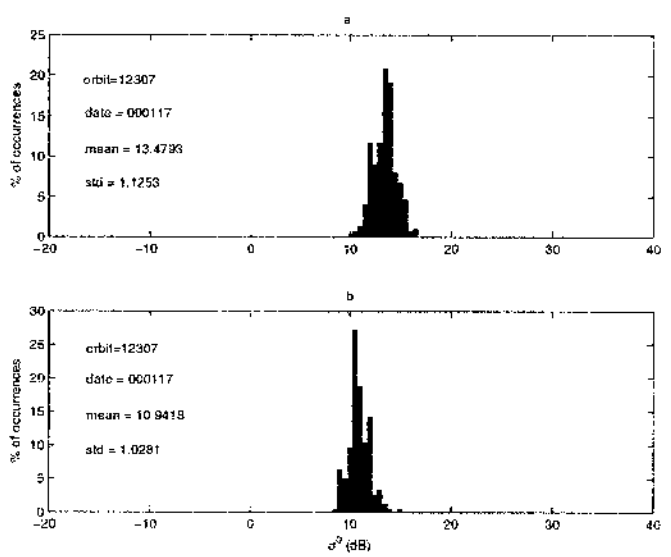

Figure 6.19: Histogram of σ^0 at nadir a) for the ocean before crossing the land and b) for the ocean after crossing the land, Orbit 12307, 01/17/2000.

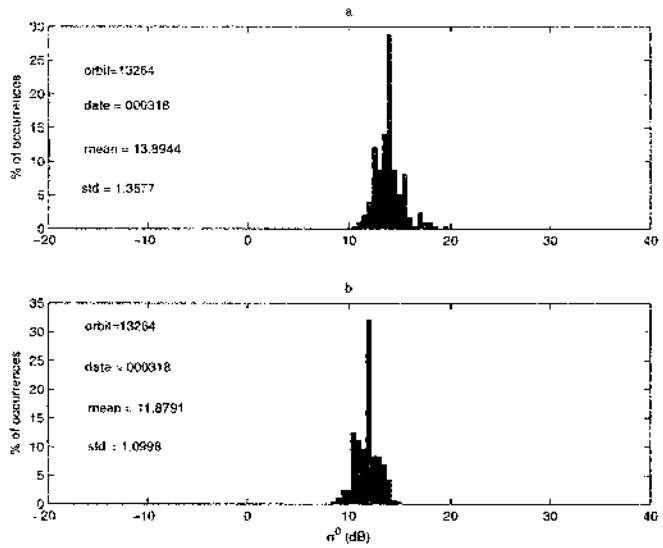

Figure 6.20: Histogram of σ^0 at nadir a) for the ocean before crossing the land and b) for the ocean after crossing the land, Orbit 13264, 03/18/2000.

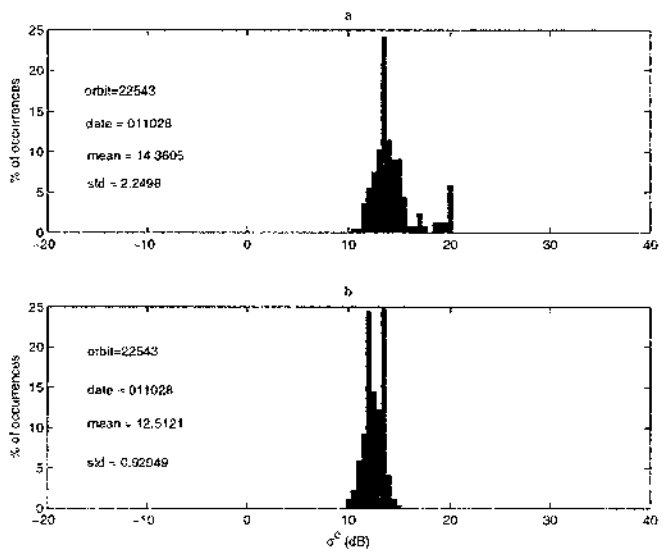

Figure 6.21: Histogram of σ^0 at nadir a) for the ocean before crossing the land and b) for the ocean after crossing the land, Orbit 22543, 10/28/2001.

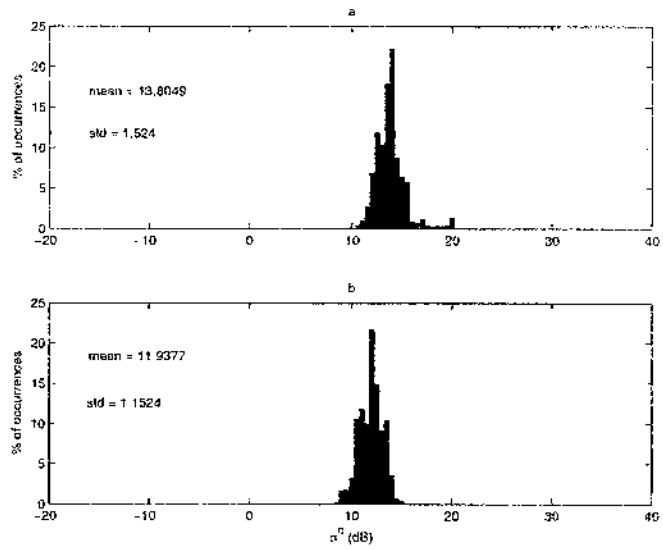

Figure 6.22: Histogram of σ^0 at nadir a) for the ocean before crossing the land and b) for the ocean after crossing the land, all four orbits together.

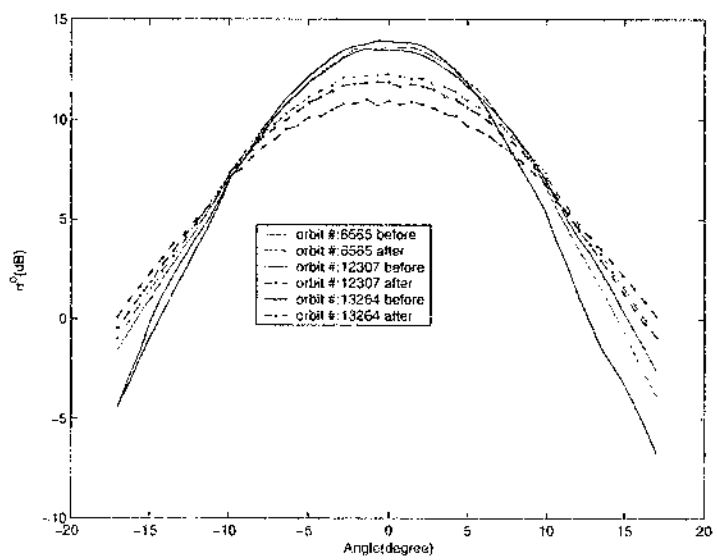

Figure 6.23: Mean of σ^0 as a function of incident angle for Case Study 3.

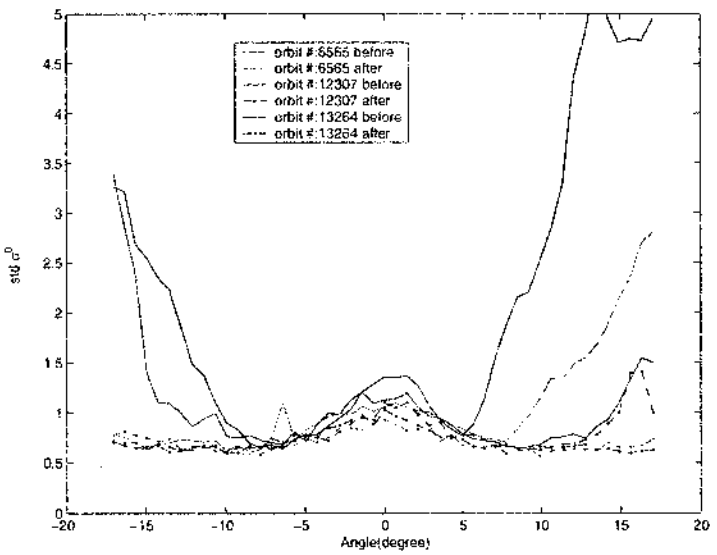

Figure 6.24: Standard deviation of σ^0 as a function of incident angle for Case Study 3.

6.5 Data Analysis: σ^0 Over Land

In this section, TRMM data was used to examine the characteristics of σ^0 over land. Three different locations were selected as an example of σ^0 over land.

6.5.1 Case Study 1: Amazon Rin Forest, Brazil

Figure 6.25 shows the location of this case study. The square box in Figure 6.25 represents 0^oN to 2^oN and -64^oE to -62^oE where the location that corresponds to the midpoint of this area is 1^oN and -63^oE. Tables 6.5 and 6.6 show the summary of data used in this case study for rain and rain-free cases, respectively.

Figures 6.26 and 6.27 show the histogram of σ^0 at nadir over the location shown in Figure 6.25 during rain and rain-free times, respectively. The mean value of σ^0 for this specific location is 9.8 dB in the case of rain, while it is 9.4 dB for rain-free cases. The standard deviation of σ^0 in the case of rain is 10.61 dB and it is 10.45 dB for rain-free cases.

Figures 6.28 and 6.29 show the mean and the standard deviation of σ^0 as a function of incident angle over the location shown in Figure 6.25, respectively.

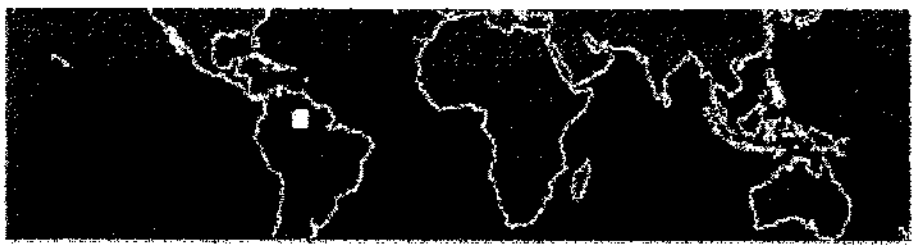

Figure 6.25: Location of Case Study 1: Amazon rain forest, Brazil , 0°N to 2°N and −64°E to −62°E .

Date	Orbit Number	Scan Number	R (mm/hr)
03/08/2000	13116	6784-6856	7.5
04/13/2000	13680	2296-2368	5.5
06/15/2000	14675	6778-6850	8
06/28/2000	14884	2302-2374	8

Table 6.5: Summary of Data Used in Case Study 1 for Rain Cases.

Date	Orbit Number	Scan Number
01/05/2000	12121	2298-2370
01/28/2000	12476	2288-2360
02/12/2000	12723	2302-2374
07/01/2000	14922	6795-6867

Table 6.6: Summary of Data Used in Case Study 1 for Rain-free Cases.

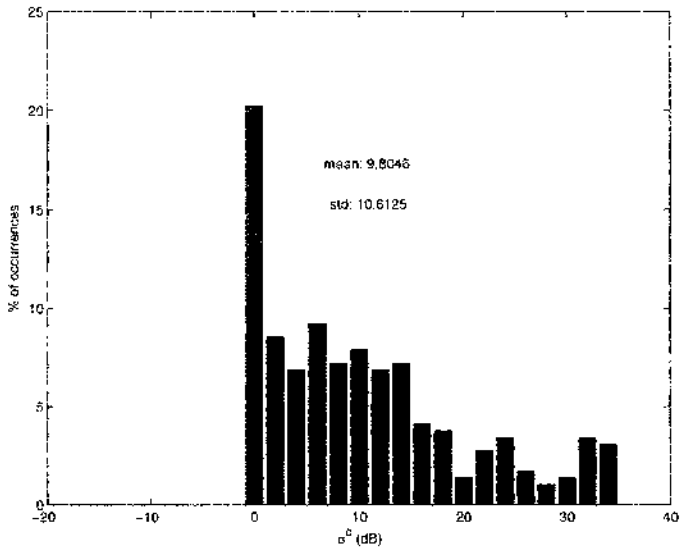

Figure 6.26: Histogram of σ^0 at nadir over Amazon rain forest, Brazil: rain.

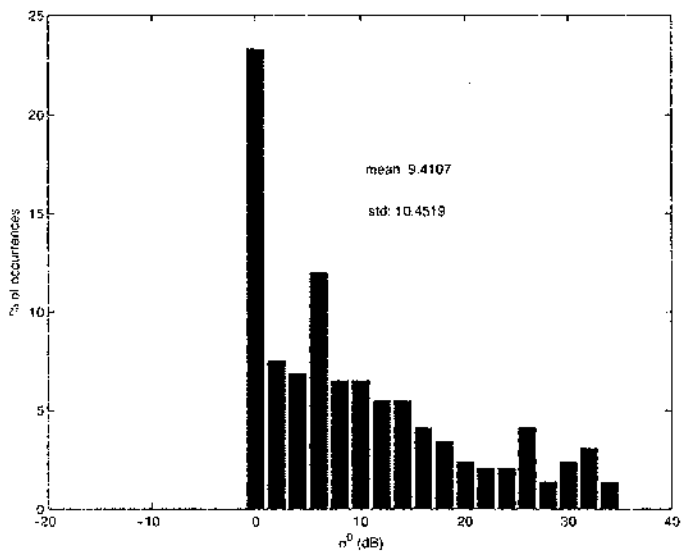

Figure 6.27: Histogram of σ^0 at nadir over Amazon rain forest, Brazil: rain-free.

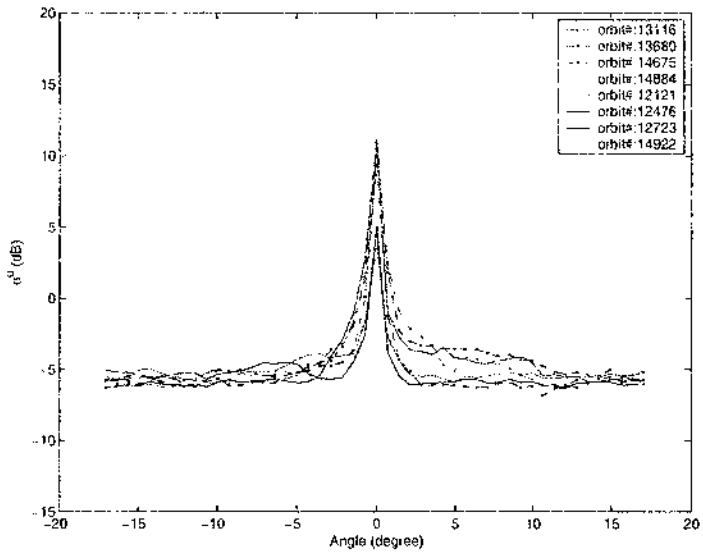

Figure 6.28: Mean of σ^0 as a function of incident angles over Amazon rain forest, Brazil: solid lines represents rain-free cases while dashed lines represent rain cases.

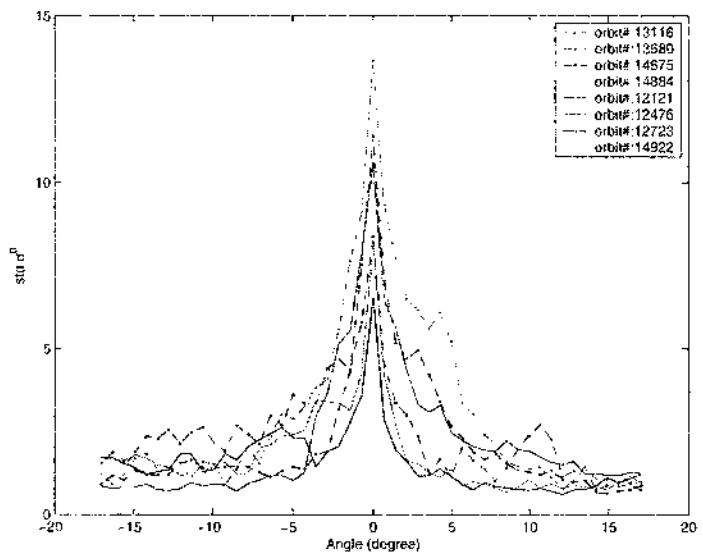

Figure 6.29: Standard deviation of σ^0 as a function of incident angles over Amazon rain forest, Brazil: solid lines represents rain-free cases while dashed lines represent rain cases.

6.5.2 Case Study 2: Darwin, Australia

Figure 6.30 shows the location of this case study. The square box in Figure 6.30 represents $-11.25°$N to $-13.25°$N and $130.04°$E to $132.04°$E where the location that corresponds to the midpoint of this area is $-12.25°$N and $131.04°$E. Tables 6.7 and 6.8 show the summary of data used in this case study for rain and rain-free cases, respectively.

Figures 6.31 and 6.32 show the histogram of σ^0 at nadir over the location shown in Figure 6.30 during rain and rain-free times, respectively. The mean value of σ^0 for this specific location is 16.3 dB in the case of rain, while it is 18.3 dB for rain-free cases. The standard deviation of σ^0 in the case of rain is 6.5 dB and it is 6.3 dB for rain-free cases.

Figures 6.33 and 6.34 show the mean and the standard deviation of σ^0 as a function of incident angle over the location shown in Figure 6.30, respectively.

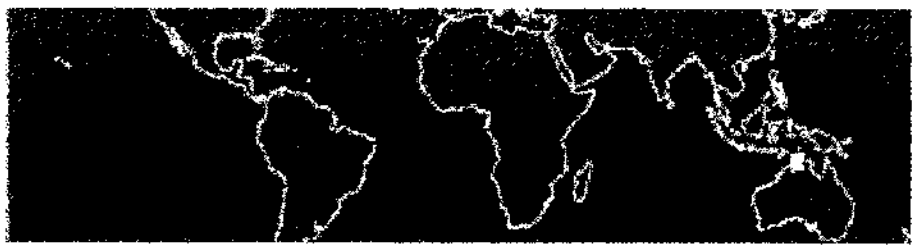

Figure 6.30: Location of Case Study 2: Darwin, Australia , $-11.25°$N to $-13.25°$N and $130.04°$E to $132.04°$E .

Date	Orbit Number	Scan Number	R (mm/hr)
01/20/2000	12352	7323-7392	13
02/03/2000	12575	1718-1787	21
02/11/2000	12707	7316-7385	12
03/03/2000	13038	1681-1750	6.5

Table 6.7: Summary of Data Used in Case Study 2 for Rain Cases.

Date	Orbit Number	Scan Number
01/06/2000	12136	7377-7446
01/29/2000	12491	7364-7433
03/07/2000	13093	7373-7442
06/03/2000	14489	1702-1771

Table 6.8: Summary of Data Used in Case Study 2 for Rain-free Cases.

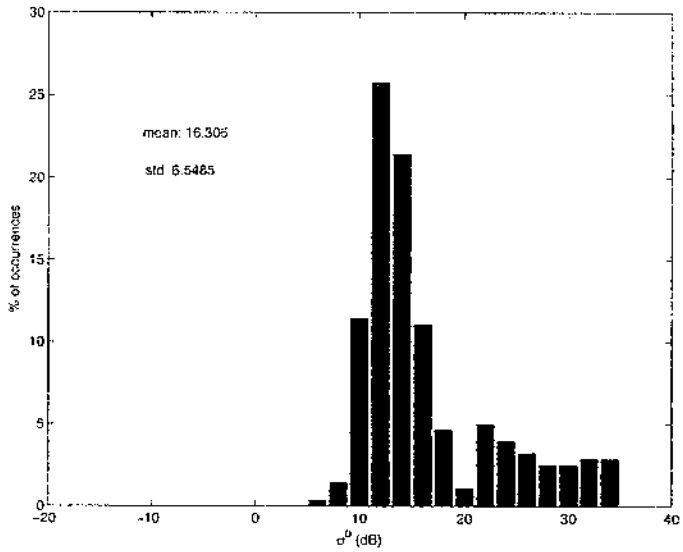

Figure 6.31: Histogram of σ^0 at nadir over Darwin, Australia: rain.

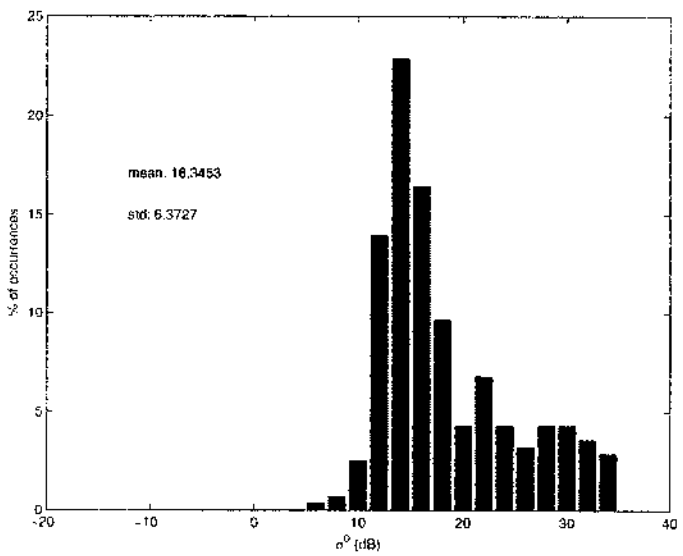

Figure 6.32: Histogram of σ^0 at nadir over Darwin, Australia: rain-free.

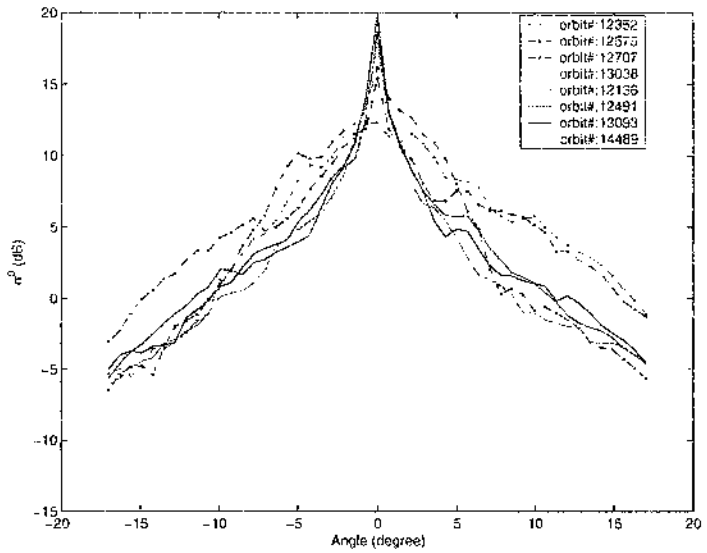

Figure 6.33: Mean of σ^0 as a function of incident angles over Darwin, Australia: solid lines represents rain-free cases while dashed lines represent rain cases.

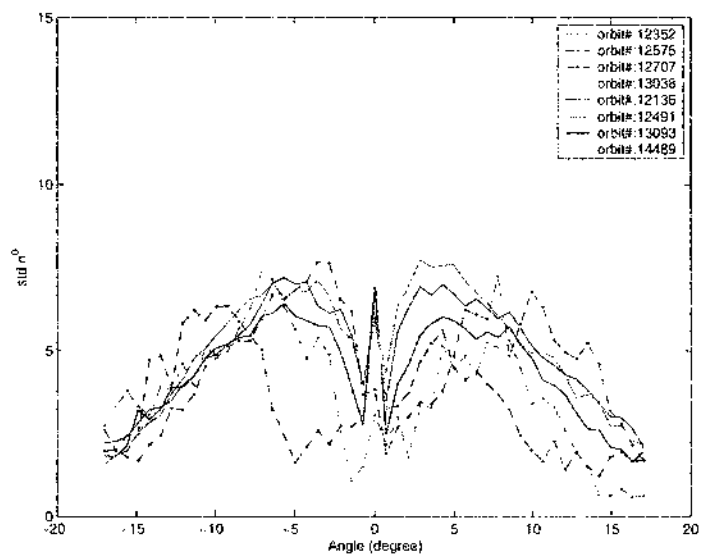

Figure 6.34: Standard deviation of σ^0 as a function of incident angles over Darwin, Australia: solid lines represents rain-free cases while dashed lines represent rain cases.

6.5.3 Case Study 3: Melbourne, Florida

Figure 6.35 shows the location of this case study. The square box in Figure 6.35 represents 27°N to 29°N and −81°E to −79°E where the location that corresponds to the midpoint of this area is 28°N and −80°E. Tables 6.9 and 6.10 show the summary of data used in this case study for rain and rain-free cases, respectively.

Figures 6.36 and 6.37 show the histogram of σ^0 at nadir over the location shown in Figure 6.35 during rain and rain-free times, respectively. The mean value of σ^0 for this specific location is 17 dB in the case of rain, while it is 15.7 dB for rain-free cases. The standard deviation of σ^0 in the case of rain is 8.1 dB and it is 7.95 dB for rain-free cases.

Figures 6.38 and 6.39 show the mean and the standard deviation of σ^0 as a function of incident angle over the location shown in Figure 6.35, respectively.

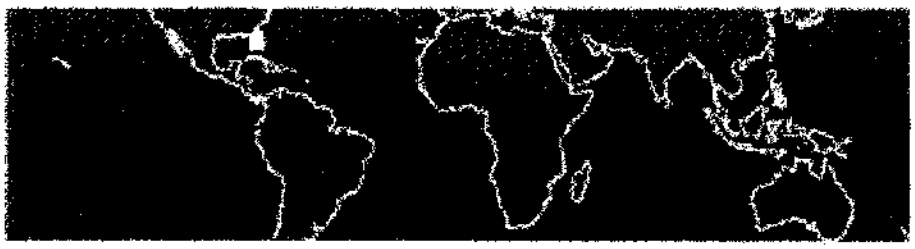

Figure 6.35: Location of Case Study 3: Melbourne, Florida , 27°N to 29°N and −81°E to −79°E .

Date	Orbit Number	Scan Number	R (mm/hr)
01/24/2000	12417	3681-3715	10.7
04/14/2000	13698	3599-3633	8.7
07/15/2000	15149	3622-3656	5.2

Table 6.9: Summary of Data Used in Case Study 3 for Rain Cases.

Date	Orbit Number	Scan Number
06/14/2000	14652	7376-7410
10/28/2000	16804	5449-5483
10/31/2000	16847	3660-3694

Table 6.10: Summary of Data Used in Case Study 3 for Rain-free Cases.

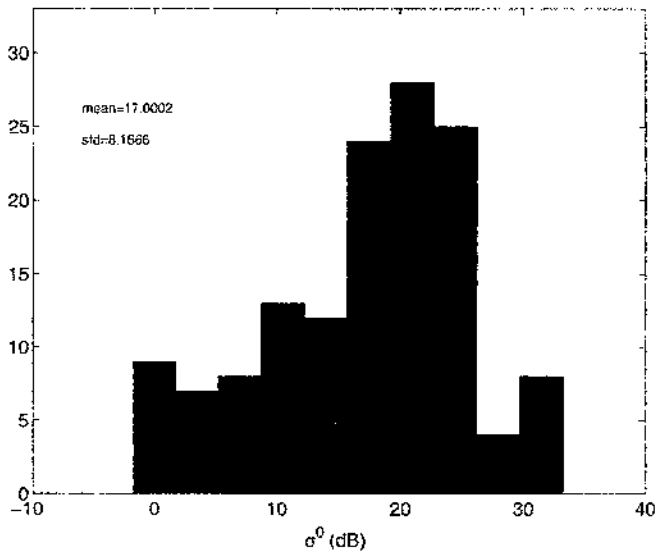

Figure 6.36: Histogram of σ^0 over Melbourne, Florida: rain.

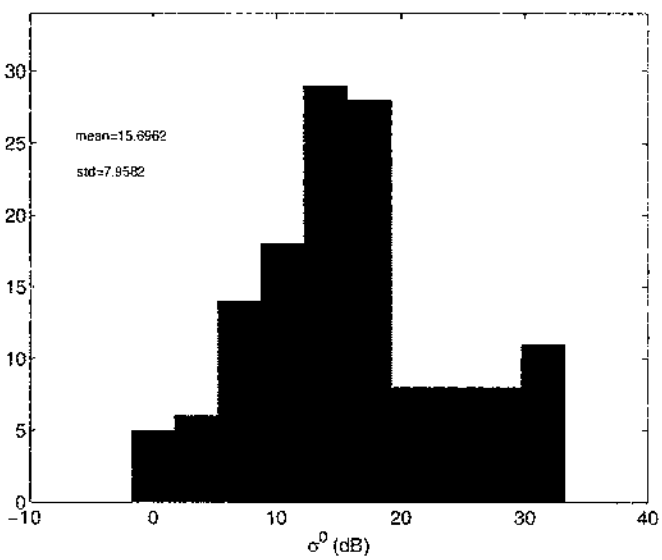

Figure 6.37: Histogram of σ^0 over Melbourne, Florida: rain-free.

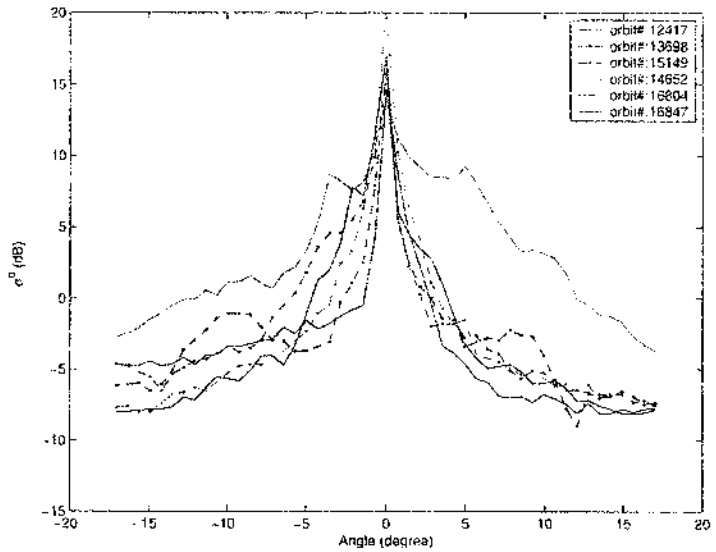

Figure 6.38: Mean of σ^0 as a function of incident angles over Melbourne, Florida: solid lines represents rain-free cases while dashed lines represent rain cases.

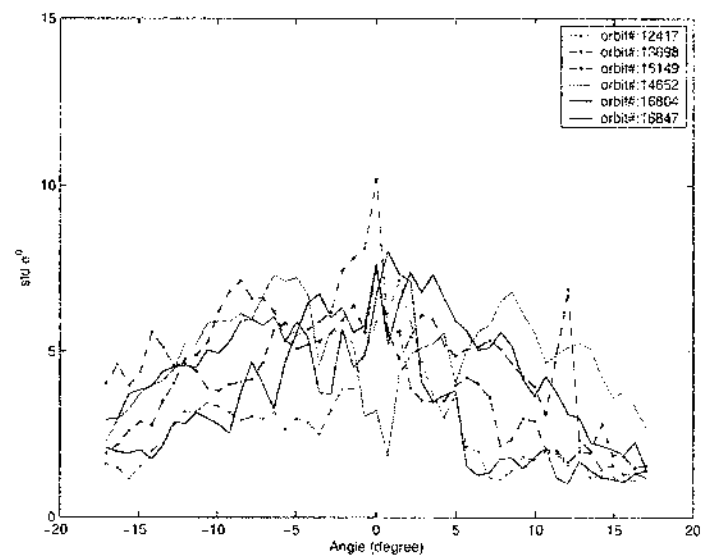

Figure 6.39: Standard deviation of σ^0 as a function of incident angles over Melbourne, Florida: solid lines represents rain-free cases while dashed lines represent rain cases.

6.5.4 Discussion

The over land σ^0 is more complex than over the ocean. We can conclude the following results from the previous sections:

- The standard deviation of σ^0 at nadir over land is higher than it is over the ocean. Over land, the standard deviation at nadir is in excess of 8 dB on average while it is below 2.5 dB over the ocean (Meneghini et al. (2000). Contributing to the large standard deviation is the frequent occurrences of extremely high cross sections. For example, under rain-free conditions, about 10% of the σ^0 data exceed 20 dB, and about 2% exceed 25 dB. In contrast, at nadir incident over the ocean, only about 1.4% of the data exceed 20 dB and 2% exceed 25 dB (Meneghini et al., 2000). Table 6.11 shows the percentage of σ^0 exceeding 20 and 25 dB under rain and rain-free conditions for the locations which were selected as an example of σ^0 over land.

Location	Rain		Rain-free	
	$\sigma^0 \geq$ 20 dB	$\sigma^0 \geq$ 25 dB	$\sigma^0 \geq$ 20 dB	$\sigma^0 \geq$ 25 dB
Amazon rain forest	17.46%	10.61%	18.15%	12.32%
Darwin	23.57%	13.92%	32.5%	18.21%
Melbourne	40.57%	13.04%	24.4%	14.07%

Table 6.11: Percentage of σ^0 exceeding 20 and 25 dB under rain and rain-free conditions.

- Maximum of σ^0 occurs at the nadir, and in moving to off-nadir angles, it decreases rapidly.

- Maximum of the standard deviation of σ^0 occurs at nadir, and in moving to off-nadir angles, it decreases rapidly.

6.6 σ^0 Related Observation over a Hurricane

The PR measurements were taken on 25 August 1998 over Hurricane Bonnie located off the southeast coast of the United States. Figure 6.40 shows the location of this hurricane. The square box represents 28.16°N to 33.03°N and −77.33°E to −67.54°E where the location that corresponds to the midpoint of this area is 30.59°N and −72.43°E and the overpass occurred at 1114 UTC. Figure 6.41 shows the apparent σ^0 over Hurricane Bonnie. The horizontal scale represents an 860 km segment along the satellite track, while the vertical scale which is equal to the swath of the PR is 215 km. Figures 6.42, 6.44, 6.46, 6.48, and 6.50 represent the profile of the radar return power (dBm) at 0°, 3.548°, 7.097°, 10.648°, and 17.032°, respectively, while Figures 6.43, 6.45, 6.47, 6.49, and 6.51 show the corresponding apparent σ^0. Two sets of broken horizontal lines are shown at the bottom of the figures, where a blue line indicates the presence of rain (as detected by the PR) and the black line indicates the correction for the surface reference, ϵ. Note that the regions of strong attenuation in these figures correspond to a loss of the mirror-image signal. This result is not suprising, because the mirror-image return is proportional to the four-way rather than the two-way attenuation and is normally not detected over heavy rain (Liao et al., 1999). Table 6.12 shows the percentage of rain, correction surface reference, and finally the ratio of correction surface reference to the rain as a function of incident angles over Hurricane Bonnie. Table 6.13 shows the mean and the standard deviation of σ^0 as a function of incident angles in the Hurricane Bonnie region during rain-free conditions. It is clear from Table 6.13 as the angle increases, the surface return is broadened in range and rain-free σ^0 decreases.

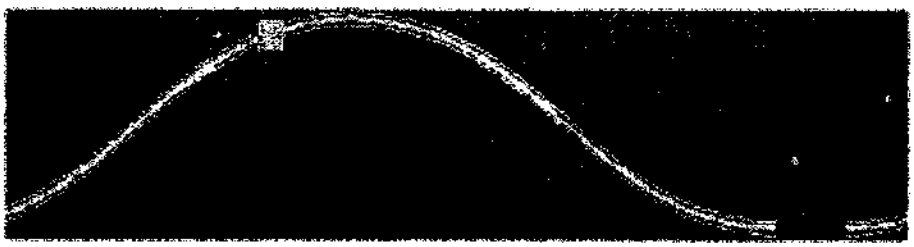

Figure 6.40: Location of Hurricane Bonnie, 25 August 1998, orbit 4267.

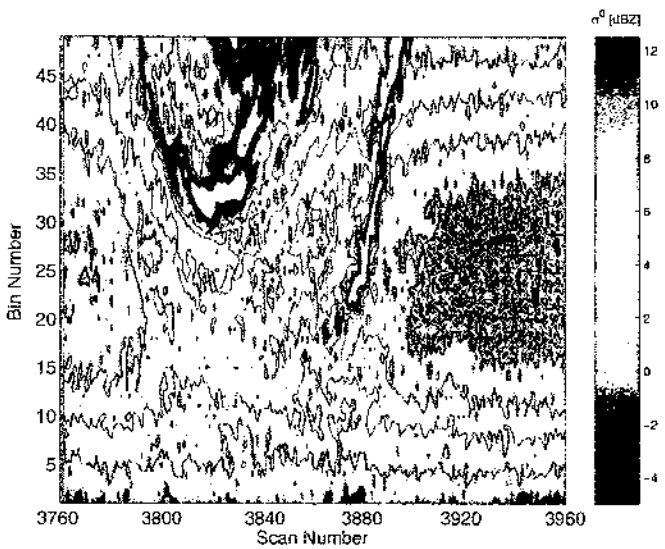

Figure 6.41: The apparent σ^0 over Hurricane Bonnie, vertical and horizontal scales represent distances of 215 and 860 km.

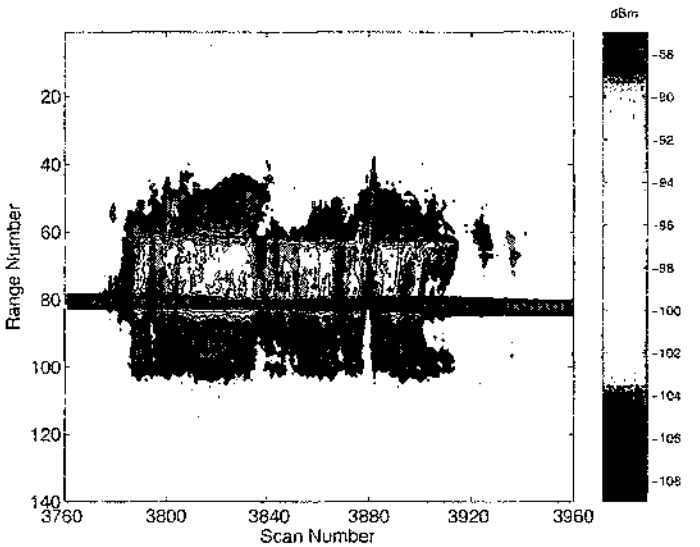

Figure 6.42: Range profile of the radar return power (dBm) at an incident angle of 0^o over Hurricane Bonnie.

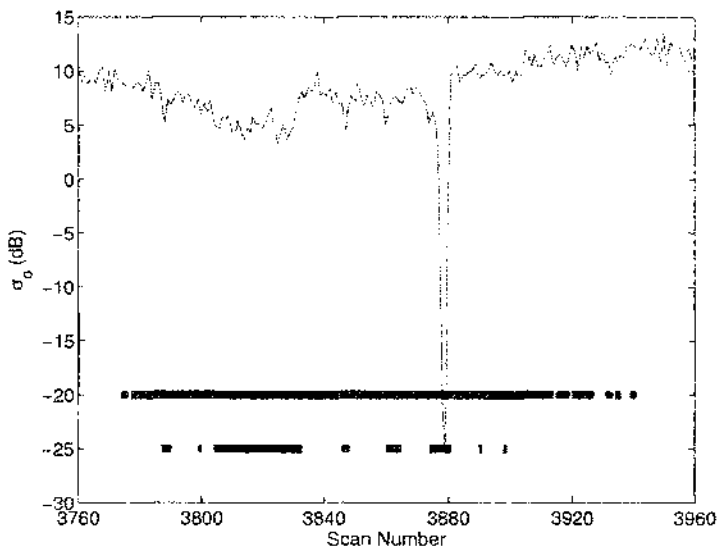

Figure 6.43: σ^0 at an incident angle of 0^o over Hurricane Bonnie.

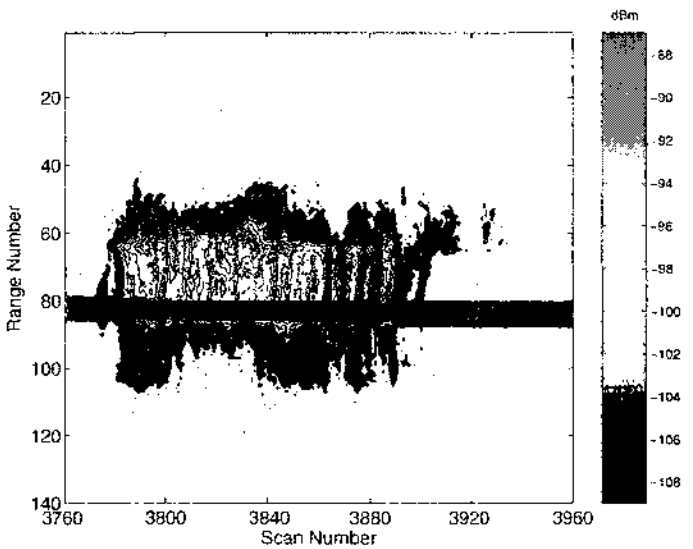

Figure 6.44: Range profile of the radar return power (dBm) at an incident angle of 3.55° over Hurricane Bonnie.

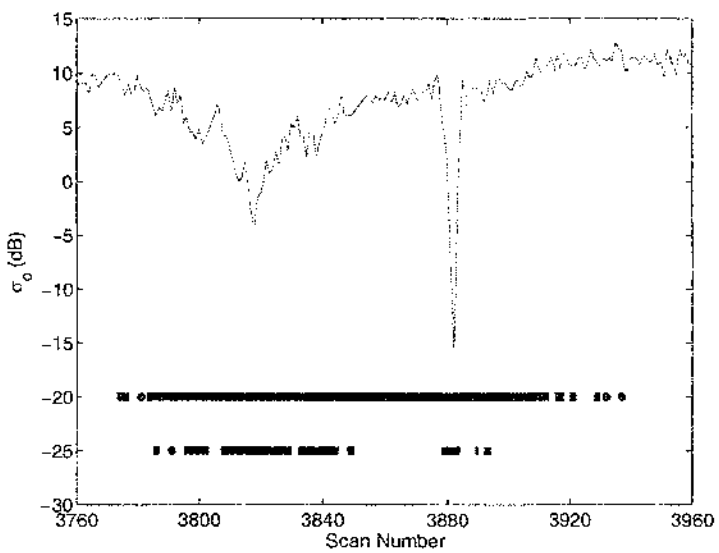

Figure 6.45: σ^0 at an incident angle of 3.55° over Hurricane Bonnie.

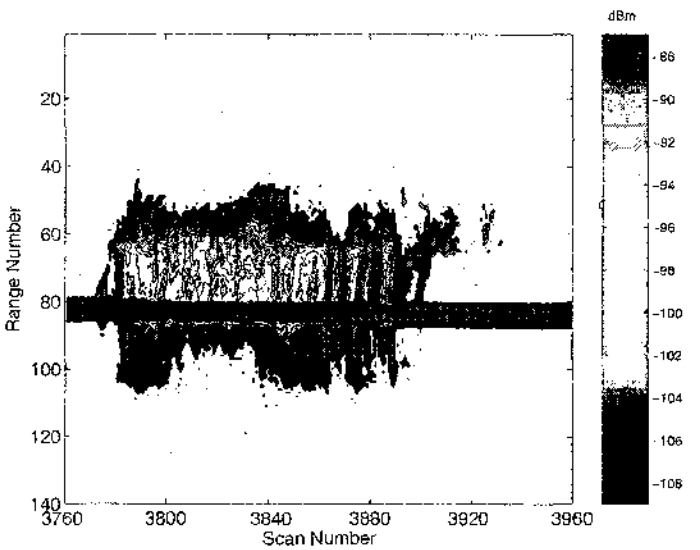

Figure 6.46: Range profile of the radar return power (dBm) at an incident angle of 7.1° over Hurricane Bonnie.

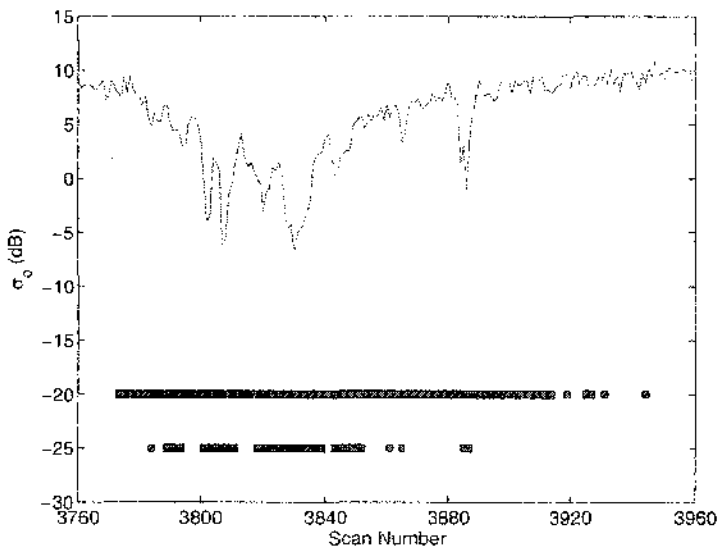

Figure 6.47: σ^0 at an incident angle of 7.1° over Hurricane Bonnie.

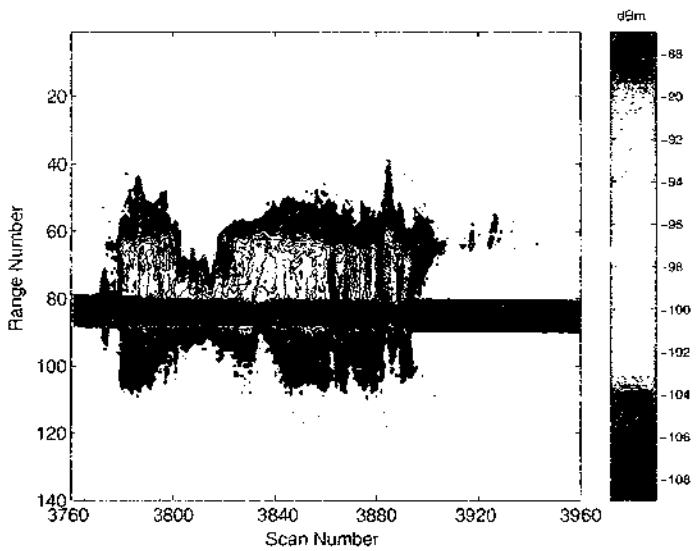

Figure 6.48: Range profile of the radar return power (dBm) at an incident angle of 10.65° over Hurricane Bonnie.

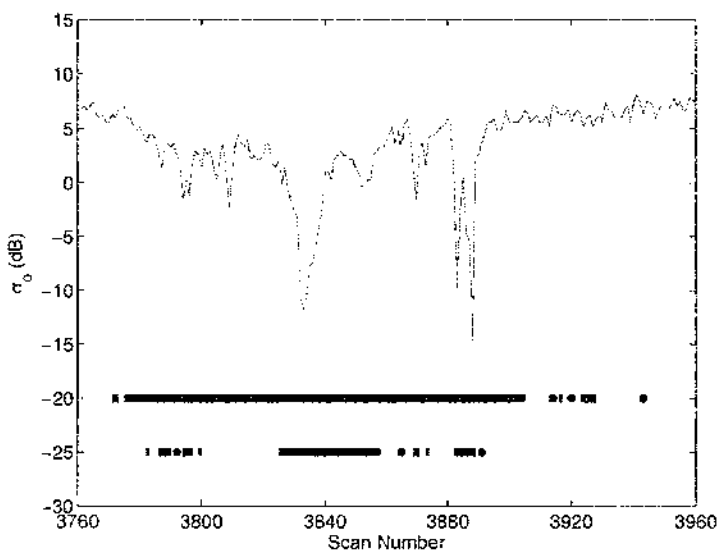

Figure 6.49: σ^0 at an incident angle of 10.65° over Hurricane Bonnie.

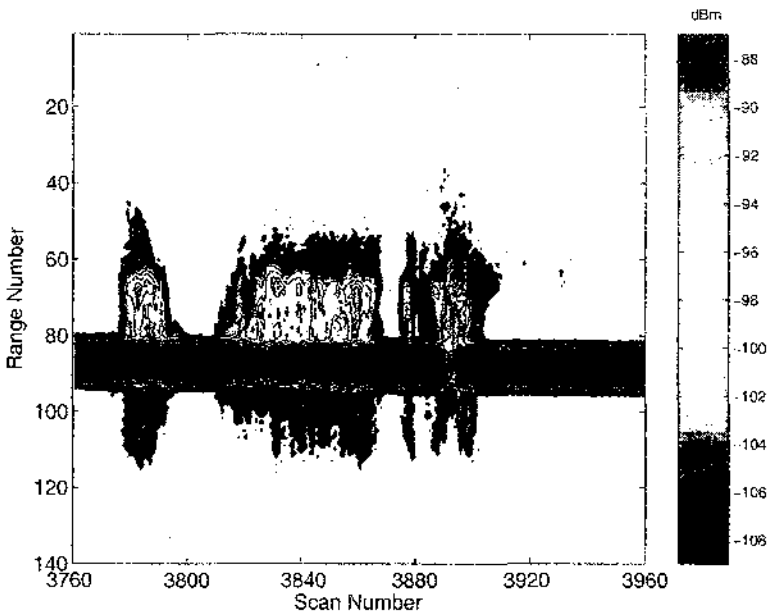

Figure 6.50: Range profile of the radar return power (dBm) at an incident angle of 17.03° over Hurricane Bonnie.

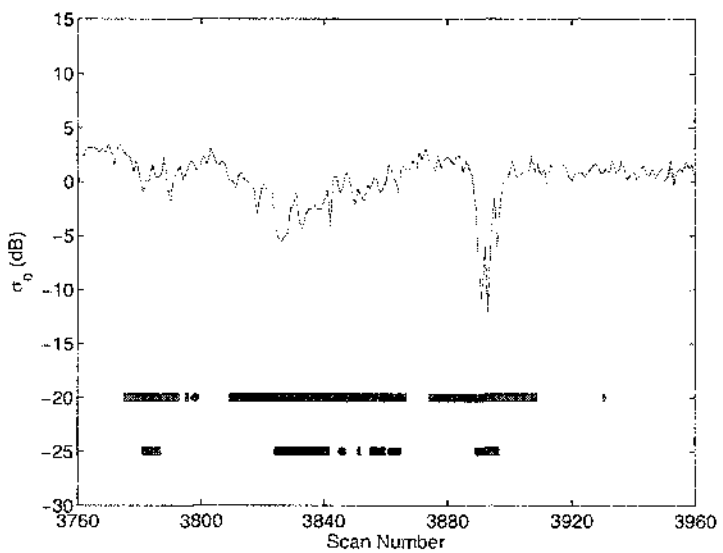

Figure 6.51: σ^0 at an incident angle of 17.03° over Hurricane Bonnie.

Angle (degree)	Rain%	$\epsilon\%$	$\epsilon/rain$
0.000	76.61	27.36	0.3571
0.711	77.11	25.37	0.3290
1.420	78.60	30.84	0.3924
2.129	75.62	29.85	0.3947
2.841	75.12	36.31	0.4834
3.548	74.13	32.83	0.4429
4.258	73.63	31.84	0.4324
4.970	72.63	31.34	0.4315
5.677	72.63	34.32	0.4726
6.389	74.13	37.31	0.5033
7.097	75.62	33.33	0.4407
7.810	73.63	31.84	0.4324
8.517	72.63	30.84	0.4246
9.231	74.12	32.83	0.4429
9.937	72.63	29.35	0.4041
10.648	72.13	31.34	0.4344
11.359	72.63	27.86	0.3835
12.068	70.64	27.86	0.3943
12.777	71.14	30.34	0.4265
13.487	66.16	30.34	0.4586
14.195	66.66	26.36	0.3955
14.904	60.69	24.37	0.4016
15.613	55.22	24.80	0.4504
16.328	58.70	26.36	0.4491
17.032	59.20	22.88	0.3865

Table 6.12: The Percentage of Rain, ϵ and ϵ/rain as a Function of Incident Angles.

Angle (degree)	mean (σ^0)	STD (σ^0)
0.000	10.93	1.43
0.711	10.89	1.29
1.420	10.95	1.28
2.129	10.86	1.39
2.841	10.78	1.12
3.548	10.55	1.20
4.258	10.39	1.20
4.970	10.13	0.93
5.677	9.85	0.91
6.389	9.46	0.86
7.097	9.27	0.78
7.810	8.48	0.62
8.517	8.30	0.65
9.231	7.80	0.74
9.937	7.20	0.65
10.648	6.64	0.71
11.359	5.96	0.69
12.068	5.31	0.69
12.777	4.75	0.72
13.487	4.20	0.84
14.195	3.60	0.58
14.904	3.02	0.79
15.613	2.40	0.82
16.328	2.01	0.77
17.032	1.49	0.96

Table 6.13: Mean and Standard Deviation of σ^0 as a Function of Incident Angles in the Hurricane Bonnie Region During Rain-free Conditions.

6.7 Monthly Maps of σ^0

TRMM PR observations are used to develop monthly maps of σ^0 at Ku-bands. For each month there are three maps. The first map shows σ^0 at nadir, the second map shows σ^0 at 5.68°, while the last map shows σ^0 at 13.49°. Note that these maps were generated only during rain-free time. In the monthly map plots, the data area is from 35N to 35S and from 180E to 180W. The color scales are adjusted to the full scale of each map. Each pixel in the plot is (0.5° x 0.5°) area and therefore of fairly high resolution. The overlay shows the standard map of land/ocean boundaries. Table 6.14 provides an itemized list of figures.

Figure	Title Description
Figure 6.52	σ^0 at nadir for January 2000
Figure 6.53	σ^0 at nadir for February 2000
Figure 6.54	σ^0 at nadir for March 2000
Figure 6.55	σ^0 at nadir for April 2000
Figure 6.56	σ^0 at nadir for May 2000
Figure 6.57	σ^0 at nadir for June 2000
Figure 6.58	σ^0 at nadir for July 2000
Figure 6.59	σ^0 at nadir for August 2000
Figure 6.60	σ^0 at nadir for September 2000
Figure 6.61	σ^0 at nadir for October 2000
Figure 6.62	σ^0 at nadir for November 2000
Figure 6.63	σ^0 at nadir for December 2000
Figure 6.64	σ^0 at 5.68^o for January 2000
Figure 6.65	σ^0 at 5.68^o for February 2000
Figure 6.66	σ^0 at 5.68^o for March 2000
Figure 6.67	σ^0 at 5.68^o for April 2000
Figure 6.68	σ^0 at 5.68^o for May 2000
Figure 6.69	σ^0 at 5.68^o for June 2000
Figure 6.70	σ^0 at 5.68^o for July 2000
Figure 6.71	σ^0 at 5.68^o for August 2000
Figure 6.72	σ^0 at 5.68^o for September 2000
Figure 6.73	σ^0 at 5.68^o for October 2000
Figure 6.74	σ^0 at 5.68^o for November 2000
Figure 6.75	σ^0 at 5.68^o for December 2000
Figure 6.76	σ^0 at 13.49^o for January 2000
Figure 6.77	σ^0 at 13.49^o for February 2000
Figure 6.78	σ^0 at 13.49^o for March 2000
Figure 6.79	σ^0 at 13.49^o for April 2000
Figure 6.80	σ^0 at 13.49^o for May 2000
Figure 6.81	σ^0 at 13.49^o for June 2000
Figure 6.82	σ^0 at 13.49^o for July 2000
Figure 6.83	σ^0 at 13.49^o for August 2000
Figure 6.84	σ^0 at 13.49^o for September 2000
Figure 6.85	σ^0 at 13.49^o for October 2000
Figure 6.86	σ^0 at 13.49^o for November 2000
Figure 6.87	σ^0 at 13.49^o for December 2000

Table 6.14: Figure Number List of Monthly Average σ^o.

Figure 6.52: Average σ^0 at nadir for January 2000: rain-free.

Figure 6.53: Average σ^0 at nadir for February 2000: rain-free.

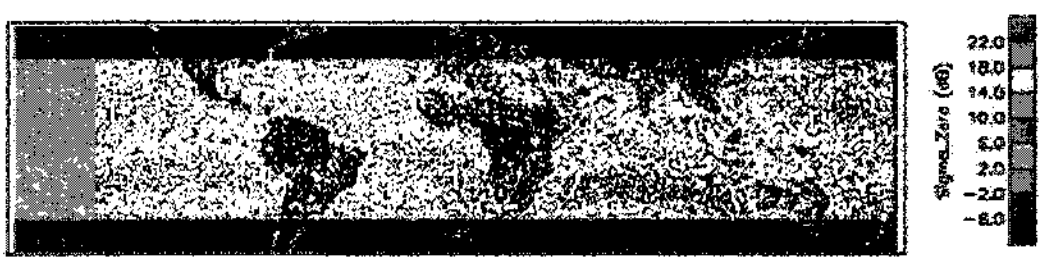

Figure 6.54: Average σ^0 at nadir for March 2000: rain-free.

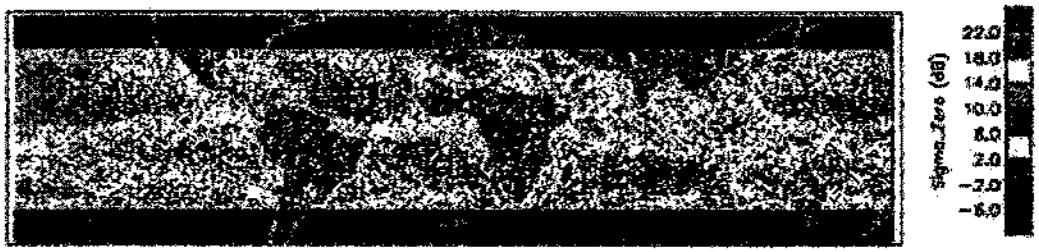

Figure 6.55: Average σ^0 at nadir for April 2000: rain-free.

Figure 6.56: Average σ^0 at nadir for May 2000: rain-free.

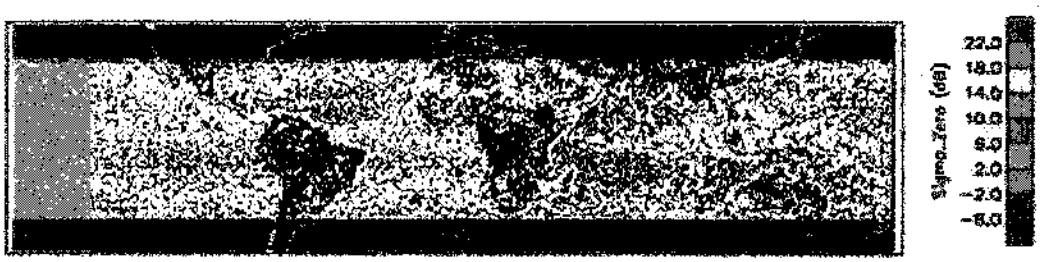

Figure 6.57: Average σ^0 at nadir for June 2000: rain-free.

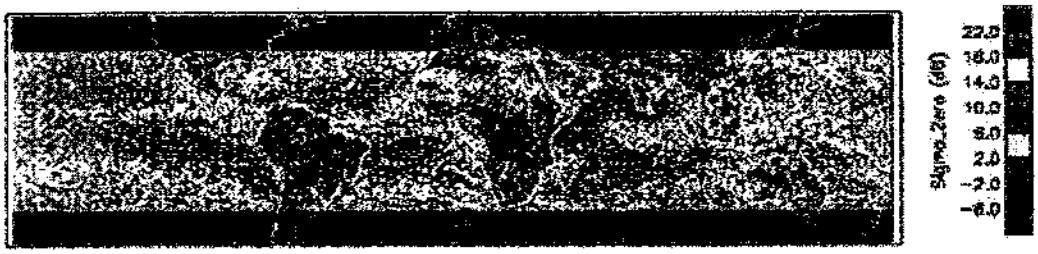

Figure 6.58: Average σ^0 at nadir for July 2000: rain-free.

Figure 6.59: Average σ^0 at nadir for August 2000: rain-free.

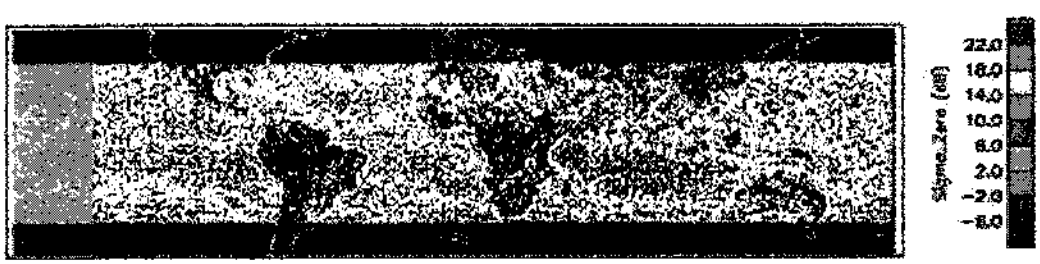

Figure 6.60: Average σ^0 at nadir for September 2000: rain-free.

Figure 6.61: Average σ^0 at nadir for October 2000: rain-free.

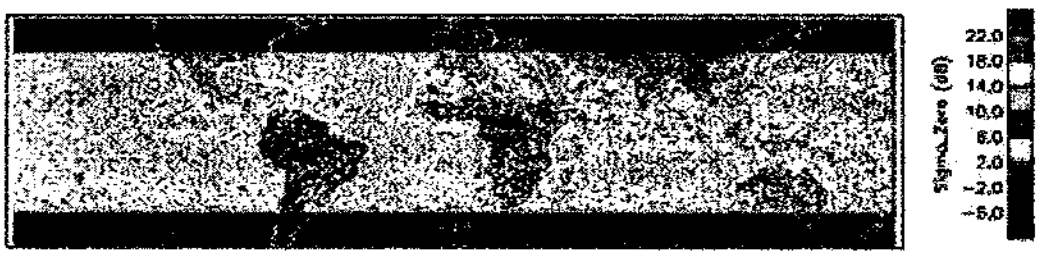

Figure 6.62: Average σ^0 at nadir for November 2000: rain-free.

Figure 6.63: Average σ^0 at nadir for December 2000: rain-free.

Figure 6.64: Average σ^0 at 5.68° for January 2000: rain-free.

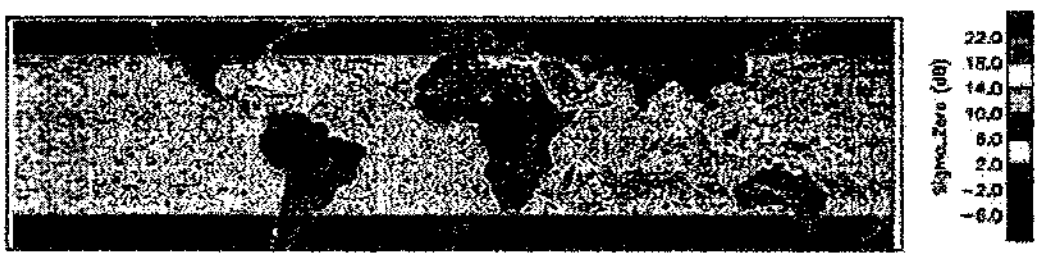

Figure 6.65: Average σ^0 at 5.68° for February 2000: rain-free.

Figure 6.66: Average σ^0 at 5.68° for March 2000: rain-free.

Figure 6.67: Average σ^0 at 5.68^o for April 2000: rain-free.

Figure 6.68: Average σ^0 at 5.68^o for May 2000: rain-free.

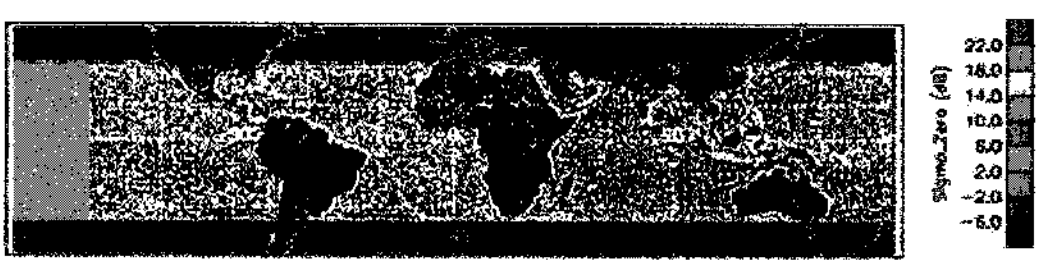

Figure 6.69: Average σ^0 at 5.68^o for June 2000: rain-free.

Figure 6.70: Average σ^0 at 5.68° for July 2000: rain-free.

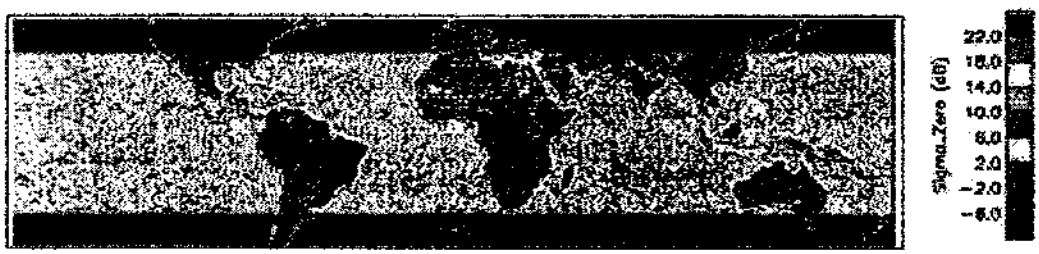

Figure 6.71: Average σ^0 at 5.68° for August 2000: rain-free.

Figure 6.72: Average σ^0 at 5.68° for September 2000: rain-free.

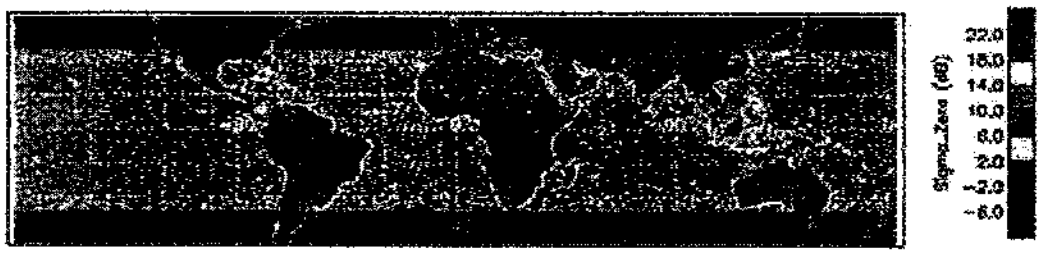

Figure 6.73: Average σ^0 at 5.68° for October 2000: rain-free.

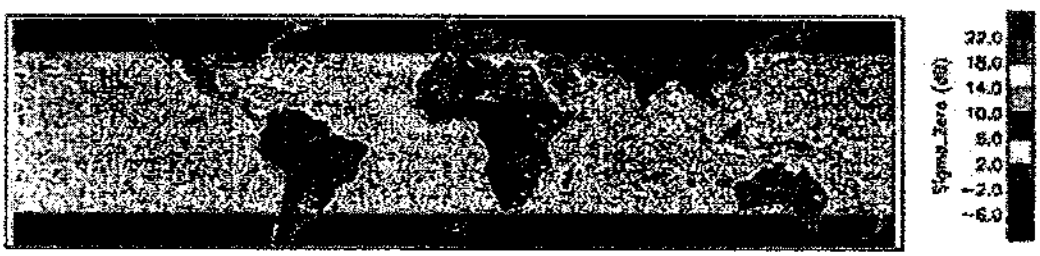

Figure 6.74: Average σ^0 at 5.68° for November 2000: rain-free.

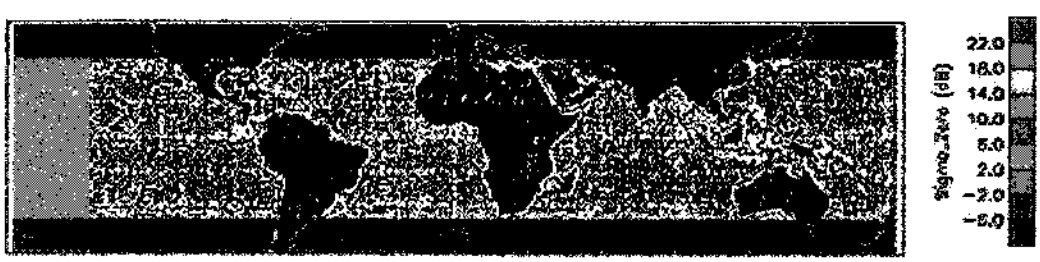

Figure 6.75: Average σ^0 at 5.68° for December 2000: rain-free.

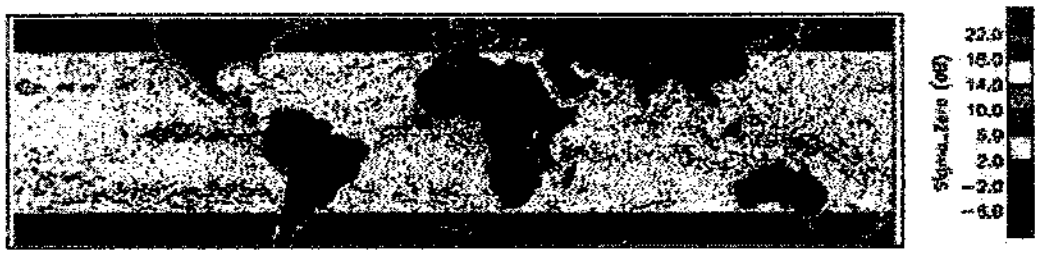

Figure 6.76: Average σ^0 at 13.49° for January 2000: rain-free.

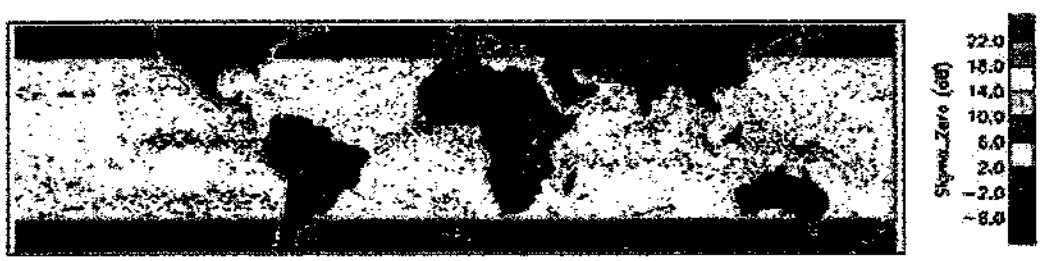

Figure 6.77: Average σ^0 at 13.49° for February 2000: rain-free.

Figure 6.78: Average σ^0 at 13.49° for March 2000: rain-free.

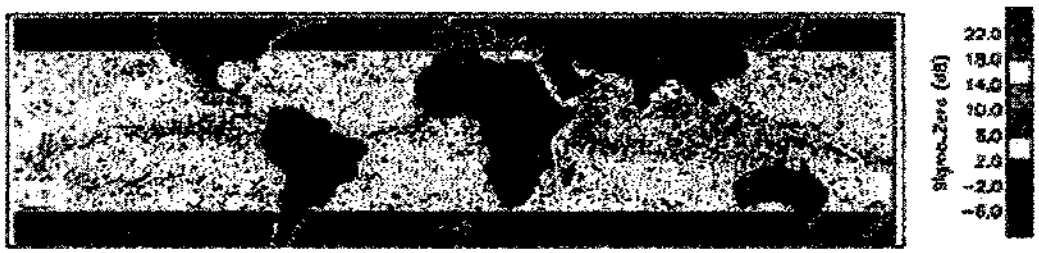

Figure 6.79: Average σ^0 at 13.49° for April 2000: rain-free.

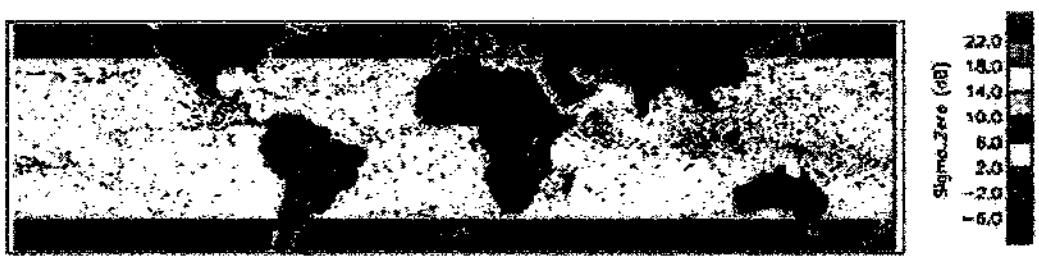

Figure 6.80: Average σ^0 at 13.49° for May 2000: rain-free.

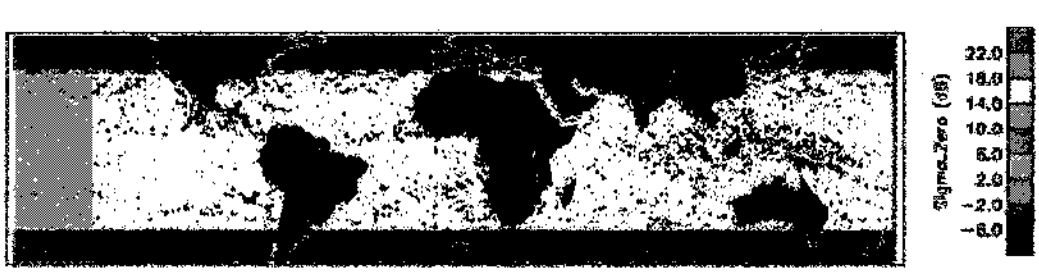

Figure 6.81: Average σ^0 at 13.49° for June 2000: rain-free.

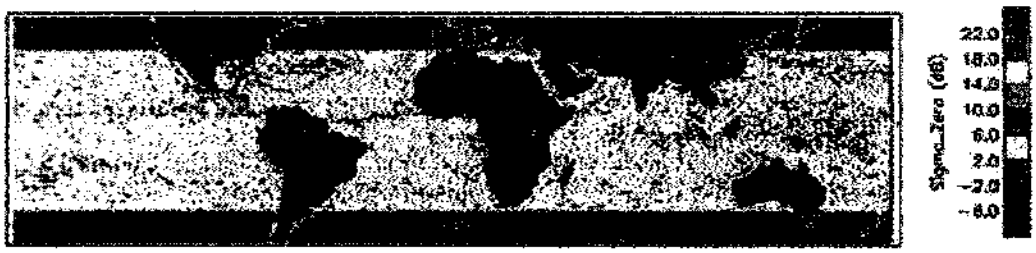

Figure 6.82: Average σ^0 at 13.49° for July 2000: rain-free.

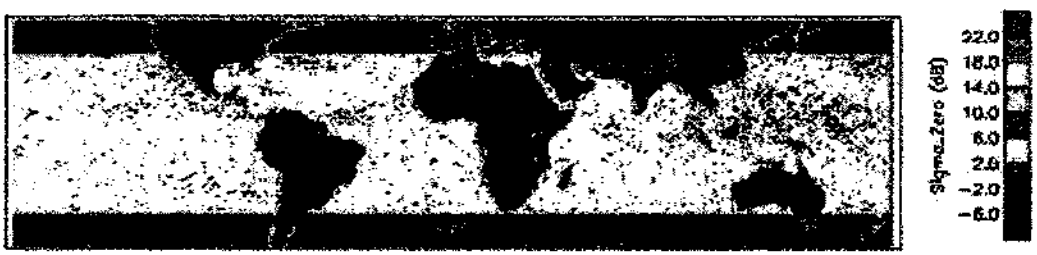

Figure 6.83: Average σ^0 at 13.49° for August 2000: rain-free.

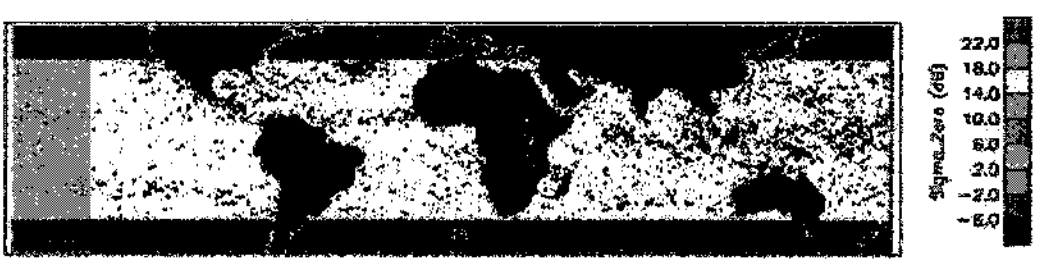

Figure 6.84: Average σ^0 at 13.49° for September 2000: rain-free.

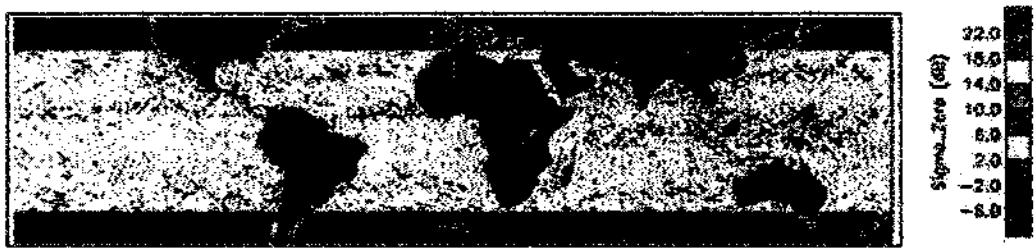

Figure 6.85: Average σ^0 at 13.49° for October 2000: rain-free.

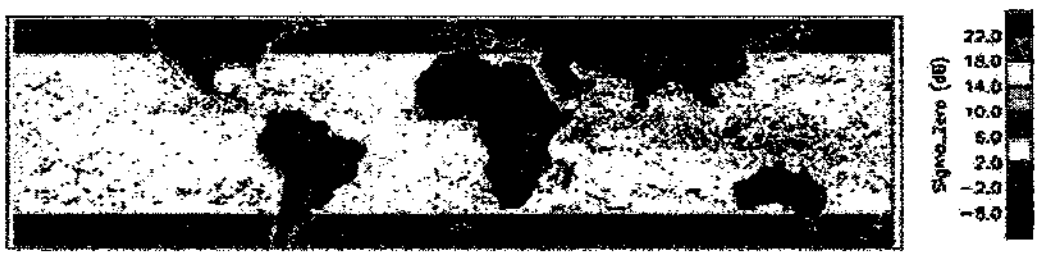

Figure 6.86: Average σ^0 at 13.49° for November 2000: rain-free.

Figure 6.87: Average σ^0 at 13.49° for December 2000: rain-free.

Chapter 7

MELTING LAYER

7.1 Introduction

Radar observations of the melting layer of precipitation have been made since the dawn of radar meteorology (Marshall et al., 1947; and, Cummingham, 1947). It has been known since then that the melting of precipitation is often associated with an enhancement of the reflectivity of weather targets. The primary cause of the enhancement is a rapid increase in the dielectric constant of hydrometeors at the top of the melting layer followed by an increase of the velocities of melting snowflakes toward the end of the melting process (Battan, 1973). The radar bright band results mostly from melting of snowflakes as they fall through the 0^oC isotherm. As the ice is gradually transformed to liquid, the refractive index and, hence, the backscattering cross section increase, and the radar echo intensity increases to a maximum at $\approx 200m$ below the 0^oC isotherm. The decrease of echo intensity below the bright band level is mostly the result of decreases of particle concentration caused by increases of terminal velocity as the particles melt. 2A23 data provides information about the height of bright band (HBB) as well as the height of freezing. HBB is generally close to the height of freezing (usually within $\pm$ 2 km).

In general, the bright band height is obviously linked with the height of the 0^oC isotherm in the atmosphere and consequently dependent on the time of the

year and on the climate (and hence the location). Therefore, it is very important to develop global maps of height of bright band and height of freezing as monthly maps. HBB is very important in the case of stratiform, while the freezing height is important in convective cases.

In this chapter, data from the TRMM PR are used to generate monthly maps of the height of bright band (HBB) over the globe for the year 2000, 3dB thickness of BB is developed, HBB over ocean and land and during some events such as hurricane are examined.

7.2 Global mapping of Height of Bright Band (HBB)

Table 7.1 provides an itemized list of the figures of the monthly average of height of bright band for the year 2000. The scales are adjusted to the full scale of each map. Each pixel in the plot is (0.5^o x 0.5^o) area, and therefore, of fairly high resolution. The overlay shows the standard map of land/ocean boundaries. The plots are restricted to the latitude of $\pm 35^o$ degrees coinciding with the coverage of TRMM PR.

Figure Number	Title Description
Figure 7.1	Height of bright band for January 2000
Figure 7.2	Height of bright band for February 2000
Figure 7.3	Height of bright band for March 2000
Figure 7.4	Height of bright band for April 2000
Figure 7.5	Height of bright band for May 2000
Figure 7.6	Height of bright band for June 2000
Figure 7.7	Height of bright band for July 2000
Figure 7.8	Height of bright band for August 2000
Figure 7.9	Height of bright band for September 2000
Figure 7.10	Height of bright band for October 2000
Figure 7.11	Height of bright band for November 2000
Figure 7.12	Height of bright band for December 2000

Table 7.1: Figure Number List of the Monthly Average of Height of Bright Band (HBB).

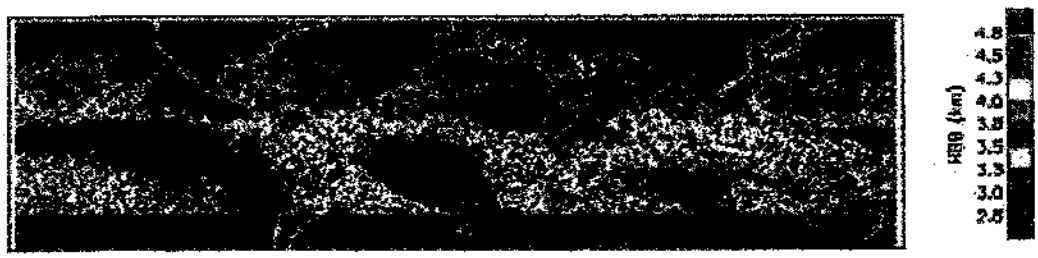

Figure 7.1: Height of Bright Band (HBB) for January 2000.

Figure 7.2: Height of Bright Band (HBB) for February 2000.

Figure 7.3: Height of Bright Band (HBB) for March 2000.

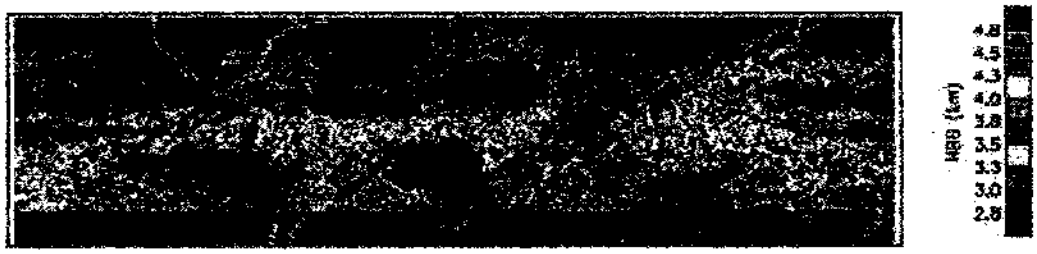

Figure 7.4: Height of Bright Band (HBB) for April 2000.

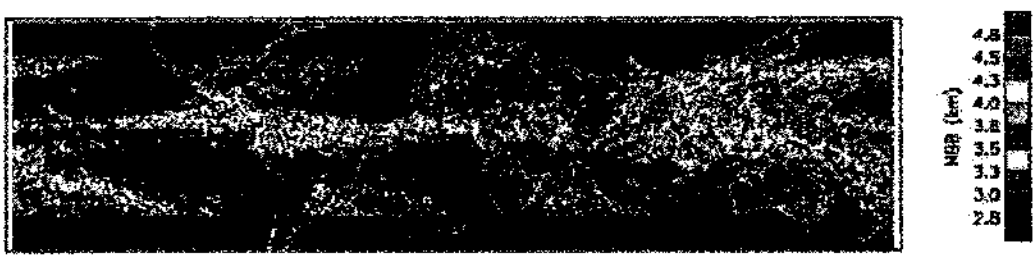

Figure 7.5: Height of Bright Band (HBB) for May 2000.

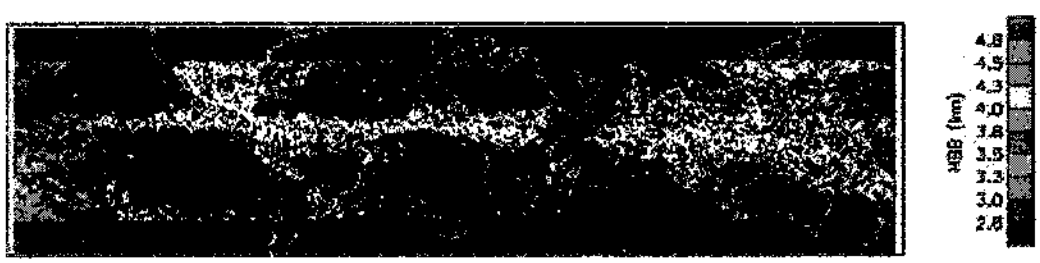

Figure 7.6: Height of Bright Band (HBB) for June 2000.

Figure 7.7: Height of Bright Band (HBB) for July 2000.

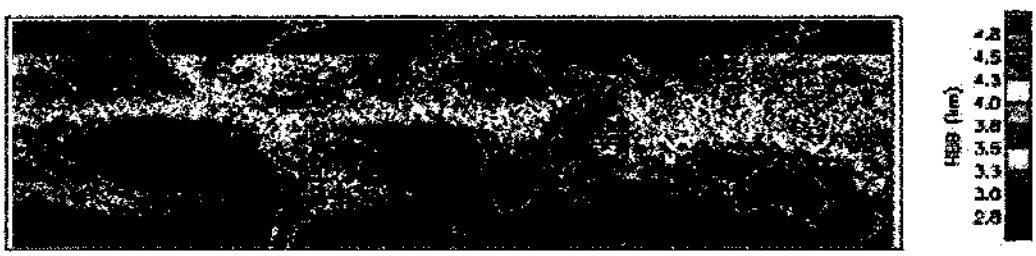

Figure 7.8: Height of Bright Band (HBB) for August 2000.

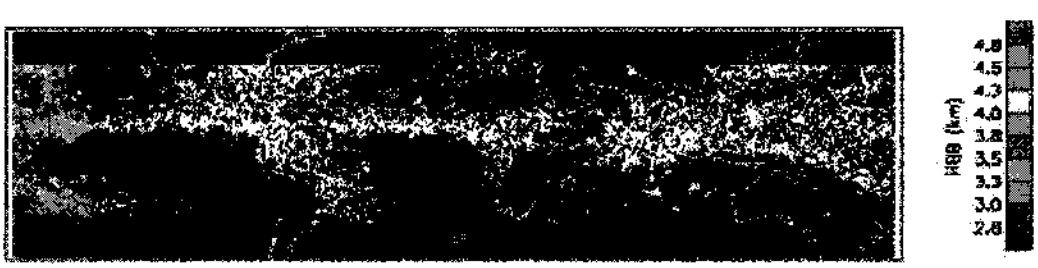

Figure 7.9: Height of Bright Band (HBB) for September 2000.

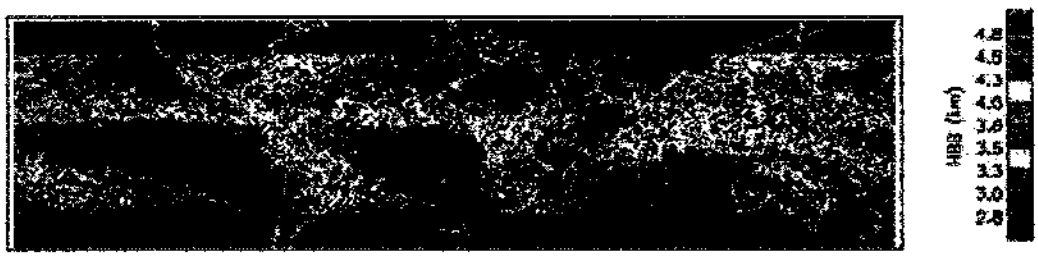

Figure 7.10: Height of Bright Band (HBB) for October 2000.

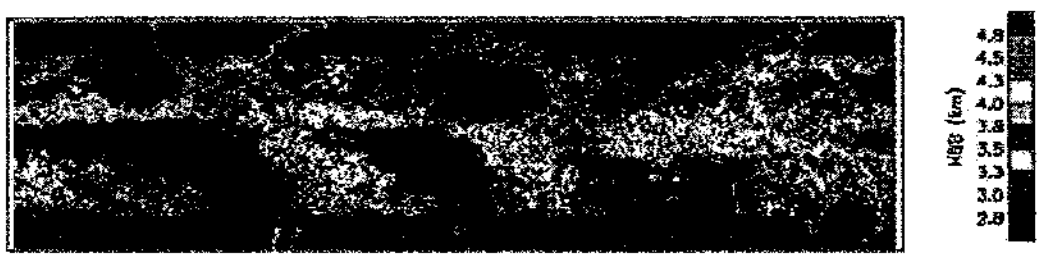

Figure 7.11: Height of Bright Band (HBB) for November 2000.

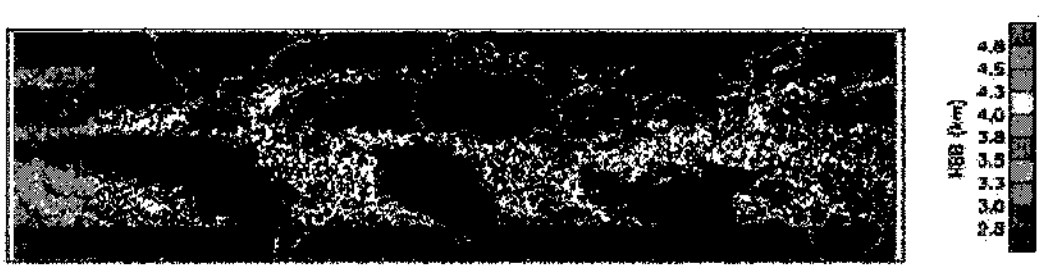

Figure 7.12: Height of Bright Band (HBB) for December 2000.

7.3 3dB Thickness of Bright Band

Although the qualitative explanation of the reflectivity enhancement causing the bright band was made earlier (Ryde, 1946), there is still no consensus after 50 years as to a quantitative assessment because the bright band is usually more intense than predicted. Early quantitative estimates (Austin and Bemis, 1950; Wexler, 1955; Wexler and Atlas, 1956; Lhermitte and Atlas, 1963) and models (Ekpenyong and Srivastave, 1970) either confirmed this observation or attempted to explain the differences through shape effects (non-sphericity of snowflakes and melting snowflakes, Atlas et al., 1953) or by growth of precipitation through condensation and aggregation at the top of the melting layer followed by breakup below. This aggregation-breakup combination appeared essential in all cases to explain the bright band intensity and several in-situ or aircraft measurements were attempted to verify this claim. Recent models (Dissanayake and McEwan, 1978; Klaassen, 1988; Hardaker et al., 1991) either obtain correct reflectivity enhancement or overestimate the bright band intensity by considering the bright band enhancement to be caused by the melting of low-density snowflakes alone.

Figure 7.13 shows the schematic of the current TRMM model for the bright band thickness for the case of stratiform precipitation. From Figure 7.13, it is clear that the current TRMM bright band thickness is considered to be 1km and this is not accurate. Therefore, it is necessary to develop a model to estimate the bright band thickness.

Figure 7.14 illustrates a smooth profile with bright band thickness and various parameters that are related to it. Z_{max} is the maximum reflectivity and occurred at the peak of the bright band, h_{top} is the height of the bright band top, h_{bot} is the height of the bright band bottom, and B is the bright band thickness. The following steps are used to estimate the 3dB thickness of BB:

1. The first step is to locate the maximum reflectivity (Z_{max}).

2. The second step is to locate the height of the bright band top (h_{top}). Klaassen (1988) uses either the height where the reflectivity reaches a value equal to the reflectivity of the rain below the bright band or the height at which the slope of the reflectivity profile is maximum. Fabry (1994) defined h_{top} as the height at which the curvature in $\log(Z)$ is maximum. In this research, since the TRMM data are used and these profiles are not smooth compared to ground radar data, it was decided to define h_{top} as the height at which the Z_{max} dropped by 3dB.

3. The third step is to locate the height of the bright band bottom (Z_{bot}). Similar criterion to h_{top} are used to define Z_{bot}.

Once the bright band boundaries are determined, the 3dB thickness, B, of reflectivity can be estimated as

$$B = h_{top} - h_{bot} \tag{7.1}$$

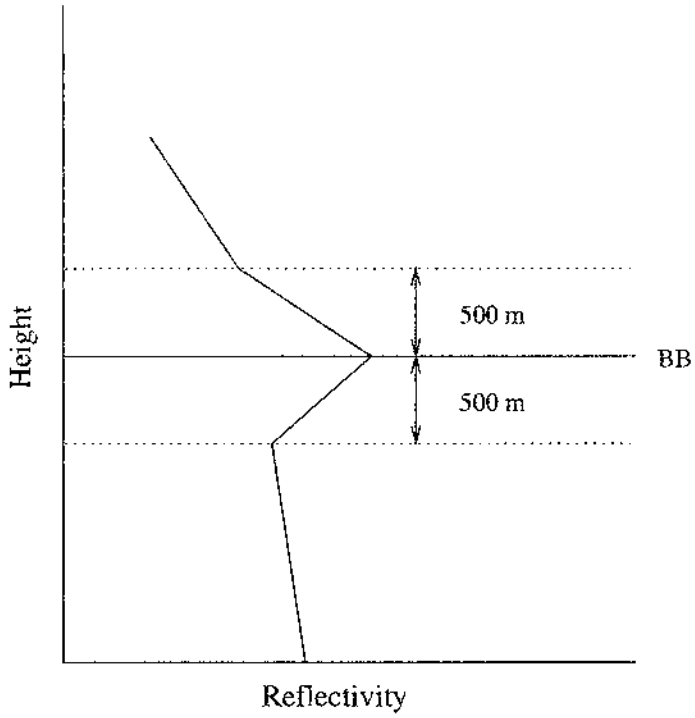

Figure 7.13: Schematic illustrating bright band thickness for TRMM stratiform.

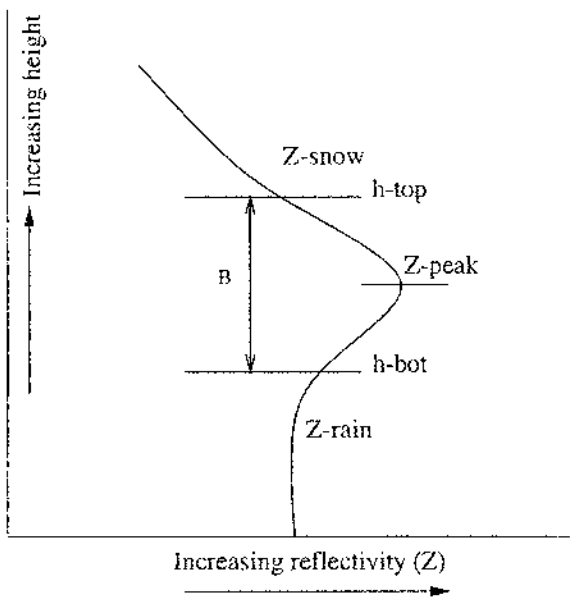

Figure 7.14: Schematic illustrating bright band thickness.

Figure 7.15: Orbit path of Case Study 1: 13 August 1998, Orbit 4085.

7.3.1 Data Analysis

Using the dataset collected by the TRMM PR, the above algorithm was used to estimate the bright band thickness for stratiform precipitation. Several cases were studied; three specific case studies are presented in detail. For each case study, there are six vertical cases, scatterplot of B versus Z_{max} and finally the histogram of B.

7.3.1.1 Case Study 1: 13 August 1998

In this case study, the data from the August 13 1998 orbit number 4085 is used to examine the 3dB thickness of reflectivity by using the algorithm that has been developed in the previous section. Figure 7.15 shows the location of this specific orbit. Figures 7.16 to 7.21 show the vertical reflectivity profiles with estimated 3dB thickness and the bright band boundaries. Note that the De-noising wavelet is first applied to the vertical reflectivity profile in order to make it smooth and then the bright band algorithm is used. The mean value of 3dB thickness is found to be 0.87 km for this specific orbit. Figures 7.24 and 7.25 show the histogram of 3dB thickness of BB over land and the ocean at the incident angles between $\pm 5^{\circ}$ from nadir.

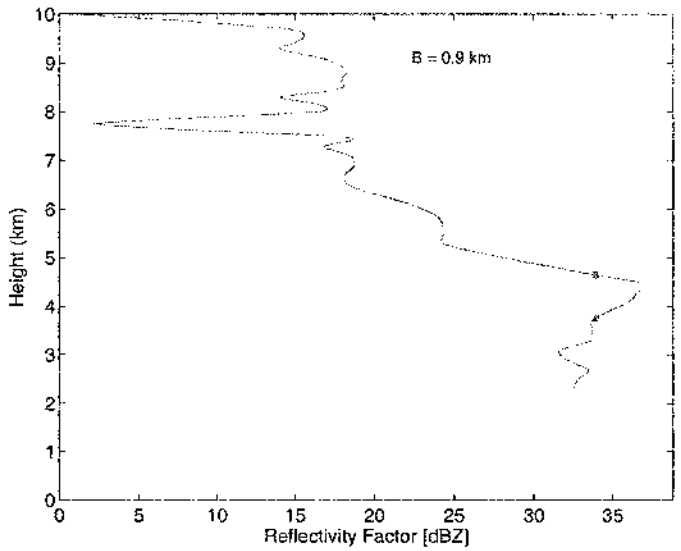

Figure 7.16: 3dB thickness of BB for Case Study 1, ray 12 and scan 1994.

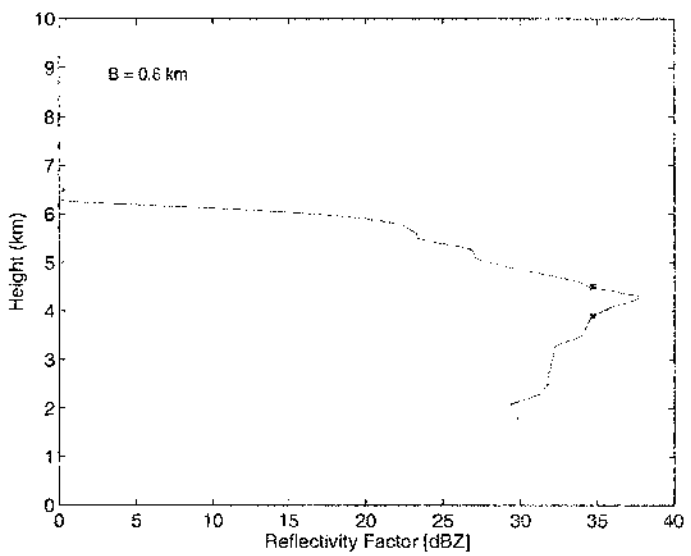

Figure 7.17: 3dB thickness of BB for Case Study 1, ray 13 and scan 1994.

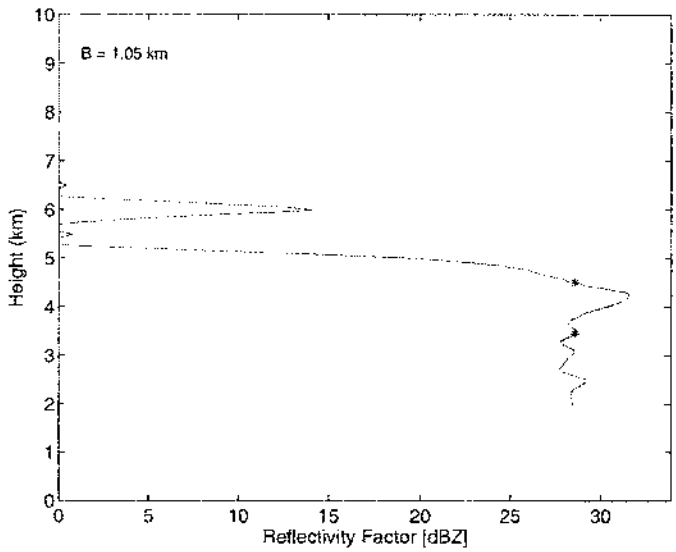

Figure 7.18: 3dB thickness of BB for Case Study 1, ray 13 and scan 2001.

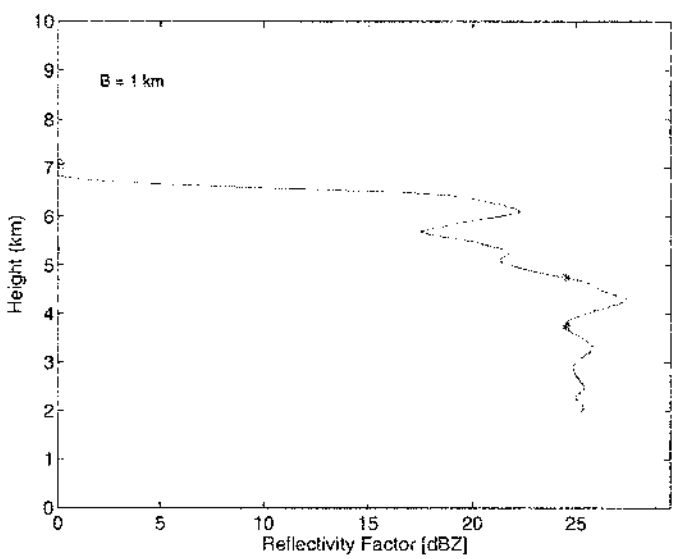

Figure 7.19: 3dB thickness of BB for Case Study 1, ray 35 and scan 2665.

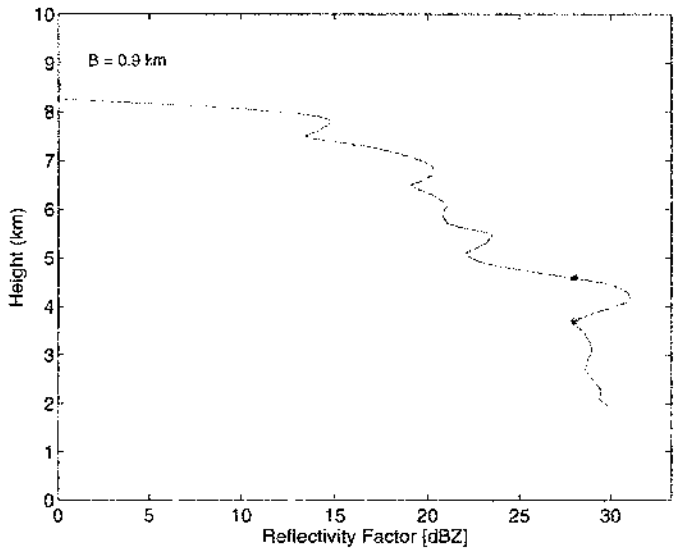

Figure 7.20: 3dB thickness of BB for Case Study 1, ray 12 and scan 2730.

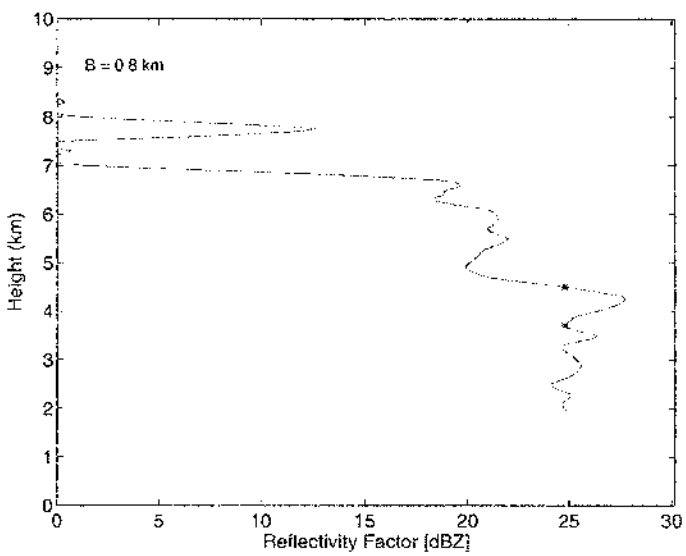

Figure 7.21: 3dB thickness of BB for Case Study 1, ray 13 and scan 2730.

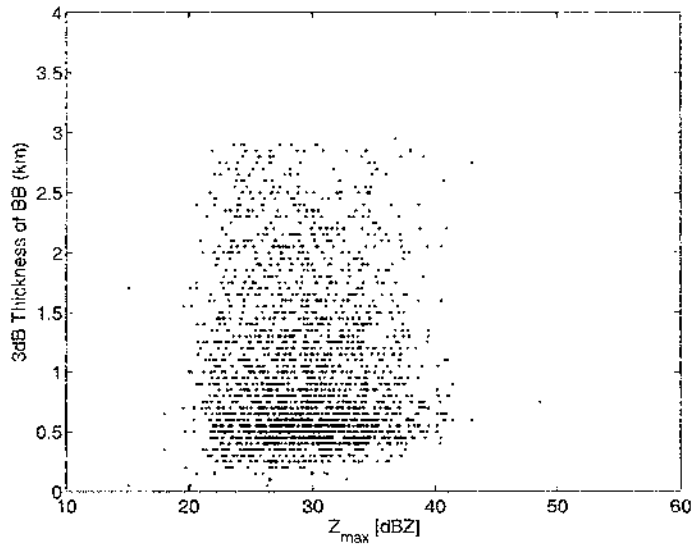

Figure 7.22: Scatterplot of Z_{max} versus 3dB thickness of BB for Case Study 1.

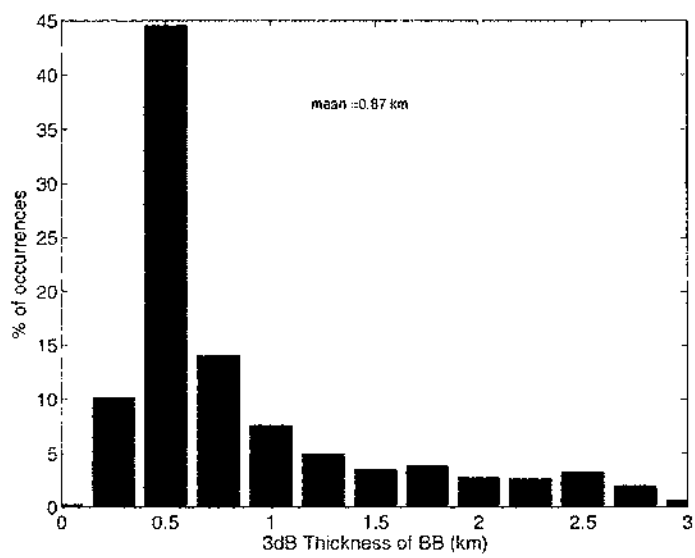

Figure 7.23: Histogram of 3dB thickness of BB at the incident angles between $\pm 5^o$ for Case Study 1.

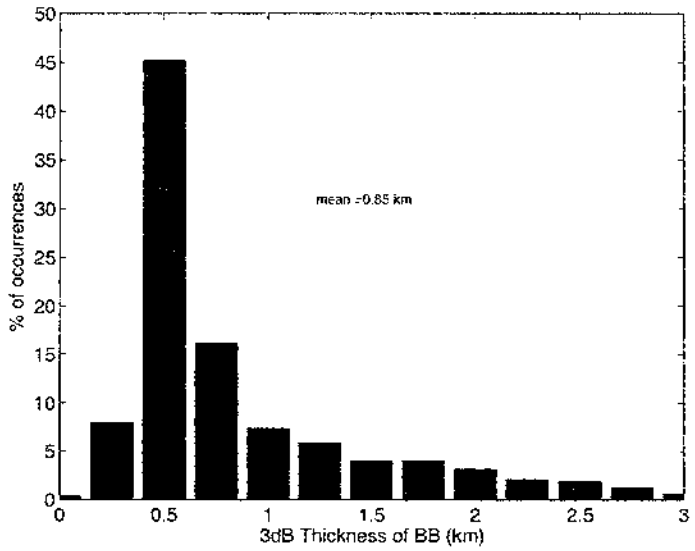

Figure 7.24: Histogram of 3dB thickness of BB for Case Study 1 over land at the incident angles between $\pm 5^o$.

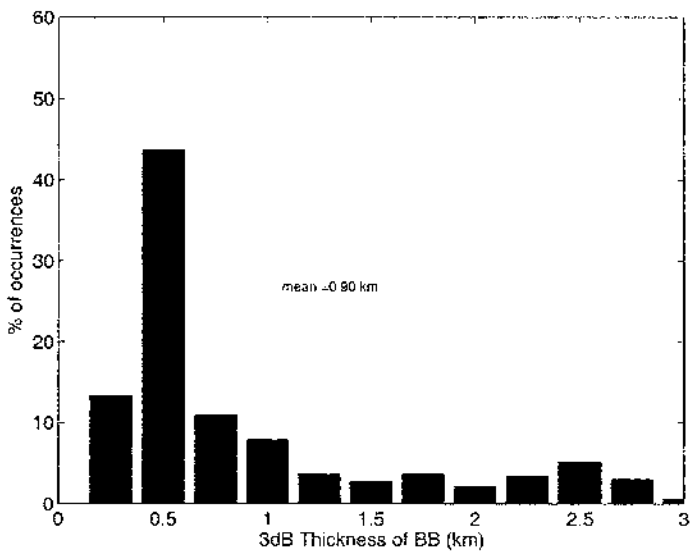

Figure 7.25: Histogram of 3dB thickness of BB for Case Study 1 over the ocean at the incident angles between $\pm 5^o$.

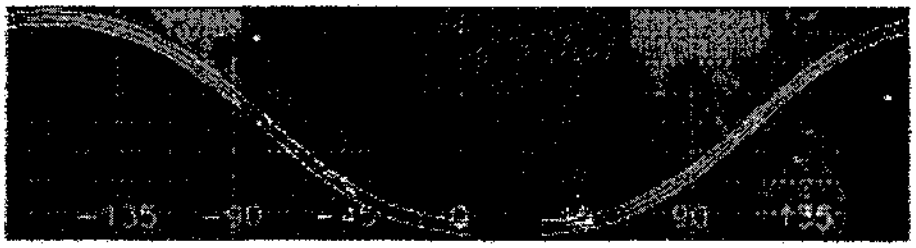

Figure 7.26: Orbit path of Case Study 2: 25 February 1999, Orbit 7174.

7.3.1.2 Case Study 2: 25 February 1999

In this case study, the data from the February 25, 1999 orbit number 7174 is used to examine the 3dB thickness of reflectivity by using the algorithm that has been developed in the previous section. Figure 7.26 shows the location of this specific orbit. Figures 7.27 to 7.32 show the vertical reflectivity profiles with estimated 3dB thickness and the bright band boundaries. Note that the De-noising wavelet is first applied to the vertical reflectivity profile in order to make it smooth and then the bright band algorithm is used. The mean value of 3dB thickness is found to be 0.78 km for this specific orbit. Figures 7.35 and 7.36 show the histogram of 3dB thickness of BB over land and the ocean at the incident angles between $\pm 5^{o}$ from nadir.

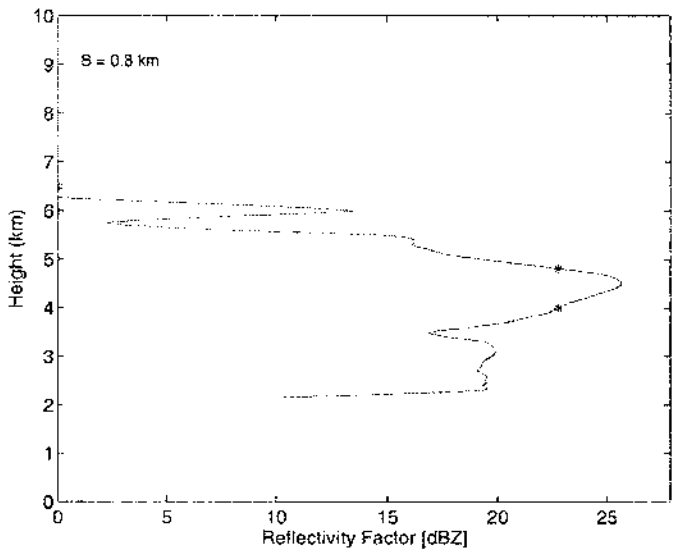

Figure 7.27: 3dB thickness of BB for Case Study 2, ray 41 and scan 5078.

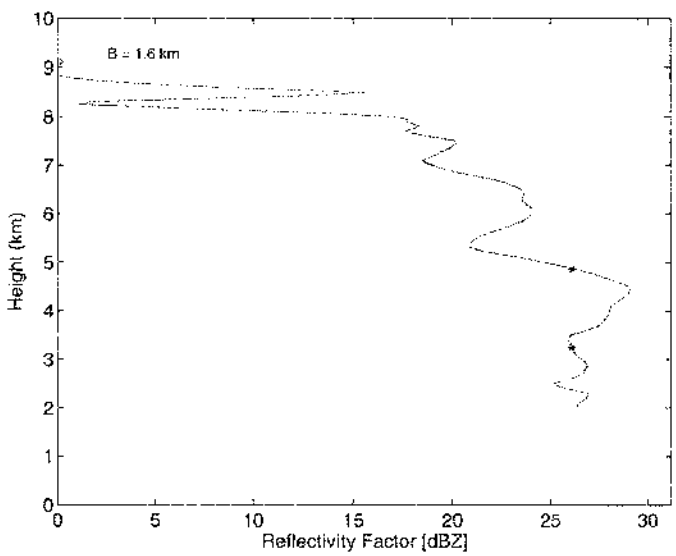

Figure 7.28: 3dB thickness of BB for Case Study 2, ray 41 and scan 5120.

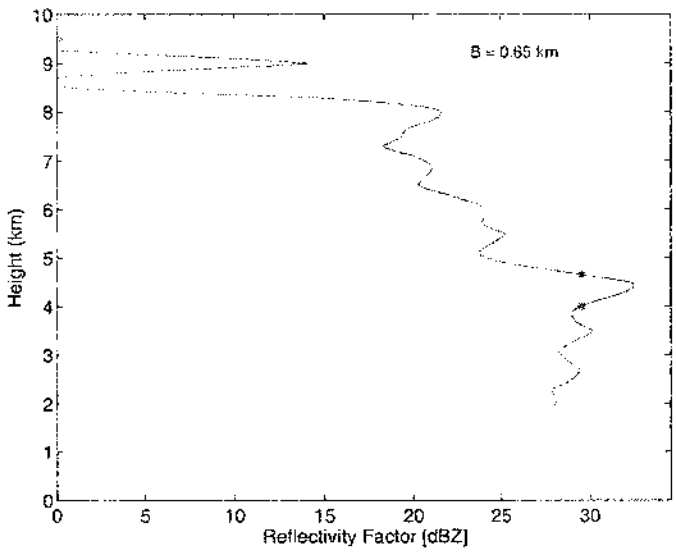

Figure 7.29: 3dB thickness of BB for Case Study 2, ray 42 and scan 5120.

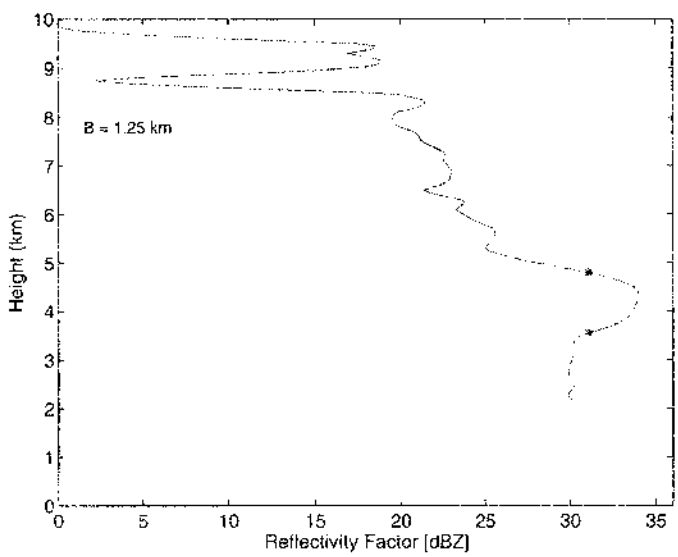

Figure 7.30: 3dB thickness of BB for Case Study 2, ray 44 and scan 5120.

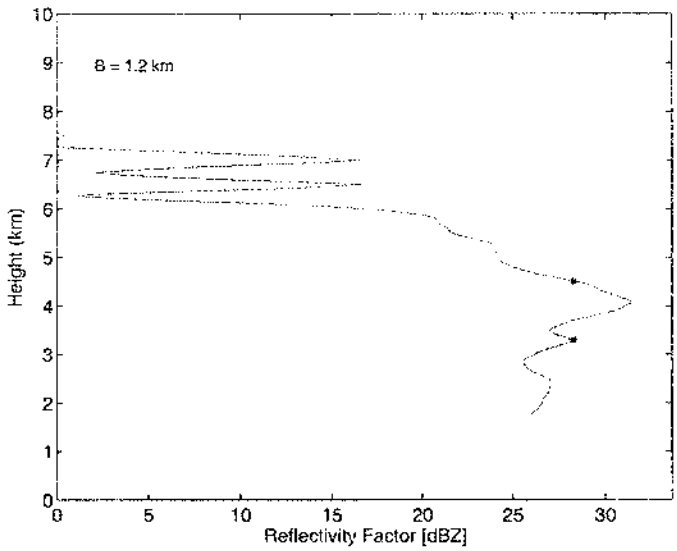

Figure 7.31: 3dB thickness of BB for Case Study 2, ray 39 and scan 5125.

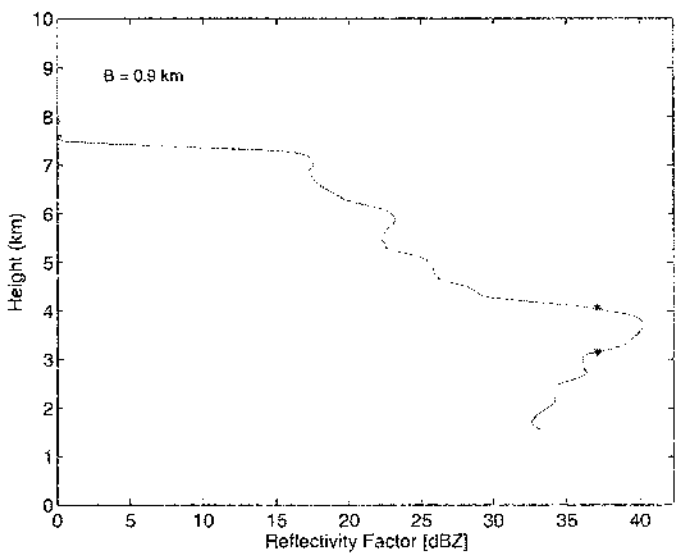

Figure 7.32: 3dB thickness of BB for Case Study 2, ray 26 and scan 5231.

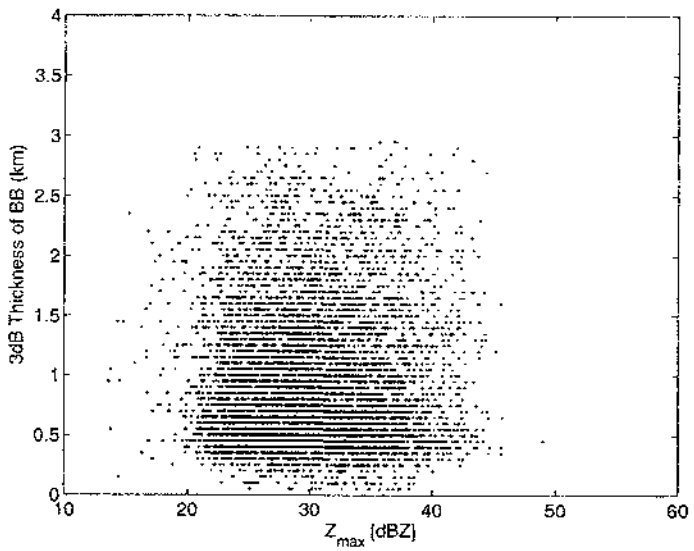

Figure 7.33: Scatterplot of Z_{max} versus 3dB thickness of BB for Case Study 2.

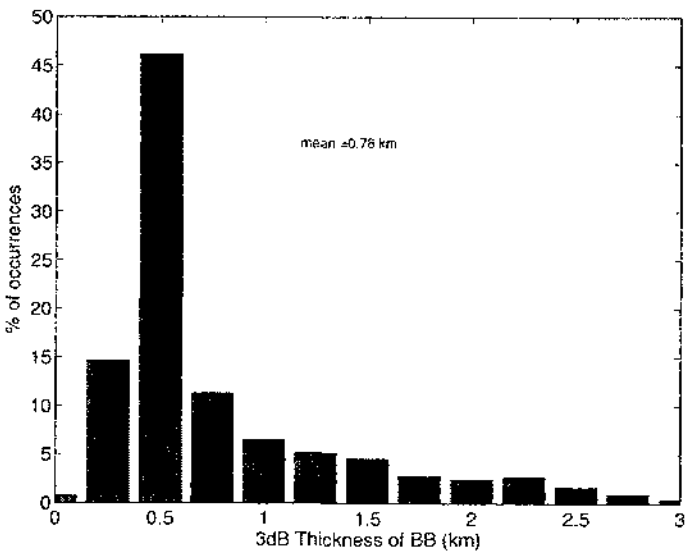

Figure 7.34: Histogram of 3dB thickness of BB at the incident angles between $\pm 5^o$ for Case Study 2.

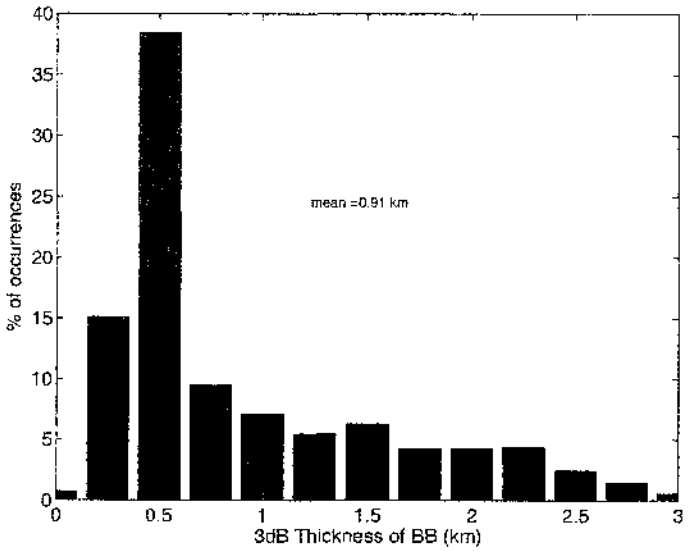

Figure 7.35: Histogram of 3dB thickness of BB for Case Study 2 over land at the incident angles between $\pm 5^{o}$.

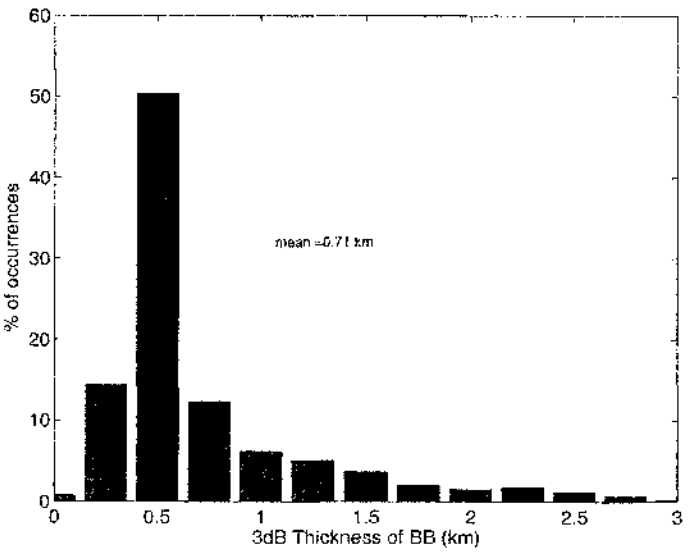

Figure 7.36: Histogram of 3dB thickness of BB for Case Study 2 over the ocean at the incident angles between $\pm 5^{o}$.

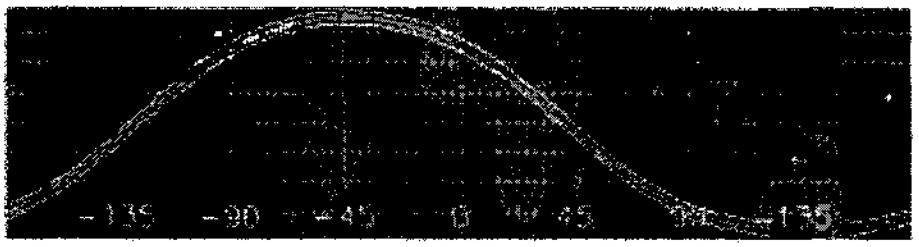

Figure 7.37: Orbit path of Case Study 3: 1 July 2000, Orbit 14933.

7.3.1.3 Case Study 3: 1 July 2000

In this case study, the data from the July 1st 2000 orbit number 14933 is used to examine the 3dB thickness of reflectivity by using the algorithm that has been developed in the previous section. Figure 7.37 shows the location of this specific orbit. Figures 7.38 to 7.43 show the vertical reflectivity profiles with estimated 3dB thickness and the bright band boundaries. Note that the De-noising wavelet is first applied to the vertical reflectivity profile in order to make it smooth and then the bright band algorithm is used. The mean value of 3dB thickness is found to be 0.74 km for this specific orbit. Figures 7.46 and 7.47 show the histogram of 3dB thickness of BB over land and the ocean at the incident angles between $\pm 5^{o}$ from nadir.

It is clear from these figures that 3dB thickness of reflectivity is very close to what has been suggested by TRMM for the bright band of stratiform precipitation (1 km).

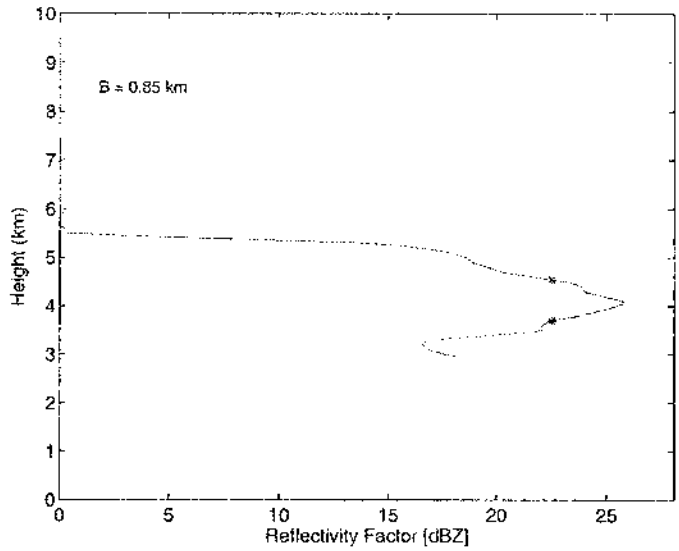

Figure 7.38: 3dB thickness of BB for Case Study 3, ray 3 and scan 1271.

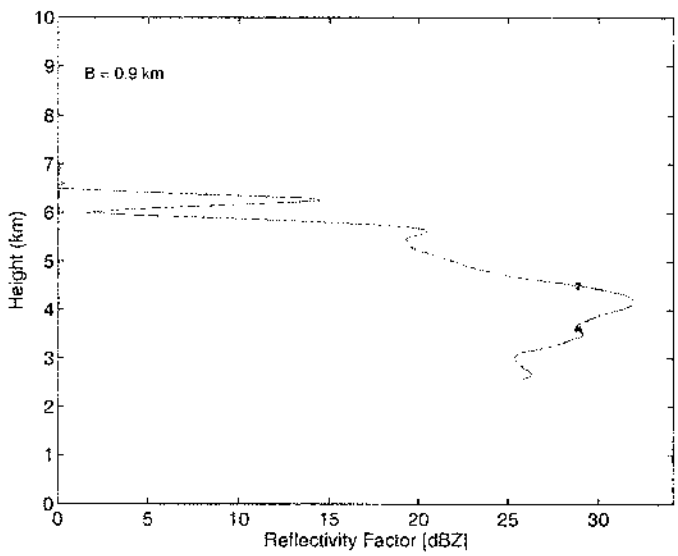

Figure 7.39: 3dB thickness of BB for Case Study 3, ray 44 and scan 1433.

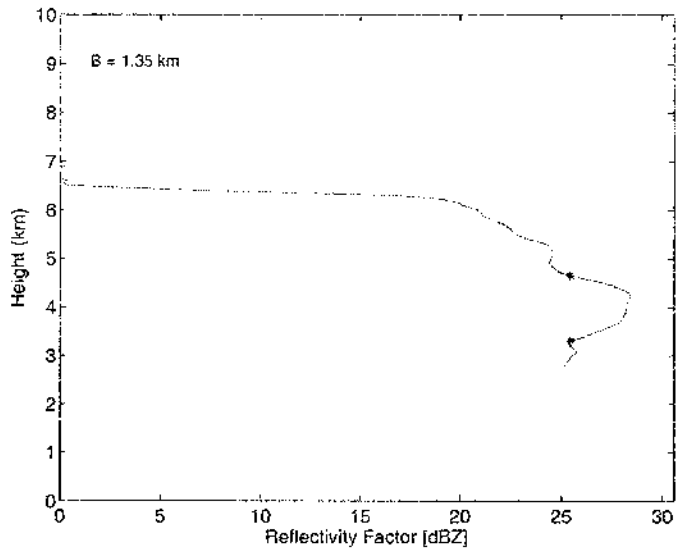

Figure 7.40: 3dB thickness of BB for Case Study 3, ray 42 and scan 1434.

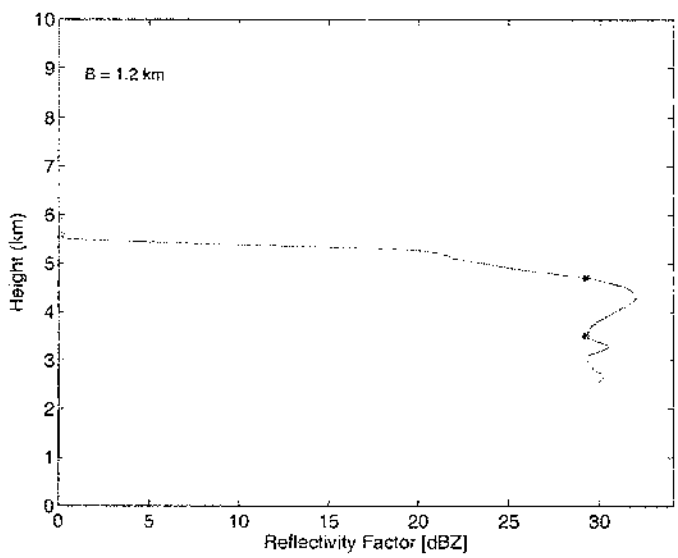

Figure 7.41: 3dB thickness of BB for Case Study 3, ray 42 and scan 1436.

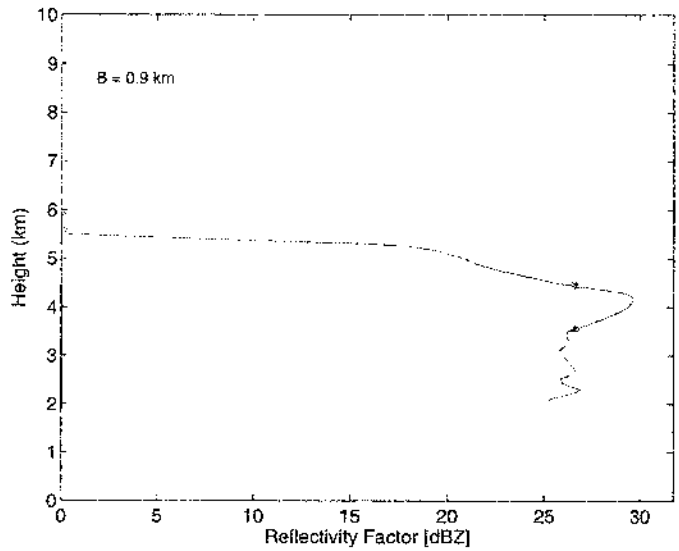

Figure 7.42: 3dB thickness of BB for Case Study 3, ray 12 and scan 1477.

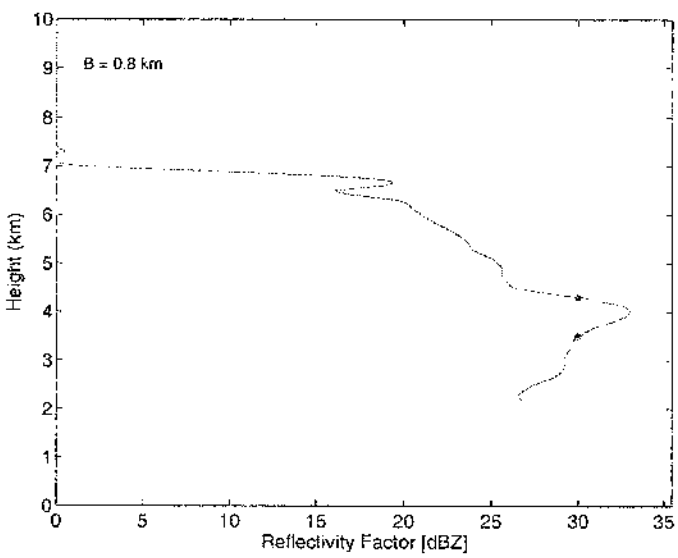

Figure 7.43: 3dB thickness of BB for Case Study 3, ray 16 and scan 1481.

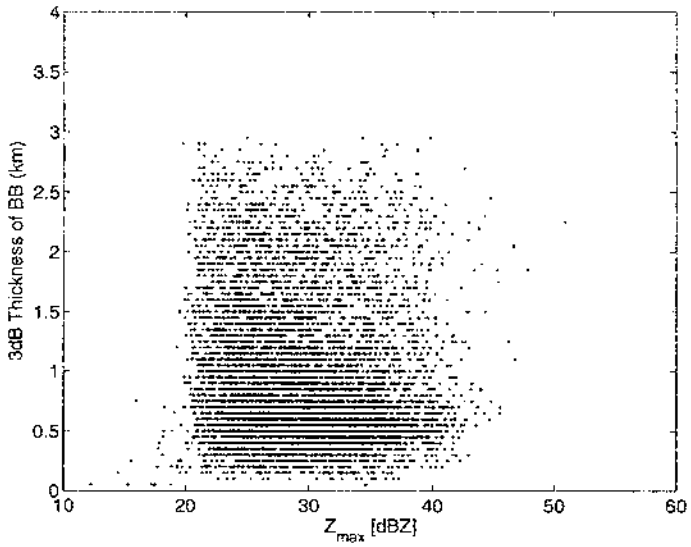

Figure 7.44: Scatterplot of Z_{max} versus 3dB thickness of BB for Case Study 3.

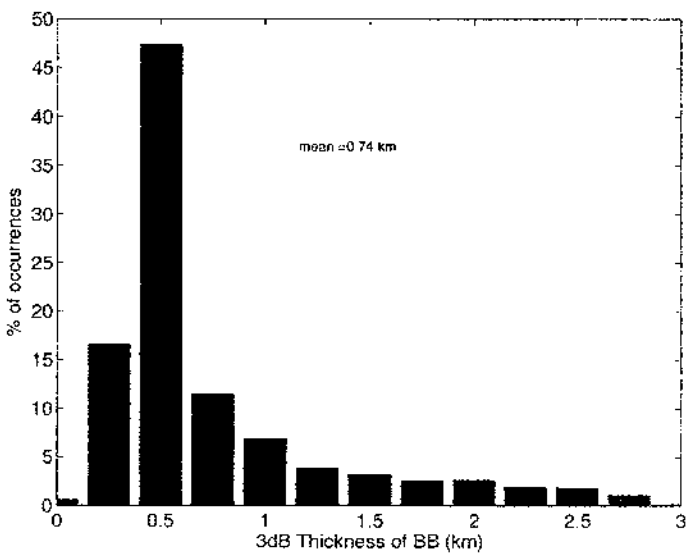

Figure 7.45: Histogram of 3dB thickness of BB at the incident angles between $\pm 5^o$ for Case Study 3.

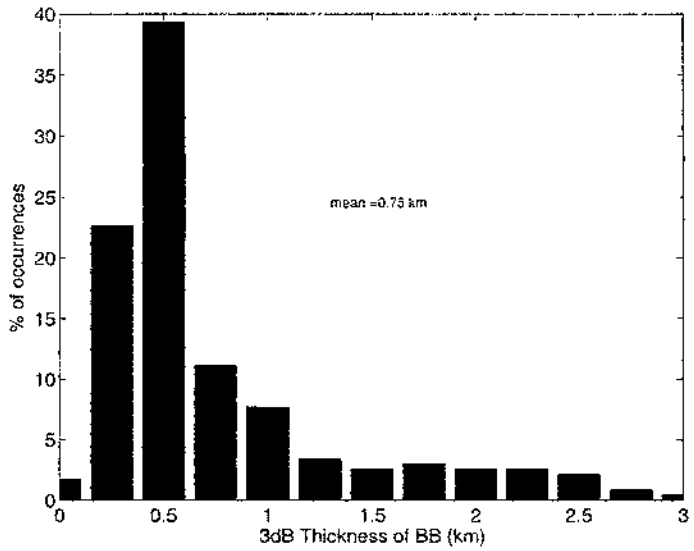

Figure 7.46: Histogram of 3dB thickness of BB for Case Study 3 over land at the incident angles between $\pm 5^{o}$.

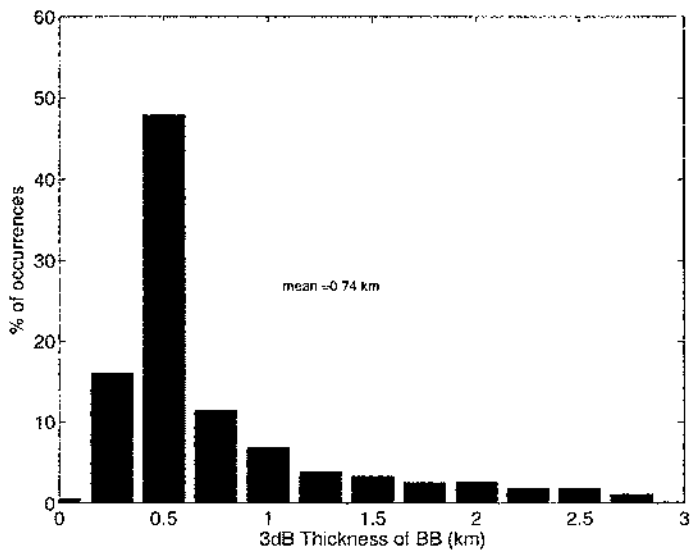

Figure 7.47: Histogram of 3dB thickness of BB for Case Study 3 over the ocean at the incident angles between $\pm 5^{o}$.

7.4 Examination of HBB during Hurricane Events

Data from TRMM PR were used to examine HBB during huge events, such as hurricanes. Two different examples were selected as case studies.

7.4.1 Case Study 1: Hurricane Bonnie, 25 August 1998

The PR measurements were taken on 25 August 1998, orbit number 4267, over Hurricane Bonnie located off the southeast coast of the United States as it is shown in Figures 7.48 and 7.49. The overpass occurred at 1114 UTC where the location that corresponds to the midpoint of the square box in Figure 7.48 is $30.59^{o}N$ and $-72.43^{o}E$. Table 7.2 shows the summary of the data used for analysis in this case study. Figure 7.50 shows histograms of HBB over the Hurricane Bonnie location during the hurricane time and non-hurricane time. Note that the first plot in Figure 7.50, a, corresponds to the HBB during the hurricane time, while the rest of the plots, b to f, correspond to the same location but during normal rain. It is clear from these plots that the HBB changes from season to season, while the standard deviation keeps stays almost the same.

Date	Orbit Number	Scan Number
08/25/1998	4267	3760-3960
01/24/1998	902	3741-3941
05/11/1999	8345	5406-5606
04/16/2000	13729	3891-4091
09/29/2000	16353	3741-3941
12/29/2000	17776	5318-3518

Table 7.2: Summary of Data Used to Examine HBB over the Hurricane Bonnie Region.

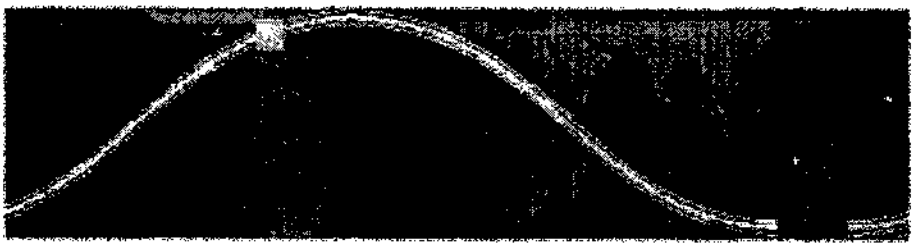

Figure 7.48: Location of Hurricane Bonnie, 25 August 1998.

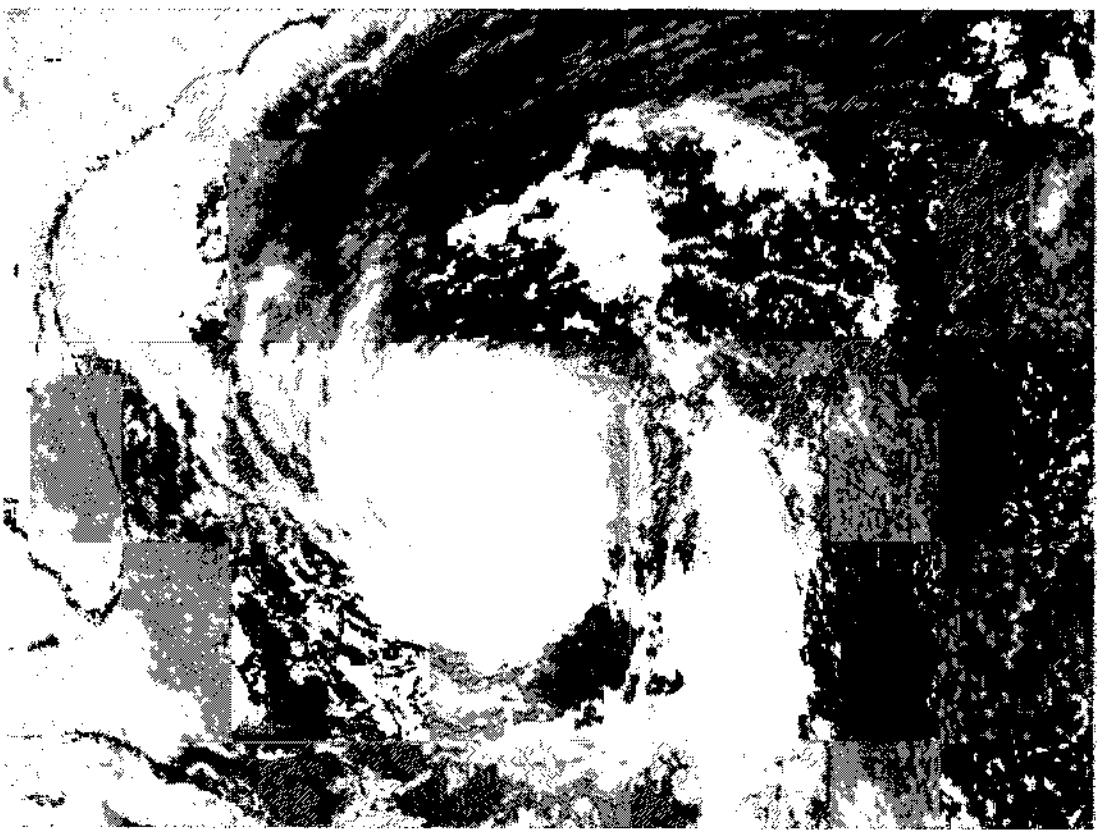

Figure 7.49: Hurricane Bonnie, 25 August 1998.

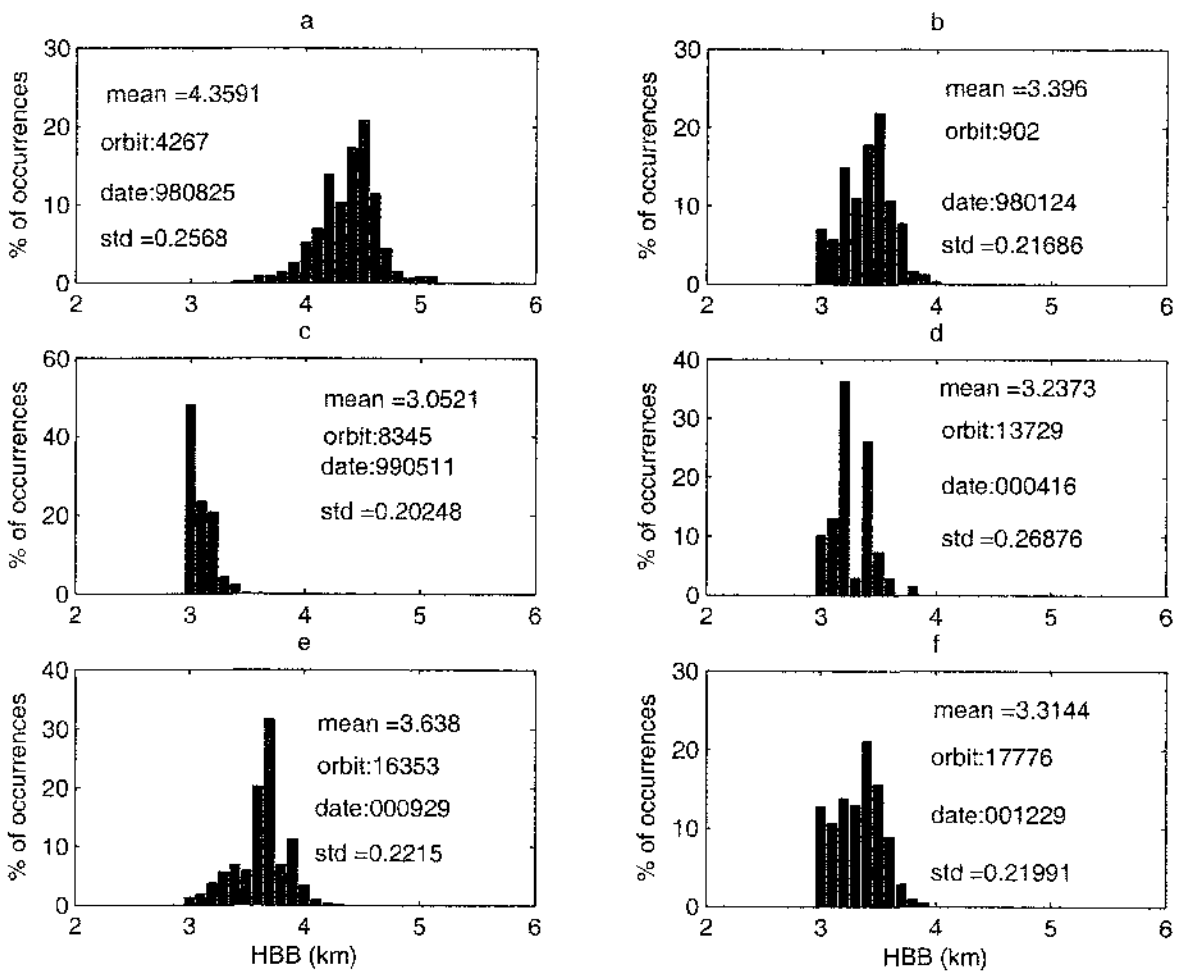

Figure 7.50: Histograms of HBB: a) during Hurricane Bonnie b-f) same location during other times but different months.

7.4.2 Case Study 2: Typhoon Jelawat, 7 August 2000

The PR measurements were taken on 7 August 2000, orbit number 15514, over Typhoon Jelawat located near the island of Minami Daito Jima, Japan in the western Pacific as it is shown in Figures 7.51 and 7.52. The overpass occurred at 1701 UTC where the location that corresponds to the midpoint of the square box in Figure 7.51 is $26.74^{o}N$ and $128.47^{o}E$. Table 7.3 shows the summary of the data used for analysis in this case study. Figure 7.53 shows histograms of HBB over the Typhoon Jelawat location during the typhoon time and non-typhoon time. Note that the first plot in Figure 7.53, a, corresponds to the HBB during the typhoon time, while the rest of the plots, b to f, correspond to the same location but during normal rain. It is clear from these plots that the HBB changes from season to season while the standard deviation stays almost the same. Figure 7.54 shows the histograms of HBB during the Typhoon Jelawat time and the normal rain but for the same month. It is clear from this figure that the HBB for the same month is almost constant for the same location even if there is a huge events such as a typhoon.

Date	Orbit Number	Scan Number
08/07/2000	15514	5487- 5617
03/23/2000	13353	5488-5618
04/01/2000	13492	5524-5654
05/22/2000	14291	3518-3648
07/30/2000	15387	3556-3686
07/31/2000	15486	5513-5643

Table 7.3: Summary of Data Used to Examine HBB over the Typhoon Jelawat Region.

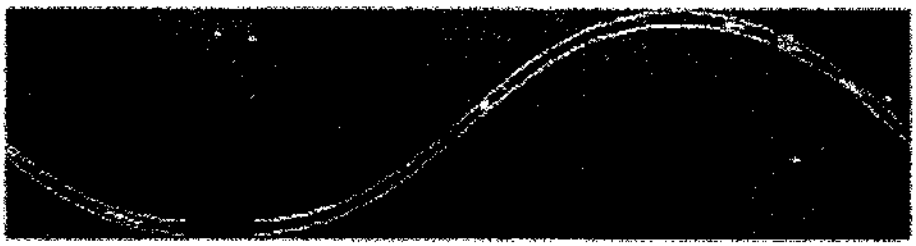

Figure 7.51: Location of Typhoon Jelawat, 7 August 2000.

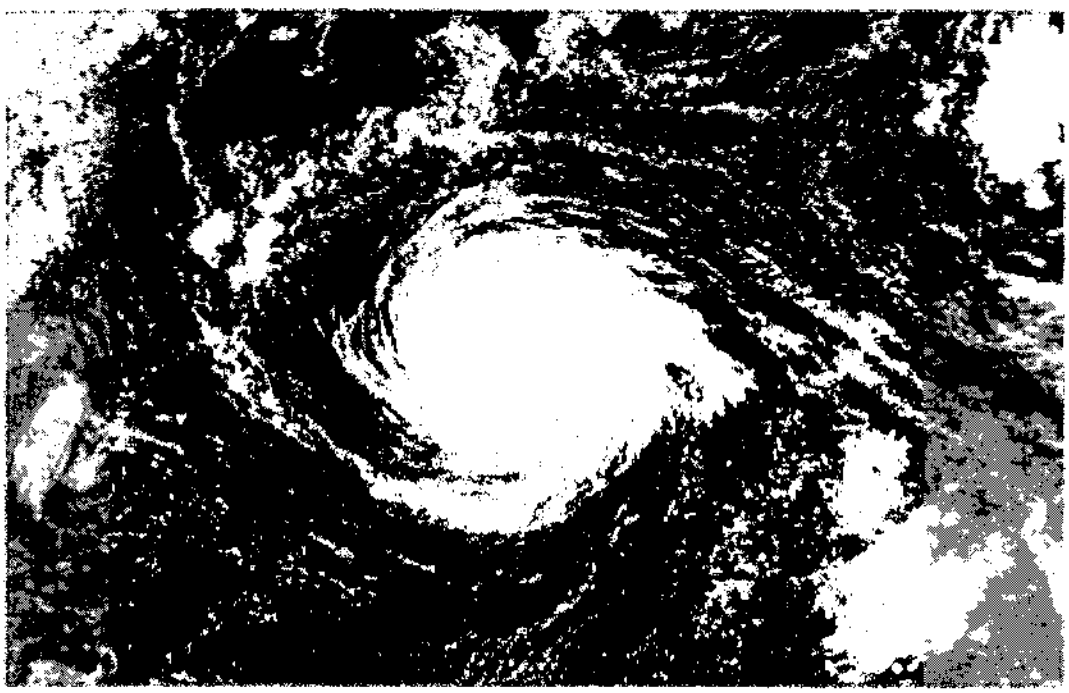

Figure 7.52: Typhoon Jelawat, 7 August 2000.

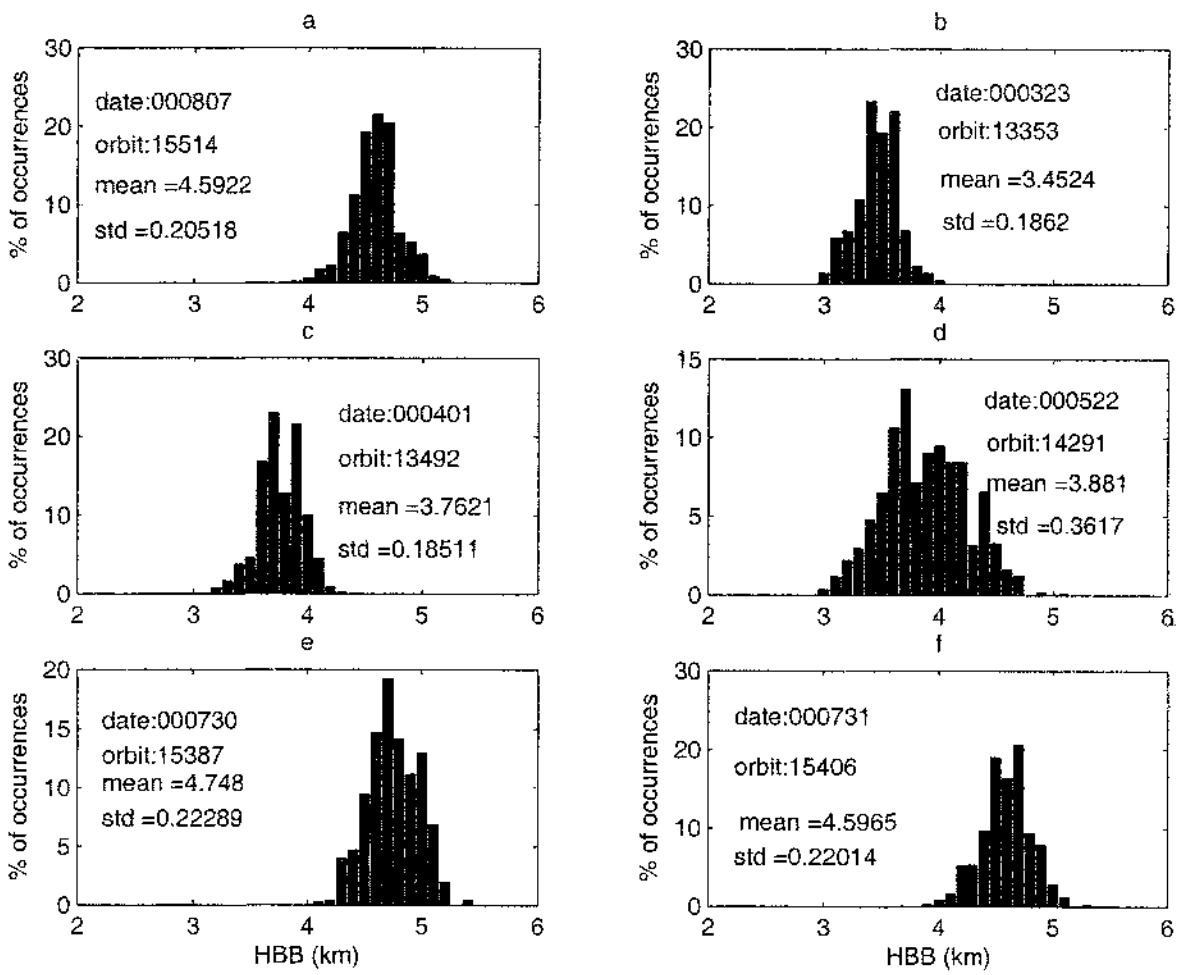

Figure 7.53: Histograms of HBB: a) during Typhoon Jelawat b-f) same location during other times but different months.

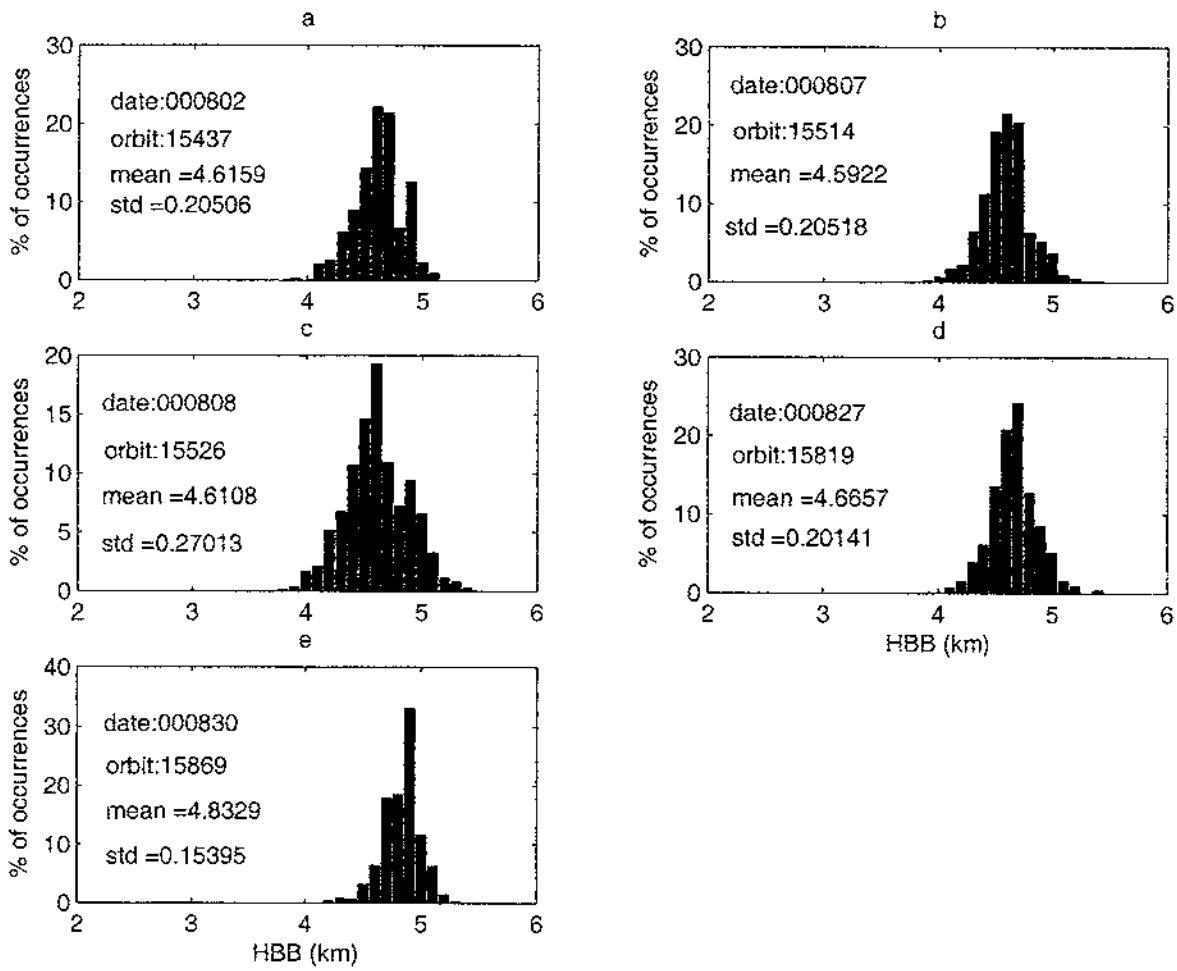

Figure 7.54: Histogram of HBB during Typhoon Jelawat and other times for the same month and same location.

Chapter 8

SUMMARY, CONCLUSION AND SUGGESTIONS FOR FUTURE WORK

8.1 Summary and Conclusion

The following is the summary and conclusion of this research:

- The distribution of precipitation and its vertical structure dominates the electromagnetic propagation properties of earth-space radio frequency (RF) paths at frequencies higher than S-band. Cumulative path attenuation due to precipitation is the most significant effect. Using measurements from the TRMM PR, monthly maps of attenuation are developed over the globe. The variability of these attenuation maps is studied over a 12-month seasonal cycle for the year 2000. The attenuation maps showed the expected seasonal variability of attenuation between northern and southern hemisphere. In addition, the observation shows the contrast between land and ocean. A simple microphysical model was developed to estimate the reflectivity and attenuation due to precipitation at Ka-band based on the observations at Ku-band. This model incorporated the variability in the microphysical structure between convective and stratiform precipitation that has been extensively studied in the TRMM program. The estimation of attenuation at Ka-band is useful for the design of space systems at Ka-band. In addition, the estimation

of observed reflectivity at Ka-band provides a basis to estimate the fraction when Ka-band measurements will be completely lost due to attenuation, indicating that dual-frequency techniques cannot be used. Analysis over a 12 month seasonal cycle using TRMM observations indicate that, using 2 km altitude as a reference, the Ka-band observations are lost only for a small fraction of the observations. Figure 8.1 shows the block diagram of the summary of the procedures used to estimate PIA at Ka-band from the TRMM PR observations data (Ku-band).

- Precipitation radar uses the surface reference method to estimate the attenuation encountered in the observation of radar reflectivity. The cumulative attenuation (A) measured from the surface reference method can be distributed along the radar range using a power law relationship between the specific attenuation (k) and reflectivity factor (Z) written as, $k = \alpha Z^{\beta}$. A commonly used approximation is that β is constant and α changes according to the drop size distribution. More recently, physical interpretation of the α has been provided with the normalized drop size distributions. Chapter 5 describes a procedure to estimate the RSD parameters from the measured attenuation and reflectivity values obtained from TRMM precipitation radar observations. The α adjustment data is used to derive an equivalent Nw using the concept of normalized Gamma RSD. Coincident data collected with ground radar during the TRMM field campaigns have been used to cross-validate the estimates of RSD parameters obtained from TRMM precipitation radar measurements with those obtained from ground polarimetric radar observations. The results of cross-validation show fairly good agreement with the RSD parameters retrieved from TRMM precipitation radar and the ground radar based estimates, although a few of the comparisons were off. The procedure presented in this research provides a powerful scheme to study RSD

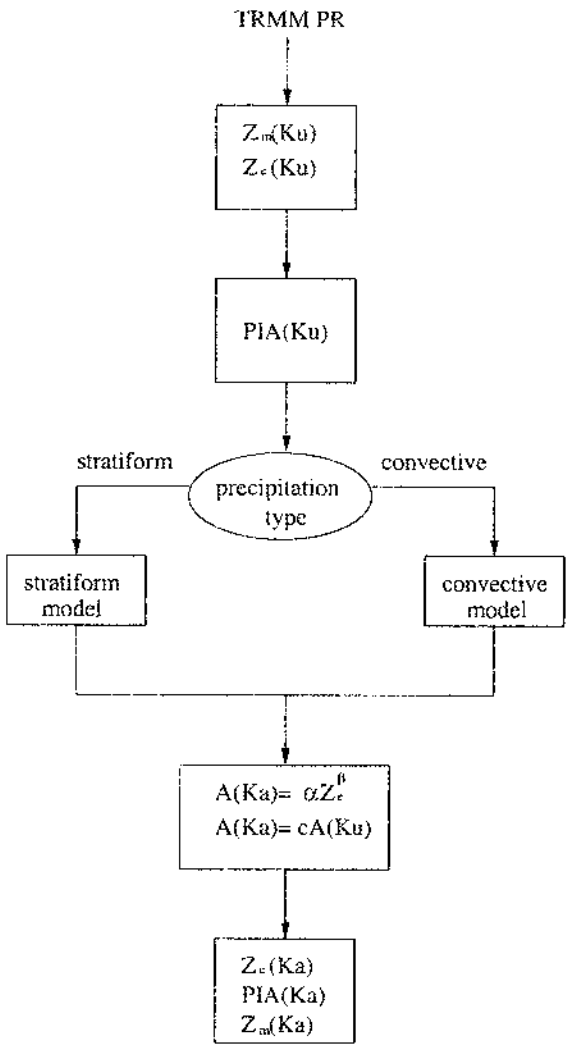

Figure 8.1: Block digram of procedures to estimate PIA at Ka-band from the TRMM PR (Ku-band).

parameters on a global scale; therefore, the algorithm is used to generate monthly global maps of RSD parameters.

- An accurate estimate of rain rate from the TRMM PR requires correction for attenuation. Because the Hitschfeld-Bordan method tends to become unstable at higher rain rates, the surface reference technique is used in the PRMM PR algorithms to complement it. Despite the simplicity of the basic concept, an assessment of the reliability of the technique is difficult because the statistical properties of the surface return depend not only on surface type (land/ocean) and incident angle, but also on the detailed nature of the surface scattering. Using measurements from the TRMM PR, monthly maps of σ^0 at different incident angles are developed over the globe. The variability of these σ^0 maps is studied over a 12-month seasonal cycle for the year 2000. Also, TRMM PR data was used to examine σ^0 over land and ocean during rain and rain-free time. It is induced from Chapter 6 that the incident angle has the strongest effect on the backscattering coefficient rather than other system parameters. The average standard deviation over land surface is higher than the average standard deviation over the ocean. Finally, in moving to off-nadir, σ^0 becomes more uniform. In addition, single orbit data had lower standard deviation than historical data, there by providing guidance on the choice of data for surface reference.

- The radar bright band results mostly from melting of snowflakes as they fall through the $0°C$ isotherm. As the ice is gradually transformed to liquid, the refractive index and, hence, the backscattering cross section increase, and the radar echo intensity increases to a maximum at $\approx 200m$ below the $0°C$ isotherm. In general, the bright band height is obviously linked with the height of the 0o C isotherm in the atmosphere, and consequently is dependent

on the time of the year and on the climate (and hence the location). Using measurements from the TRMM PR, monthly maps of HBB and the height of freezing are developed over the globe. The variability of these HBB maps is studied over a 12-month seasonal cycle for the year 2000. Also, TRMM PR data are used to examine the bright band widths as a function of 3dB of peak reflectivity. The first analysis does not show any clear correlation. The mode value of 3dB width was 0.5 km, whereas the mean value is 1 km. This issue must be studied further with type of melting.

8.2 Suggestions for Future Work

The following are suggestions for future work in this area of research:

- Research is needed on how well this attenuation computation can be used in low earth orbit satellite communication and radar system designs in order to change the way communication system designs are done.
- The simple microphysical model used in this research should be improved in the future by considering a multilayer precipitation that includes different types of aggregate and graupel such as dry and wet.
- σ^0 analysis must be extended over a much larger data set, especially over land in order to examine the statistical properties of the surface return, specially critically examine the role of ??0 in the accuracies of retrievals. .
- Study the reliability of the SRT during different types of precipitation.
- Alternate definitions of BB thickness specifically designed the PR should be pursued.

Bibliography

[1] Amayenc, P. and Marzoug, M., *A survay of algorithms studies developd at CRPE for range profiling of rain rate from a spaceborne radar*, Proc. Int. Workshop on the Processing and Utilization of the Rainfall Data Measured from Space, Tokyo, Japan, Communication Research Laboratory, pp 289–294, 1992.

[2] Atlas, D., Merker, M. and Hitschfeld, W., *Scattering and attenuation by nonspherical atmospheric particles*, J. Atmos. Terr. Phys., vol. 3, pp 108–119, 1953.

[3] Austin, P. and Bemis, A., *A quantitative study of the bright band in radar precipitation echoes*, J. Meteor., vol. 7, pp 145–151, 1950.

[4] Battan, L., *Radar observations of the atmosphere*, University of Chicago Press., pp 279, 1973.

[5] Beaver, J. and Bringi V. N., *The application of S-band polarimetric radar measurements to Ka-band attenuation prediction*, Proc. IEEE, vol. 85, no. 6, pp 893–909, 1997.

[6] Bolen, S. and Chandrasekar, V., *Quantitative cross validation of space-based and ground-based radar observations*. J. Appl. Meteor., vol. 39, pp 2071–2079, 2000.

[7] Bringi, V. N. and Chandrasekar, V., *Polarimetric doppler weather radar: principles and applications*. Cambridge University Press, New York, Ny, 2001.

[8] Bringi, V. N., Huang, G. and Chandrasekar, V., *A Methodology for estimating the parameters of a gamma raindrop size distribution model from polarimetric radar data: application to a squall-line event from the TRMM/Brazil campaign*. J. Atmospheric and Oceanic Technology, Vol. 19, pp 633- 645, 2002.

[9] Cunningham, R., *A different explanation of the bright line*, J. Meteor., vol. 4, pp 163, 1947.

[10] Dennis, A. S., *Fundemental limitations on precipitation observations from satellites*, NASA CR-52848, Stanford Research Institute, Menlo Park, Calif, 1963a.

[11] Dennis, A. S., *Rainfall determinations by meteorological satellit radar*, NASA CR-50193, Stanford Research Institute, Menlo Park, Calif, 1963b.

[12] Dissanayake, A. and McEwan, N., *Radar and attenuation properties of rain and bright band*, IEEE Conf. Publ. Antenna and Propagation, London, UK, pp 125 129, 1978.

[13] Durden, S. and Haddad, Z., *Comparison of radar rainfall retrieval algorithms in convective rain during TOGO COARE*, J. Atmos. Oceanic Technol., vol. 15, pp 1091–1096, 1998.

[14] Eckerman, J. and Wolf, E. A., *Spaceborne meteorological radar measurements requirements meeting*, NASA X-900-75-198, GSFC, Greenbelt, Maryland, vol. 57, pp 57, 1975.

[15] Ekpenyong, B. and Srivastave, R., *Radar characteristics of the melting layer-A theoretical study*, Preprints, 14th Int. Conf. on Radar Meteorology, Tucson, AZ, Amer. Meteor. Soc., pp 161 166, 1970.

[16] Fabry, F. and Zawadzki, I., *Long-term radar observations of the melting layer of precipitation and their interpretation*. Journal of the Atmospheric Sciences, vol. 52, no. 7, pp 838 851, 1994.

[17] Fujita, M., *An algorithm for estimating rain rate by dual-freqency radar*, Radio Sci., vol. 18, pp 697-708, 1983.

[18] Fujita, M., Okamota, K., Masuko, M., Yoshikado, S. and Nakamura, K., *Interferenceof rain rate profile and path-integrated rain rate by an airborne microwave rain scatterometter*, Radio Sci., vol. 20, pp 631-642, 1985.

[19] Goldhirsh, J., *Analysis of algorithms for retrievel of rain rate profiles from a spaceborne dual-wavelength radar*, IEEE Trans. Geosci. Remote Sens., vol. 26, pp 98 114, 1988.

[20] Gorgucci, E., Chandrasekar, V., Bringi, V. N. and Gianfranco S., *Estimation of raindrop size distribution parameters from polarimetric radar measurements*. Journal of the Atmospheric Sciences, Vol. 59, no. 15, pp. 2373-2384, 2002.

[21] Hardaker,P., Holt, A. and Collier, C., *A theoretical study of the scattering effects of the melting layer*, Preprints, 25th Conf. on Radar Meteorology, Paris, France. Amer. Meteor. Soc., pp 725 728, 1991.

[22] Hitschfeld, W. and Bordan, J., *Errors ingerent in the radar measurement of rainfall at attenuating wavelengths*. J. Meteor., vol. 11, pp 58 67, 1954.

[23] Iguchi, T. and Meneghini, R., *Intercomparison of single-frequency methods for retrieving vertical profile from airborne or spaceborne radar data*, J. Atmos. Oceanic Technol., vol. 11, pp 1507-1516, 1994.

[24] Iguchi, T., Kozu, T., Meneghini, R., Awaka, J. and Okamoto, K., *Rain-profiling algorithm for the TRMM precipitation radar*, J. Appl. Meteor., vol. 39, pp 2038-2052, 2000.

[25] Im, E. and Kelloge, K., *Spaceborne radar for rain and cloud measurements: A conceptual design*, Proc. IGARSS'90 Symp., College Park, Maryland, pp 424-428, 1990.

[26] Im, E. and Li, F., *Tropical rain mapping radar on the space station*, Proc. IGRASS'89 Symp., Vancouver, BC Canda, pp 1485-1490, 1989

[27] Klaassen, W., *Radar observations and simulation of the melting later of precipitation*, J. Atmos. Sci., vol. 45, pp 3741-3753, 1988.

[28] Kozu, T. and Nakamura, K., *Rainfall parameter estimation from dual radar measurements combining reflectivity profile and path-integrated attenuation*, J. Atmos. Oceanic Technol., vol. 8, pp 259-270, 1991a.

[29] Kozu, T., Nakamura, K., Mengehini, R. and Boncyk, C., *Dual-parametrs radar rainfall measurement from space: A test result from an aircraft experiment*, IEEE Trans. Geosci. Remote Sens., vol. 29, pp 485-592, 1991b.

[30] Lhermitte, R. and Atlas, D., *Doppler fall speed and particle growth in stratiform precipitation*, Preprints, 10th Radar Meteorology Conf., Wshington, DC, Amer. Meteor. Soc., pp 297-302, 1963.

[31] Liao, L., Meneghini, R. and Iguchi, T., *Simulations for mirror image return of air/space-borne radar in rain and their applications in estimating path attenuation*, IEEE Trans. Geosci. Remote Sens., vol. 37, pp 1107-1121, 1999.

[32] Marecal, V., Tani. T., Amayenc, P., Klapisz, C., Obligis. E. and Vitard, N., *Rain relations inferred from microphysical data in TOGO COARE and their use to test a rain-profiling method from radar measurements at Ku-band*, J. Appl. Meteor., vol. 12, pp 1629–1646, 1997.

[33] Marshall, J., Langille, R. and Palmer, W., *Measurement of rainfall by radar*, J. Meteor., vol. 4, pp 186 192, 1947.

[34] Marzoug, M. and Amayenc, P., *Experimental tests of an improved sigle frequency algorithm for rain rate frofiling using airborne radar data*, Proc. 25th Int Conf. on Radar Meteorol., Paris, France, Am. Meteor. Soc., pp 396 399, 1991.

[35] Marzoug, M. and Amayenc, P., *A class of single- and dual- frequency algorithms for rain-rate profiling from a spaceborne radar. Part I: Principle and test from numerical simulations*, J Atmos. Oceanic Technol., vol. 11, pp 1480–1506, 1994.

[36] Marzoug, M. and Amayenc, P., *A new class of dual-frequency algorithms for rain rate profiling from a spaceborne radar: Principle and tests*, Proc. IGARSS'92., Houston, Texas, pp 1376–1379, 1992.

[37] Marzoug, M. and Amayenc, P., *Algorithms for range oprofiling of rain rate from a spaceborne radar: Overall validation using airborne radar data*, Proc. 26th conf. on radar meteoral., Norman, Okla., Am. Meteorol. Soc., pp 690–693, 1993.

[38] Mengehini, R., *Rain-rate estimates for an attenuation radar*, Radio Sci., vol. 13, pp 459 470, 1978.

[39] Mengehini, R., Eckerman, J. and Atlas, D., *Dtermination of rain rate from a spaceborne radar using measurements of total attenuation*, IEEE Trans. Geosci. Remote Sens., vol. 21, pp 34-43, 1983.

[40] Mengehini, R. and Nakamura, K., *Range profiling of the rain rate by an airborne weather radar*, Remote Sens. Environ., vol. 31, pp 193-209, 1990.

[41] Meneghini, R., Nakamura, K., Ulbricth, C. W. and Atlas, D., *Experimental test of methods for measurement of rainfall rate using and airborne dual-wavelength radar*, J. Atmos. Oceanic Technol., vol. 6, pp 637-651, 1989.

[42] Meneghini, R. and Kozu, T., *Spaceborne Weather Radar*, Artech House, Inc., Norwood, Mass., 1990.

[43] Meneghini, R., Iguchi, T., Kozu, T., Liao, L., Okamoto, K., Jones, J. and Kwiatkowski, J., *Use of the surface reference technique for path attenuation estimates from the TRMM precipitation radar*, Journal of Applied Meteorology, vol. 39, pp 2053-2070, 2000.

[44] Meneghini, R., Kozu, T., Kumagai, H. and Boncyke, W., *A study of rain estimation methods from space using dual-wavelength radar measurements at near-nadir inicidence over ocean*, J. Atmos. Oceanic Technol., vol. 9, pp 364-382, 1992.

[45] Pruppacher, H. and Klett, J., *Microphysics of clouds and precipitation*, 2nd ed., Dordrecht, Kluwer Academic Publishers, 1997.

[46] Ryde, J. W., *The attenuation and radar echoes produced at centimetre wavelengths by varoius meteorological phenomena*, Meteorological Factors in Radio Wave Propagation, Phys. Soc., pp 169-188, 1946.

[47] Sekhon, R. and Srivastava, R., *Doppler radar observations of drop size distributions in a thuderstorm*, J. Atmos. Sci., vol. 28, pp 983-994, 1971.

[48] Testude, J., Amayenc, P. and Marzoug, M., *Rainfall rate retrieval from a spaceborne radar: Comparison between single-frequency, dual-frequency, and dual-beam techniques*, J. Atmos. Oceanic Technol., vol. 9, pp 599 623, 1992.

[49] Testud, S., Black, R., Amayence, P. and Dou, X., *The concept of normalized distribution to describe raindrop spectra: A tool for cloud physics and cloud remote sensing*, J. Appl. Meteor., vol. 40, pp 1118-1140, 2001.

[50] *TRMM Science Data and Information System Vol.3 Release 5.03*, National Space Development Agency of Japan(NASDA) and National Aeronautics and Space Administration(NASA), 2000.

[51] Ulbrich, C. W., *Natural variations in the analytical form of the drop size distribution*, J. Climate Appl. Meteor., vol. 22, pp 1764-1775, 1983.

[52] Wexler, H., *Observing the weather from a satellite vehicle*, J. Brit. Interplanetary Soc., pp 269 276, 1954.

[53] Wexler, H., *The satellite and meteorology*, J. Astronaut., vol. 4, pp 1–6, 1957.

[54] Wexler, R., *An evaluation of the physical effects in the melting layer*, Preprints, Fifth Weather Radar Conf., Fort Monmouth, N.J. Amer. Meteor. Soc., pp 329 334, 1955.

[55] Wexler, R. and Atla, D., *Factors influencing radar echo intensities in the melting layer*, Quart. J. Roy. Meteor. Soc., vol. 82, pp 349 351, 1956.

[56] Widger, W. K. and Touart, C. N., *Utilization of satellite observations in weather analysis and forecasting*, Bull. Am. Meteorol. Soc., vol. 38, pp 521 533, 1957.

[57] Willis, P. T., *Functional fits to some observed drop size distribution and parameterization of rain*, J. Atmos. Sci., vol. 41, pp 1648-1661, 1984.